**King's College London**
**Division of Imaging Sciences and Biomedical Engineering**

# Curvilinear Analysis and Approximation of Cardiac DTI In-Vivo

## PhD Thesis

Nicolas Toussaint

PhD Advisors: Philip G. Batchelor, Maxime Sermesant,

Sebastian Kozerke, and Tobias Schaeffter

defended July, $26^{th}$, 2012 in **London**

*To Philip*

# Abstract

Diffusion Tensor MRI can be used to depict the anisotropy of tissue. Translation of this technique to moving objects such as the beating heart has recently become feasible, but remains a challenging task, often leading to high noise levels and limited accuracy. Ultimately, knowledge of the 3D fibre architecture of the myocardium *in-vivo* should allow for a better understanding of the cardiac function both in healthy and pathological situations.

The main goal of the work presented in this thesis is to overcome the difficulties that such technology presents, by introducing a combination of image processing and analysis approaches. In particular, the characteristic ellipsoidal shape of the left ventricular chamber is used to introduce a shape-based prolate spheroidal coordinate frame that allows for comprehensive, robust and dedicated analysis of diffusion tensor data within the myocardial wall. It is shown that the description of this information is more compact in this coordinate frame. Furthermore, it is demonstrated that the acquisition limitations can be overcome by introducing an approximation scheme based on this coordinate frame. These techniques are tested on *ex-vivo* datasets to assess their fidelity and sensitivity. Finally, these techniques are applied *in-vivo* on a group of healthy volunteers, where 2D DTI slices of the LV were acquired at end diastole and end systole, using cardiac dedicated diffusion MR acquisition. Results demonstrate the advantages of using curvilinear coordinates both for the analysis and the approximation of cardiac DTI information. Resulting *in-vivo* fibre architectures were found to agree with previously reported studies on *ex-vivo* specimens. The outcome of this work can open the door for clinical applications and cardiac electrophysiology modelling, and improve the understanding of the left ventricular structure and dynamics.

**Keywords:**

cardiac DTI, cardiac fibre architecture, curvilinear coordinates, prolate spheroidal coordinates, kernel-based interpolation, group-wise analysis, cardiomyopathy

# Acknowledgments

First and foremost, I would like to offer my deepest gratitude, profound respect and admiration to Philip Batchelor, under whose supervision I carried my PhD, until his sudden death in August 2011. His knowledge and open-mindedness of a large spectrum of scientific topics were incredibly helpful along this project. I greatly admired his style of work and his selfless dedication to science. Each discussion with him about a single question would eventually lead to a multitude of constructive conclusions and interesting (usually theoretical) other questions. I am glad that since the beginning of the PhD project, Philip allowed me to take responsibilities. For instance, only a few months after starting the project, I went to Zürich for a month to collaborate with Sebastian Kozerke and Christian Stoeck. I felt privileged to have been given so early these opportunities to shape the project according to everyone's needs, collaborating with physicians and clinicians in order to define the demands and challenges that are at stake.

I am extremely grateful to Maxime Sermesant, my second PhD advisor. Our regular meetings and discussions have always been very constructive and fruitful. His great expertise in cardiac physiology, imaging, and medical imaging techniques in general were of crucial help during all these years of collaboration.

This project could not have been accomplished without the unforgettable support of Nicholas Ayache, Research Director of the Asclepios research team at INRIA. I admire his expertise and skills allowing him to always foresee the future paths of medical imaging. I am deeply grateful for his warm welcome in the Asclepios team on multiple occasions, each of them was a veritable boost to my PhD project. I want to thank all Asclepios members for some really interesting interactions. In particular, Xavier Pennec helped me apprehending some theoretical aspects of my projects, as well as Stanley Durrlemann for his help on the application of the current theory on fibre field dissimilarities. Being part of the conception of the MedINRIA project was also a greatly interesting part of my time in Asclepios. For that I would like to express my gratitude to all the people I have worked with on these matters : Maxime Sermesant, Jatin Relan, Benoît Bleuzé, Pierre Fillard, John Stark, Olivier Clatz, Michael Knopke, and Florian Vichot. I thank Isabelle Strobant, without whom none of these visits to Sophia Antipolis would have been possible. I would not have achieved any of this without the influence and the great help of Pierre Fillard. He greatly inspired me and passed on to me the interest and curiosity on medical imaging in general.

I could not be grateful enough to my collaborators from ETH Zürich. Sebastian Kozerke, my third PhD advisor, welcomed me on two occasions at the Biomedical Engineering research lab, each of those occasions was a most helpful and productive stay. I would like to express all my thanks to Christian Stoeck, who performed all the MR acquisitions that allowed the application of my methodologies to *in-vivo* data. The dedication he showed to the improvement of the MR sequences used in this thesis has shown to be very fruitful all along the project.

I would like to show my appreciation to my referees Prof. Daniel Alexander and Prof. Olaf Dössel for accepting and taking the time to read and review my manuscript.

Finally, I would like to thank all my colleagues at King's College London. Interactions with Gerald Greil, Kawal Rohde, Geoff Charles-Edwards, and all researchers in the lab were of great influence. In particular, I would like to thank Reza Razavi.

He welcomed me and my PhD project, always showing great interest in the latest advances of the project, and is helping in attempting to move this work towards clinical applications. Many thanks to Tobias Schaeffter, who has accepted to replace Philip Batchelor as PhD advisor for the last months of the project. These three years would not have been the same without the support of Christian Bürger, Alberto Gomez, Daniel Giese and Markus Henningson, partners at work and in crimes, Radomir Chabiniok, Markand Patel for the collaborative work on the anterior commissure, and Jedrzej Burakiewicz for his countless provision of coffee. The constant support of my family during this time has been extremely important to me and I would like to thank all of them.

# Contents

Chapter 1

# Introduction

## Contents



## 1.1 Motivations and Challenges

Understanding the cardiac function has always generated a great academic interest and many investigations [Mall 1911, Fernandez-Teran 1982]. Over the last decades, there has been an important and growing interest in attempting to unveil the macroscopic and microscopic architecture of the heart, and the relation between cardiac function and structure.

The heart has the critical role of ensuring blood flow in the entire vascular system. The right heart receives deoxygenated blood from the vena cava and pumps it to the lung system for re-oxygenation. The left heart receives oxygenated blood from the pulmonary veins and ejects it to the entire vascular system through the aorta. These two systems are correlated through a constant amount of blood in the body. The anatomical structure of the heart is illustrated in Fig. 1.1. The function of the heart can be observed at different levels. The mechanical movement is the macroscopic phenomenon that is directly observed by medical imaging techniques. This motion is obtained by the contraction of microscopic myocardial cells, the myocytes. The contraction is induced by an electrical impulse propagating throughout the heart. The electrical activity of the heart can be observed indirectly with the help of electrodes placed on the chest of the patient or volunteer, resulting in an electrocardiogram (ECG). The sequence of actions of the ventricular function is illustrated in Fig. 1.2. The beginning of the systolic phase is marked by the R-wave. As the ventricular pressures increases, the aortic valve opens to allow rapid ejection of the blood into the vascular system through the aorta. After contraction (end systole), the aortic valve closes, quickly followed by the opening of the mitral valve, to allow filling of the ventricle from the pulmonary system during the diastolic phase.

The cardiac myocytes are elongated mono-nucleated cells about 10-20$\mu m$ wide and 80-100$\mu m$ long. Macroscopically speaking, they are highly connected with each other adjacently, and with a branching structure. The electrical impulse triggering cell contraction is propagating at very high speed in the direction of the myocytes. The propagation velocity in the direction of the myofibre directions is about three times greater than in the perpendicular plane. Therefore, the spatial arrangement of these myocytes is of great importance as it explains the complex contraction of

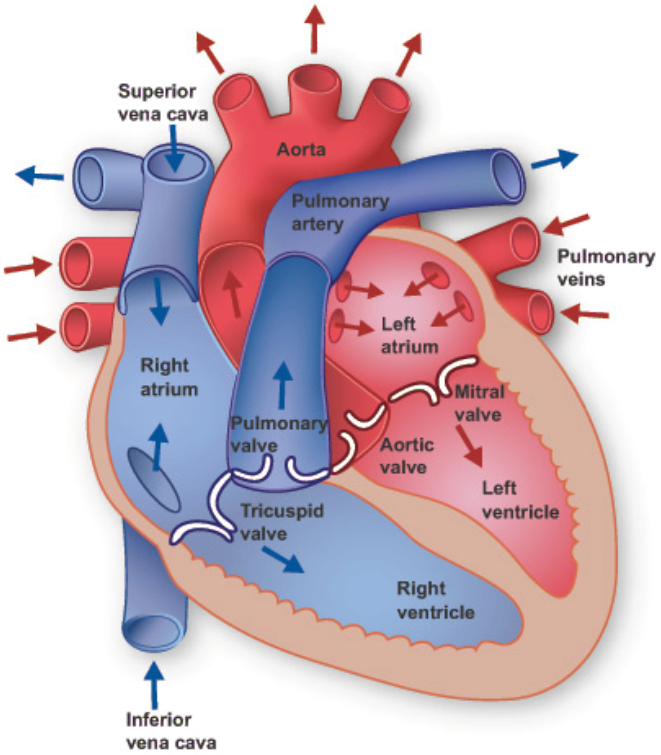


**Figure 1.1: Heart Anatomy**: *The right heart (in blue) ejects deoxygenated blood to the lungs. The left heart (red) ejects reoxygenated blood to the vascular system (from* http://www.texasheart.org*)*

the atria and ventricles, and by extension the cardiac function [Goergen 2011]. The myocardial fibres are organized into layers, known as laminar sheets [LeGrice 1995], which are 3 to 4 cells thick. These layers are separated by an extra-cellular collagen network. The electrical coupling is strong within a laminar sheet and sparse between laminae. In early studies [Streeter 1969, Streeter 1979, Fernandez-Teran 1982], the authors already describe the orientation of the myocyte fibres throughout the left ventricle (LV) as a complex and very organized structure. In multiple studies these orientations were found to have a significant importance in the cardiac output [Bovendeerd 1992, Kanai 1995, Vendelin 2002], and in remodelling of the heart after infarction [Ursell 1985, Fieno 2004, Wu 2006]. In particular it was found that the torsion and the local stress of the ventricle seems to be very sensitive to the local distribution of fibre orientations [Bovendeerd 1994]. These fibre orientations therefore have a crucial role in the understanding of patient specific cardiac function, for instance through modelling [Seemann 2006, Sermesant 2008].

Depicting the arrangement of cardiac fibres has been and still is challenging. Early descriptions from [Streeter 1969, Grimm 1976, Fernandez-Teran 1982, LeGrice 1995] have used histology studies. While these techniques remain gold standard for quantification, they present some significant drawbacks. The most obvious is the invasiveness of the technique. These studies are performed post-mortem. Secondly, the methodology damages the tissue during dissection which can introduce a potential bias in the resulting fibre orientation quantification. Thirdly, these histology studies are (mostly) limited to a selection of ventricular sections, as a complete analysis of the ventricle(s) wall(s) would be too time consuming.

Recently, emergence of diffusion magnetic resonance imaging (MRI) and its

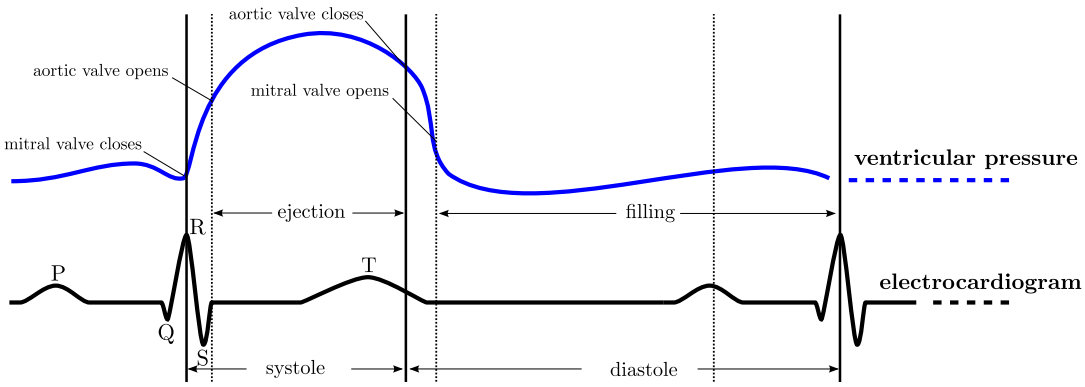


**Figure 1.2:** *The electrocardiogram, or ECG (bottom curve) measures the electrical activity of the heart, which triggers contraction and relaxation of cardiac myocyte fibres, and therefore explains cardiac function. Left ventricular pressure (top curve) is correlated to the ECG and allows understanding the different steps of ventricular function.*

derivatives (e.g. diffusion tensor imaging - DTI) have allowed the depiction of preferred orientation in tissue [Basser 1996]. It has been shown that the main eigenvectors of tensors as acquired with DTI correlate with the direction of the elongated myocytes in the ventricles [Scollan 1998, Hsu 1998]. Post-mortem studies then revealed with great detail the fibre architecture of the LV in healthy animals and humans [Helm 2005, Peyrat 2006, Lombaert 2012]. In the case of pathological hearts, DTI can also potentially provide useful information. For instance, an infarction of the myocardium provokes a change of ventricle shape and a remodelling of the fibre architecture around the infarcted zone [Fieno 2004, Wu 2006]. Post-mortem studies of this remodelling process have been done [Wu 2007, Chen 2003, Helm 2006] where diffusion tensor imaging facilitates the understanding of this complex process in a comprehensive and quantitative way. Measuring this re-orientation on a beating heart is yet to be done.

Most of the literature reporting successful applications of DTI techniques to *in-vivo* environment have been performed on a single slice [Garrido 1994, Edelman 1994, Reese 1995, Tseng 1999]. Those studies demonstrate the feasibility of such acquisition in 2D. In [Sosnovik 2009] the different possible MR acquisition techniques are discussed. It has become clear that such DTI technique translated to *in-vivo* beating heart situations can be of great interest, as it allows to correlate the cardiac structure with its function [Goergen 2011].

Despite the recent acquisition advances cited above, a certain number of challenges are still to be addressed. In particular, it is crucial to adapt the classical image processing and analysis techniques to the specific situation of the LV in order to extract physiologically meaningful information. Additionally, methods allowing robust analysis of the fibre architecture within a population are necessary in order to understand the characteristics of such population, and potentially detect discrepancies between a healthy population and pathological situations such as myocardial infarction or ventricular hypertrophy.

Additionally, the acquisition techniques presented here still require a significant amount of scan time. They often yield limited amount of measures, and high levels of noise. These limitations justify the need of image processing techniques that allow the estimation of the full ventricular fibre architecture information from a limited amount of acquisition measurements, corrupted with significant noise. Fur-

thermore, electrophysiological (EP) modelling of the cardiac function is becoming increasingly important in clinics as it could help the description of pathologies. As these models necessitate global fibre information throughout the ventricle, full estimation techniques as mentioned above would help calibrating the EP models to a specific patient and would potentially improve patient response to treatments such as in cardiac resynchronisation therapy [Niederer 2011].

## 1.2 Problem Statement and Contributions

The three main motivations for this thesis are the following: first, what are the necessary modifications to apply to image and tensor processing tools in order to extract meaningful orientation information from the specific situation of (beating) heart? Second, can the global fibre architecture of the entire LV be approximated from a limited amount of measurements using optimal and adapted methods? And third, can we apply these methods in an *in-vivo* situation in order to estimate the fibre architecture of the heart whilst beating, and confront these results with the literature.

It is therefore the objective of this thesis to address the challenges in depicting the fibre architecture of the beating heart, to provide solutions in the field of biomedical image analysis by developing new image processing tools for the comprehensive interpretation of DTI information of the left ventricle. The main contributions of this thesis can be summarized as follows:

- **Chapter 3**: Develop a conformal mapping methodology that allows the description of (tensor) data in the LV in a robust and reproducible way. This methodology involves a non-linear registration step and a change of coordinates to a Prolate Spheroidal frame where the data is described and analyzed. The method is demonstrated on a database of explanted canine hearts.

- **Chapter 4**: Define an approximation scheme that is dedicated to the estimation of a dense tensor field within the LV from a limited amount of measurement slices. The method and its parameters are tested on an explanted human heart.

- **Chapter 5**: Investigate the influence of certain MRI acquisition parameters on the resulting fibre tractograms through the definition of a local distance metric between tractograms. The method is evaluated on a set of explanted lamb hearts.

- **Chapter 6**: Apply the tools defined in Chapters 3 and 4 in *in-vivo* situation, on a database of 10 healthy volunteers and investigating the dynamics of the fibre architecture.

## 1.3 Organization of the Manuscript

An illustration of the organization of this manuscript is given in Fig. 1.3. In **Chapter 2**, an introduction on theoretical concepts of MRI, and diffusion MR is presented, as well as the concepts of cardiac MRI. The topology of the space of tensors as symmetric definite positive matrices is introduced. Finally, recent advances in *in-vivo* cardiac DTI acquisition are presented.

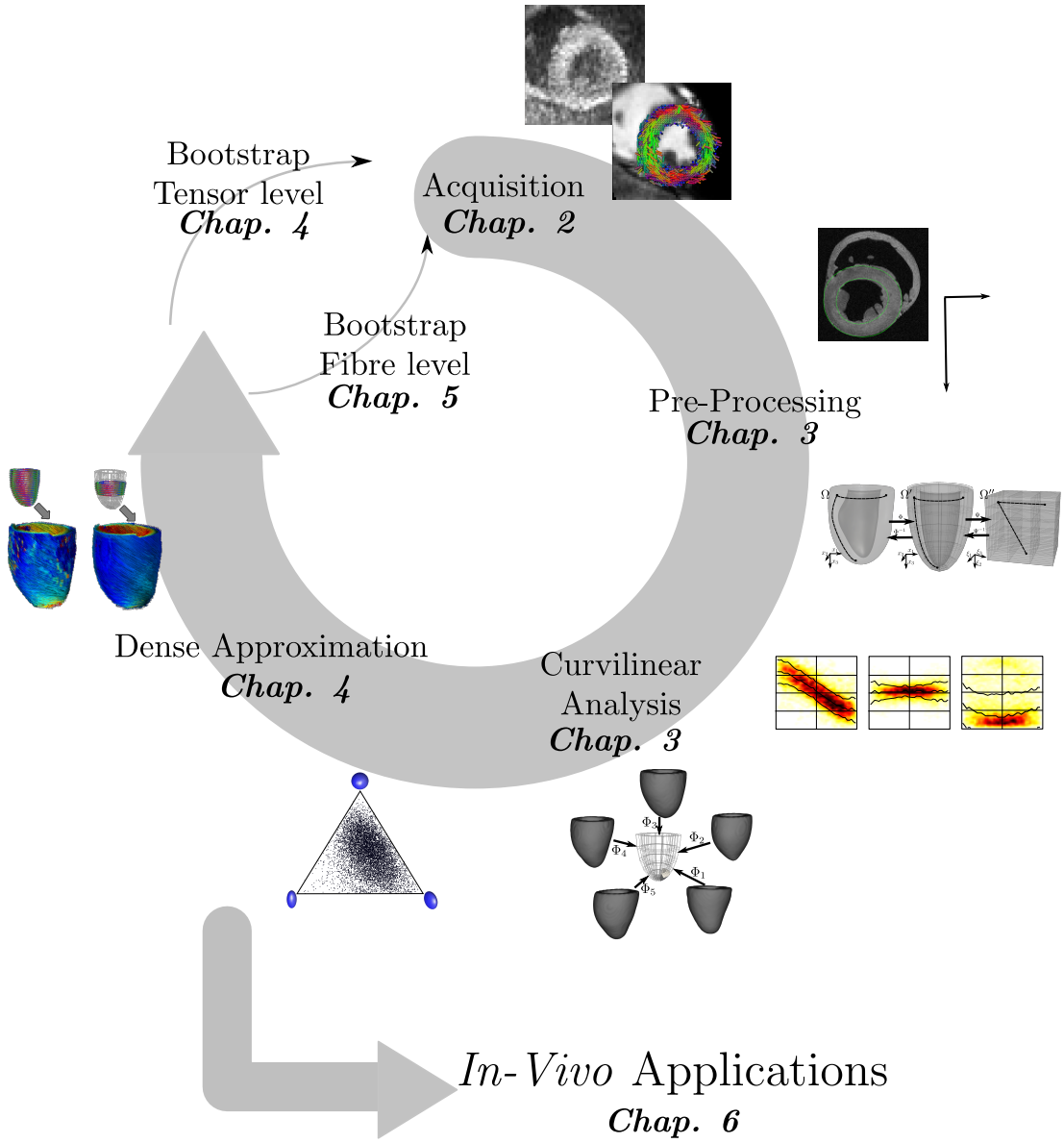


**Figure 1.3: Global Work-flow**: *Chart illustrating the workflow of information, from the acquisition of diffusion weighted images to full left ventricular fibre arrangement approximation. Chapter 6 is dedicated to in-vivo applications.*

**Chapter 3** is dedicated to the description of the main methodological contribution of this thesis. After the introduction of the prolate spheroidal (PS) coordinate system, its suitability to describe information in the LV is demonstrated. A work-flow to transform data from an anatomical LV towards a PS frame is proposed. In particular, the proposed method allows transformation of diffusion tensors from different LV of a population into a normalized reference PS frame. The introduced concepts are illustrated through three concrete examples, where features of interest are extracted from a database of *ex-vivo* canine hearts. Finally, the sensitivity of this method with regards to certain parameters is presented.

**Chapter 4** introduces a dense approximation method from sparsely acquired LV noisy diffusion tensors. An approximation operator in PS coordinates is presented. The operator makes use of a convolution kernel bandwidth matrix parameter. Using an *ex-vivo* human DTI dataset, optimal values of this matrix parameter are found

by defining a least square criterion on the approximated tensor field. A performance comparison between the proposed PS operator and the same operator in Cartesian coordinates is presented. A detailed study on the sensitivity of the proposed method is presented. Finally, the dense approximation scheme is extended to allow for localised approximation of tensors using zone-dependent kernel parameters.

In **Chapter 5**, the influence of acquisition parameters on the output fibre tractography results is investigated. A method allowing the comparison of fibre fields without point correspondence is proposed. This methods utilizes the concept of currents to derive a distance index between fibre fields. The proposed scheme is tested on synthetic fibre tractography and applied to a *ex-vivo* lamb DTI dataset to assess the influence of noise and acquisition plane orientation on the global fibre architecture.

**Chapter 6** presents the *in-vivo* applications of the methods introduced in this thesis. A description of two cardiac specific DTI acquisition protocols is given. Necessary registration and restoration preprocessing steps are defined and illustrated. From the sparse DTI data acquired at end systole and end diastole on a small group of healthy volunteers, a detailed group-wise data analysis of the fibre architecture in the healthy left ventricle is derived. The dynamics of this fibre architecture is investigated. Additionally, a method to depict and visualise the laminae structure of the beating LV is presented and applied to systolic *in-vivo* dataset.

Finally, **Chapter 7** concludes this thesis by discussing contributions and providing various perspectives on the presented research.

## 1.4 Personal Publications Related to the Thesis

**[1]** Markand Patel, **Nicolas Toussaint**, Geoffrey Charles-Edwards, Jean-Pierre Lin and Philip Batchelor. *Distribution and fibre field similarity mapping of the human anterior commissure fibres by diffusion tensor imaging.* Journal of Magnetic Resonance Materials in Physics, Biology and Medicine, vol. 23, pages 399–408, 2010. 10.1007/s10334-010-0201-3.

**[2]** Christian T. Stoeck, **Nicolas Toussaint**, Philip G. Batchelor and Sebastian Kozerke. *Sequence Timing Optimization in Multi-Slice Diffusion Tensor Imaging of the Beating Heart.* In Proc. of the the annual meeting of International Society of Magnetic Resonance in Medicine (ISMRM'11), 2011. Abstract 282.

**[3]** Christian T. Stoeck, **Nicolas Toussaint** and Sebastian Kozerke. *Adaptative Trigger delay for Cardiac Diffusion Weighted MR.* In Book of Abstracts, Intl. Soc. in Magn. Reson. Med., Sockholm, June 2010 (ISMRM'10), 2011.

**[4]** Christian T. Stoeck, **Nicolas Toussaint**, Peter Boesinger and Sebastian Kozerke. *Dual Heart-Phase Cardiac DTI Using Local-Look STEAM.* Proceedings of Intl. Soc. Mag. Reson. Med.(ISMRM), vol. 20, 2012.

**[5]** **Nicolas Toussaint**, Christian T. Stoeck, Maxime Sermesant, Sebastian Kozerke, Philip G. Batchelor and Tobias Schaeffter. *In Vivo Human Cardiac Fibre Architecture Estimation using Shape-based Diffusion Tensor Processing.* (manuscript under review).

**[6]** **Nicolas Toussaint**, Stanley Durrleman, Maxime Sermesant, Sebastian Kozerke and Philip G. Batchelor. *Error Assessment on Myocardial Fiber Orientations from DTI Measurements.* In Book of Abstracts, European Society of Magnetic Resonance in Medicine (ESMRMB) 26th Annual Scientific Meeting, vol. 22, no. 1, page 59,

2009.
**[7] Nicolas Toussaint**, Maxime Sermesant, Christian Stoeck, Sebastian Kozerke and Philip G. Batchelor. *In Vivo Human 3D Cardiac Fibre Architecture: Reconstruction Using Curvilinear Interpolation of Diffusion Tensor Images*. In Tianzi Jiang, Nassir Navab, Josien Pluim and Max Viergever, editors, Medical Image Computing and Computer-Assisted Intervention - MICCAI 2010, volume 6361 of *Lecture Notes in Computer Science*, pages 418–425. Springer Berlin / Heidelberg, 2010.
**[8] Nicolas Toussaint**, Christian T. Stoeck, Maxime Sermesant, Sebastian Kozerke and Philip G. Batchelor. *Three-dimensional Prolate Spheroidal Extrapolation for Sparse DTI of the In-vivo Heart*. In Book of Abstracts, International Society in Magnetic Resonance in Medicine, Sockholm, June 2010 (ISMRM'10), 2-7 June 2010.
**[9] Nicolas Toussaint**, Christian T. Stoeck, Sebastian Kozerke, Maxime Sermesant and Tobias Schaeffter. *Statistical Atlas of the Human Left Ventricular Fibre Architecture Using In-Vivo DT-MRI*. Proceedings of Intl. Soc. Mag. Reson. Med.(ISMRM), vol. 20, 2012.

Chapter 2

# Cardiac Diffusion Tensor MRI

## Contents



## 2.1 Magnetic Resonance Imaging

The principles of magnetic resonance imaging originally come from another area of physics : Nuclear Magnetic Resonance (NMR). The dynamics of electrically charged nuclei such as protons ($^1H^+$) make them behave like microscopic magnetic dipoles, rotating at a certain speed. This speed can be explained, or quantified by its oriented angular moment – or spin $\overrightarrow{S}$. Thanks to this movement, the particle induces a magnetic moment $\overrightarrow{\mu}$. Macroscopically speaking, the sum of several such particle's magnetic moments will result in a net magnetization $\overrightarrow{M}$. In a null magnetic field environment, the net magnetization $\overrightarrow{M}$ is the null vector $\overrightarrow{0}$. Magnetic moments $\overrightarrow{\mu}$ are randomly distributed.

**Net magnetization:** Since in presence of an external static magnetic field $\overrightarrow{B_0}$ in the z-direction, these moments $\overrightarrow{\mu}$ align parallel (or anti-parallel) to the direction of $\overrightarrow{B_0}$. The energy state of the anti-parallel state is slightly higher than the parallel one. Thus the number of particles aligned parallel to $\overrightarrow{B_0}$ is slightly higher than those aligned anti-parallel : $N_\uparrow/N_\downarrow > 1$. In presence of a static magnetic field $\overrightarrow{B_0}$, the net magnetization, written $\overrightarrow{M_0}$ is not null and oriented towards the static field. This property is very important as all MR signal measurements rely on this inequality.

**Precession:** Since there is an angle between $\overrightarrow{\mu}$ and $\overrightarrow{B_0}$, there is a torque generated leading to the precession around $\overrightarrow{B_0}$.It *precesses* around it with the *Larmor frequency* $\omega_0 = \gamma B_0$, where $\gamma$ is the gyro-magnetic ratio, depending on the charge and mass of the particle of interest. For instance, protons have a gyro-magnetic ratio of approximately $42MHz.T^{-1}$. Although all proton spins precess at the same frequency (assuming no inhomogeneities in $B_0$), their phases are incoherent. Therefore all vector components perpendicular to the external magnetic field are canceling out and a net magnetization parallel to $\overrightarrow{B_0}$ is formed.

**Radio-Frequency (RF) pulse:** In a population of protons at equilibrium state in an external static magnetic field $\overrightarrow{B_0}$, all spins are precessing around $\overrightarrow{B_0}$ at the Larmor frequency $\omega_0$. Consider now that a time-varying RF electromagnetic field is applied in direction perpendicular to $\overrightarrow{B_0}$ at the exact frequency $\omega_0$ which is equivalent to adding a rotating magnetic field $\overrightarrow{B_1}$, rotating around $B_0$ at the Larmor frequency. Spins then enter a resonance state. This phenomenon is called *excitation*. From a macroscopic point of view, the net magnetization is tilted away from the $\overrightarrow{B_0}$ axis towards the perpendicular plane $xy$. In other words, the longitudinal magnetization $M_z$ decreases while the transverse magnetization $M_{xy}$ increases.

Excitation can also be described as a precession phenomenon with respect to the rotating field $B_1$. The precession also follows the Larmor equation $\omega_1 = \gamma B_1$. The flip angle is defined as the angle between the spin net magnetization and the longitudinal axis $z$, it depends on the strength of the RF pulse $\|B_1\|$ and its duration $\delta$:

$$\alpha_{flip} = \omega_1 \delta = \gamma \delta \|B_1\| \tag{2.1}$$

For instance, for proton spins in a 1.5T MRI, and $\|B_1\| = 10\mu T$, a $\pi/2$ flip angle (maximal transversal magnetization) would require the RF pulse to last $0.585ms$.

**Relaxation, $T_1$ and $T_2$:** When the RF pulse is stopped, the system slowly returns to its equilibrium state, spins loose phase coherence and $M_z$ increases to the initial value while $M_{xy}$ decreases to zero. This phenomenon is called *relaxation*, and two independent processes with two different relaxation times $T1$ and $T2$ can be identified: the longitudinal relaxation (increase of $M_z$) and the transverse relaxation (decrease of $M_{xy}$). The longitudinal relaxation corresponds to the magnetization recovery due to spins jumping back to lower energy states. The transverse relaxation is due to the dephasing of the spins in the $xy$ plane.

Both phenomena are described in Fig. 2.1, they follow exponential behaviours:

$$M_{xy} = M_0.e^{-t/T2} \tag{2.2a}$$

$$M_z = M_0.(1 - e^{-t/T1}) \tag{2.2b}$$

where $M_0$ is the net longitudinal magnetization. $T1$ and $T2$ are respectively called longitudinal and transversal relaxation times.

**Rotating Frame:** As mentioned above, the spins enter a resonance state during the RF pulse. They rotate at the Larmor frequency around the z axis. The net transversal magnetization in Eq. (2.2a) is expressed in a *rotating frame*. In the fixed $xyz$ frame, Eq. (2.2a) would actually correspond to the carrier wave of the true magnetization : $M_x = M_0 e^{-t/T2} \cos(\omega_0 t + \phi)$.

Faraday induction will produce a time-varying voltage at the ports of the receive coil. The voltage produced is proportional to $\omega_0 M_{xy}$. Hence through this coil, a direct measure of $M_{xy}(t)$ can be calculated.

## 2.2 Diffusion MR: Measuring Water Motion

Diffusion as occurring at a microscopic level is the movement of molecules in a medium. This movement is a random path known as Brownian motion. It was first observed by the botanist Robert Brown in 1827 and later explained by Einstein's theory on molecular kinetics in [Einstein 1905].

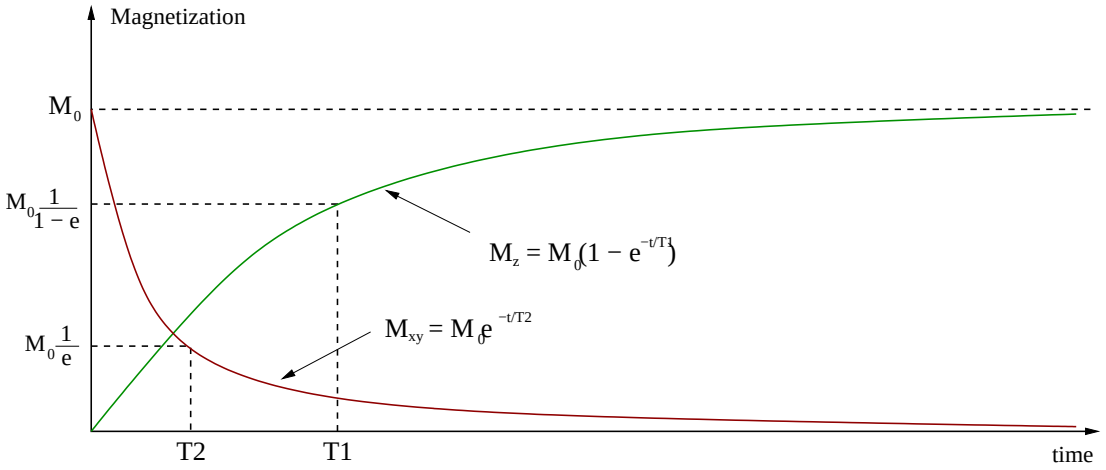


**Figure 2.1: Relaxation process:** *After a* $90^o$ *excitation pulse, spins return to an equilibrium state following exponential relaxation laws. The longitudinal magnetization* $M_z$ *regains amplitude with a time constant* $T_1$*, while transversal magnetization* $M_{xy}$ *decays due to the loss of phase coherency, with a time constant* $T_2$*.*

At a macroscopic level, this random walk of molecules in a medium is characterized by a scalar diffusion coefficient $\mu$, that can be related to the microscopic level by the following statement: the probability of a particle to move by a distance $r$ during a time $\tau$ follows a Gaussian distribution of variance $V = 2\tau\mu$. This expression is true when the medium has isotropic diffusion properties. When the diffusion is anisotropic, this model is not sufficient. The introduction of a spatial diffusion property distribution is necessary. Under the first assumption that the Brownian motion follows a Gaussian distribution in space [Alexander 2002], it can be described by a tensor $D$ of rank 2:

$$D = \begin{pmatrix} D_{xx} & D_{xy} & D_{xz} \\ D_{xy} & D_{yy} & D_{yz} \\ D_{xz} & D_{yz} & D_{zz} \end{pmatrix} \tag{2.3}$$

The $3 \times 3$ matrix $D$ is real, positive and semi-definite, and can be seen as a covariance matrix of the particle movements. The diagonalisation form $\Sigma$ with $D = U\Sigma U^T$ is commonly used for describing tensor $D$. The diagonal elements of $\Sigma$ are known as the eigenvalues of the tensor, denoted $\lambda_1, \lambda_2$ and $\lambda_3$. Let us denote $U = (u_1, u_2, u_3)$, $u_1, u_2$ and $u_3$ are the eigenvectors of $D$. It is common to visualise $D$ as an ellipsoid where $\lambda_1 u_1, \lambda_2 u_2$ and $\lambda_3 u_3$ are its three radii. This representation is shown in Fig. 2.2. $D$ can be also seen as a representation of the covariance matrix of the Brownian motion walk mentioned above. The probability of a particle to move to a distance $r$ in a direction $d$ during a time $\tau$ follows a Gaussian distribution of variance $V = 4\tau d^T D d$.

In organic fibrous tissue, such as brain white matter or muscle, water molecules move more freely along the fibres than in the perpendicular plane. Thus the diffusion process is anisotropic.

**The pulsed-gradient spin echo sequence**: To measure the effect of diffusion in a tissue, the commonly used pulse sequence is the spin echo (SE) sequence introduced by [Stejskal 1965], also called the diffusion weighted sequence. It consists of the following steps (see Fig. 2.3):

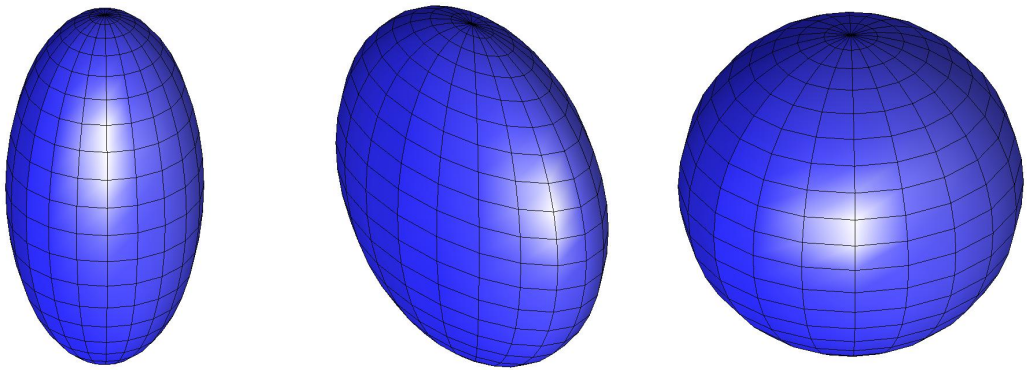

**Figure 2.2: tensor representations:** *A tensor can be represented as an ellipsoid. Three characteristic shapes are shown. (left) Cigar shape indicates a high diffusion anisotropy in a single direction. (middle) Planar shape indicates an "ambiguity" in the tissue anisotropy direction. This can be due to partial volume effect that occurs in fibre crossing in brain white matter, or in the myocardium as an effect of the sheet structure if myo-fibres. (right) The spherical shape indicates an absence of diffusion anisotropy.*

1. The 90 deg RF excitation pulse is applied to tip the magnetization vector perpendicular to $\overrightarrow{B_0}$. Spins precess in phase at the Larmor frequency

2. A gradient $G_d$ of direction $d$ is applied during a time $\delta_d$. The phase of the spins is offset gradually in direction $d$. The value $q$ of this offset is proportional to the gradient strength:
$$q = \gamma \delta_d g \tag{2.4}$$
where $g$ is the projection of the gradient over $\overrightarrow{B_0}$.

3. An inversion pulse (180 deg) is applied to invert all spins.

4. Another gradient $G_d$ is applied during a duration $\delta_d$, the spins rephase gradually in direction $d$. The period between gradients is $\Delta$. If spins have not moved during this period, their phase recovery will be total. However if spins have moved from $x_1$ to $x_2$ along direction $d$, i.e. a displacement of $r = x_1 - x_2$, due to a diffusion process, then the phase will not be entirely recovered. The residual phase is then $qr$, and the altered magnetization at echo time $TE$ is then $m_d(q) = M_0 \exp(iqr)$, where $M_0$ is the magnetization without gradient.

5. At the echo time TE, the signal is acquired. The magnetization being attenuated by the diffusion process, a reference signal (without any diffusion gradient) is needed to measure the diffusion effect relatively to this reference, which is the b-0 image.

To express the net magnetization $M$, the sum the magnetization of each possible spin displacement is calculated:

$$M_d(q) = M_0 \int p(r) \exp(iqr) dr \tag{2.5}$$

Assuming a noise-free signal, the imaginary part is null. A normalized format of the magnetization is derived: the signal net attenuation $A(d, q) = M_d(q)/M_0$.

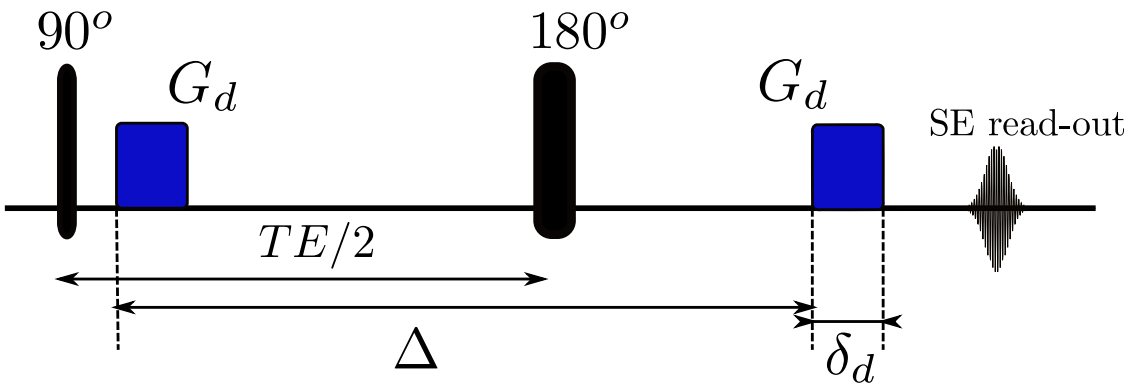


**Figure 2.3: pulsed-gradient spin echo sequence:** *This is the standard sequence used for diffusion encoding measurement. A double gradient $G_d$ is applied in direction $d$ to phase-shift the spins that have moved in this direction during the period $(\Delta - \delta/3)$. The sequence has to be repeated $N > 6$ times to reconstruct a diffusion Gaussian profile, i.e. a tensor.*

Following calculus of the attenuation expression detailed in [Stejskal 1965] or in [Basser 1994, Rohmer 2006] leads to:

$$\log(A_d(q)) = -\gamma^2\delta^2(\Delta - \delta_d/3)g^2 d^T D d \tag{2.6}$$

This calculus derives from the integral function of the gradient over the time of diffusion. Recalling that $\gamma$ is the gyro-magnetic ratio of the particle (in $s^{-1}.T^{-1}$) and $g$ is the constant projection of the gradient among $\overrightarrow{B_0}$ (in $T.m^{-1}$). The scalar coefficient $b = \gamma^2\delta^2(\Delta - \delta_d/3)g^2$ is called the b-factor (in $s.m^{-2}$). The equation can be rewritten as follows:

$$\log(A_d) = -b d^T D d \tag{2.7}$$

This expression of the attenuation assumes a Gaussian model for the diffusion process. Several authors propose other higher order models. For instance the spherical harmonics have been used by [Alexander 2002] to model the diffusion profile on a sphere. A mixture of more than one Gaussian can be considered for the probability function $p$. The model is called *Multi-Compartment*. The attenuation is then written as $A_d = \sum_{i=1}^{n} a_i \exp(-b d^T D_i d)$, where $n$ is the order of the model (number of compartments) and $a_i$ are the compartments' volume fractions.

Diffusion Tensor MRI [Basser 1996] hence consists of measuring – observing -- at each position the signal attenuation $A_d$ due to the diffusion along direction $d$. Recalling that the covariance tensor $D$ has 6 degrees of freedom, at least 6 non-collinear directions $d_i$ are needed to reconstruct $D$, leading to 6 different observations of the attenuation. Fig. 2.4 illustrates this by presenting an example of an acquisition of a brain, where the baseline and the N=6 diffusion weighted images are shown. The method that is commonly used to estimate $D$ is a linear least square fitting scheme. Let us consider $N$ non-collinear directions acquisitions of the attenuation. The tensor reconstruction therefore satisfies:

$$\underset{D}{\operatorname{argmin}} \sum_{i=1}^{N} \left(\log(A_{d_i}) + b d_i^T D d_i\right)^2 \tag{2.8}$$

The more directions acquired – the larger $N$ – the more over-determined is the system, and the better will be the fit of $D$. The gradient directions must be uniformly

distributed on the unit sphere. Jones and colleagues suggested optimal gradient schemes in [Jones 1999, Jones 2004b], based on electro-static repulsion analogies, that are now widely used by MR vendors for the diffusion sequences.

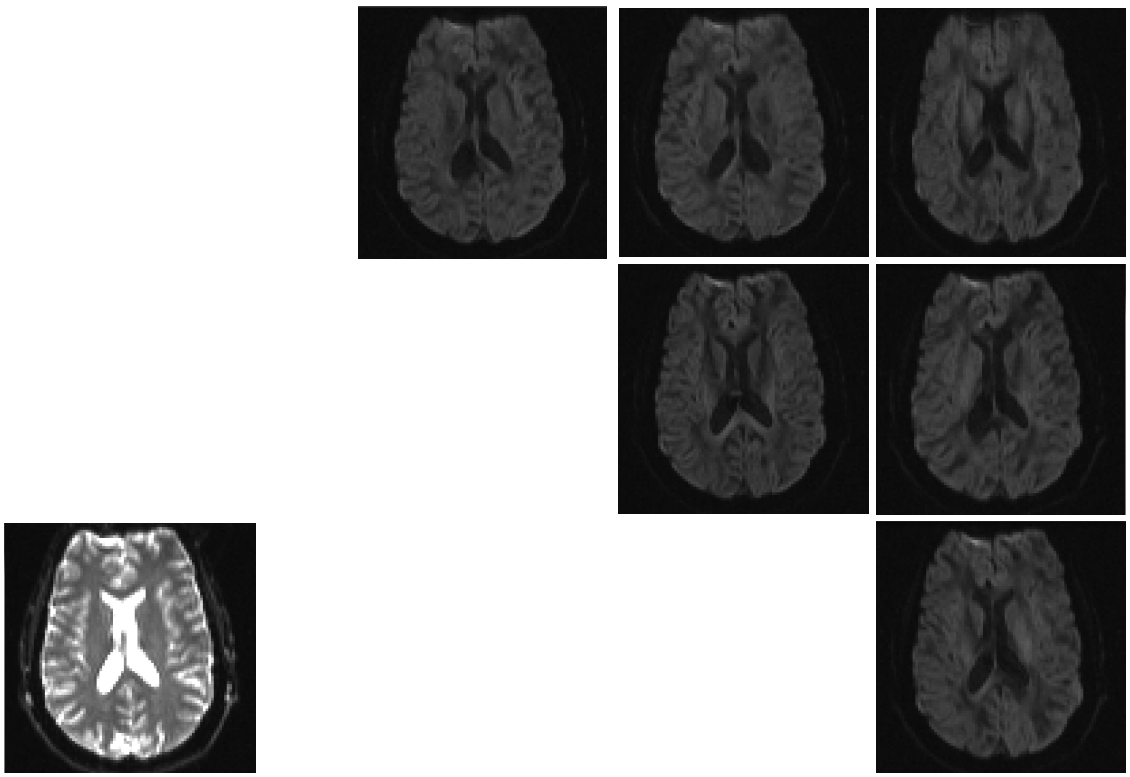

(a) b-0 signal (b) diffusion weighted signal

**Figure 2.4:** *(a) The baseline (b-0) image does not have any gradient encoding and serves as a reference signal $S_0$ for tensor estimation. (b) Here 6 DWIs have been acquired in the directions (x),(xy),(xz),(y),(yz),(z).*

## 2.3 Topology of the Tensor Space

Symmetric positive-definite matrices, or tensors, are commonly used in many different contexts. In mechanics, they express stress [Usyk 2000] for instance. Structure tensors are also used to classify texture [Brox 2003]. In DT-MRI, they are used to express the covariance matrix of the probability distribution of water molecule movement due to their diffusion process within tissue.

From a mathematical point of view, a diffusion tensor belongs to the space of $3 \times 3$ real square matrices that are positive definite. That is, symmetric matrices $M$ that satisfy $\forall x \in \mathbb{R}^3, x^T M x > 0$.

Matrix calculus applies with usual operations, such as addition, difference, average of a set of tensors. A crucial definition is the distance between two tensors. As mentioned by Batchelor *et al.* in [Batchelor 2005], if the distance function is taken as the linearly component definition – $d^2(D_1, D_2) = \sum_{ij} \left(D_{1_{ij}} - D_{2_{ij}}\right)^2$ – then it leads to the property stating that a difference between two positive definite tensors may not be a positive definite tensor, i.e. its eigenvalues may be negative. This behaviour raises the need for a more robust and efficient mathematical framework

for the calculus on the space of tensors. It has been found in [Batchelor 2005] and later in [Arsigny 2006] that the use of the matrix logarithm allows desirable properties for the distance. Indeed, in these frameworks, tensors with null or negative eigenvalues are at infinite distance to any strictly positive eigenvalues tensor.

In particular, Pennec *et al.* defined in [Pennec 2005a, Arsigny 2006] a new adapted metric called Log-Euclidean. In this formulation, the tensor addition and scalar multiplication are re-defined using the matrix-exponential and matrix-logarithm. Assuming two tensors $\Sigma_1$ and $\Sigma_2$, the following equation can be written:

$$\Sigma_1 \oplus \Sigma_2 = \exp(\log \Sigma_1 + \log \Sigma_2) \tag{2.9}$$

$$\lambda \odot \Sigma = \exp(\lambda . \log \Sigma) \tag{2.10}$$

These operators give the space of tensors a structure of vector space when working in the logarithm map. Calculus is therefore very simplified as the tensor interpolation or extrapolation are ensured to stay in the space of positive definite matrices.

Thanks to this vector space structure operations on tensors can be computed in an easier manner: all operations are performed on the matrix logarithm of tensors. The result is mapped to the Euclidean space with the matrix exponential.

The weighted average of a set of tensors, in that sense, is thus defined as followed:

$$S(D_1, w_1 ... D_N, w_N) = \exp\left(\sum_{i=1}^{N} w_i \log(D_i)\right) \tag{2.11}$$

where $w_i$ are weights on tensors.

This metric guaranties the monotony of the tensor's determinant during interpolation, which is a desirable property. It is acknowledged that this framework is not the only one that could be used. In particular, Kindlmann *et al.* introduced a geodesic interpolation method on loxodromes [Kindlmann 2007b] that infers a monotonic variation of the tensor's invariants. In the remaining of this thesis, the Log-Euclidean metric is often used to perform operations on tensors. Tensors denoted $L$ will refer to tensors in the "Log-space", such that $L = \log(D)$

Furthermore, as noted in [Arsigny 2006], one can use the "vec" operator in order to simplify notations and calculus. The vec operator corresponds to a minimal representation of a $3 \times 3$ (symmetric) matrix by a 6 dimensional line vector, that is, a projection of the tensor onto the 6-dimensional orthonormal basis of $Sym^+_{\mathbb{R}}$:

$$\begin{aligned} &\text{vec} : L \mapsto l \\ &\text{with} \begin{cases} L = \begin{bmatrix} L_{11} & L_{12} & L_{13} \\ L_{13} & L_{22} & L_{23} \\ L_{13} & L_{23} & L_{33} \end{bmatrix} \\ l = \left[L_{11}, \sqrt{2}L_{12}, L_{22}, \sqrt{2}L_{13},\ \sqrt{2}L_{23},\ L_{33}\right] \end{cases} \end{aligned} \tag{2.12}$$

This isomorphic operator is useful to minimize representation for statistical operations, and the Euclidean $L_2$ norm of the tensor $L$ is equal to the classical Euclidean norm over vectors of $l$. The $\sqrt{2}$ factors on the off-diagonal coefficients of $L$ are explained by the fact that they are counted twice in the $L_2$ norm over matrices [Kindlmann 2007a]. This notation is particularly used in Chap. 3 in order to simplify notations and calculus.

The invariants of a second order tensor $D$ are the the one dimensional real valued coefficients of the characteristic polynomial of $D$, that is:

$$p(D) := \det(A - \alpha E) \tag{2.13}$$

with E the identity second order tensor and $\alpha$ the indeterminate of $p$ ($\lambda \in \mathbb{C}$). For instance, the tensor trace $\mathrm{Tr}(D)$ and determinant $\det(D)$ are two tensor invariants. In [Kindlmann 2007a], the authors make sure that the introduced metric on tensor monotonically interpolates these tensor invariants.

The shape of a tensor $D$ is fully described by the relationship between its eigenvalues, extracted from the diagonalisation $D = U\Sigma U^T$ (Fig. 2.2). In the isotropic case, the three eigenvalues are equal, $\lambda_1 \sim \lambda_2 \sim \lambda_3$. If $\lambda_1$ is predominant, i.e. $\lambda_1 \gg \lambda_2 \sim \lambda_3$, the tensor has a prolate spheroidal *cigar* shape. Finally, if $\lambda_1 \sim \lambda_2 \gg \lambda_3$, then the tensor is called *planar* and has an oblate spheroidal shape. To quantify these shape characteristics, positive real-valued coefficients have been introduced. For instance, the Fractional Anisotropy [Basser 1996] (FA) is defined as follows:

$$FA = \frac{1}{\sqrt{2}} \frac{\sqrt{(\lambda_1 - \lambda_2)^2 - (\lambda_2 - \lambda_3)^2 - (\lambda_1 - \lambda_3)^2)}}{\sqrt{\lambda_1^2 + \lambda_2^2 + \lambda_3^2}} \tag{2.14}$$

While FA measures the global anisotropy of the tensor, some more geometrical coefficients can be extracted. For instance, the tensor can be separated into its *linear* $D_l$, *planar* $D_p$, and *spherical* $D_s$ parts [Westin 2002]. After normalization by the trace of the tensor, three geometrical coefficients can be derived to describe the tensor:

$$c_l = \frac{\lambda_1 - \lambda_2}{\lambda_1 + \lambda_2 + \lambda_3},\ c_p = \frac{2(\lambda_2 - \lambda_3)}{\lambda_1 + \lambda_2 + \lambda_3},\ \text{and } c_s = \frac{3\lambda_3}{\lambda_1 + \lambda_2 + \lambda_3} \tag{2.15}$$

One can note the obvious identity $c_l + c_p + c_s = 1$, and that each component is ranged between 0 and 1. These components are useful in characterizing the shape of tensors more specifically than the Fractional Anisotropy. One particular interesting use of these coefficients is the three-phase barycentric plot [Alexander 2000]. An example of this plot is presented in Fig. 2.5. It is an efficient way to characterize the distribution of tensor shapes within a dataset.

# High Angular Diffusion MRI

In the sections above, the probability density function that describes the diffusion of water molecules in tissue was assumed to follow a multi-variate zero-mean Gaussian distribution, resulting in a full description of the process by a second order tensor. This assumption is sufficient in tissue with relatively simple architecture, where the underlying anisotropy of cells is restricted to a single preferred direction. It is the case for instance in the Corpus Callosum (the main fibre pathway interconnecting the two hemispheres of the brain). However, as shown by Tuch, Wedeen and colleagues in [Tuch 2002] and later in [Alexander 2002], this assumption is insufficient in the case of fibre crossing as it occurs in the brain white matter architecture.

In order to account for this tissue heterogeneity, many groups have studied diffusion under non-Gaussian profiles. For instance, [Alexander 2002] proposed to model the apparent diffusion coefficient distribution as a mixture of Gaussian profiles. The

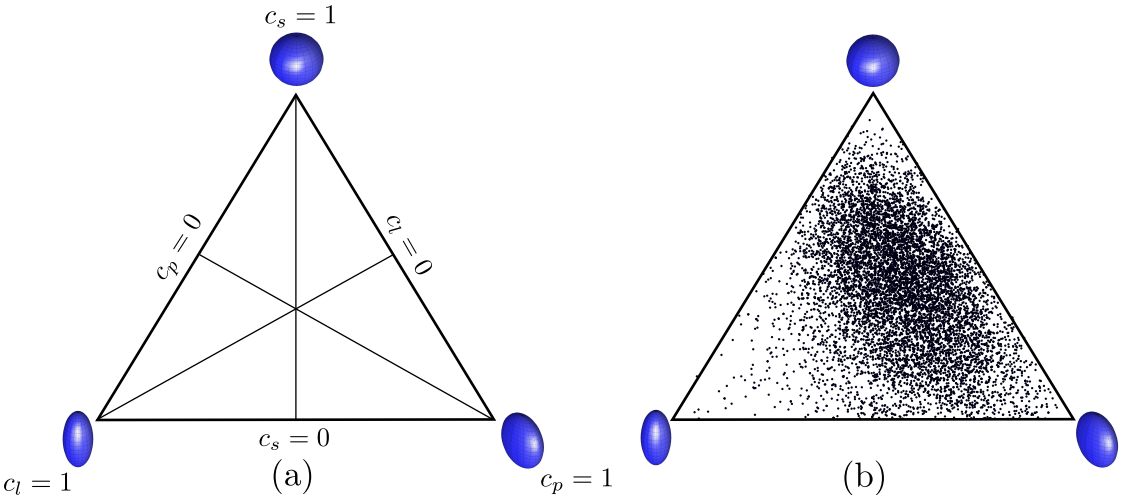


**Figure 2.5:** *Barycentric plot. (a) The shape of a tensor D is described by its geometrical coefficients $c_l$, $c_p$ and $c_s$. (b) Example of such plot in an in-vivo cardiac DTI dataset acquired in systole.*

model was able to depict the heterogeneity of tissue in regions of fibre crossings in the brain. Tuch et al. proposed a technique referred to as Q-Ball imaging [Tuch 2004] which samples the spatial dimensions together with the b-value dimension (Q-space) and estimate the Orientation Distribution Function (ODF) of the diffusion process. Those techniques and their derivatives are able to depict the potential heterogeneity of tissues within a voxel [Jansons 2003, Tournier 2004, Descoteaux 2007] and proved useful for instance in improving fibre tracking results [Perrin 2005, Fillard 2011].

As detailed in Sec. 1.1, the cardiac muscle tissue consists of elongated myocite cells organised in laminae layers. Water diffusion occurs in the inter-cellular medium between myocardial fibres, as well as in the embedded myocardial capillary system, which runs parallel to the myocardial fibres [Phillips 1979]. The work presented in this thesis is restricted to the analysis of the major orientations of the fibres in the left ventricle. Therefore in this case, the multi-variate Gaussian model will be used as it is sufficient to describe the underlying tissue orientation for fast diffusion [Hsu 2001].

## 2.4 Motion in Cardiac MR

One of the most important requirements for successful cardiac MR imaging is the accurate synchronization of the data acquisition with respect to the motion of the beating heart. The images produced then accurately reflect the state of the heart during its different stages of contraction and relaxation and have minimal motion artefacts. To achieve such synchronization, the electrical activity of the myocardium is simultaneously recorded through the Electrocardiogram (ECG) so that the actual image acquisition can be *triggered* with it (See Fig. 2.6).

The trigger delay $T_d$ then corresponds to the period between the detected R-wave and the initial RF-pulse. There is a minimum for $T_d$, therefore the remaining period of time where the acquisition can take place is below 100 % of the R-R interval.

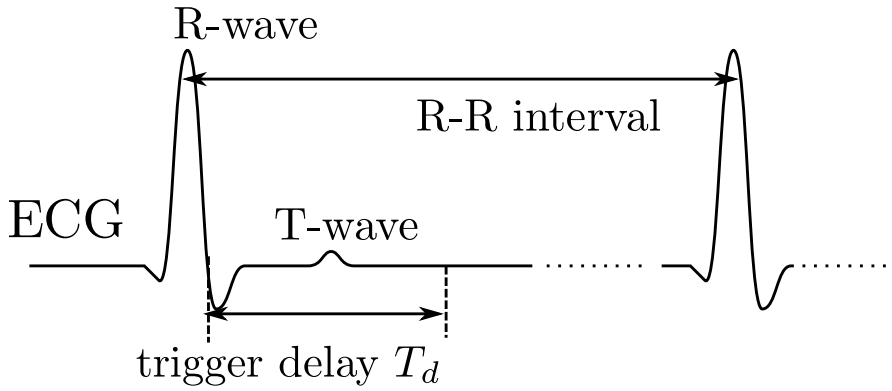


**Figure 2.6: ECG gating:** *The Electrocardiogram of the heart is recorded at all time. By detecting the R-wave, the image acquisition is triggered at the desired cardiac phase. Therefore, multiple acquisitions are synchronized at the same cardiac phase, assuming constant heart rate.*

### 2.4.1 Cardiac Planes

The orientation of the heart obeys specific semantics where three planes are defined (as shown in Fig. 2.7): the short axis view, the 2-chamber and the 4-chamber views – also respectively called vertical and horizontal long axis views.

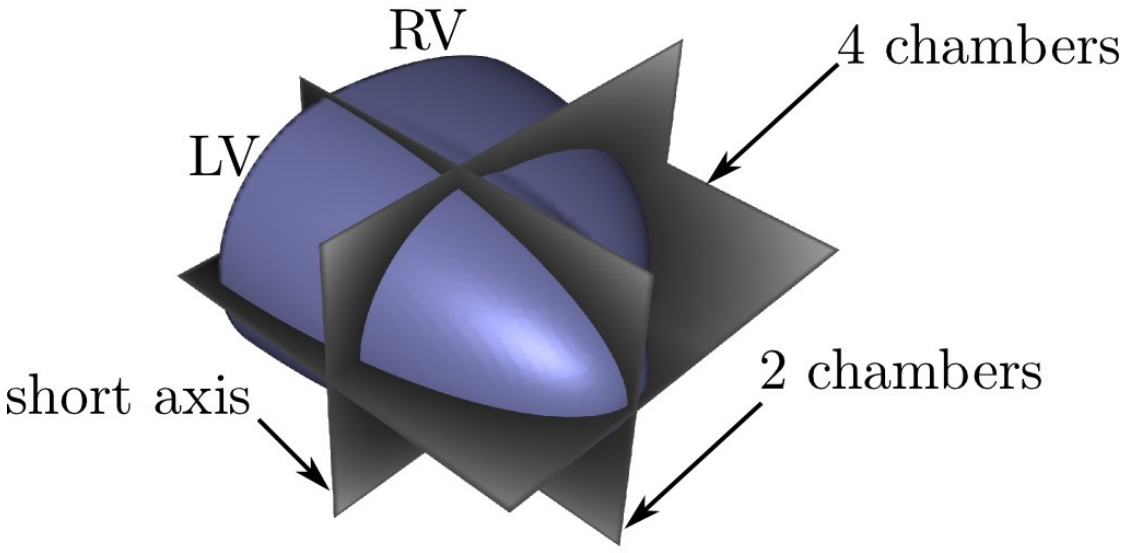


**Figure 2.7: Heart planes:** *The acquisition has to be done in the geometry of the heart, which differs for each patient / volunteer. The three orthogonal axes in this figure represent the views of the myocardium that are commonly used by clinicians / radiographers.*

These planes are not aligned with the scanner physical referential. This property is of great importance especially in DTI. Indeed, each oblique diffusion weighed image is intrinsically coupled with an encoded gradient direction. Great care must be taken to reorient the gradient direction in the image acquisition referential in order to accurately solve the system in Eq. 2.8.

### 2.4.2 Breath-holds and Navigating

The respiratory movement shifts the diaphragm and thus the heart moves during inspiration and expiration phases. This movement mainly occurs in the foot-head direction: the diaphragm pushes the heart towards the head direction during inspiration. To account for this movement, one can use breath-holds. In order to ensure that the heart stays at the same position during successive breath-holds, a 1D profile image of the diaphragm / lung interface is acquired at the beginning of each breath hold, in the foot-head direction, as shown in Fig. 2.8. The $(i+1)^{th}$ profile is compared to the $i^{th}$ and if they differ too much the data is not acquired. The tolerance window is in $mm$ and is set considering precision requirements.

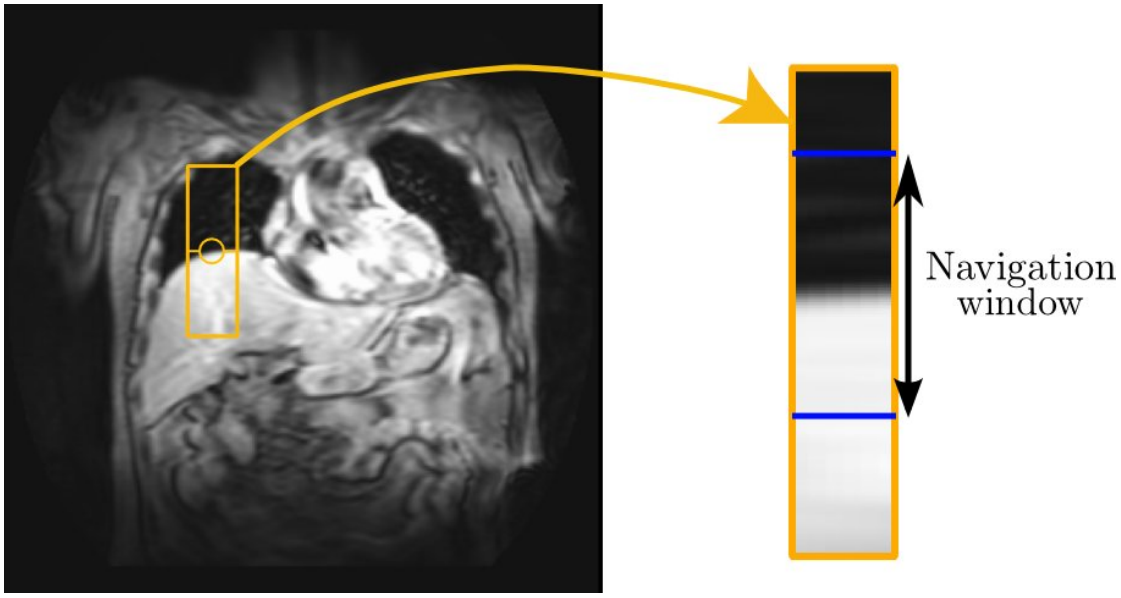


**Figure 2.8: Navigator:** *To detect foot-head motion due to respiration, the 1D profile around the diaphragm is acquired. Then a tolerance window (right) will check the misalignment and reject acquisitions that don't lie within.*

An additional technique allows to *track* this profile and then shift the acquisition Field Of View (FOV) according to the observed shift in the profiles. This technique is called Slice-Tracking.

## 2.5 Cardiac DTI Acquisition: Recent Advances

As pointed out earlier, the main problem addressed in that matter is the motion involved in the beating heart. One could think of acquiring the data during the rest period of diastole, as this is the cardiac phase of relative stasis. Unfortunately, this phase coincides with a very thin thickness of the myocardial wall. To maximize signal between endocardium and epicardium, data can be acquired in the systole phase. However, contraction of the myocardium during systole provokes distortions in the MR signal. Several solutions have been proposed in the literature to tackle this motion sensitivity.

Originally, [Edelman 1994] suggested the use of a Stimulated Echo pulse, or STEAM pulse sequence (instead of Stejskal-Tanner Spin Echo (SE) sequence [Stejskal 1965]), synchronized with the cardiac cycle. That is, the two diffusion sensitizing gradients of the sequence are applied to the exact same cardiac phase

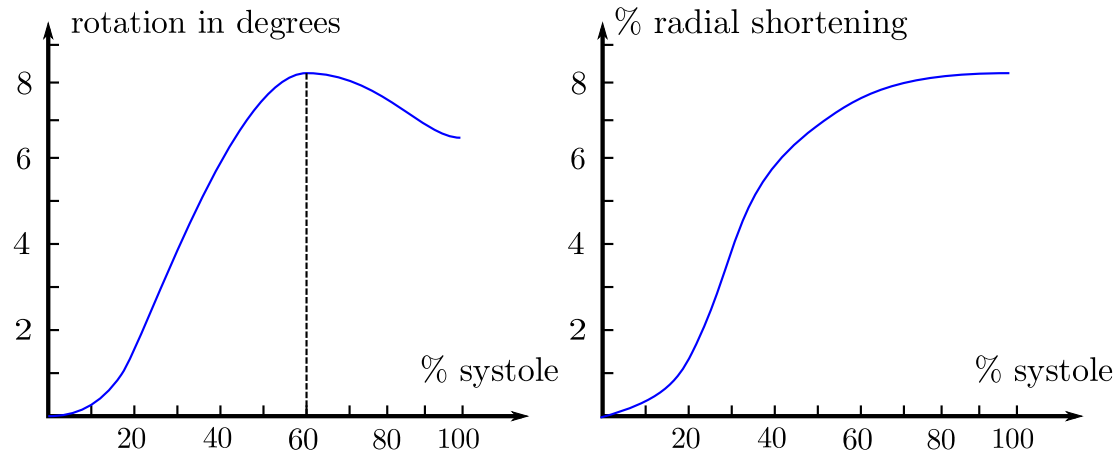


**Figure 2.9: rotation and shortening:** *During cardiac systole, the left ventricle is shortened to ensure maximal blood ejection in the arteries. A rotation, or twist of the ventricle is also observed, caused by the myocardial sheet shearing with each other. If diffusion is to be encoded when there is spin motion in the diffusion direction, a phase shift is induced on the signal, depending on the position and speed of the displacing spin. By encoding diffusion at symmetric points around the systolic peak (around 60 % of the systole phase), this phase shift cancels out, overcoming the distortion effect.*

in two consecutive cycles. This sequence has the disadvantage to take two entire cardiac cycles to acquire a diffusion weighted image. Moreover, tissue deformation occurring during the acquisition interval (both in-plane rotation and through-plane motion) alters intensively the signal and thus leads to unpredictable outputs.

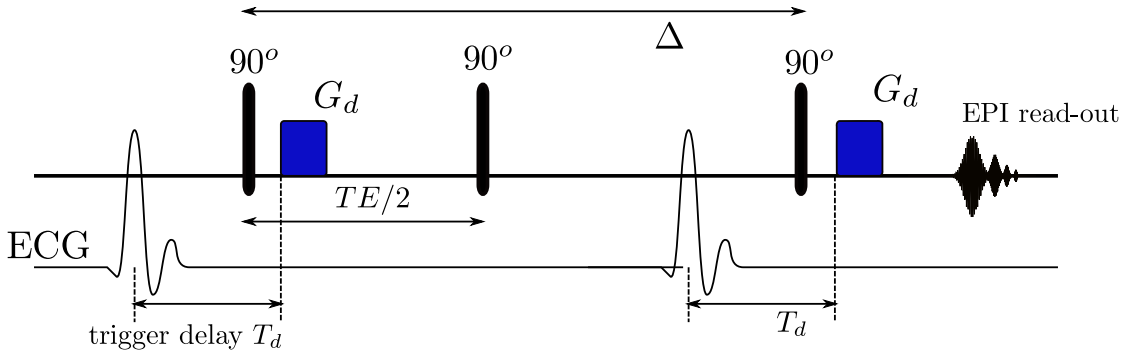


**Figure 2.10: STEAM pulse sequence:** *the Stimulated Echo Acquisition Method consists in letting spin diffuse over the entire cardiac cycle. In this case, the rotation that affects the diffusion encoding is narrowed.*

Reese, Tseng, Dou *et al.* suggested a workaround by explicitly expressing the alteration of the signal by cardiac strain [Reese 1995, Tseng 1999, Dou 2003]. Thus, by applying additional velocity-encoding gradients, the strain tensor can be estimated over the cardiac cycle. The altered tensor $D_{obs}$ is expressed as a function of the Strain Tensor $S_t$ and the intrinsic tensor $D_0$ by the following equation:

$$D_{obs} = D_0 - \Delta^{-1}\left[D_0 \int_\Delta S_t(\tau)d\tau + \left(D_0 \int_\Delta S_t(\tau)d\tau\right)^T\right] \tag{2.16}$$

where $\Delta$ denotes the cardiac period. This expression is an approximation assuming small strain eigenvalues.

In 2007, Gamper, Kozerke *et al.* suggested to go back to the Spin Echo sequence (SE) and use bipolar gradient lobes as well as a reduced Field Of View (FOV) [Gamper 2007]. In this work, a synthetic study of the effect of systolic motion over the k-space signal is explained. This motion results in a spin phase shift depending on the direction and speed of the spins during the acquisition. This phase shift induces distortion of the image when the voxel in-plane resolution is not sufficient enough. By using bipolar gradients introduced in [Dou 2002], the diffusion sequence is less sensitive to this phase shift and the voxel resolution requirements are thereby relaxed.

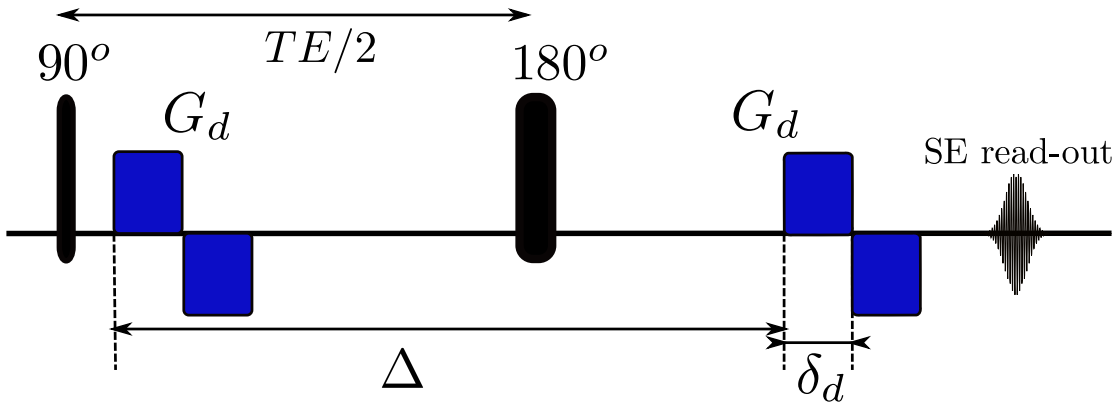


**Figure 2.11: Bipolar diffusion sequence:** *by using two bipolar diffusion gradient lobes instead of one, the strain effect is nullified, assuming $2\delta_d$ is still much inferior to $\Delta$. This sequence uses Spin Echo (SE) read-out as in the standard diffusion sequence in Fig. 2.3, instead of the Echo Planar used in the STEAM sequence.*

The SE sequence is faster (one cardiac cycle) and has a better signal to noise ratio (SNR) performance than the STEAM sequence. The diffusion encoding gradients have to be applied symmetrically around the 180 deg pulse. To compensate for strain distortion effect, the trigger delay has to be tuned in order to place this pulse at the systolic peak, that is, at around 60 % of the systolic phase (see Fig. 2.9). Accordingly, the phase shift induced in the first $G_d$ is nullified after the second $G_d$.

The two sequences shown here are meant to encode a single diffusion direction for one 2D slice. As explained earlier, this measurement has to be repeated $N$ times ($N > 6$) to reconstruct the full Gaussian probability distribution, i.e. the tensor. Therefore, $N+1$ cardiac cycles are needed to acquire the tensor field over a single 2D slice. Moreover, to improve the SNR of the dataset, each measurement is repeated $k_{NSA}$ times and a signal average is performed, leading to a total of $k_{NSA}(N+1)$ cardiac cycles for a DTI slice acquisition.

## Acquisition Examples

Figure 2.12 shows short axis slices acquired on healthy volunteers. It is clear from these DWIs images that the SNR performances are limited when compared to the brain DWIs presented in Fig. 2.4. Additionally, net differences are observed in terms of artefacts patterns and image contrast between SE and STEAM sequences. As the STEAM sequence has an intrinsic fat suppression embedded, there is no need for any pre-pulse to achieve that in this case, whereas this pre-pulse is necessary in the SE case. Consequently, the STEAM DWIs appear less affected by fat induced

artefacts than their SE equivalents. When reconstructing the tensors, Fig. 2.12(second line) shows main eigenvectors consistent with anatomical general knowledge in both acquisition techniques. However apparent noise levels seem to be lower in the SE case. Both acquisitions have taken approximately 12-13 minutes. The STEAM acquisition needed breath-holds, whereas the SE acquisition was realized in free breathing, using respiratory navigation.

The single Gaussian model assumption is mostly used in the case of the cardiac muscle. Indeed, cardiac myocytes are organized in a linear manner, embedded in a collagen mesh structure. There is no specific reason to assume any fibre crossing in healthy myocardial tissue. However, in some localised areas, such as the junction between the RV wall and the LV wall for instance, or in damaged tissue after an infarct, the tensor model might not hold and the underlying tissue might be heterogeneous within a voxel. Attempts to apply High Angular diffusion techniques and higher order reconstructions have been reported in *ex-vivo* hearts in [Dierckx 2009]. The study shows some genuine heterogeneity (fibre crossings) in the junction between ventricles. The resolution and SNR in *in-vivo* cardiac DTI restricts the diffusion model and for the remaining of the thesis the simple tensor model is considered.

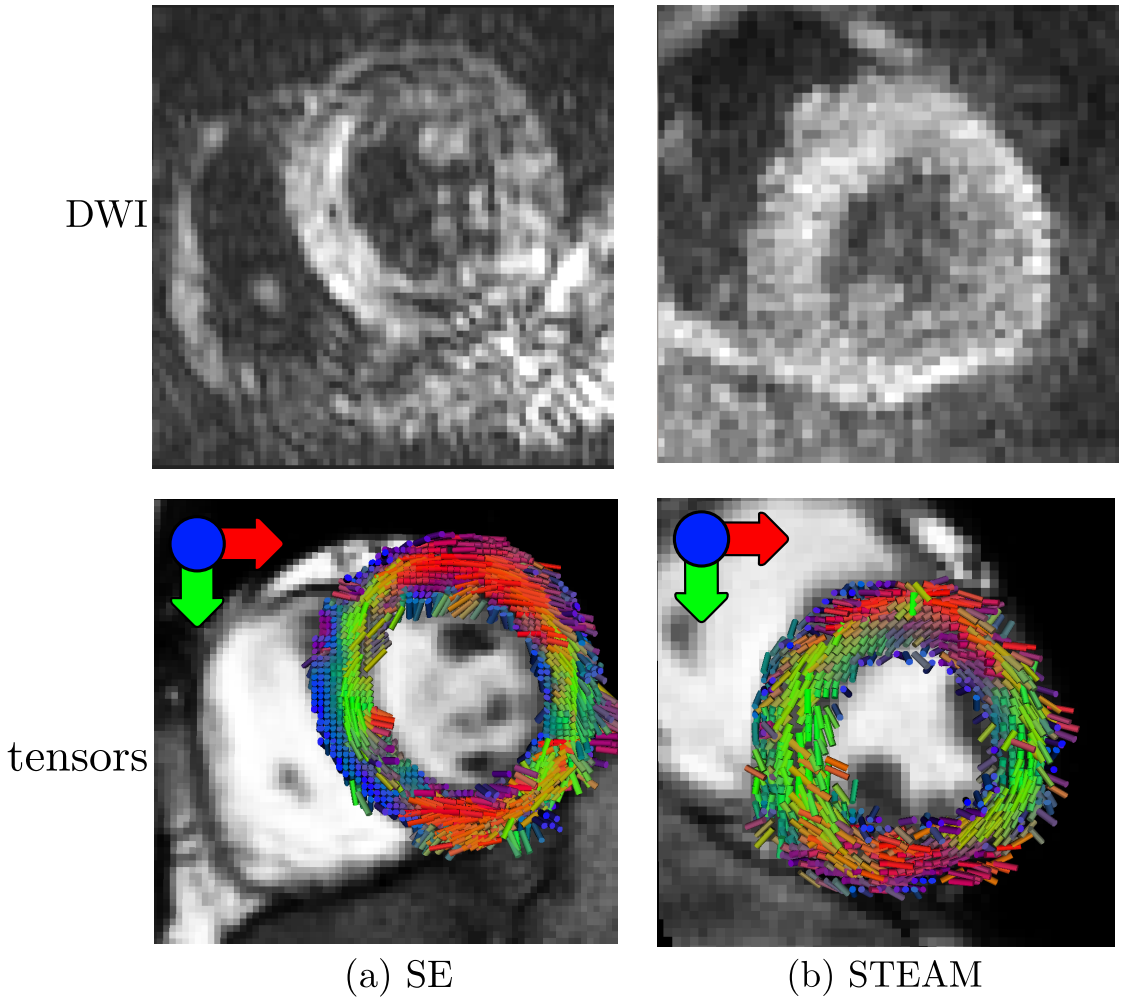


**Figure 2.12:** *Examples of a DTI acquisitions on two different healthy volunteers in the mid-ventricle area, using (a) the Spin Echo (SE) bipolar sequence from [Gamper 2007] and (b) the Stimulated Echo protocol (STEAM) from [Tseng 1999]. The first line shows one of the diffusion weighted images and the second shows the tensor reconstruction. Tensors are shown using their first eigenvectors, color coded with their direction.*

Chapter 3

# Prolate Spheroidal Frame for Cardiac DTI Data Analysis

## Contents



## 3.1 Motivations

Representing information in a coordinate system which is adapted to the shape of the object can have a crucial impact on performance when processing this information. The prolate and oblate spheroidal coordinates belong to the restricted family of coordinate systems where the Laplace equation can be solved with the method of

separation of variables [Zipoy 1966]. This property is used in the field of astrophysics for instance. It is indeed common to represent the shape of the Earth (or other celestial object) as an oblate spheroid, and translate any given problem (such as the resolution of gravitational or vacuum fields) into the corresponding oblate spheroidal coordinates [Gates 2004].

The LV wall is a relatively thin and non-convex structure with a shape close to an ellipsoid. The prolate spheroidal (PS) coordinates are therefore well adapted to represent such an object, and have the advantage of being physiologically meaningful with respect to the ventricular shape and fibre architecture [Nielsen 1991, Costa 1996, LeGrice 2001, Rohmer 2006].

This chapter presents a new approach for representing the LV DTI data in PS coordinates, highlighting the practical advantages of such technique. This approach is then applied to a series of experiments, using *ex-vivo* canine heart dataset, in order to extract comprehensive features from LV DTI data.

## 3.2 Insight to the PS Coordinates

The PS coordinate system is a curvilinear yet orthogonal system in $\mathbb{R}^3$. This means that the intersecting surfaces of constant coordinate are orthogonal to each other. The transformation operator from Cartesian coordinates $x = (x_1, x_2, x_3)^T$ to PS coordinates $\xi = (\xi_1, \xi_2, \xi_3)^T$ is denoted $\Psi : x \to \xi = \Psi(x)$. However, it is more commonly given in its inverse form $\Psi^{-1}$:

$$\Psi^{-1} : \begin{cases} x_1 &= f \sinh(\xi_1) \sin(\xi_2) \cos(\xi_3) \\ x_2 &= f \sinh(\xi_1) \sin(\xi_2) \sin(\xi_3) \\ x_3 &= f \cosh(\xi_1) \cos(\xi_2) \end{cases} \tag{3.1}$$

The scaling parameter $f$ is the semi-foci distance. Figure 3.1 illustrates the construction of the coordinate system. The first coordinate $\xi_1$ is defined in $]0, \infty[$ and can be interpreted as the through-wall depth, $\xi_2$ is the long axis angular abscissa going from 0 at the apex to $\pi/2$ at base level, and $\xi_3$ as a circumferential angular abscissa from 0 to $2\pi$.

The contravariant base vectors $(g_1, g_2, g_3)$ of a (curvilinear) coordinate system are the vectors that are orthogonal to each of the coordinate isosurfaces. They are defined as $g_i = \frac{\partial x}{\partial \xi_i}$. In the common Cartesian system, the contravariant basis is stationary in $\mathbb{R}^3$, i.e. $\frac{\partial x}{\partial x_i} = e_i$. The PS equivalent, here denoted $\mathcal{G} = (g_1, g_2, g_3)$ varies in space as illustrated in Fig. 3.1. Their detailed expression is as follows:

$$g_1 = f \cdot \begin{bmatrix} \cosh(\xi_1) \sin(\xi_2) \cos(\xi_3) \\ \cosh(\xi_1) \sin(\xi_2) \sin(\xi_3) \\ \sinh(\xi_1) \cos(\xi_2) \end{bmatrix} \quad g_2 = f \cdot \begin{bmatrix} \sinh(\xi_1) \cos(\xi_2) \cos(\xi_3) \\ \sinh(\xi_1) \cos(\xi_2) \sin(\xi_3) \\ -\cosh(\xi_1) \sin(\xi_2) \end{bmatrix}$$
$$g_3 = f \cdot \begin{bmatrix} -\sinh(\xi_1) \sin(\xi_2) \sin(\xi_3) \\ \sinh(\xi_1) \sin(\xi_2) \cos(\xi_3) \\ 0 \end{bmatrix} \tag{3.2}$$

Where $f$ is the semi-foci distance (See Fig. 3.1). The null component in $g_3$ confirms that this vector is always parallel to the $(x, y)$ plane, as the derivation of the third line of Eq. 3.1 with respect to $\xi_3$ is null. The basis $\mathcal{G}$ is direct and

orthogonal, but not orthonormal. The norm of each vector $g_i$ depends on the so-called coordinates *scaling factors*, which are defined as $\Psi^{-1}$ local derivatives : $h_i = \partial x/\partial \xi_i$, leading to the relationship $\|g_i\| = 1/h_i$. The PS coordinates are defined everywhere in $\mathbb{R}^3$, except on a singularity segment located between foci, as detailed in App. A.

The contraction of the ventricle can therefore be mostly described by 1) a twisting movement along $g_3$, 2) an apex to base shift along $g_2$, and 3) a wall thickening along $g_1$. Those considerations justify the use of the PS coordinate system for describing left ventricular shape and function [Costa 1996, LeGrice 2001, Rohmer 2006].

In the literature the usual convention appears to take an indirect basis $(g_1, g_2, -g_3)$ instead of the basis described in this chapter. When using the indirect convention, the helix angle is positive in the endocardium and negative at the epicardium, as in [Streeter 1973a, Greenbaum 1981, Scollan 1998]. In this thesis, the opposite convention is used. The basis is kept direct for mathematical consistency. However, in order to compare graphs with the literature, they are shown in the indirect convention (i.e. the helix angle is positive at the endocardium).

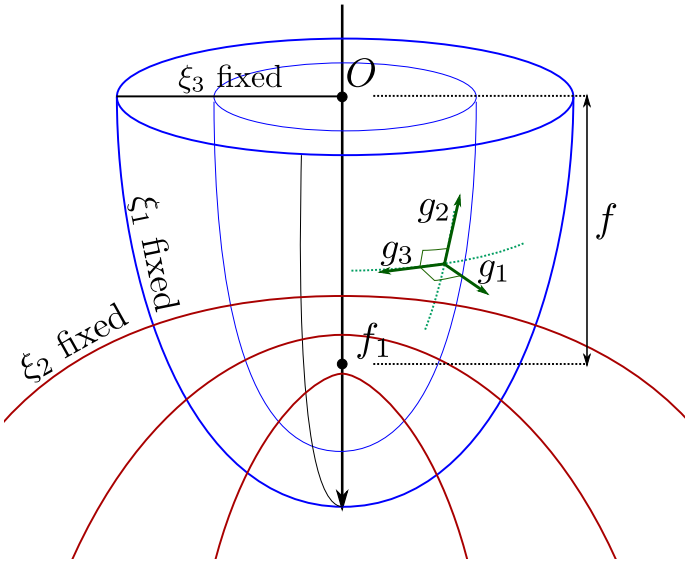


**Figure 3.1:** *The PS coordinate system, defined at each position in $\mathbb{R}^3$ depends on the position of an ellipsoid centre $O$, a focus $f_1$. $f$ is the semi-foci distance. Iso-lines of constant coordinates are drawn to illustrate its suitability to the ventricular shape.*

Prolate spheroidal coordinates have the advantage of describing the highly non convex volume that is the ventricle wall as a parallelogram, as shown in Fig. 3.2. In the PS frame, the shortest path from two distinct points of the ventricle remains in the ventricle. Therefore, a metric defined in this frame becomes *geodesically convex*.

## 3.3 Practical Properties of the PS Coordinates

### 3.3.1 AHA Subdivision

Representing left ventricular data in a PS coordinate frame has several advantages. The natural normalization of the coordinate system allows straightforward division into regions (or zones) as defined by the American Heart Association (AHA) [Cerqueira 2002]. Indeed, since $\xi_2$ is the apico-basal coordinate and $\xi_3$ is


**Figure 3.2:** *Convexity: A left ventricle volume (left) is non convex in a Cartesian frame whereas the same volume expressed in a PS frame (right) becomes a convex box.*

the circumferential coordinate, dividing linearly the segments $[0, \xi_{base}]$ and $[0, 2\pi]$ into equal lengths yields to appropriately distributed AHA segments.

Figure 3.3(a) shows an example of such division. The $\xi_3 = 0$ plane is aligned with the limit between AHA zones 1 and 2, i.e. the limit between the anterior wall and the right ventricle.

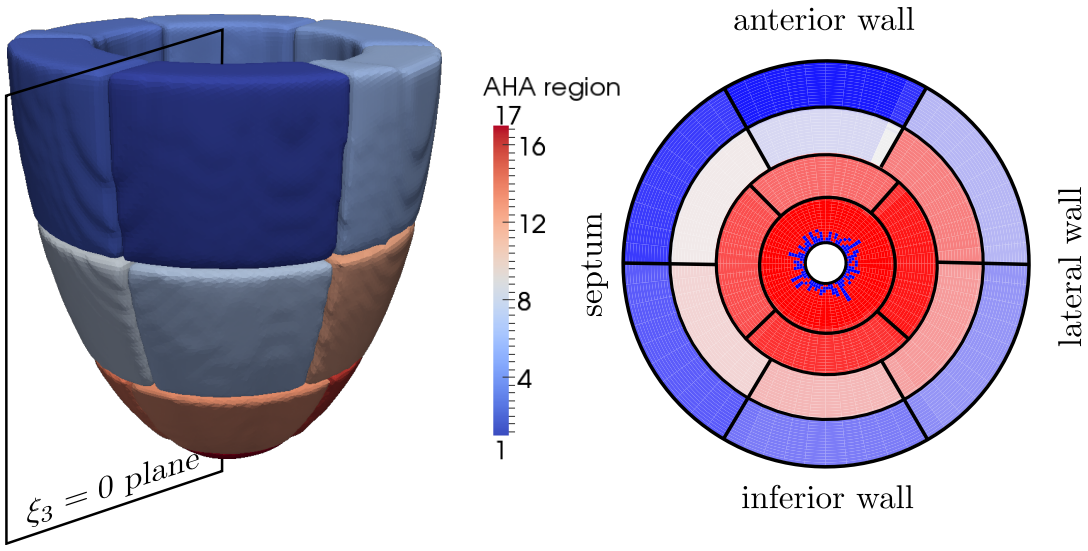


**Figure 3.3:** *AHA segments in the PS sense. The segments are linear divisions of the naturally normalized coordinate system. The plane ($\xi_3 = 0$) is aligned with the limit between the anterior wall and the right ventricle.*

Another practical use of this curvilinear representation is the bullseye representation of data in the left ventricle. A bullseye map is a projected polar representation of the LV shape, as seen from the apex point of view. Thanks to the PS coordinate frame, the bullseye map is derived in a straightforward way, with any required subdivision levels (see Fig. 3.3(b)).

### 3.3.2 Expressing Diffusion Tensors in PS Coordinates

When diffusion tensors are expressed into the local PS basis $\mathcal{G}$, each component of the tensor can be interpreted in a physiologically meaningful way. For instance, the main eigenvector of tensors $D_\xi$ can be calculated. Their projection on $\mathcal{G}$ provide comprehensive measure of the fibre architecture. Three projections are defined as follows (see illustration in Fig. 3.4(b)):

- The helix angle, denoted $\alpha$, is the signed angle between the tensor's main eigenvector $v_1$ and the transmural short axis plane $(g_1, g_3)$. Its variation with respect to the transmural depth $(\xi_1)$ is of particular interest as it follows a recognizable pattern on healthy subjects.
- The transmural angle $\beta$ is the signed angle between $v_1$ and the wall surface $(g_2, g_3)$. It measures the deviation of the fibre from circumferential direction.
- The sheet angle $\gamma$ as the signed angle between $v_3$ and the wall surface $(g_2, g_3)$. The laminar structure of the myocardial fibres can also be described by the DTI data. As the plane defined by the vectors $v_1$ and $v_2$ is parallel to the laminar sheet, the direction of $v_3$ fully describes the sheet orientation. A high absolute value of $\gamma$ implies that the local laminar sheet is close to be parallel to the wall surface.

Using the PS expression of the diffusion tensor, these angles are therefore mathematically defined as:

$$\alpha = \arcsin(v_1, g_2);\ \beta = \arcsin(v_1, g_1);\ \gamma = \arcsin(v_3, g_1); \tag{3.3}$$

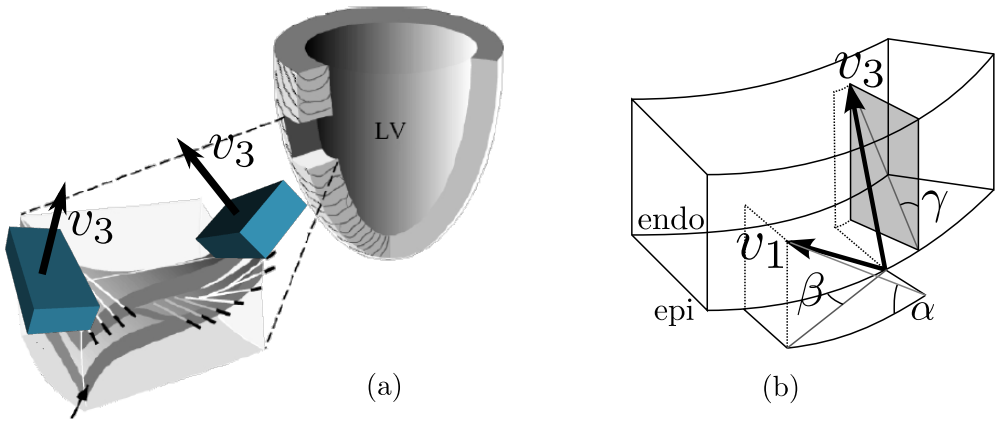


**Figure 3.4:** *(a) Sheet structure of the left ventricle. (b): Helix ($\alpha$), transverse ($\beta$) and sheet ($\gamma$) angles are defined in PS coordinates w.r.t the tensor's eigenvectors.*

### 3.3.3 Natural Normalization of the System

The PS frame constructed with this approach allows an interesting set up for the comparison of different datasets, as it is naturally normalized. That is, independently of the subject, the third component $\xi_3$ is naturally normalized between 0 and

$2\pi$. The $\xi_3 = 0$ position is imposed to be the intersection between the anterior wall and the the Right Ventricle (RV). Similarly, the second component $\xi_2$ is naturally normalized between 0 at the apex and $\xi_{base}$ at the basal region. The value $\xi_{base}$ depends on the basal cutting performed on the manual segmentation $S$. In the experiments carried out in this thesis, $\xi_{base}$ is found to be $107\,\text{deg} \pm 4\,\text{deg}$. The range of the first component $\xi_1$, on the other hand, is not naturally normalized, and depends on both the radius of the LV and its thickness. However, the lower (endocardial) and upper (epicardial) limits of $\xi_1$ are very stable among a population. Therefore the PS coordinates provide an easy and comprehensive way to compare DTI data within a population of hearts.

## 3.4 Workflow: from Anatomical LV to Normalized PS Frame

### 3.4.1 Non-Linear Registration

In order to ensure that the curvilinear coordinate system strictly follows the shape of a specific LV, the segmented ventricle has to be registered to a perfectly shaped truncated ellipsoid volume. The source image $S$ and target image $T$ of this non-rigid registration step are respectively the binary mask of the segmented LV and the binary mask of a corresponding approximated truncated ellipsoid volume (See Fig. 3.5). As detailed further in this chapter, the DTI data will be transformed to the ellipsoid and back to the anatomical geometry. The registration process has to fulfil three requirements:

- The transformation provided by the registration needs to be invertible.
- The displacement fields needs to be smooth, in order to avoid strong rotation components of the transformation.
- As binary masks are used, there is no *feature* in the mid-wall regions of $S$ and $T$ to drive the registration process. Therefore a plasticity/elasticity property of the registration is needed to ensure physiologically plausible displacements.

Those requirements drove the choice over the registration towards the symmetric version of the log-domain diffeomorphic demons [Dru 2009]. This registration algorithm has the crucial characteristic to provide symmetric invertible displacement fields. To add an elasticity constraint on the displacement, methods described in [Mansi 2011] are used. The Poisson ratio $\kappa$ controlling the degree of global elasticity (Eq. 9 in [Mansi 2011]) has to be chosen small (of the order of 1), as too large values result in *incompressible* displacements. In our setting, there is no reason to impose such a strong constraint on the displacement field, because there is no reason to believe that the source and target masks have the same volume. This technique provides forward $\Phi$ and backward $\Phi^{-1}$ transformations between the volunteer's anatomy and a volumetric truncated ellipsoid. $S$ is obtained by a manual segmentation of the myocardium using a 3D anatomical MRI image. The software CardioViz3D [Toussaint 2008] was used for this purpose. It provides an interactive segmentation based on variational implicit surfaces, as proposed in [Turk 1999].

The centre of mass and main axis of symmetry of $S$ are used to produce the target volumetric truncated ellipsoid image $T$ that is the closest to $S$. Fig. 3.5 shows a superposition of masks $S$ and $T$ onto the anatomical image.

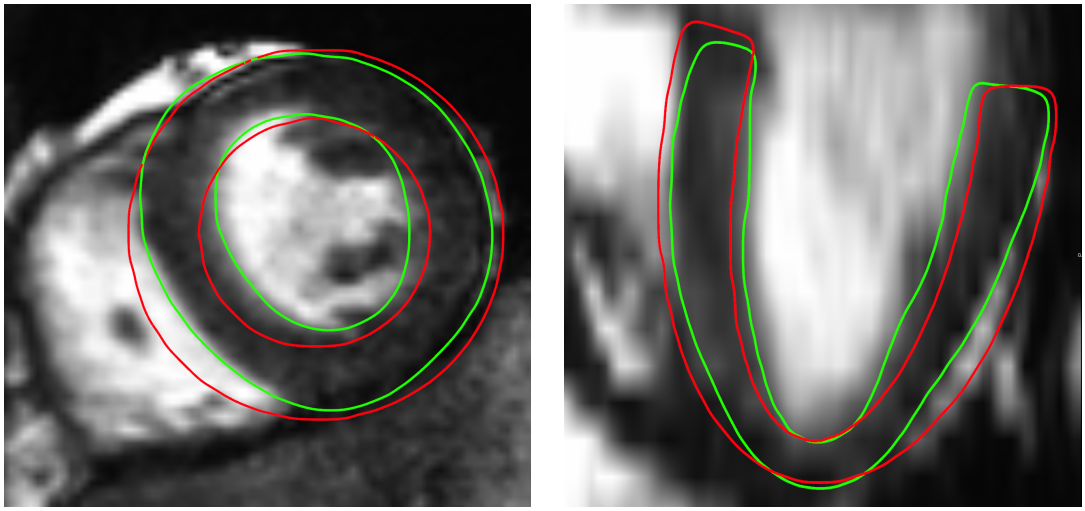

**Figure 3.5:** *The binary mask $S$ of the anatomical left ventricle (in green in on the images) is obtained by manual segmentation. From the centre of mass and main axis of revolution of $S$ is derived the closest volumetric truncated ellipsoid mask $T$ (in red in the image). $S$ and $T$ are then registered using symmetric diffeomorphic demons algorithm.*

Now that the subject's LV is transformed onto the perfectly shaped truncated ellipsoid volume $T$, the operator $\Psi$ can be used to express this information in PS coordinates. Position transformation from Cartesian to PS coordinates is defined by inverting the system in Eq. 3.1. Details of the inversion are given in Appendix A.

The overall transformation process towards a common PS frame can be summarized as follows:

$$\xi = \Psi \circ \Phi(x) \tag{3.4}$$

The operators $\Phi$ and $\Psi$ are fully invertible, apart from the singularity segment (see Appendix A). As a consequence, it is possible to transform any LV input data into the PS frame, process it in a well adapted coordinate system, and transform it back to the anatomical referential.

The global transformation process is illustrated in Fig. 3.6. The anatomical left ventricular wall volume $\Omega$ is transformed to the convex box $\Omega''$ that is the PS frame. A natural path lying within the LV wall (dotted lines in $\Omega$) becomes a straight line in $\Omega''$. Therefore, any process, such as interpolation or geodesic distance definition, described in PS frame will follow the natural shape of the LV. In particular, dense approximation benefits from this characteristic, as presented in Chapter 4.

### 3.4.2 Extension to Tensors: a Finite Strain Approach

In our work, the type of data is not scalar but consists in tensors. A series of adjustments to the transformation operators are needed in order to account for that increased data dimensionality. Let us denote $\tilde{\Phi}$ the *induced* transformation from $\Phi$ on tensors. Transforming the diffusion tensors implies a reorientation scheme using the Jacobian $\mathcal{J}_{\Phi^{-1}}$ (in our case directly available from $\Phi^{-1}$).

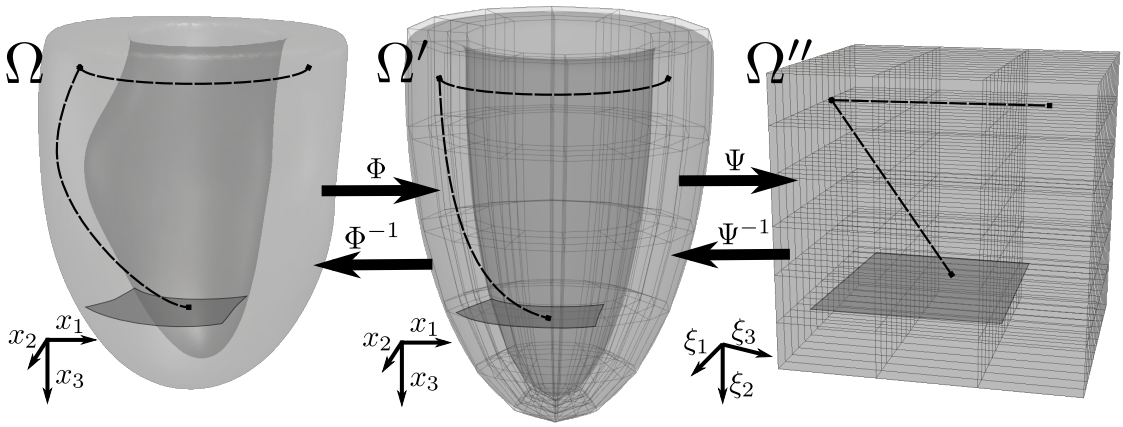


**Figure 3.6:** ***Workflow****: this diagram shows the data transformation throughout the procedure. The anatomical LV (Ω) is registered onto a truncated volumetric semi-ellipsoid (Ω′) with the displacement field Φ. The change of coordinate system from Cartesian to PS is performed with the operator Ψ, which results in a convex representation of the ventricular volume (Ω″).*

In [Alexander 2001], two different reorientation strategies were compared to address the problem:

- The Finite Strain (FS) method separates the deformation in a rigid rotation and a pure deformation one, and only applies the rotation $\hat{\mathcal{J}}_{\Phi^{-1}}$ to the tensor.
- the Preservation of Principal Direction (PPD) method takes the full Jacobian to reorient the tensor.

The study concludes that FS strategy is sufficient if the deformation is close to be rigid, and that PPD must be used if the deformation includes significant non-rigid parameters such as large shearing for instance. In [Peyrat 2006], the same strategies were compared and it was found that Finite Strain (FS) was best suited for preserving the geometrical properties of diffusion tensors in the context of diffusion tensors registration in the myocardium. The FS strategy was chosen for this reason and its computational efficiency. Additionally, the Jacobian determinant of the displacement fields $\Phi$ and $\Phi^{-1}$ obtained in Sec. 3.4.1 appears close to 1 (i.e. close to isovolumic displacements), as shown in Fig. 3.7. Indeed, the elasticity constraint added in the registration process yields to smooth deformation fields and pushes the displacements towards rigid ones.

Extending the change of coordinate to tensors necessitates the *induced* transformation of the operator $\Psi$. The Jacobian of $\Psi$ corresponds to the contravariant basis $\mathcal{G}$ (Eq. 3.2). This matrix is orthogonal by definition (PS coordinates is an orthogonal coordinate system), but not orthonormal. The norm of the contravariant vectors correspond to the scale factors of the coordinate system, which are the local derivatives $h_i = \partial x / \partial \xi_i$. In our setting, the domain of definition is a volumetric ellipsoid, and factors $h_i$ vary spatially within the domain. In particular, they decrease with the distance to the long-axis. Therefore, taking the full Jacobian of $\Psi$ to reorient the tensors and performing interpolation in the PS frame would privilege tensors of endocardial regions against epicardial ones, which is not desirable. Consequently, only the rotational component of $\tilde{\Psi}$ is used: let us denote $\hat{\mathcal{G}}$ the matrix constructed from the normalized column vectors of $\mathcal{G}$, using the scale factors $h_i$ (see

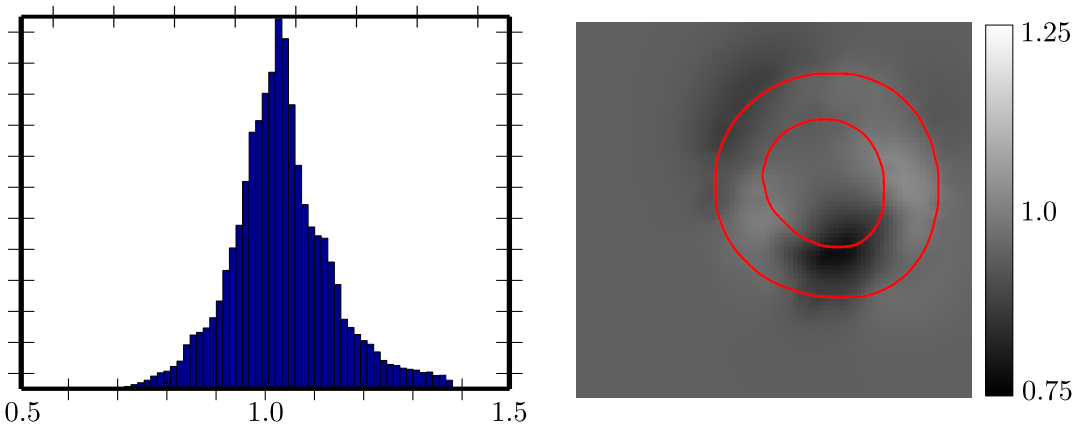


(a) Histogram of the Jacobian determinant of $\Phi$ (b) Slice of the Jacobian determinant of $\Phi$

**Figure 3.7:** *Jacobian determinants. (a) histogram of the determinant of the Jacobian matrix $\mathcal{J}_{\Phi^{-1}}$. (b) Short axis view of the Jacobian determinant, with a left ventricle delineation superimposed.*

Appendix A). Recalling that $\mathcal{G}$ is direct and orthogonal, $\hat{\mathcal{G}}$ has therefore by construction a determinant equal to 1. Eq. 3.4 is rewritten with the induced transformations on tensors:

$$\xi = \Psi \circ \Phi(x) \text{ and } D_\xi = \tilde{\Psi} \circ \tilde{\Phi}(D_x)$$
$$with : \begin{cases} \tilde{\Phi} : D \to \tilde{\Phi}(D) = \hat{\mathcal{J}}^T_{\Phi^{-1}}.D.\hat{\mathcal{J}}_{\Phi^{-1}} \\ \tilde{\Psi} : D \to \tilde{\Psi}(D) = \hat{\mathcal{G}}^T.D.\hat{\mathcal{G}} \end{cases} \tag{3.5}$$

The induced transformations $\tilde{\Phi}$ and $\tilde{\Psi}$ both represent the finite strain transformations of tensors under $\Phi$ and $\Psi$.

## 3.5 Differential Operator in PS Coordinates

### 3.5.1 Gradient Computation

In data analysis, it is often important to be able to quantify the local variation of a quantity over space. The spatial differential operator of a function is well defined when the measure points (centres) are regularly distributed on an orthogonal grid, using finite differences. However, as our tensor data is transformed to a PS frame, the data centres are *not regularly* distributed in the PS frame, and the density of this distribution is heterogeneous within the domain of definition. These properties are illustrated in Fig. 3.8(a). In this section, a description of a computation method for the local gradient of a tensor field in such situation is provided.

Let us denote $L = \log D$, the local gradient in PS coordinates is defined as $\nabla L = (\partial_{\xi_i} L)$, $i = 1..3$ where $\partial_{\xi_i} L$ are projection of $\nabla L$ on the axes of the coordinate system.

For clarity, we use the "vec" operator as defined in 2.3: $l = \text{vec}(L)$. The local gradient therefore becomes $\nabla l = (\partial_{\xi_i} l), i = 1..3$, and $\nabla l$ is of dimension $3 \times 6$. On a regular lattice, the directional gradients in the orthogonal directions $u_i$ are defined as $\partial_{u_i} l(\xi) = 1/2(l(\xi + u_i) - l(\xi - u_i))$. In case the measure centres are irregularly distributed (Fig. 3.8(b)), the above computation is not feasible, and the non-symmetric version has to be considered: $\partial_{u_i} l(\xi) = l(\xi + u_i) - l(\xi)$, where $\partial_{u_i} l(\xi)$

are projections of the total gradient $\nabla l_{\mathcal{V}}$ on the directions $u_i$ in a neighborhood $\mathcal{V}$ (see Fig. 3.8(b)).

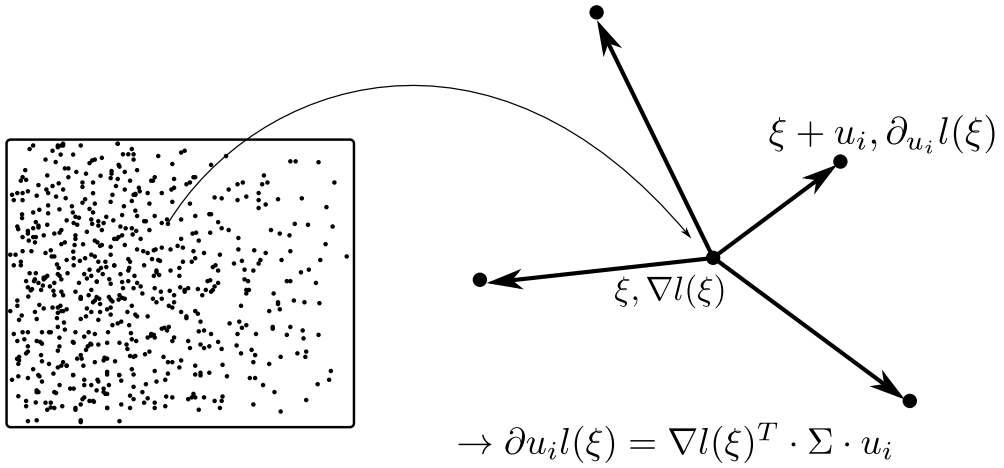


(a) measurement distribution in PS (b) local directional gradient

**Figure 3.8:** *(a) In the PS frame, spatial distribution of measurement points is not regular, and the distribution density is heterogeneous. (b) The local spatial gradient $\nabla l_{\mathcal{V}}(\xi)$ is a weighted combination of its projections onto each known direction of a neighborhood $\mathcal{V}$, i.e. $\partial u_i l(\xi)$. The least square solution gives an approximation of this gradient at position $\xi$, using the local PS metric tensor $\Sigma$.*

Furthermore, one has to be careful if the spatial metric is not isotropic, which is the case in PS coordinates (i.e. the scale coefficients $h_i$ are not equal). Since an *Euclidean* representation of the spatial variation is needed, a metric correction is necessary. Using the metric tensor of the PS coordinates $\Sigma$ at position $(\xi + u_i)$, the corrected non-symmetric directional gradient is written as follows (see Fig. 3.8(b)):

$$\Sigma = \begin{bmatrix} h_1(\xi+u_i) & 0 & 0 \\ 0 & h_2(\xi+u_i) & 0 \\ 0 & 0 & h_3(\xi+u_i) \end{bmatrix} \rightarrow \partial u_i l(\xi) = \nabla l_{\mathcal{V}}(\xi)^T \cdot \Sigma \cdot u_i \quad (3.6)$$

In Eq. 3.6, $\nabla l_{\mathcal{V}}(\xi)$ is the unknown gradient to be estimated from its projections $\partial u_i l(\xi)$. When considering a neighborhood $\mathcal{V}$ of centres around $\xi$, this problem can be solved in the least square sense. Let us perform a change of variable using $u_i^{\Sigma} = \Sigma \cdot u_i$. The following set of equations can be written:

$$\begin{cases} & \partial_{u_i} l(\xi) = l(\xi + u_i) - l(\xi) \\ \forall u_i \in \mathcal{V}, & \partial u_i l(\xi) = \nabla l_{\mathcal{V}}(\xi)^T \cdot u_i^{\Sigma} \end{cases} \quad (3.7)$$

Let us define the matrix $U^{\Sigma}$, with each line $i$ being directional vector $u_i^{\Sigma}$, and the matrix $\partial_U l$, with line $i$ being $\partial u_i l(\xi)$. Eq. 3.7 can then be written in its matrix form:

$$\nabla l(\xi)^T \cdot U^{\Sigma T} = \partial_U l(\xi)^T \iff U^{\Sigma} \nabla l(\xi) = \partial_U l(\xi) \quad (3.8)$$

This least square problem is solved by minimizing the residual $\|\nabla l_{\mathcal{V}}(\xi)^T \cdot U^{\Sigma} - \partial_U l(\xi)\|^2$. As described in [Pennec 2005b] (Sec. 5.2), the least square solution involves the pseudo-inverse of $U^{\Sigma}$:

$$\nabla l_{\mathcal{V}}(\xi) = (U^{\Sigma T} U^{\Sigma})^{-1} U^{\Sigma T} \cdot \partial_U l(\xi) \quad (3.9)$$

In the case where $U$ is restricted to the $3 \times 3$ diagonal matrix $\text{diag}(sp_1, sp_2, sp_3)$, it can be noticed that this gradient reduces to the case of the one of a regular lattice of spacing $[sp_1, sp_2, sp_3]$.

The size and cardinality of the neighborhood $\mathcal{V}$ is particularly influent in the resulting gradient solution in Eq. 3.9. However, the influence of projection $\partial u_i l(\xi)$ is linearly decreasing with its distance from $\xi$. One efficient way to proceed is first to estimate the average (prolate spheroidal) spacing of the dataset and then define $\mathcal{V}$ as the ball neighborhood of twice this spacing around $\xi$.

### 3.5.2 Inertia Matrix Computation

In the previous section, Equations 3.8 and 3.9 therefore present a calculation of the local differential operator in the Prolate Spheroidal frame. This operator allows us to measure the local derivative of a tensor field. In addition to computing the spatial gradient, it is sometimes interesting to detect features in the tensor field. In image analysis, this can be achieved by quantifying the *inertia matrix* [Knutsson 2011] (also called gradient tensor [Bigun 1987]) of the quantity of interest. This matrix is constructed as the outer product of the local gradient $\nabla l \cdot \nabla l^T$. As diffusion tensors are seen as *vectors* $l$ in the Log-Euclidean sense, the *inertia matrix* of this set of *vectors* is defined as follows:

$$\begin{aligned} S_{\mathcal{V}}(\xi) &= \nabla l \cdot \nabla l^T \\ &= \begin{bmatrix} \|\partial_{\xi_1} l\|^2 & \langle \partial_{\xi_1} l | \partial_{\xi_2} l \rangle & \langle \partial_{\xi_1} l | \partial_{\xi_3} l \rangle \\ \langle \partial_{\xi_2} l | \partial_{\xi_1} l \rangle & \|\partial_{\xi_2} l\|^2 & \langle \partial_{\xi_2} l | \partial_{\xi_3} l \rangle \\ \langle \partial_{\xi_3} l | \partial_{\xi_1} l \rangle & \langle \partial_{\xi_3} l | \partial_{\xi_2} l \rangle & \|\partial_{\xi_3} l\|^2 \end{bmatrix} \end{aligned} \tag{3.10}$$

As we are set in the log-space (i.e. $l = \text{vec}(L) = \text{vec}(\log(D))$), the norm $\|.\|$ and scalar products $\langle .|. \rangle$ written in Eq. 3.10 have to be taken as the classical Euclidean norm and scalar products over vectors.

From Eq. 3.9 and Eq. 3.10, the inertia matrix $S_{\mathcal{V}}(\xi)$ can be computed on an irregularly distributed set of diffusion tensor measure centres. As we will see later in this chapter, this quantity can be used to evaluate the directionality of most changes in a tensor field. The implementation algorithm of this computation is fully described in Alg. 1.

## 3.6 Experiments: Tensor Feature Extraction

In order to test and illustrate our approach, a database of 9 healthy canine hearts high resolution DTI *ex-vivo* acquisitions [1] provided by Dr. Patrick A. Helm and Dr. Raimond L. Winslow at the Centre for Cardiovascular Bioinformatics and Modeling and Dr. Elliot McVeigh at the National Institute of Health was used.

Each of the dataset consists of a DTI volume and a B0 volume. Both volumes have a high resolution voxel size ($0.4297 \times 0.4297 \times 1.0$ mm). The B0 volume was used to manually segment the left ventricular wall. Care was taken to avoid the papillary muscles, as shown in Fig. 3.9(a). The extreme basal boundaries are also intentionally avoided. As explained in Sec. 3.4.1, the truncated ellipsoid closest

[1] http://www.ccbm.jhu.edu/research/DTMRIDS.php

**Algorithm 1:** AHA Zone Tensor Variability Computation

**Data**: The set of acquired tensors $D_i$ at arbitrary Cartesian positions $x_i$
**Result**: The set of Inertia Matrices Cross-Correlations $S_{\mathcal{V}}(z)$ for $z = 1 \rightarrow 17$
*Coordinate Change*
**foreach** $(x, D_x) \in \Omega$ **do**
  $\xi = \Psi \circ \Phi(x)$
  $D_\xi = \tilde{\Psi} \circ \tilde{\Phi}(D_x)$
  $l(\xi) = \mathrm{vec}(\log(D_\xi))$
**end**
*Gradient and Inertia Matrix Computation*
**foreach** $\xi, l(\xi)$ **do**
  $i \leftarrow 0$
  **foreach** $\xi' \neq \xi$ *in* $\mathcal{V}, l(\xi)'$ **do**
    $\Sigma = \mathrm{diag}(h_i)$
    $U^\Sigma(i) = \Sigma(\xi' - \xi)$
    $\partial_U l(\xi)(i) = l(\xi') - l(\xi)$
    $i \leftarrow i + 1$
  **end**
  solve the least sq. problem $U^\Sigma \nabla l_{\mathcal{V}}(\xi) = \partial_U l(\xi)$
  $S_{\mathcal{V}}(\xi) \leftarrow \nabla l_{\mathcal{V}}(\xi) \nabla l_{\mathcal{V}}(\xi)^T$
**end**
*AHA zone Inertia Matrix Computation*
**for** $z = 1 \rightarrow 17$ **do**
  $S_{\mathcal{V}}(z) = \frac{1}{N_z} \sum_i S_{\mathcal{V}}(\xi_i)$
  $S_{\mathcal{V}}^{cart}(z) = \tilde{\Phi}^{-1} \circ \tilde{\Psi}^{-1}(S_{\mathcal{V}}(z))$
**end**

to this segmentation is found by computing the axis of symmetry of the mesh, and estimating the major-axis and minor-axis lengths. Fig. 3.9(b) illustrates this process. The grey wire-frame grid represents the ellipsoid volume found, and the surface mesh shows the LV segmentation.

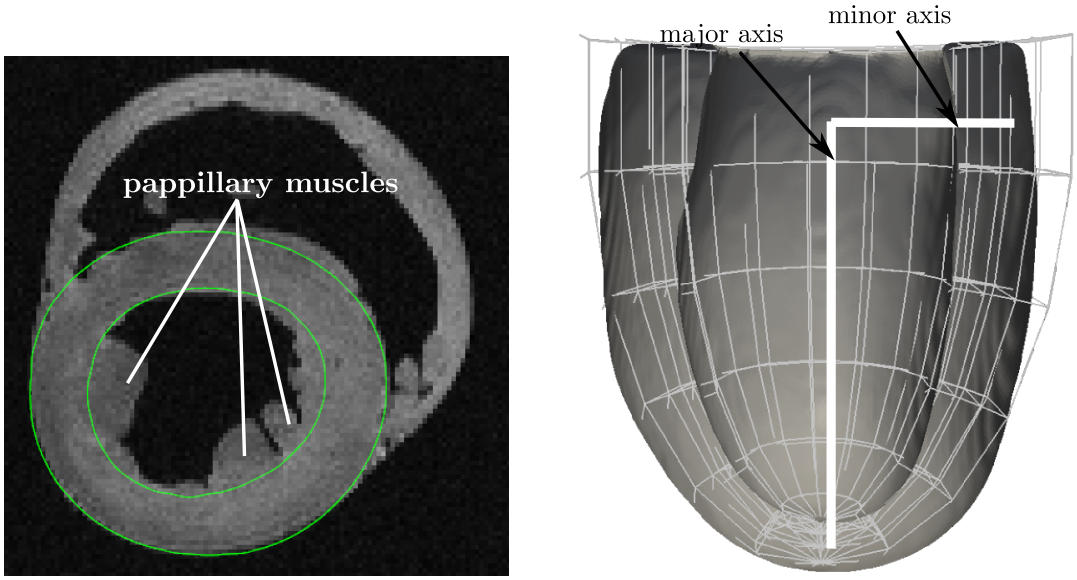


(a) B0 map and segmentation

(b) segmentation and ellipsoid

**Figure 3.9:** *(a) The B0 map of one of the canine hearts is shown together with its corresponding LV segmentation outline. (b) The long-axis of the ellipsoid (wire-frame grid) is found using the axis of symmetry of the segmentation (surface mesh), and the lengths of the axes of the ellipsoid are derived.*

Binary masks of the ellipsoid $T$ and of the LV segmentation $S$ were used for registration and DTI tensor data have been transformed to the PS frame.

To extract characteristics of interest of a tensor field within the left ventricle, three different applications of the approach described in this chapter will now be described.

### 3.6.1 Orientation Feature Extraction

The helix, transverse and sheet angles at each position were extracted as described in Sec. 3.3.1. There are several ways of visualising and interpreting these angular features. One way is, in the PS frame, to construct the joint histogram of each angle versus the transmural abscissa $\xi_1$. These joint histograms are presented in Fig. 3.10 for one of the explanted canine hearts (heart # 2). The helix angle is strongly correlated to the transmural abscissa (correlation coefficient of 0.71) and agrees with earlier analysis of the fibre directions on explanted hearts [Peyrat 2006, Lombaert 2011]. The transverse angle is very stable around zero, confirming a low deviation from circumferential direction also observed in earlier studies. The sheet angle does not seem to be significantly correlated to the transmural depth.

Another way of visualising the helix angle distribution is to take advantage of inverse operators $\Phi^{-1}$ and $\Psi^{-1}$ in order to warp back this angular information in the anatomical space of the corresponding explanted heart, as detailed in Sec. 3.4.1.

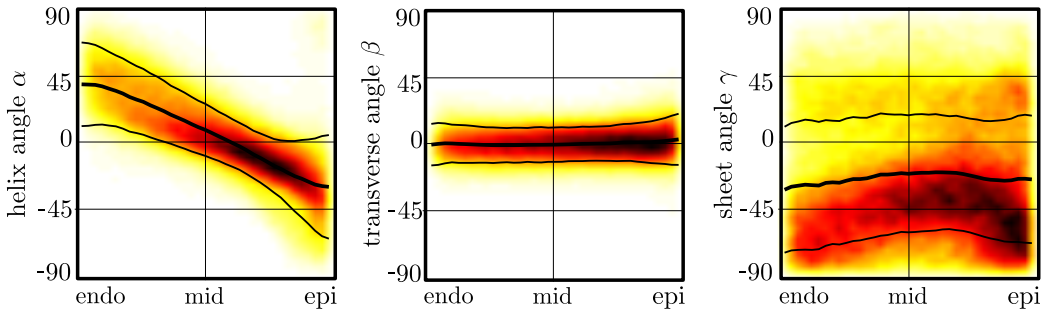


**Figure 3.10:** *Joint histograms of respectively the helix, transverse and sheet angles with respect to the transmural abscissa. The black lines indicate the mean (per column) and the window at 1 $\sigma$.*

In Fig 3.11, tractography results of explanted heart # 2 are color-coded by the extracted local helix angle $\alpha$. Helix angle boundary values are found to be $+43deg.$ at the endocardium and $-37deg.$ at the epicardium. This study can be considered as an alternative study to the work presented in [Peyrat 2009], where the same database was used to produce a statistical atlas of cardiac DTI. The discrepancy between the endocardial and epicardial boundary values of the helix angle may be explained by the intentionally strong constraints during left ventricular segmentation. The extremal regions at the endocardium for instance might include the papillary muscles where the helix angle reach very high values (details on this matter are presented in Sec. 3.7.1).

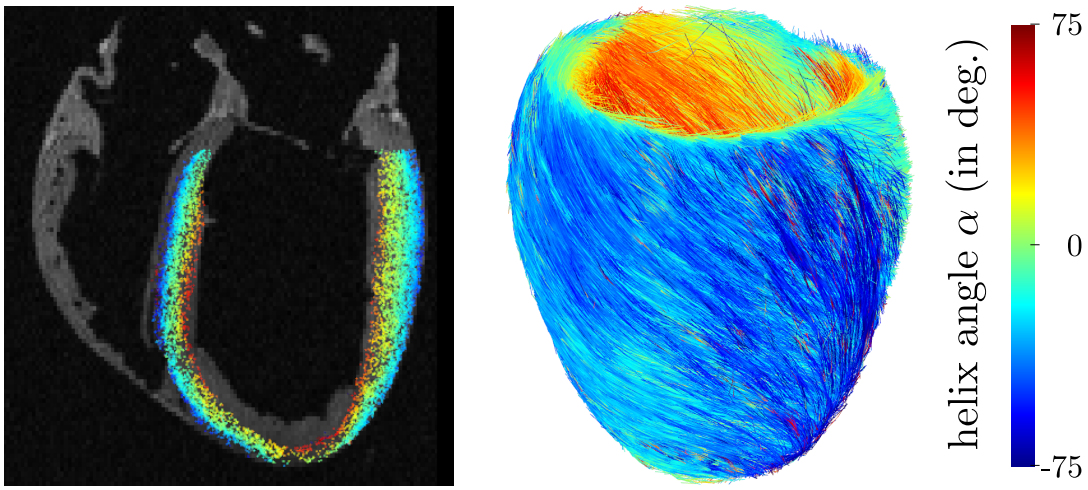


**Figure 3.11:** *Helix angle $\alpha$ mapped onto the fibre field of an explanted canine heart.*

### 3.6.2 Shape Feature Extraction

In this section, two different scalar features were extracted from a canine dataset: the fractional anisotropy $FA$ and the linear coefficient $c_l$. Both are alternative

measures of elongation of the tensor shape:

$$\begin{cases} FA & = \sqrt{\frac{3}{2}} \frac{\sqrt{\sum_{i=1}^{3}(\lambda_i - \bar{\lambda})^2}}{\sqrt{\sum_{i=1}^{3}\lambda_i^2}} \\ c_l & = \frac{\lambda_1 - \lambda_2}{\sum_{i=1}^{3}\lambda_i} \end{cases} \tag{3.11}$$

The two quantities have been evaluated on the single *ex-vivo* canine heart # 2 and are plotted on a bullseye plot in the PS sense in Fig. 3.12, as explained in Sec. 3.3.1. Linear coefficient gives a lower contrast of values than the fractional anisotropy, but both measures present the same patterns. The septal wall appears to give high anisotropy values, and generally the basal regions are more anisotropic than the apical ones.

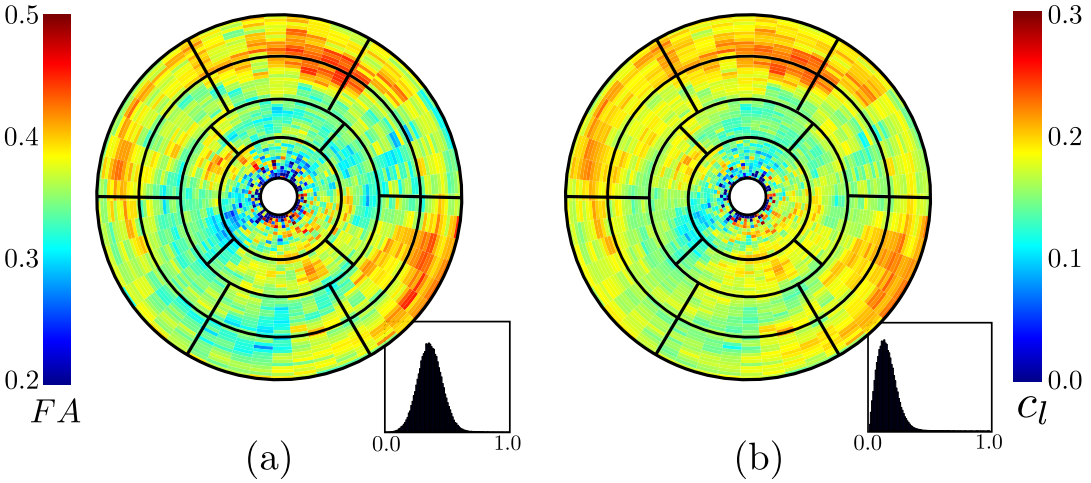


**Figure 3.12:** *Tensor shape feature extraction on a single canine ex-vivo dataset: (a) bullseye plot (in PS sense) of the fractional anisotropy FA. (b) Bullseye plot (in PS sense) of the linear component $c_l$.*

The distribution of the FA throughout the entire ventricle appears to follow a Gaussian distribution with a mean value of 0.32 and a standard deviation of 0.12. This FA value is characteristic from cardiac tissue anisotropy following necrosis, as observed in [Eggen 2012].

### 3.6.3 Variability Feature Extraction

For the purpose of this example, each PS transformed DTI dataset was divided into AHA zones as detailed in Sec. 3.3.1. Let us denote $\Omega_z$ the domain of definition of AHA zone z, and $[D_\xi]^z$ the set of tensors belonging to $\Omega_z$, with $z = 1..17$. This set of tensors can then be used to derive zone-specific quantities of interest.

For instance, it is of interest to quantify the variability of the tensor field in each AHA region. As suggested by [Basser 2007], one can consider the evaluation of the exhaustive spectral decomposition of the variability of a set of tensors by computing the full covariance $4^{th}$ order tensor. Alternatively to this very interesting approach (left for future investigation), some properties of this variability can be obtained by computing the *inertia matrix* as described in Sec. 3.5.1.

The inertia matrix quantity, $S_{\mathcal{V}}(\xi)$, computed everywhere in the ventricle wall (see Sec. 3.5.2) describes the local variability of the input DTI tensors in space.

For this application, an infinite support has been chosen for the computation of the gradient $\nabla l_{\mathcal{V}}(\xi)$, i.e. we consider the whole tensor field as neighborhood $\mathcal{V}$. As a covariance matrix, $S_{\mathcal{V}}(\xi)$ is symmetric definite positive, and can be visualised the same manner as are tensors. Fig 3.13(a,b) presents the DTI data of a long axis slice, acquired in *ex-vivo* canine hearts # 2 and # 3, and the corresponding local inertia matrices $S_{\mathcal{V}}(\xi)$ are shown in Fig 3.13(c,d). The immediate observation concerns the direction of the principal eigenvectors of $S_{\mathcal{V}}(\xi)$. They correspond to the principal direction of spatial change of the tensor field. They appear very consistently oriented in the transmural direction, suggesting that the variability of the fibre structure information is almost entirely contained in its $\xi_1$ projection.

Finally, to quantify the regularity of the inertia matrix over the LV, we evaluated the mean inertia matrix in each AHA zone $\Omega_z$:

$$S_{\mathcal{V}}(z) = \frac{1}{N_z} \sum_{i \in \Omega_z} S_{\mathcal{V}}(\xi_i) \tag{3.12}$$

With $N_z$ the number of data centres in zone $z$.

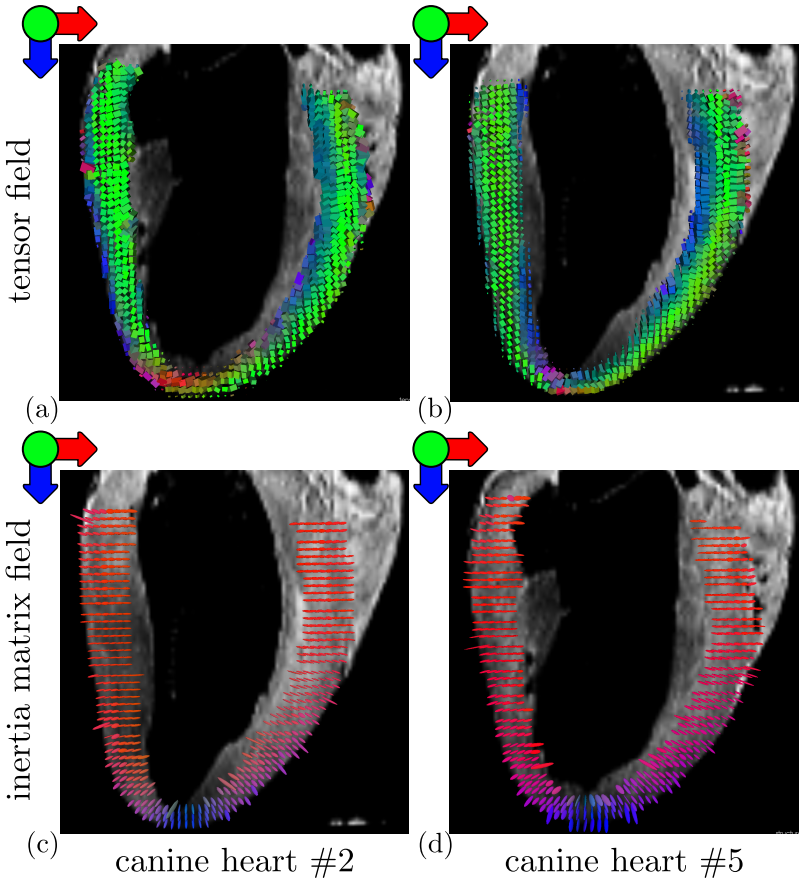


**Figure 3.13:** *(a,b) DTI slice (long axis) of one of two healthy ex-vivo canine hearts. Tensors are color-coded with their main eigenvector directions. (c,d) Inertia matrices $S_\sigma(\xi)$ of the diffusion tensor field. They illustrate the spatial variability of the tensor field. The principal eigenvectors $s(\xi)$ of the inertia matrices $S_{\mathcal{V}}(\xi)$ are mainly oriented in the transmural direction.*

Figure 3.14 shows the resulting set of mean inertia matrices $S_{\mathcal{V}}(z)$ for $z = 1 \sim 17$. They are represented as superquadrics, 3D parallelelograms with each pair of sides

are proportional to the corresponding eigenvectors and eigenvalues of $S_{\mathcal{V}}(z)$. The main direction of variation of the underlying tensor field is characterized In the first eigenvector of the mean inertia matrix. This main direction is shown to appear mostly parallel to the transmural axis. It therefore shows that the fibre architecture of a (healthy) heart is varying mostly between endocardium to epicardium, but is relatively constant in the other directions, as also observed in [Fernandez-Teran 1982]. The second mode of variation (second longest side of the parrallelogram) is in the apico-basal direction, which indicates that fibres show generally more variability in this direction than in the circumferential direction. The parallelograms are color-coded with their respective volume, which quantifies the amount of variability of the tensor field in the corresponding AHA zone. One can note the greatest variability appears at the apex, where fibre architecture is the least coherent.

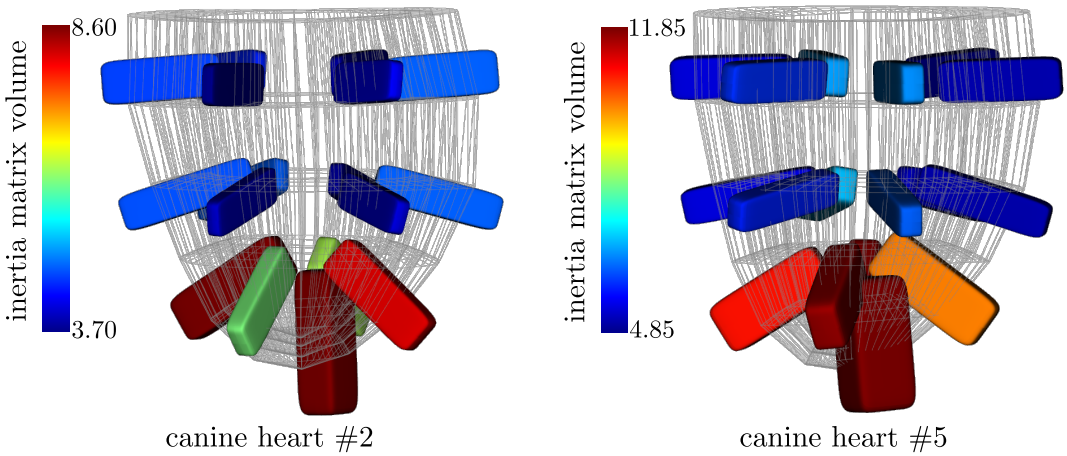


**Figure 3.14:** *Mean inertia matrices calculated over each AHA zone for 2 different ex-vivo canine hearts. These symmetric matrices are represented as superquadrics and are color-coded with the matrix determinant. They illustrate that the main direction of change of the fibre architecture is along transmural depth. The greatest variability appears at the apex.*

## 3.7 Workflow: Sensitivity to Parameters

This approach to tensor data representation in the left ventricle depends on several steps:

- The manual segmentation of the left ventricular endocardium and epicardium.
- The definition of the closest ellipsoid. That is, its centre, major and minor axes.
- The diffeomorphic registration performed between the LV binary mask and the ellipsoid binary mask.

Each of those three steps can introduce inaccuracy. In this section the influence of these three potential errors in the final results is discussed. Additionally, the accumulation of error during the entire workflow is quantified.

### 3.7.1 Manual Segmentation

As detailed in Sec. 3.4.1, the anatomical shape of the ventricle is extracted through manual segmentation, and the closest truncated ellipsoidal volume is extracted using this segmentation. It can be argued that the workflow is therefore subject to segmentation errors and might bias the statistical study. One important characteristic of the presented workflow is that it relies on a registration between this segmented ventricle and the truncated ellipsoid. Measure positions and DTI data are transformed to this ellipsoid simply for statistical analysis and interpolation purposes. Since tensors are reoriented according to the Jacobian of the transformation $\Phi$, it can be argued that only the rotation components of $\Phi$ can potentially bias the accuracy of the statistical results. It is therefore important that the segmentation is smooth to prevent for strong rotation components of the transformation $\Phi$ that would cause an anatomically inaccurate extra rotation of the tensors.

Additionally, a misevaluation of the segmented wall will provoke the inclusion or exclusion of tensor data at the boundaries of the LV. As shown in Fig. 3.9, the endocardial boundary of the segmentation was carefully monitored to avoid the papillary muscles. To illustrate the influence of the segmentation on helix angle graphs, Fig. 3.15(b) shows two elevation angle graphs when including or excluding the endocardial papillary muscles.

### 3.7.2 Ellipsoid Definition

The axis of rotation of the truncated ellipsoid is defined as the main axis of mass of the segmented LV. A variation of this axis will impact the resulting statistical study. For instance, its effect on the graphs presented in Fig. 3.10 would be an increase/decrease of the vertical standard deviations of the angles $\alpha$, $\beta$, and $\gamma$ with no impact on the mean values. Indeed, the mean bias cancels out around the $\xi_3$ direction. However, it is important to note that a misevaluation of this axis by only 10 deg. at the base would already deviate the apex location by 1cm, and the error would be straightforward to pick during the process. In this case a manual adjustment of the axis is necessary to ensure a good overlap of the ellipsoid and the LV volume.

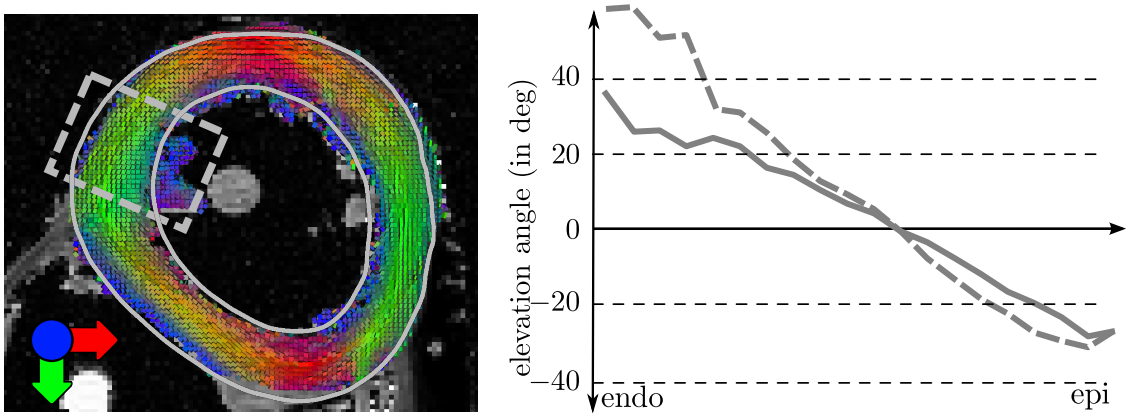


**Figure 3.15:** *(a) A DTI slice of one of the ex-vivo datasets. (b) The elevation (helix) angle is reported with respect to the transmural depth. The dotted line concerns the dotted rectangle*

### 3.7.3 Diffeomorphic Registration Accuracy

The accuracy of the registration can be quantified by computing the overlap between the target image $T$ and the transformed source image $\Phi(S)$. A common way to evaluate this overlap is through the Dice coefficient [Dice 1945]: $d = (T \wedge \Phi(S))/(T \vee \Phi(S))$. Values of $d$ close to 1 denote a good overlap. The Dice coefficient was computed for the 9 *ex-vivo* canine cases and a value of $d = 0.95 \pm 0.003$ was obtained (mean $\pm$ standard deviation). This indicates a very good overlap between masks. However, the initial source and target binary masks are already close together: the Dice coefficient between initial $S$ and $T$ is already $d_{init} = 0.80 \pm 0.05$. It can be explained by the fact that the ellipsoid is constructed for this aim, and that the segmentation is constrained to a certain degree of smoothness.

### 3.7.4 Error Accumulation

The transformation steps applied to the DTI data are the following: the position and tensor data are transformed to the PS frame using the two operators $\Phi$ and $\Psi$, and transformed back to the initial anatomical geometry using $\Psi^{-1}$ and $\Phi^{-1}$. Error can accumulate during this process. In order to quantify this accumulation, two quantities are computed:

- The spatial misalignment $\varepsilon_x$ between each Cartesian measurement centre $x$ of the domain $\Omega$ and the corresponding transformed point.
- The angular difference $\varepsilon_v$ between the first eigenvector $v_1$ of initial tensor $D_x$ at Cartesian position $x$, and its corresponding transformed one

$$\begin{cases} \varepsilon_x(x) & = \|\Phi^{-1} \circ \Psi^{-1} \circ \Psi \circ \Phi(x) - x\| \\ \varepsilon_v(x) & = \tilde{\Phi}^{-1} \circ \tilde{\Psi}^{-1} \circ \tilde{\Psi} \circ \tilde{\Phi}(D_x) - D_x \end{cases} \tag{3.13}$$

Histograms and bullseye maps of these errors are shown in Fig 3.16. Histograms show very low position and angular errors. The position error $\varepsilon_x$ presents a peak misalignment value at the antero-lateral wall region (indicated by the arrow). However this peak has a value of 0.02 mm, which corresponds to less than 5% of the voxel

size. From these results it can be concluded that the error accumulation in position and tensor orientation is not significant. In practice, this error quantification can be used as an implementation error detection. If there is an inaccuracy in one of the steps of the workflow, it will reflect in this test with high error values.

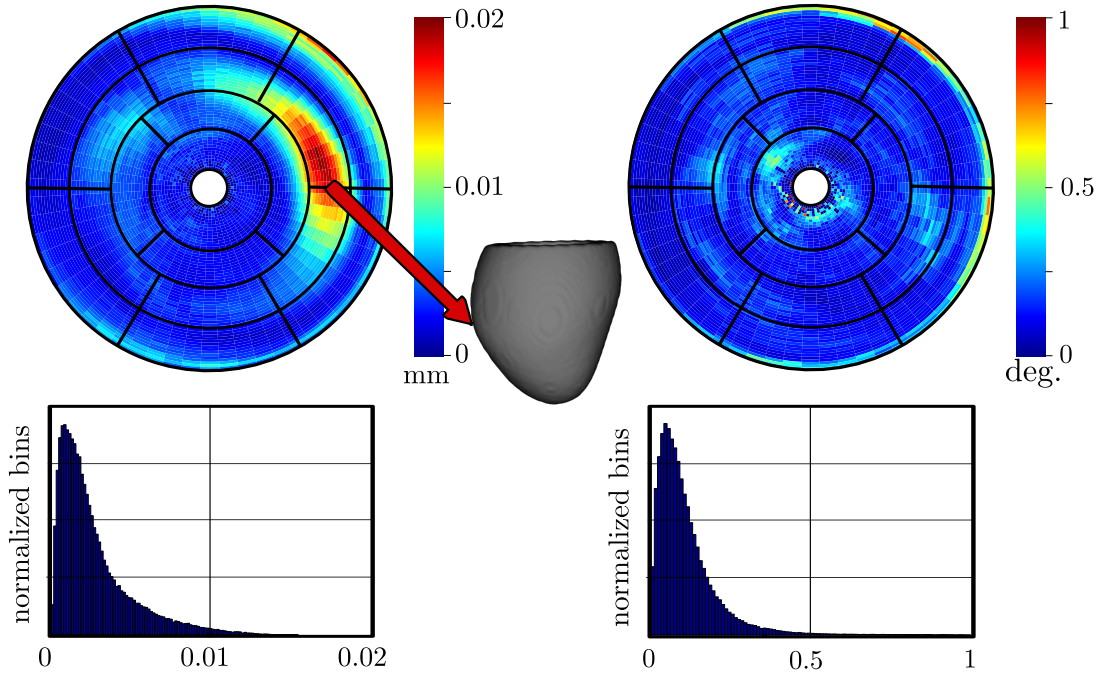


(a) Position accumulated error $\varepsilon_x$ (in mm.) (b) Angular accumulated error $\varepsilon_v$ (in deg.)

**Figure 3.16:** *Accumulated error during the global workflow. (a) The spatial misalignment between initial point and transformed one. (b) The directional error (in deg.) between initial tensor and transformed one.*

To summarize, the diffeomorphic registration accuracy and the error accumulation in terms of position and orientations are found to be not significant. On the other hand, the sources of error involving manual input can influence the quantitative analysis output. Especially, the segmentation of the myocardial wall is subject to inter-operator variability. This variability provokes the inclusion or exclusion of the papillary muscles borders at the endocardial wall and the septum, explaining the relative instability of helix angle ranges reported in the literature. In the remaining of this thesis, care has been taken to minimize the inclusion of the endocardial papillary muscles in order to reflect the fibre architecture of the myocardial wall alone.

## 3.8 Note on AHA Subdivisions

The AHA segmentation of the left ventricle detailed in this chapter is based on a linear division of the ellipsoid in PS coordinates. Especially, it assumes that the septum is 2 segments wide, that is, 120 deg. We discovered that this assumption does not hold on the canine heart database used in these experiments. Figure 3.17(a) demonstrates that if the usual AHA segmentation is kept and if the anterior wall / RV separation is imposed as the limit between zone 1 and 2, then a significant mismatch of the other end of the septum is observed. To address this problem,

the definition of the AHA segmentation is extended to take a septum width of 150 deg. The result is shown in Fig. 3.17(b). The 150 deg. width is kept for the first 2 layers of AHA zones (i.e. zones 1∼12). This correction appeared necessary for all canine hearts encountered in the John Hopkins database. Interestingly, it was not necessary in the human heart of the same database, or in any of the *in-vivo* volunteer's data encountered later. This finding may indicate an anatomical difference between the two species, however the low number of datasets cannot allow us any strict conclusion.

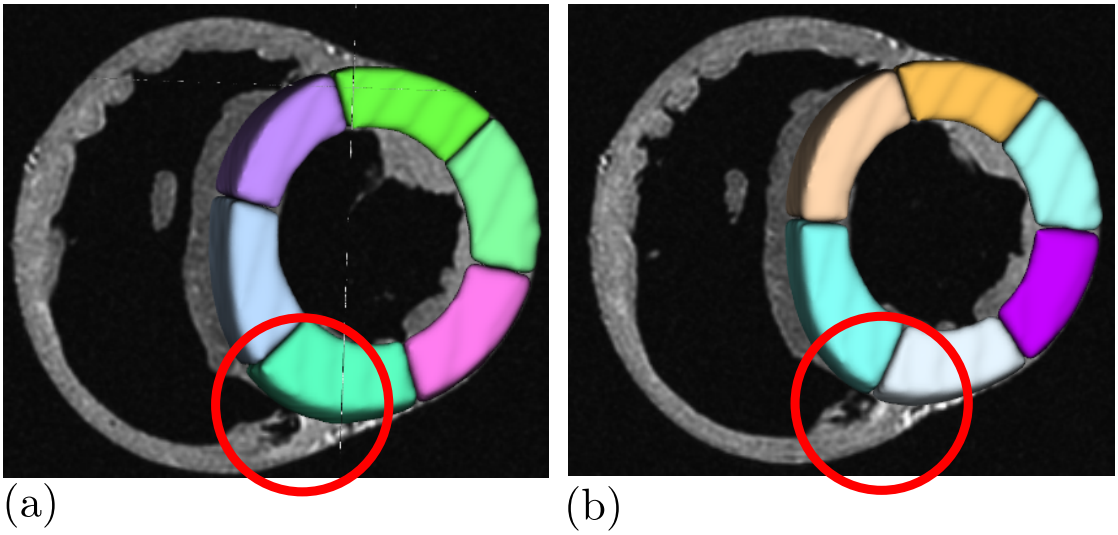


**Figure 3.17:** *(a) The usual AHA segmentation which assumes 120 deg. for the width of the septum appears to introduce a mismatch (red circle) in the canine hearts. (b) A correction is necessary to consider a septum width of 150 deg. The AHA zones are separately color-coded for distinction.*

## 3.9 Conclusions

This chapter presented the PS coordinate system and showed its suitability to describe information in the left ventricular wall. By using a symmetric and elastic registration scheme, any scalar information contained in the anatomical LV can be mapped onto a naturally normalized PS frame. Using Finite Strain reorientation, this approach was extended to higher order data such as tensors.

This reference frame gives the opportunity to analyse and quantify features from the initial data along PS coordinates, which are physiologically meaningful. These concepts were illustrated by applying them to a database of *ex-vivo* canine DTI datasets. Features of interest such as the helix and transverse angle transmural variations were extracted. This approach provides powerful tools for data analysis and visualisation. For instance, this chapter showed the analysis of the variability of the fibre architecture via the computation of the inertia matrix of the DTI data in PS coordinates. This variability information could be used as a prior information for more complex processing such as approximation. For instance, one can use the inverse of the cross-correlation $S_{\mathcal{V}}^{-1}(z)$ as optimal kernel $H^z$ presented in Sec. 4.5. Further investigations on this matter could include the computation of the quantity

defined as $T_\sigma = G_\sigma * \nabla l_\mathcal{V}^T \cdot \nabla l_\mathcal{V}$ (swapping the transpose sign from Eq. 3.10). This would describe the variability in the tensor space rather than in the physical space.

Sensitivity of our approach to a number of potential input errors was quantified. In particular the error accumulation during the application of operators $\Phi$ and $\Psi$ has been studied. Results indicate error values below any significance in terms of position and tensor orientations. As discussed in the next chapter, this data description approach can appear very useful when applied to complex processing such as the dense approximation of a tensor field from sparsely acquired DTI data. Additionally, as opposed to mesh-based PS parameterizations - such as in [Lamata 2011] -, the approach described in this chapter gives continuous (and symmetric) mappings between the anatomical space and the PS normalized frame, which can become a very desirable characteristic for instance when interpolating data. For potential external use, we publicly released the complete c++ implementation of our approach [2] (see App. C for details). It is already used in several external contexts, and is scheduled to be partly integrated in the medical imaging software medInria [3].

[2] https://github.com/ntoussaint/Cardiac-Prolate-Spheroidal-ToolKit
[3] http://med.inria.fr

Chapter 4

# Dense Approximation of Fibre Architecture

## Contents



## 4.1 Motivations

In Sec. 2.5 the recent advances in cardiac DTI acquisition were reviewed. It was shown that the challenges of such techniques make it difficult to acquire the diffusion information in the entire left ventricle, both for clinical time reasons and because of complex motion patterns in the apical and basal regions. However, it is of interest to obtain an approximation of this information in the entire volume, in order to exploit it for instance in patient specific electrophysiological models. Indeed, although the myocardial fibre orientations have a great influence on the cardiac electrical activity and motion, most studies still rely on prior models of the fibre architecture (see e.g. [Sermesant 2008, Seemann 2006, Vadakkumpadan 2012]). In this chapter, a method is introduced to approximate a dense tensor field lying in the LV wall from a set of data sparsely acquired. It involves an approximation operator used in the common PS frame described in Chap. 3. This operator has a tri-variate kernel width as parameter which is optimized using a human *ex-vivo* dataset.

## 4.2 Theory

Representing data in a continuous frame presents a number of advantages. In particular, any parameter of interest requiring a spatial differentiation could not easily be evaluated on a sparsely sampled dataset. In [Pajevic 2002], the authors show that a smooth approximation of a sparse set of noisy diffusion tensors allows a robust and reliable evaluation of characteristics of the underlying tissue of interest. In their setting, they consider a *regularly* sampled set of data *centres*, and build a mathematical framework in order to *approximate* the underlying continuous tensor field. The method described in this section shares the goals of [Pajevic 2002], but considering an *irregularly* sampled set of data *centres*.

### 4.2.1 Approximation Operator in PS Coordinates

As explained in Sec. 3.5.1, data in the PS frame is *not regularly* distributed and heterogeneous. This heterogeneity is further increased in *in-vivo* situations as a limited amount of DTI slices are acquired. Let us consider the estimation of a dense 3D tensor field from a set of sparse DTI measurements *irregularly* distributed across the ventricle. Let us consider a set $P$ of $M$ measured positions and tensors $P = (x_i, D_{x_i})_{i=1:M}$ (i.e. centres). An operator $\mathcal{W}_P$ is defined over a domain $\Omega$ (covering the ventricle wall volume), describing how to recover data at position $X$ from noisy and scattered input data:

$$\forall x \in \Omega,\ D_x := \mathcal{W}_P(x) \tag{4.1}$$

where $\Omega$ refers to the spatial target domain where samples are *needed*. It can be of lower or higher cardinality than $P$ and may not be necessarily defined on a regular grid nor constrained within the convex hull of $P$. Solutions to approximate missing data and data fitting have been explored extensively in the past. For instance, in [Fillard 2005], the authors used Radial Basis Functions (RBFs) in order to find a smooth solution for $\mathcal{W}_P$ that satisfies the interpolant constraint, that is: $\mathcal{W}_P(x_i) = D_{x_i}$, for $i = 1, 2, \ldots M$. More precisely, they find the set of scalar coefficients $\gamma_i$ that satisfy the following system of linear equations :

$$\text{RBF approach: find } [\gamma] \text{ s.t. } \forall j : D_{x_j} = \sum_{i=1}^{M} \gamma_i h(\|x_i - x_j\|) \tag{4.2}$$

with $h$ being a univariate multi-scalar function. Alternatively, [Pajevic 2002] propose a method to create a continuous representation of a tensor field from a *regularly* sampled measure grid.

However, because our input data can be corrupted by significant noise, and does not lie on a regular lattice, an *approximation* operator (or regularized estimation) was considered rather than a rigorous *interpolation* operator. An interpolation operator gives back the input data at measure points (i.e. $\mathcal{W}_P(x_i) = D_{x_i}$), whereas a regularized estimation can approximate results ($\mathcal{W}_P(x_i) \neq D_{x_i}$). Methods to regularize noise corrupted tensor fields have been proposed in the literature [Jones 2002, Fillard 2007, Frindel 2009]. In this study, the approximation operator takes the role of integrating the regularisation. The operator $\mathcal{W}_P$ therefore consists of taking a weighted mean of surrounding tensors as an estimate. The following question remains: which type of interpolation should be used to compute

this weighted mean ? Over the recent years, many different options have been introduced. As indicated in Sec. 2.3, symmetric definite positive matrices do not lie on a vector space. It has been therefore pointed out by several studies that using Euclidean interpolation is inappropriate as it does not reflect physical meaning. To avoid swelling effect on tensors and to address the fact that the spatial density of $P$ can be low in the practical case, the mean in the log-Euclidean sense is used [Arsigny 2006].

$$\mathcal{W}_P : x \to \mathcal{W}_P(x) = \exp\left(\frac{\sum_{i=1}^{N} K(x - x_i)\log(D_{x_i})}{\sum_{i=1}^{N} K(x - x_i)}\right) \tag{4.3}$$

The kernel $K$ is, in our study, tri-variate and not necessarily isotropic:

$$K_H : dX \to K_H(dx) = \det(H)^{-1} k\left(\sqrt{dx^T H^{-2} dx}\right) \tag{4.4}$$

where $H$ is a $3 \times 3$ matrix that has to be optimized [Härdle 1985]. The function $k$ is a given univariate kernel function. In this work, two different functions were taken into consideration, $k_1$ the Normal Gaussian function, and $k_2$ the Kaiser-Bessel function, commonly used in k-space gridding [Jackson 1991]:

$$\begin{aligned} k_1(x) &= \frac{1}{\sqrt{2\pi}} \exp\frac{-x^2}{2} \\ k_2(x) &= \begin{cases} \frac{I_0(\beta\sqrt{1-(2x/W)^2})}{I_0(\beta)} & \text{if } -W/2 \le x \le W/2 \\ 0 & \text{otherwise} \end{cases} \end{aligned} \tag{4.5}$$

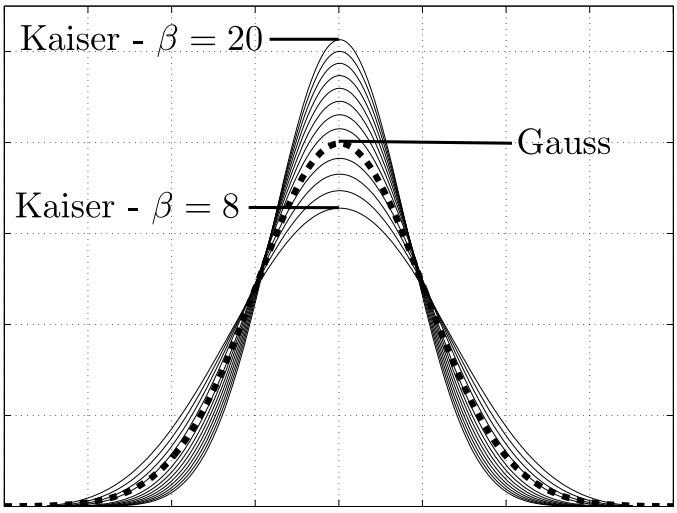


**Figure 4.1:** *Shapes of different univariate kernel functions. In dotted line is the Normal Gauss function. All Kaiser-Bessel functions shown in plain lines have a fixed window size of* $W = 7.0$*, and the parameter* $\beta$ *is varying from* 8 *to* 20*.*

In this proposed approximation scheme, spatial coherence is enforced independently in each of the main directions of the heart anatomy (e.g. radial, circumferential and longitudinal in PS coordinates). In consequence, the bandwidth matrix $H$ is constrained to be diagonal. Therefore diagonal values of $H$ control the resulting

approximation. In other words, as opposed to the RBF approach in Eq. 4.2, as detailed later in this chapter, our approach finds $H$ (of tri-variate kernel $K_H$) that minimizes global discrepancy between $\mathcal{W}_P(x)$ and $D_x$:

$$\text{Quasi-Interpolant: find } H \text{ s.t. } H = \operatorname{argmin} \|\mathcal{W}_P(\Sigma) - \Sigma\| \tag{4.6}$$

where $\Sigma$ denotes the input tensor field.

The approximation scheme in Eq. 4.3 can be applied on the set of pairs $P'' = (\xi, D_\xi)$ in the PS frame (see Chap. 3). To be precise, it is important to note that, in addition to the centres $P$, the operator $\Psi \circ \Phi$ also needs to be applied to each position $X$ of the target domain $\Omega$ where estimates are needed. Each resulting estimates $\mathcal{W}_P(\xi)$ are eventually transformed back to Cartesian coordinates and warped back to the initial geometry using invert operators, that are defined and available everywhere except at the singular section (details of the inversion and the singularity are provided in Appendix A), and the approximation operator can therefore be written as:

$$\mathcal{W}_P(x) = \Phi^{-1} \circ \Psi^{-1} \circ \mathcal{W}_P(\xi) \tag{4.7}$$

**Algorithm 2:** Dense Approximation in PS coordinates

**Data**: The set of acquired tensors $(D_x)$ at arbitrary positions $(x)$ and a kernel width $H$
**Result**: The dense tensor field $D'_x$ on a dense regular lattice $(x')$ (i.e. $\Omega$)
*Data Coordinate Change*
**foreach** $(x, D_x) \in P$ **do**
  $\xi = \Psi \circ \Phi(x)$
  $D_\xi = \tilde{\Psi} \circ \tilde{\Phi}(D_x)$
  $l(\xi) = \text{vec}(\log(D_\xi))$
**end**
*Approximation operator*
**foreach** $(x') \in \Omega$ **do**
  $\xi' = \Psi \circ \Phi(x')$
  $l(\xi') = 0$
  $W = 0$
  **foreach** $(\xi, l(\xi))$ **do**
    $d\xi = \xi - \xi'$
    $w = \det(H)^{-1} k\left(\sqrt{d\xi^T H^{-2} d\xi}\right)$
    $l(\xi') = l(\xi') + w l(\xi)$
    $W = W + w$
  **end**
  $l(\xi') = l(\xi')/W$
  $D'_\xi = \exp\left(\text{vec}^{-1}(l(\xi'))\right)$
  $D'_x = \tilde{\Phi}^{-1} \circ \tilde{\Psi}^{-1}(D'_\xi)$
**end**

### 4.2.2 Kernel Width Optimization using *Ex-Vivo* Data

As explained in the previous section, the dense approximation depends on a $3 \times 3$ matrix denoted $H$. This matrix describes the shape of the tri-variate kernel. This matrix was constrained to be diagonal, however the optimal diagonal components that minimize the error between measured and approximated data remain to be estimated, while keeping a certain degree of smoothness. To do so, a high resolution DTI *ex-vivo* acquisition of a human heart [1] provided by Dr. Patrick A. Helm and Dr. Raimond L. Winslow at the Centre for Cardiovascular Bioinformatics and Modeling and Dr. Elliot McVeigh at the National Institute of Health was used. This dataset provides a ground truth that was manipulated to *simulate in-vivo* situations.

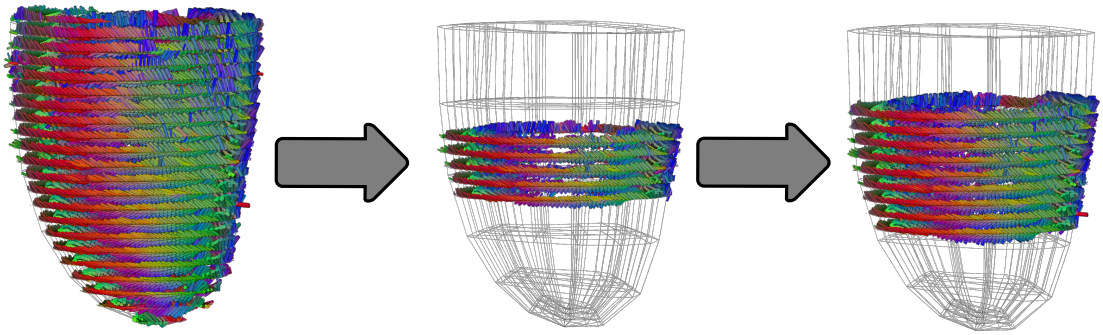

**Figure 4.2:** *Reference tensor field was down sampled and reoriented to obtain a voxel size of $2 \times 2 \times 4mm$ in a short axis way (left). Then the number of slices $N$ was varied to simulate different in vivo acquisition situations.*

It is hypothesised that a typical *in-vivo* cardiac DTI acquisition would consist of a limited amount of short axis (SA) slices. Furthermore, these slices are usually constrained to the equatorial part of the ventricle as motion pattern and partial volume effects around the apex hamper acquisition of images with sufficient quality. In consequence, $N$ SA equatorial slices from the *ex-vivo* dataset were extracted while avoiding the apex and base boundaries, as shown in Fig. 4.2 (centre). Each of the $N$ slices was then transformed to a series of 6 DWIs, using the $L_2$ norm over the tensors as a baseline image and 6 non-collinear gradient orientations uniformly distributed on the sphere. Complex Rician noise of variance $V$ was added to the DWIs, as illustrated in Fig. 4.3.

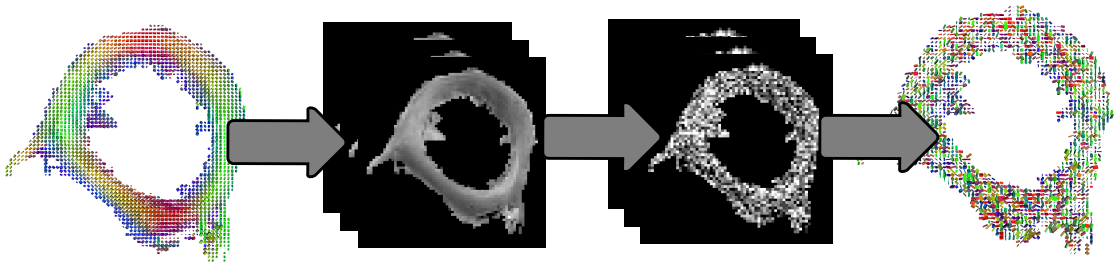

**Figure 4.3:** *Ex-vivo experiment: 6 Diffusion Weighted Images (DWIs) were artificially computed from the reference tensor field. Each DWI was corrupted by additive Rician noise, and the tensor field was then estimated. The variance of the added Rician noise in this example was $V = 0.04$ for each DWI, which results in a signal to noise ratio of 10.0.*

[1] http://www.ccbm.jhu.edu/research/DTMRIDS.php

The DWIs were then used as input data for the approximation scheme detailed in Sec. 4.2.1 and the full ventricular tensor field was computed. The output was compared to the true tensor field in a voxel-wise manner. The similarity map is used to optimize matrix $H_{opt}$, as a trade-off over the entire ventricle domain $\Omega$ between a Least Square ($LS$) term that describes the data fit and a smoothness term ($Reg$):

$$H_{opt} = \underset{H \in Diag(3)}{\operatorname{argmin}} \left(LS(H) + \lambda . Reg(H)\right),$$
$$\text{with} \begin{cases} LS(H) & = \sum_* dist\left(D_*, \mathcal{W}_P(*)\right)^2 \\ Reg(H) & = \sum_* \parallel \partial \mathcal{W}_P(*) \parallel^2 \end{cases} \tag{4.8}$$

where $*$ refers to $x \in \Omega$ in Cartesian coordinates or $\xi \in \Omega''$ in PS coordinates, and $\lambda$ to the scalar controlling the influence of the regularisation. Among different existing similarity measures between tensors (named *dist* in the formula), the Log-Euclidean metric distance [Arsigny 2006] was used. That is, the Frobenius norm of the matrix-log difference: $dist(A, B) = \parallel \log(A) - \log(B) \parallel$. The smoothness term (or regularisation term) can be seen as an equivalent of the total variation of the tensor field, i.e. the squared norm of the tensor field gradient in the log domain: $\partial \mathcal{W}_P(*) = \nabla \log(\mathcal{W}_P(*))$.

In the case where the Gaussian function was chosen for Eq. 4.3 (i.e. $k = k_1$), the parameter space of this minimization problem only consists of the three diagonal elements of the bandwidth matrix $H$. In the situation where the Kaiser-Bessel function is chosen ($k = k_2$), The window size is fixed to $W = 20$ and the parameter space therefore consisted of the scalar $\beta$ in addition to the diagonal elements of $H$. The minimization of Eq. 4.8 was performed using a gradient-free multivariate optimization scheme [Powell 2008].

The residual error made on the tensor field estimation depends on several variables: the Rician noise level (of variance $V$), the input data distribution (number of slices $N$), and of course the choice of coordinate system. In Sec. 4.3.1 the performance of the overall approximation process with respect to these factors is reported. Note that in the case where Cartesian coordinates are used, the approximation operator described in Eq. 4.1 is taken as it is, in Cartesian coordinates. In this particular case, there is no need of any non-linear registration. The matrix $H$ is optimized the same way.

For a better comprehension of the noise levels, the signal to noise ratio (SNR) of the noisy DWIs was computed. A region of interest $R$ was drawn in the exterior wall of one of the DWIs. Then the SNR was calculated as follows: $SNR = mean(R)/std(R)$. For instance, the reference *ex-vivo* dataset used as a ground truth has a value of $SNR = 36$.

### 4.2.3 Residual Error Computation

The optimization of the diagonal matrix $H$ was performed for different case scenarios of values of $N$ and values of $SNR$. The residual mean error between the reference tensor field and the approximated one was calculated. This error was defined as the angle difference between main eigenvectors of the reference and the approximated tensor, denoted $\varepsilon$, in a voxel-wise manner. If $\varepsilon$ is considered a random variable, then it can be seen as the combination of two independent random variables that are the polar angular errors $\varepsilon_1$ and $\varepsilon_2$. To be calculated, those polar angular errors

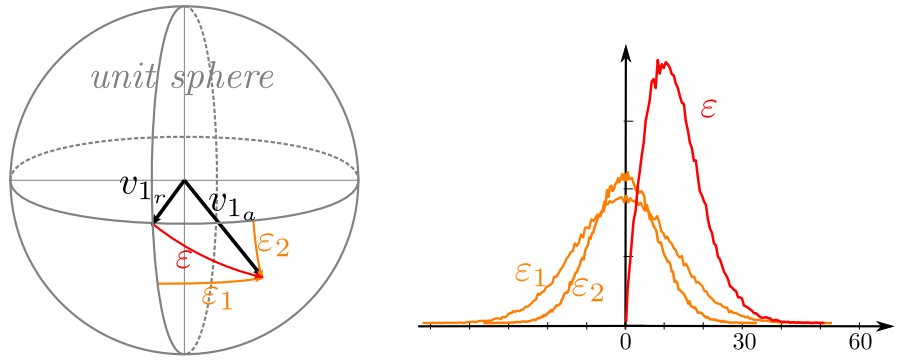


(a) Angular error $\varepsilon$ as a combination of polar angles

(b) Corresponding statistical distributions

**Figure 4.4:** *(a) Residual error $\varepsilon$ due to the approximation scheme on the angle between the approximated tensor's first eigenvector $v_{1_a}$ and that of the reference tensor $v_{1_r}$. $\varepsilon$ can be seen as a combination of two independent polar signed angles $\varepsilon_1$ and $\varepsilon_2$. (b) If $\varepsilon_1$ and $\varepsilon_2$ have a zero-mean Gaussian distribution, then the distribution of $\varepsilon$ is strongly skewed, and depends on the standard deviations of the polar angle errors.*

need the definition of two arbitrary planes going through the reference tensor's first eigenvector $v_{1_r}$, then $\varepsilon_1$ and $\varepsilon_2$ are the respective (signed) projections of the approximated tensor's first eigenvector $v_{1_a}$ onto each of the planes, as shown in Fig. 4.4(a). Spherical trigonometry therefore infers that $\varepsilon$ follows the distribution of $\arccos(\cos\varepsilon_1 . \cos\varepsilon_2)$. An example of such distribution is simulated in Fig. 4.4(b). In this simulation $\varepsilon_1$ and $\varepsilon_2$ are chosen to have a zero-mean Gaussian distributions. The distribution of $\varepsilon$ is *computed* (shown in red in Fig. 4.4) and shows a strongly skewed shape. The value of the mode (or peak) is therefore a good indicator of the most probable angular error, and of the performance of the approximation scheme.

### 4.2.4 Fibre Tractography

Fibre Tractography [Basser 2000] is a common way of visualising the main paths of white matter tracts that are derived from DT-MRI information. In the heart the tracts correspond to the main myocyte orientation paths throughout the ventricles. In order to facilitate the interpretation of the approximation scheme, tractography results was computed from the resulting dense tensor fields. Fibres were tracked from each voxel of the tensor field, using a propagation term as described in [Fillard 2003] and a fourth order Runge-Kutta integration. The fibre tractography approach used here utilizes advection-diffusion terms derived from [Weinstein 1999, Lazar 2003]. At any spatial position $p$, the local diffusion tensor $D$ is estimated (tri-linearly), and the next direction $v_{out}$ is calculated from the previous one $v_{in}$ using:

$$v_{out} = c_l e_1 + (1 - c_l)\big((1 - g)v_{in} + gD \cdot v_{in}\big) \tag{4.9}$$

where $e_1$ and $c_l$ are respectively the first eigenvector and the linear coefficient of $D$, as suggested in [Weinstein 1999], and $g$ is a smoothness parameter that has to be chosen manually. As the fibres are not intended to be constrained to a superficial smoothness, and due to the potential high curvature of the helical cardiac fibres, a small value of $g = 0.2$ was chosen.

First, fibre fields were produced using the reference fully sampled tensor field. Second, fibre fields were produced using the dense approximated tensor fields in the

case scenario of (N=7, SNR=10). For comparison purposes, fibres were computed both in the case PS coordinates were used for the approximation operator, and in the case Cartesian coordinates were used.

## 4.3 Results

### 4.3.1 Kernel Optimization and Sensitivity Analysis using *Ex-Vivo* Data

The approximation bandwidth matrix $H$ was optimized for different cases of number of slices $N$ and different $SNR$ using the reference *ex-vivo* tensor field. For each case the resulting kernel values (diagonal elements of $H_opt$, in mm) are reported in Fig. 4.5(a,b,c). In the case of PS approach, the kernel sizes $(k_{\xi_1}, k_{\xi_2}, k_{\xi_3})$ are by definition not in the same scale than in Cartesian coordinates $(k_x, k_y, k_z)$. In order to be able to compare these values, they were divided by their respective PS scaling factor $(h_1, h_2, h_3)$ corresponding to the derivative $h_i = \|\partial\xi_i/\partial x_i\|$. It is acknowledged that these factors are not homogeneous in space. The graphs presented here were computed using their mean values in the domain of definition $\Omega$. In Fig. 4.5(d) the determinant of the optimal kernel bandwidths was computed ($|K_{H_{opt}}$, in $mm^3$). Here again this determinant had to be divided by the product of the scale factors $\Pi(h)$ in the PS case in order for the values to be compared.

### 4.3.2 Residual Error with respect to parameters and position

For each case scenarios, the voxel-wise distribution of the residual error $\varepsilon$ between reference field and approximated field, defined in Sec. 4.2.2, was extracted and its mode value reported in Fig. 4.6.

The two maps show this mode value as a function of both the number of slices $N$ and the SNR of the DWIs, when using Cartesian coordinates (left) and PS coordinates (right) for the approximation scheme. As an example, we present in Fig. 4.7 the local distributions of $\varepsilon$ along the ventricle for the specific case of (N=7, SNR=10). The mode value of these distributions was 11.5 deg and 8.3 deg when applying the approximation scheme respectively in Cartesian or in PS coordinates. The grey rectangles represent the location of the 7 input noisy slices.

### 4.3.3 Fibre Tractography

Fibre tractography results are reported in Fig. 4.8. In (a) the result of tractography from the fully sampled reference tensor field are shown. In (b) and (c) the tractography resulting from the dense tensor fields approximated in PS coordinates and in Cartesian coordinates are respectively shown, using the set of noisy tensors (N=7, SN=10).

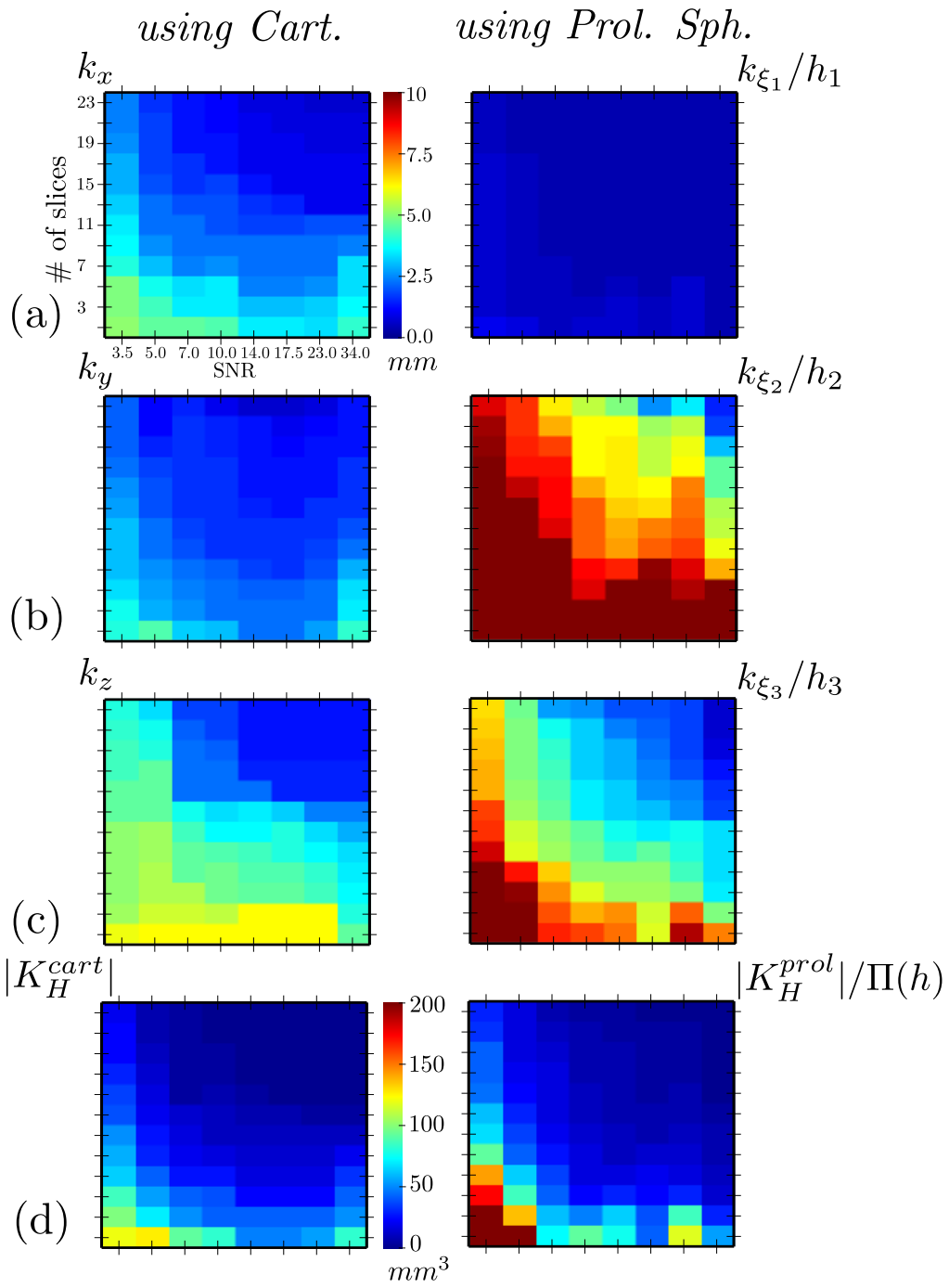


**Figure 4.5:** *(a,b,c) The optimal kernel values are reported in the three coordinates of each system (Cartesian and PS). They are normalized by the scale factors to be comparable. (d) Determinant of the kernels as an measure of their volumes.*

## 4.4 Discussions

### Optimal Kernel Values

The values of the optimal kernel bandwidth matrices $H_{opt}$ shown in Fig. 4.5(a,b,c) are interesting to discuss. It can be seen that in the Cartesian approach, the three different diagonal values are balanced with each other. For instance they converge around $2 \sim 3$mm in the case (N=7,SNR=10). In the PS approach however, most of the weight is concentrated in the $\xi_2$ and $\xi_3$ directions, leaving very small values

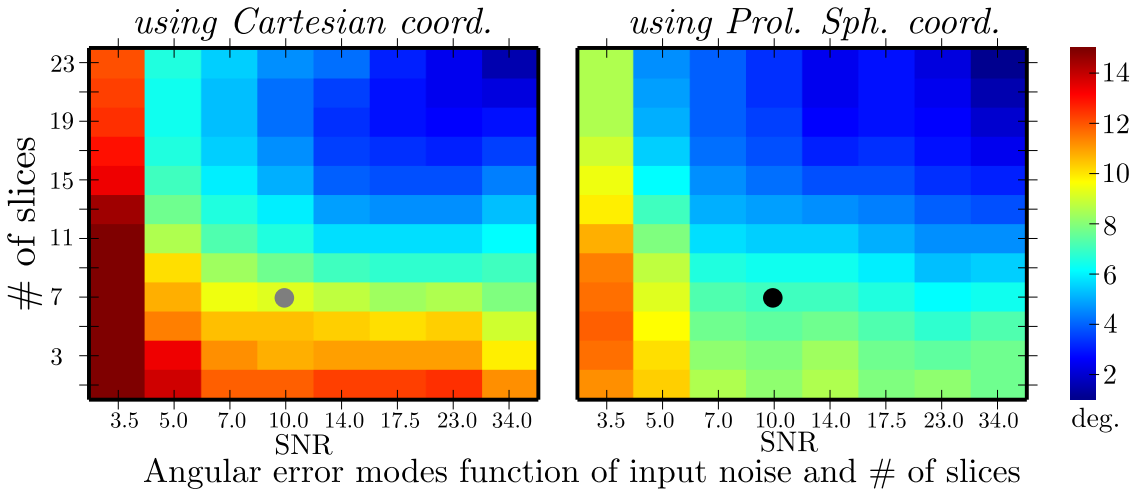


**Figure 4.6:** *Modes of the residual angular error $\varepsilon$ of the approximation process showed as a function of both the number of slices $N$ and the SNR of the DWIs.*

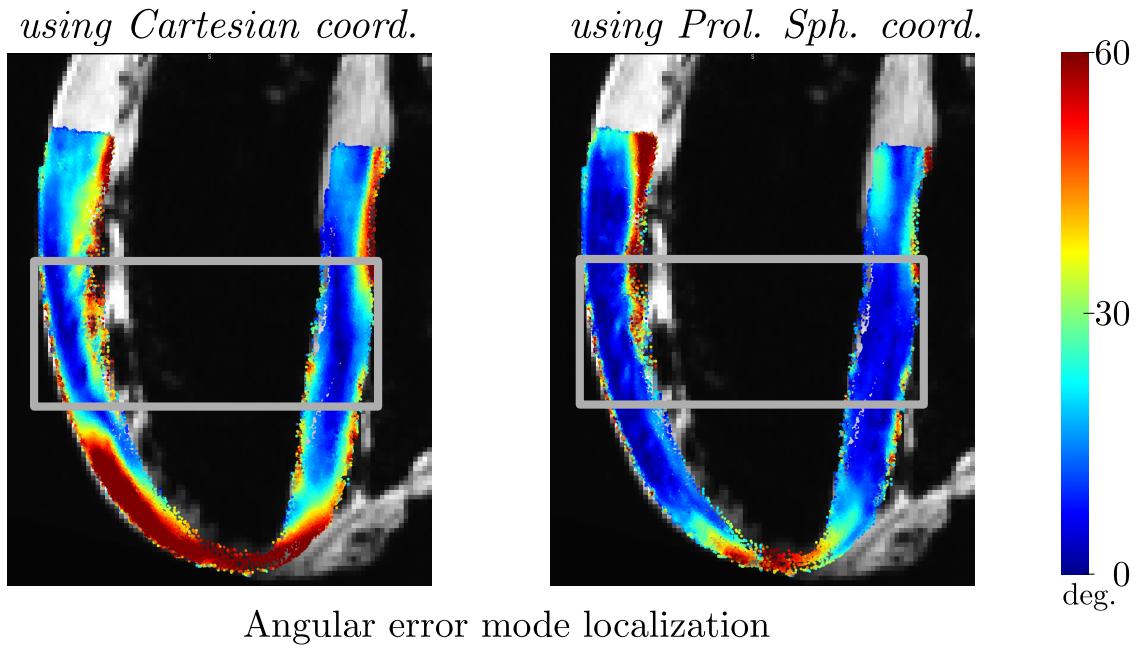


**Figure 4.7:** *Maps of the angular error $\varepsilon$ for the case $N$=7 and SNR=10. Results are presented for both Cartesian (left) and PS (right) coordinates. Grey rectangle: region covered by the 7 slices.*

in the wall depth direction. The determinant of this bandwidth matrix, shown in Fig. 4.5(d) can be seen as a representation of the volume of the kernel. It is interesting to notice that, apart from the extreme cases where noise is maximum and $N$ is minimum, both the PS and the Cartesian approaches give approximately the same total kernel volumes. It is indeed natural that the volume of information (number of data centres) needed for optimal approximation is independent of the coordinate system used for interpolation. Using PS approach, the topology of the region where those centres are taken is modified to follow the natural paths of the ventricle.

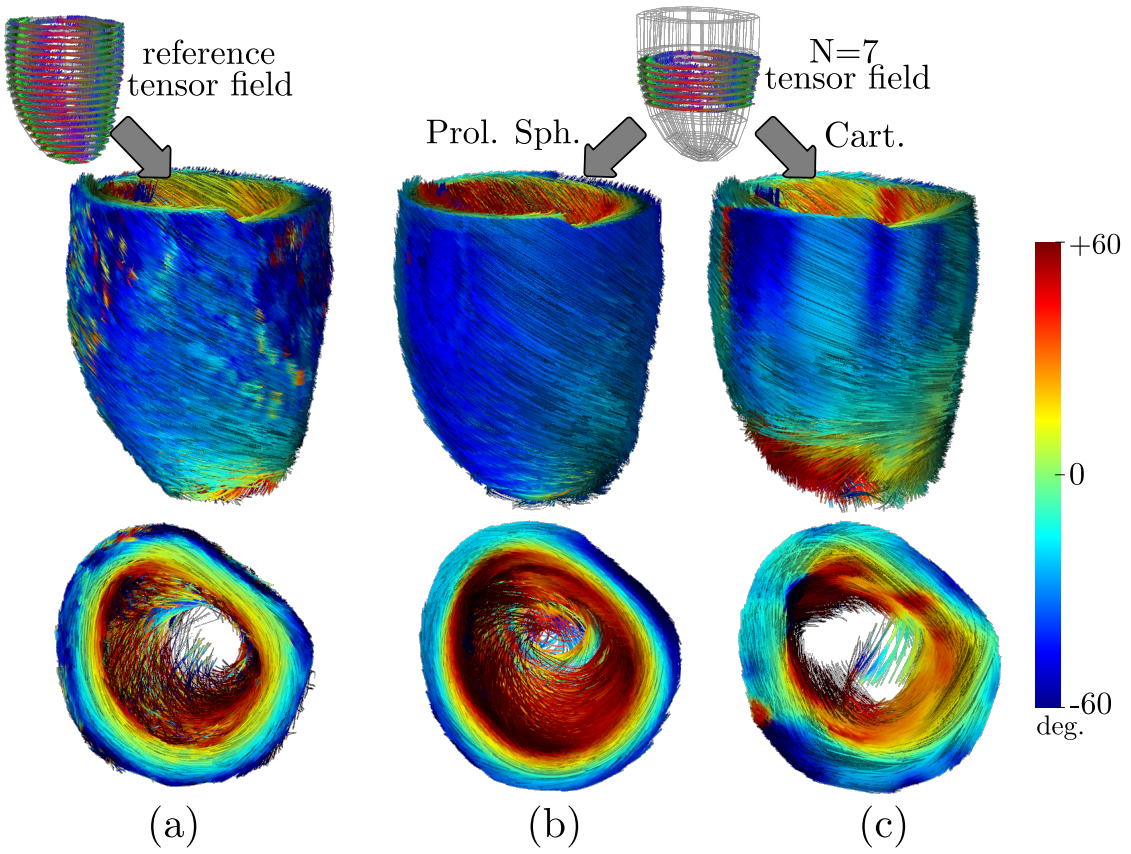


**Figure 4.8:** *(a) Tractography result from the reference fully sampled tensor field. (b) and (c) Tractography results from approximated tensor fields when using the noisy set of tensors (N=7, SNR=10), and respectively PS approach and Cartesian approach.*

## Sensitivity to Coordinate System

The angular error modes shown in Fig. 4.6 confirmed that in all the situations studied in this experiment it was preferable to use PS coordinates in the dense approximation rather than Cartesian coordinates. As predicted, both approaches gave similar performances when the number of slices approached its maximal values (i.e. at full ventricle coverage). It is here again natural to think that, at full sampling, the performance of the approximation is independent of the coordinate system used for interpolation. However, the lower the number of slices, the stronger was the discrepancy between approaches. These results, together with the comparison of kernel volumes in Fig. 4.5(d), help us conclude that even if the same volume of data is taken into consideration, the shape of the kernel is crucial in the outcome performance of the approximation scheme, as seen in Fig. 4.7.

In Fig. 4.8 the fibre tractography resulting from both approaches are compared in the case scenario of (N=7, SNR=10). The stripes that appear in the Cartesian approach (Fig. 4.8(c)) are an undesirable effect of the Cartesian interpolation. Using the shape adapted PS interpolation removes this artifact.

## Error Localisation

The maps presented in Fig. 4.7 show that the majority of the high frequency of $\varepsilon$ appears in the apical region and at the endocardial borders of the ventricle. The localisation of the initial data is indicated by the grey rectangle. Therefore, tensors

outside this region represent an approximation based on distant information (i.e. extrapolation). It is clear from this figure that choosing a curvilinear approach for the approximation gives better extrapolation performances. The low errors of distant regions in the PS map suggest that the fibre orientation structure is relatively smooth along the ventricle, except at the apex.

For instance, the modes of the error $\varepsilon$ in the specific case-scenario presented in Fig. 4.7 are 11.5 deg and 8 deg when using respectively Cartesian or PS coordinates. One could argue that this difference does not seem very significant as it is only a few degrees deviation between modes. However, it might be of interest to appreciate the overall shape of the distributions, noting that the error is better contained in lower values in the PS case, compared to the Cartesian one. For instance, if the "half energy window" of the distribution is calculated, values of respectively 17 and 28 deg are obtained for PS and Cartesian shapes respectively. The image presented in Fig. 4.7 shows that the majority of the high frequencies of $\varepsilon$ appear in the apex region and the endocardial borders of the ventricle. The localisation of the initial data is materialized by the grey rectangle. Therefore, tensors outside this region represent an approximation based on distant information (i.e. extrapolation). The low errors (indicated by blue colors in this map) of distant regions suggest that the fibre orientation structure is relatively smooth along the ventricle, apart at the apex, where error peaks above 60 deg.

## Robustness to Noise

The evolution of the error $\varepsilon$ with respect to the addition of slices (each column of the error maps in Fig. 4.6) seems to be significantly robust to noise. That is, the pattern was almost constant until reaching a $SNR \leq 5$. This is again explained by the relatively strong smoothness of the fibre orientation structure in a healthy left ventricle such as the one used as reference in this sensitivity analysis.

## Smoothing Effect

In the experiments shown in this work, a global set of kernel parameters was used throughout the ventricle. Local variations in the acquired tensor dataset can be smoothed by this process. This effect is clearly visible in Fig. 4.8(b) and Fig. 4.8(c). In the case of healthy subjects, this property might be desirable under the reasonable hypothesis that the fibre structure is relatively smooth. In clinical cases such as infarct subjects, the fibre architecture is suspected to be disoriented in the scar region. In this situation some more local approach would be necessary. For instance, one could consider using smaller kernel parameters in such regions in order to depict the fibre structure in more details. Tensor shape indices, such as the Fractional Anisotropy (FA) or the Spherical Coefficient (SC), could potentially be used as a detector of such regions in order to adjust the kernel parameters accordingly. As suggested in [Yang 2012], here a metric on tensor which avoid FA collapse should be preferred.

## Lambda parameter

The regularisation parameter $\lambda$ (Eq. 4.8) controls the influence of the tensor field smoothness in the estimation of the optimal matrix $H_{opt}$. It has therefore a great

impact on the resulting full ventricular tensor reconstruction, and has to be chosen carefully. A common technique used to choose its value is the L-curve method as described in [Hansen 1992]. The L-curve and its curvature were computed for the set of variables - $N = 10$ and $V = 0.01$ (corresponding to SNR=10) - in order to find a suitable value for $\lambda$. As shown in Fig. 4.9, the curvature of the L-curve was found almost constant. However, it indicated an inflexion point at $\lambda \sim 1 - 1.5$. The constant curvature might be explained by the fact that the system we try to solve is non-linear and does not correspond to a Tikhonov regularisation problem, as opposed to the system described in [Hansen 1992].

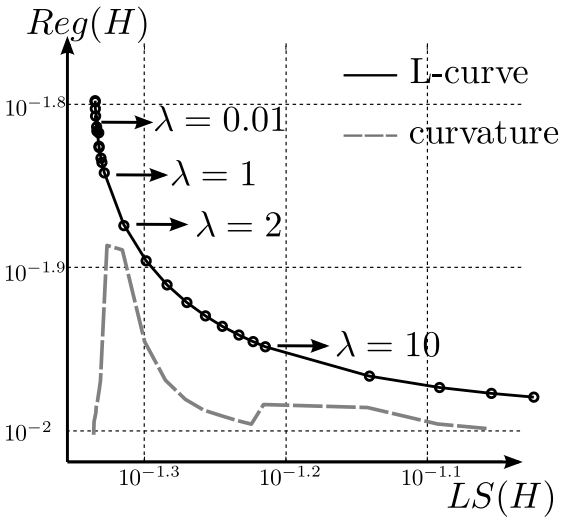


**Figure 4.9:** *L-curve experiment of the energy cost function in Eq. 4.8. The L-curve is shown in plain line, and its discreet curvature is shown in dotted line. The curvature has been magnified to be able to visualise the inflection point at* $\lambda = 1.5$.

## 4.5 Extension: Zone-dependent Approximation

As mentioned in the previous section, this dense approximation has the limitation of being global. That is, the approximation operator uses a single tri-variate kernel $K_H$ for the entire ventricle volume. The main consequence is the potential smoothing of meaningful local information. In this section we investigate an extension of the dense approximation scheme detailed above that allow localised approximation to overcome this potential loss of information.

### 4.5.1 Theory

It was shown in Chap. 3 that the PS coordinates give us the advantage of a straightforward definition of left ventricular AHA zones (see [Cerqueira 2002]).Let us denote $\Omega_z$ the anatomical region of AHA zone $z$, and $K_H^z$ the tri-variate kernel as defined in Eq.4.4, associated with this zone. For each measure point in PS coordinates $\xi_i$, the AHA zone containing $\xi_i$ is detected (i.e. $z_i$). The approximation operator (Eq. 4.1) is therefore redefined as follows:

$$\mathcal{W}'_P : \xi \rightarrow \mathcal{W}'_P(\xi) = \exp\left(\frac{\sum_{i=1}^{N} K_H^{z_i}(\xi - \xi_i)\log(D_{\xi_i})}{\sum_{i=1}^{N} K_H^{z_i}(\xi - \xi_i)}\right) \tag{4.10}$$

This formalism gives the opportunity to weight the influence of a measure according to its localisation. As previously, it is then possible to find the optimal weights to a certain sense. In our case, the criterion in Eq. 4.8 can be modified using $\mathcal{W}'_P$ instead of $\mathcal{W}_P$. This approach therefore consists of finding the set $[H_opt]_z$ of optimal bandwidth matrices that minimizes $(LS([H]_z) + \lambda.Reg([H]_z))$ with:

$$\begin{aligned} LS([H]_z) &= \sum_* dist\left(D_*, \mathcal{W}'_P(*)\right)^2 \\ Reg([H]_z) &= \sum_* \parallel \partial\mathcal{W}'_P(*) \parallel^2 \end{aligned} \tag{4.11}$$

The computing time of this minimization problem becomes very significant as the number of degree of freedom is three times the number of zones. In theory, there is no limitation on this number, and one could define a zone per measurement centre, therefore arriving to $N$ different tri-variate kernels to find. This approach then converges to the RBF approach where each centre has its own (matrix) weight, as in Eq. 4.2. However it is difficult to achieve for computation time reason. However, the 17-AHA zone division remains practically applicable to this concept and can provide us with meaningful information.

### 4.5.2 Experiment

The *ex-vivo* human dataset provided by John Hopkins university was used, and the 17-AHA zones division of the left ventricle in the PS sense was derived. The optimal series of kernels $[H]_z$ for $z = 1..17$ were computed in the sense of Eq. 4.11, in PS coordinates. This series depend on the cardinality $M$ of the input set of measured positions/tensors pairs $P$. It is important to note that $H_z$ is very influenced by the number $m_z$ of centres included in zone $z$, and is not defined if $m_z = 0$.

The local kernel optimization was performed for two different case scenarios. First, using the fully sampled dataset ($N = N_{max}$) and SNR=10. Second, using a more realistic set of tensors (N=7, SNR=10). In this second case, only kernels $[K_H^z], z = 7..12$ will be defined since there is no input data in the other AHA zones. Figure 4.10(a) shows the division of the left ventricle in 17 AHA zones. The minimization process needs an initialization state. These initial kernel shapes are shown in Fig. 4.10(b) using their "envelopes" (surfaces represent the iso-contours of the weights $K_H^z(x)$) at $K_H^z(x) = 1/2$.

### 4.5.3 Results and Discussions

Figure 4.11(a) present the envelopes of local AHA zone optimal kernels in the case $(N = N_{max}, SNR = 10)$. As predicted, they are elongated in the apex-base and the circumferential axes, and very narrowed in the transmural axis. Figure 4.11(b) presents the envelopes in the case $(N = 7, SNR = 10)$. In AHA zones where there is no information (basal and apical regions), the kernels are not defined. The elongation is more pronounced in this second scenario, enforcing the observed smoothness in apico-basal direction until regions where no information is present.

The numerical results of the optimal kernel diagonal values are gathered in Table 4.1.

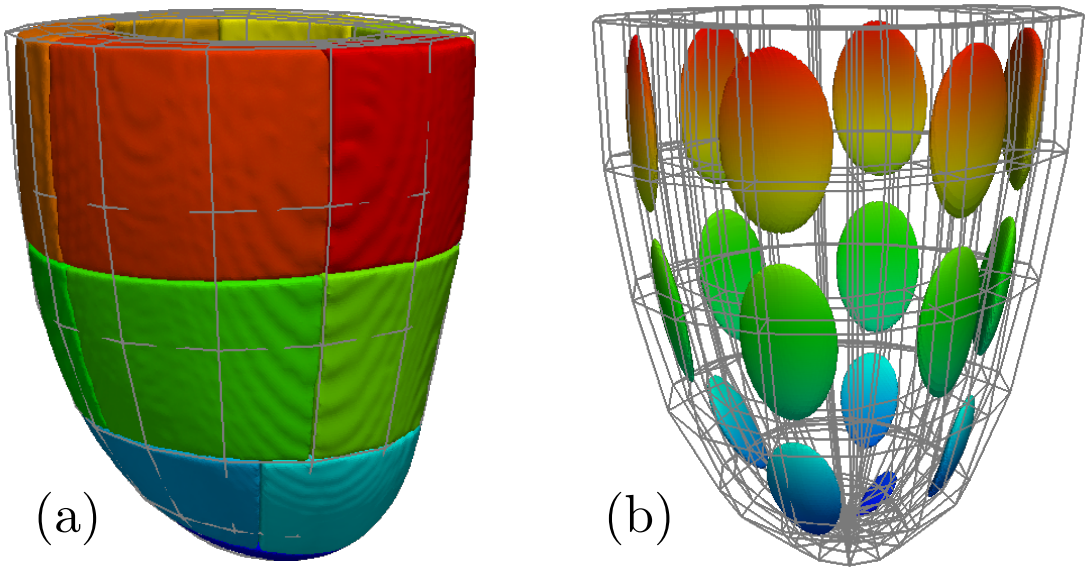


**Figure 4.10:** *(a) The 17 AHA zones of the ex-vivo human dataset. (b) All 17 kernels $K_H^z$ are initialized prior to optimization with the diagonal values* $[0.024597, 0.147368, 0.236092]$*, they are shown here with their respective envelopes at* $K_H^z(x) = 1/2$*.*

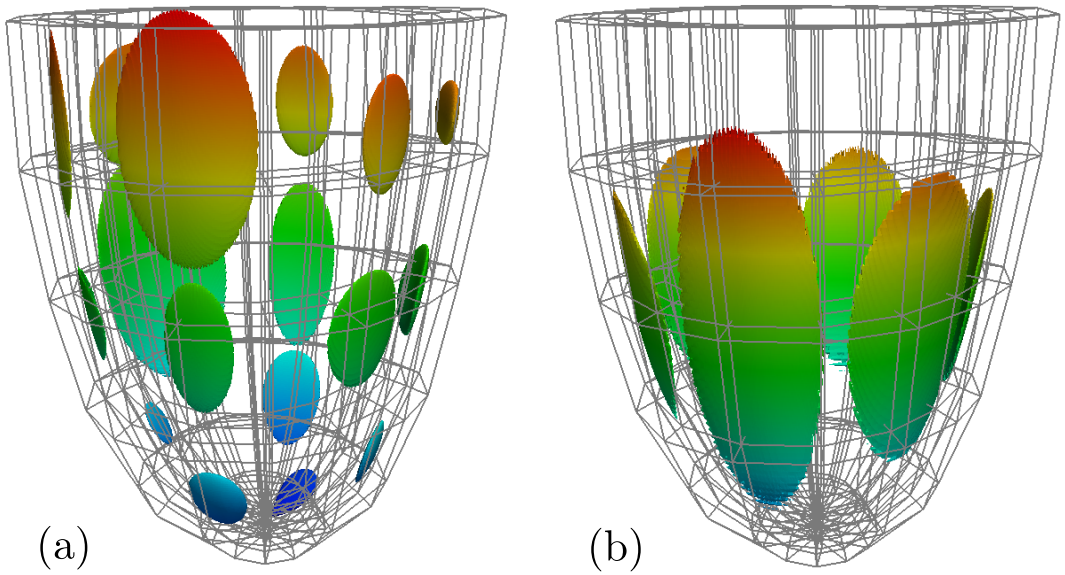


**Figure 4.11:** *Optimal kernel envelopes at* $K_{H_{opt}}^z(x) = 1/2$*. (a) when using the fully-sampled dataset, that is, the case* $(N = N_{max}, SNR = 10)$*. (b) when using 7 mid-ventricular slices* $(N = 7, SNR = 10)$*.*

## 4.6 Conclusions

In this chapter the problem of approximating a diffusion tensor field over the entire left ventricle when data is available only in sparsely distributed acquired centres was addressed. This situation is often encountered when acquiring DTI in the beating heart. The PS change of coordinates concepts presented in Chapter 3 were extensively applied. A dense approximation operator in the PS frame was introduced. It involves a tri-variate kernel as parameter. The optimal widths of this kernel are ob-

| AHA zone ↓ / axis → | transmural ($\xi_1$) | apico-basal ($\xi_2$) | circumferential ($\xi_3$) |
|---|---|---|---|
| # 1 | 0.00789481 | 0.199923 | 0.292906 |
| # 2 | 0.00591417 | 0.155381 | 0.26296 |
| # 3 | 0.00846043 | 0.117285 | 0.346664 |
| # 4 | 0.012477 | 0.106367 | 0.143527 |
| # 5 | 0.0142015 | 0.0579522 | 0.141149 |
| # 6 | 0.0123444 | 0.0996348 | 0.137482 |
| # 7 | 0.00882262 | 0.123739 | 0.166411 |
| # 8 | 0.00508657 | 0.0934024 | 0.29993 |
| # 9 | 0.00884071 | 0.254009 | 0.453831 |
| # 10 | 0.00840109 | 0.188087 | 0.190297 |
| # 11 | 0.0121165 | 0.0967548 | 0.228948 |
| # 12 | 0.010069 | 0.113458 | 0.261271 |
| # 13 | 0.020961 | 0.0798364 | 0.191824 |
| # 14 | 0.00990214 | 0.0667319 | 0.123361 |
| # 15 | 0.0140844 | 0.146883 | 0.240552 |
| # 16 | 0.0145749 | 0.0872193 | 0.184861 |
| # 17 | 0.0300814 | 0.138803 | 0.333442 |
| **mean** | **0.0120136** | **0.1250274** | **0.2352597** |

**Table 4.1:** *Local optimal kernel estimation in PS coordinates for each AHA zone (for $N = N_{max}$, SNR=10).*

tained by using an *ex-vivo* human dataset. The cost function of this optimization is a trade-off between a least-square error term and a total variation smoothness term. This set up also allowed us to compare this approach over the classical Cartesian interpolation one. Results show that embedding such a curvilinear interpolation in the approximation significantly improves the performance of the overall process and should be preferred over the Cartesian approach, especially when the data centre density is low or heterogeneous as it is the case *in-vivo*.

One of the effects of such a convolution based approximation technique is that it intrinsically smoothes the input data. Although this characteristic can be desirable for low SNR images, it might be considered inadequate in clinical cases where the aim is rather to detect or analyse regions of fibre disarray. Our approximation approach was extended to a zone-based kernel version. In this set up, the size of the kernel for each region can be refined in order to depict local variations of the fibre structure. The workflow presented in this chapter can be seen as a form of extended regularisation process. It could be of interest to further investigate in this direction, in particular to compare the performances of our approach to other techniques, where the data is regularized at the diffusion weighted image level, such as in [Parker 2000]. Another approach would have been to extend the complete mathematical framework reported in [Pajevic 2002] to an irregularly sampled grid. In this paper the authors use so-called *atomic spaces* in order to describe the data in a continuous manner. Their approach is stronger than the one used in this chapter as it allows for the control over the type of approximant. That is, it allows to control whether or not the approximation matches the interpolation constraint (the continuous field passes through the discrete measured data precisely). However they

restrict their framework to the case of discrete but regularly sampled datasets. It could be of great interest to extend the concepts presented there to the particular situation where the data density is not homogeneous along the organ of interest. These modification would for instance include the replacement of integer $k$ by real numbers in Eq. A.4 of [Pajevic 2002] for instance, and the outcome properties would still hold.

All algorithms presented here are freely available in the Cardiac Prolate Spheroidal ToolKit [2]. Details about the implementation can be found in App. C.

[2] https://github.com/ntoussaint/Cardiac-Prolate-Spheroidal-ToolKit

Chapter 5

# Accuracy Measurements on Fibre Fields

## Contents



## 5.1 Motivations

The last chapter introduces techniques that allow the full reconstruction of the left ventricular DTI information from sparsely acquired data centres. From these resulting dense DTI tensor fields fibre tracking is feasible. Those tractograms describe visually the main orientations of fibres and their variability within the ventricle. In the following work, the influence of acquisition parameters on the output tractography result is assessed. As mentioned in Sec. 2.5, in cardiac *in-vivo* situation, low SNR images and poor through plane resolution are often encountered. In this chapter, the issue of evaluating the loss of information induced by an increase of the slice thickness, as well as of a change of the acquisition plane orientation is addressed. This is achieved by comparing pairs of fibre tractography results from a number of synthetic and real experiments. Typical methods include angle or tensor difference at each voxel [Vadakkumpadan 2012]. However in the setting described in this chapter, the sampling grid is different between datasets, therefore the methods cited above cannot be used. Another potential approach to this problem would have been the direct measure of distance between tracts, such as in [Fillard 2011]. But this method requires point to point correspondence. In the method described below, a distance metric is defined globally between sets of fibre tracts, therefore removing the constraint of point to point correspondence.

## 5.2 A Similarity Measure on Fibre Fields

The common output of DT-MRI is the delineation of major continuous pathways of fibres from the diffusion tensor data [Basser 2000]. These fibre tracts are a concrete representation in space of the discrete tensor field. This kind of representation

has the advantage of not depending on the original volumetric grid. It is also reasonable to think of methods for measuring the accuracy of those tracts. The paths depend on both the diffusion model taken into account and the tractography algorithm. In [Fillard 2011] the authors benchmark 10 different combinations of diffusion models and tractography techniques on a realistic diffusion phantom. To do so they impose seed points and compare the ground truth trajectories with paths resulting from those combinations. To compare sets of fibres, they are parameterised with B-splines, and their arc length are normalized to [0,1]. Then a match score was computed based on a point to point distance between fibres, therefore they assume a point to point correspondence. In the following section, new techniques introduced in [Durrleman 2008] are used in order to introduce a solution to this problem without any parameterisation of the fibre tracts.

Estimating dissimilarities between sets of curves is not a straight forward problem. The concept of currents as introduced by Glaunès, Durrleman et al in [Glaunès 2008, Durrleman 2008], is the following: A curve is seen via the way it integrates a vector field. That is, a continuous curve, or set of polygonal lines $L$, is characterized by the path integral of a vector field $\omega$ along it:

$$\forall \omega \in \mathbb{W}, L : \omega \rightarrow \int_L \langle \omega(l), \tau(l) \rangle_{\mathbb{R}^3} dl \tag{5.1}$$

where $\tau(l)$ is the unit tangent vector of $L$ at point $l$. $\mathbb{W}$ is a constrained space of vector fields, also called test space. From this definition, curves $L$ as currents define a vector space $\mathbb{W}^*$ satisfying :

$$\begin{aligned} \forall (L_1, L_2) \in \mathbb{W}^{*2},\ & (L_1 + L_2)(\omega) = L_1(\omega) + L_2(\omega) \\ & (\lambda L)(\omega) = \lambda L(\omega) \end{aligned}$$

From [Durrleman 2008] and references, it is shown that the space of curves $\mathbb{W}^*$ can be provided with an inner product $\langle \cdot, \cdot \rangle_{\mathbb{W}^*}$. Let denote a set of curves $L$ as its polygonal elements: $\sum_k \delta_{c_k}^{\tau_k}$. That is, if $c_k$ are the centres of each segments and $\tau_k$ are their unit tangent vectors, then $\delta_{c_k}^{\tau_k}$ is a polygonal segment of the curve. thus the inner product between two sets of curves $L_1$ and $L_2$ can be written as follows:

$$\langle L_1, L_2 \rangle_{\mathbb{W}^*} = \sum_{i=1}^{n} \sum_{j=1}^{m} (\tau_i)^T . K_\lambda(c_i, c_j) . (\tau_j) \tag{5.2}$$

where the superscript $^T$ denotes the transposed vector, and $K_\lambda(c_i, c_j)$ is a Gaussian kernel defined as

$$K_\lambda(c_1, c_2) = \exp(-\|c_1 - c_2\|^2_{\mathbb{W}^*} / \lambda^2).$$

$\lambda$ is a standard deviation to be chosen. As explained in detail in [Durrleman 2008], $\lambda$ controls the desired scale to which the inner product in Eq. 5.2 will detect discrepancies between considered curves. The authors recommend to set $\lambda$ of the order of the mean distance between curves.

From this inner product, A *Hilbert distance* between two sets of curves $L_1$ and $L_2$ is defined as follows:

$$d^2(L_1, L_2) = \|L_1 - L_2\|^2_{\mathbb{W}^*} = \langle L_1 - L_2, L_1 - L_2 \rangle_{\mathbb{W}^*} \tag{5.3}$$

Thereby, the distance index $d^2$ provides us with a measure of **global** dissimilarity between two fibre fields $L_1$ and $L_2$. If $L_1$ and $L_2$ are considered as two sets polygonal segments, and compute their Hilbert distance. Although this index is already interesting by itself, it can be of interest to search for a local estimation of this distance, while keeping the non-parameterisation aspect of this approach. At any spatial position $p$, a local subset of the current $L$, denoted $L_p^*$, is defined as the convolution of $L$ with a Gaussian kernel $K_\sigma$ centered in $p$:

$$L_p^* = L * K_\sigma(p) \tag{5.4}$$

This subset is a concrete representation of the curve $L$ at position $p$. It is then argued that measuring the Hilbert distance between p-subsets of two different curves $L_{1_p}^*$ and $L_{2_p}^*$, represents an estimation of the Hilbert distance between $L_1$ and $L_2$ at position $p$.

This finally leads to the definition of a local Hilbert distance between two sets of curves at position $p$:

$$d^2(L_1, L_2)(p) = \|L_{1_p}^* - L_{2_p}^*\|_{\mathbb{W}^*}^2 \tag{5.5}$$

On a practical point of view, the difference $(L_1 - L_2)$ can be expressed by cumulatively summing all centres and tangents from both sets of curves, and take an opposite sign for tangents of $L_2$.

The local Hilbert distance introduced here depends on two spatial parameters, $\lambda$ the spatial distance on which it is intended to measure discrepancies, and $\sigma$ the spatial window on which the resulting subset $L_p^*$ is considered *local*.

## 5.3 Case Study on Synthetic Fibres

To validate this method, the behaviour of the error index measurement is investigated on synthetic tensor datasets. An ellipsoidal-shaped DTI field has been built, where the artificial tensors are restricted to have a linear and planar coefficients of $c_l = 0.5$ and $c_p = 0.3$. The main eigenvector is varying from epicardium to endocardium to match helix angles variations taken from the literature: $-40^o < \alpha_{helix} < +60^o$ from epi to endo. From this *reference* DTI dataset, noisy tensor fields are derived by adding Rician noise to corresponding DWIs, similarly to Sec. 4.2.2. Fibre tractography is applied to each tensor field using the tensor deflection propagation as detailed in Sec. 4.2.4. Let us denote $S_0$ the fibre tracts from the initial tensor field, $S_1, S_2, S_3, S_4$ the fibre tracts from noisy tensor fields using variances of respectively $V = 0.0025, V = 0.005, V = 0.01$ and $V = 0.02$. In Fig. 5.1, the initial synthetic tensor field and two levels of noisy tensor fields are shown (top row). Their corresponding fibre tractography results $S_0, S_2$ and $S_4$ are shown in the bottom row, where fibres are color-coded by the local tensor's helix angle.

The noisy fibre fields are compared against the initial one using the local Hilbert distance index introduced in the last section, using $\sigma = \lambda = 1.5$ mm. The distances values $d^2(S_0, S_1)(p)$ and $d^2(S_0, S_2)(p)$ are projected back to the initial reference fibre field structure, and the resulting distance maps are presented in Fig. 5.2. The histograms of the Hilbert distance index for 4 different Rician noise variances are presented in Fig. 5.4. Their modes are reported in Table 5.1

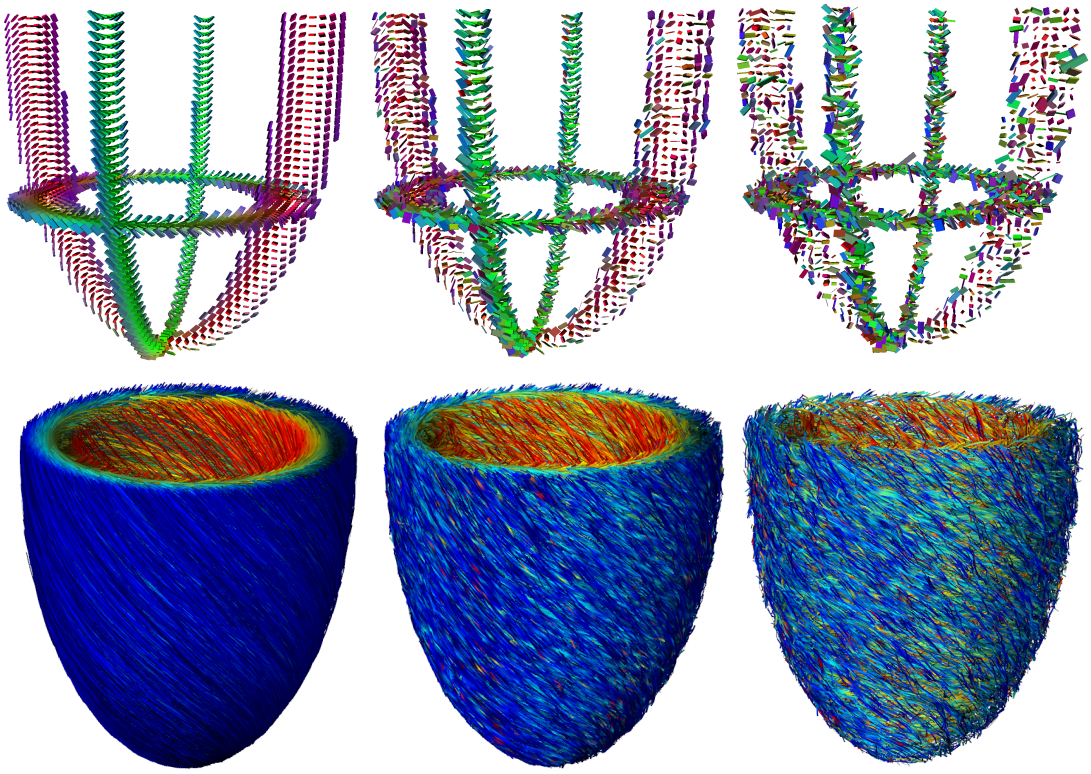

**Figure 5.1:** *(top) Synthetic tensor fields have been created reproducing the LV ellipsoidal shape. The orientation of the main eigenvector follows the variation of the helix angle $\alpha_{helix}$ of $-40^o$ to $+60^o$ from the epicardium to the endocardium. Rician distributed noise of growing variance is added to the DWIs to obtain noisy tensor field on the right. (bottom) Fibre tractography of the corresponding tensor field, color-coded with the local helix angle.*

## 5.4 Application to *Ex-Vivo* Cardiac DTI: a Reproducibility Study

In this experiment, the quantification of the impact of the image resolution and the orientation of the slice acquisition plane on the resulting fibre tractography output is investigated. To achieve that, a protocol is set up, where three DTI volumes of an *ex-vivo* heart are acquired with (1) an isotropic voxel size, (2) an anisotropic voxel size (increasing in the through plane direction) and (3) an anisotropic voxel size and a rotated acquisition plane.

**Material**: Diffusion tensor imaging has been performed on an explanted healthy lamb's heart. The excised heart was washed and put in a cylindrical box. An MR transparent solution of Fromblin was used as surrounding medium. Imaging was performed on a 3T clinical scanner (Philips, The Netherlands), with gradient strength of 80mT/m. An 8-channel head coil was used to receive the signal. Diffusion images were acquired using a Pulse-Gradient Spin Echo sequence with 12 diffusion directions. The b-value was 400 $s/mm^2$. The acquisition protocol consisted of three different DTI volumes covering the entire myocardium. First, an isotropic $1.8 \times 1.8 \times 2\text{mm}^3$ image was produced in a short axis acquisition plane. Second, an anisotropic $1.8 \times 1.8 \times 5\text{mm}^3$ image using the same acquisition plane. And third, a

| Fibre Field → | $S_0$ | $S_1$ | $S_2$ | $S_3$ | $S_4$ |
|---|---|---|---|---|---|
| Variance V | - | 0.002 | 0.005 | 0.02 | 0.05 |
| h.d. mode ($.10^{-4}$) vs. $S_0$ | - | 0.996 | 1.230 | 1.582 | 2.871 |
| # of fibres | 3521 | 3489 | 3511 | 3550 | 3487 |

**Table 5.1:** *Description of the synthetic fibre fields $S_*$. Rician noise of variance $V$ is added to reference $S_0$ to obtain $S_1$,$S_2$,$S_3$ and $S_4$. Modes of $\|S_* - S_0\|_{\mathbb{W}^*}$ are reported, as well as the number of fibres of each field.*

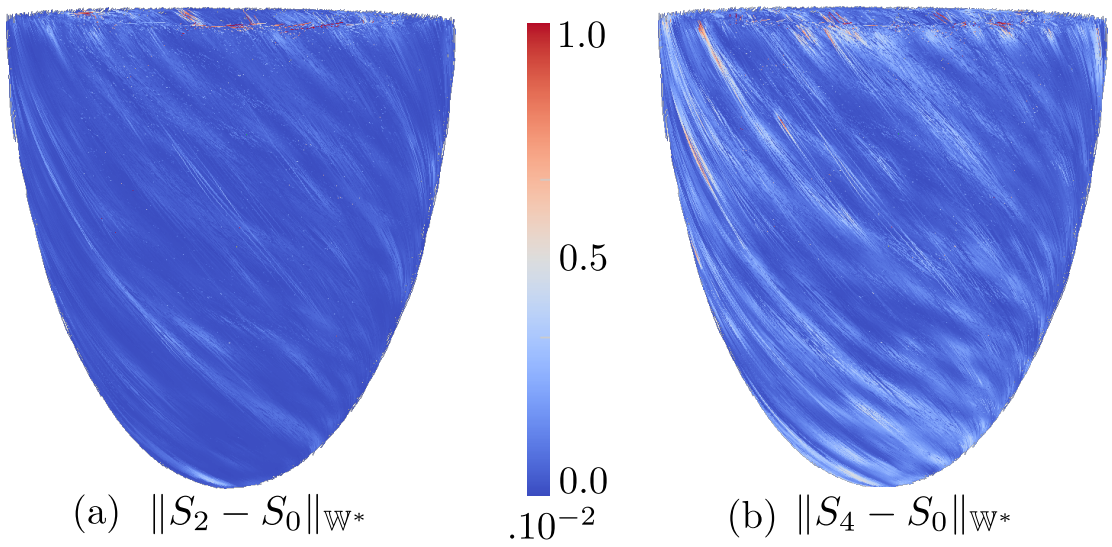


**Figure 5.2:** *The Hilbert distance is evaluated locally between different levels of noisy fibre fields $S_2$ and $S_4$ against a reference fibre field $S_0$. maps of the distance are presented in both cases.*

second anisotropic $2 \times 2 \times 5\text{mm}^3$ image was acquired, but rotating the acquisition plane by 35 deg.

**Results**: Fibre tractography was performed on the three DTI volumes. Let us denote $D_{high}$ the fibre field resulting from the first acquisition (isotropic $1.8 \times 1.8 \times 2$ mm), $D_{low}$ the fibre field from the second (anisotropic $1.8 \times 1.8 \times 5$ mm) and $D'_{low}$ from the third (35 deg rotated acquisition plane). The local Hilbert distance as in Eq. 5.5 was estimated between $D_{high}$ on one side, and $D_{low}$ or $D'_{low}$ on the other, using $\sigma = \lambda = 1.5$ mm. Figure 5.3(a) shows the resulting error map for $\|D_{high} - D_{low}\|_{\mathbb{W}^*}$. The local Hilbert distance is defined at *any* position, and not restricted to the data centres of either the first or the second fibre field. However, the distance was measured at the centres of $D_{high}$, in order to have the same amount of measures in the two different cases, i.e. distance against $D_{low}$ and against $D'_{low}$.

## 5.5 Discussions

**Synthetic simulations**: As reported in Table 5.1, the local Hilbert distance index is able to capture the discrepancies of the output fibre fields due different level of

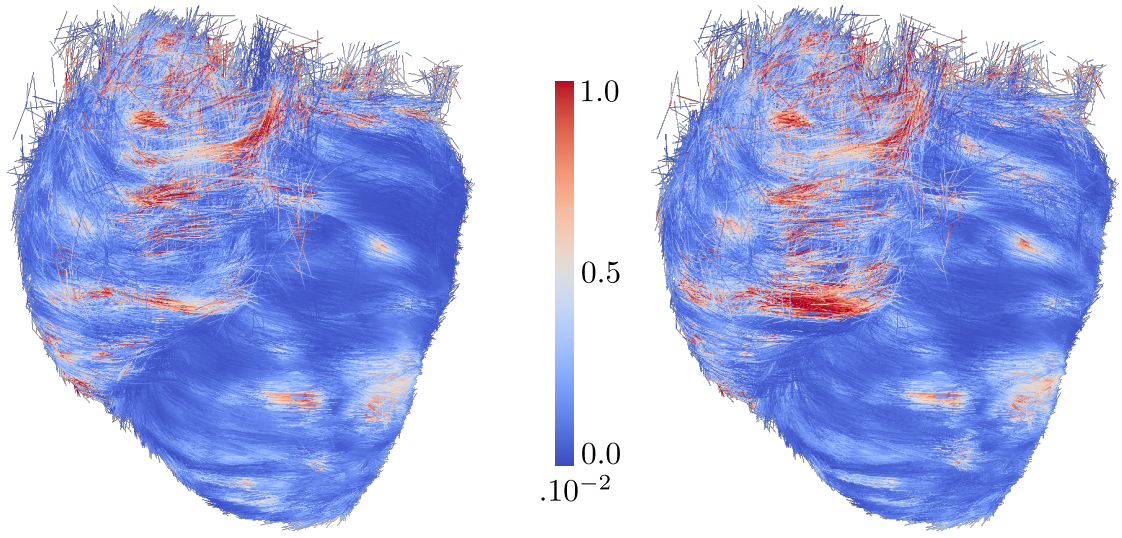


(a) $\|D_{high} - D_{low}\|_{\mathbb{W}^*}$ (b) $\|D_{high} - D'_{low}\|_{\mathbb{W}^*}$

**Figure 5.3:** *(a) Superposition of $D_{high}$ in red and $D_{low}$ in blue. Local dissimilarities between both fibre fields were measured, and mapped onto $L_{high}$ (right).*

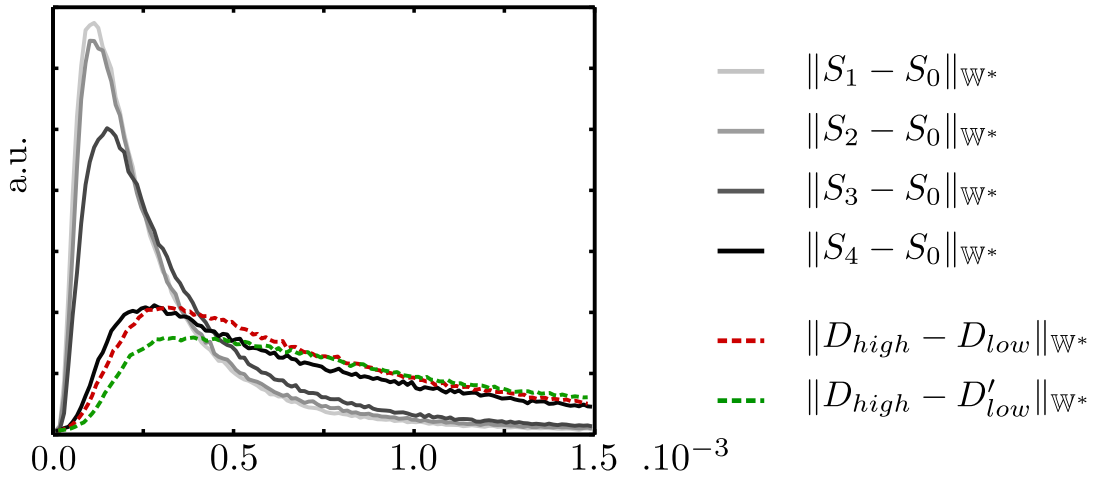


**Figure 5.4:** *Histograms of the local Hilbert distance index, for the 4 different levels of synthetic noisy fibres, and for the ex-vivo lamb heart experiment, using $\sigma = \lambda = 1.5$ mm.*

noisy tensor fields. The mode of the distance index increases with the noise variance. Interestingly, the number of fibres stays constant despite the increase of noise. The amount of fibre tracts is often used as a measure of accuracy in DTI studies, for instance when studying tensor regularisation methods (e.g. [Frindel 2009]). However, this simple experiment suggests that this might not be a valid measure to quantify fibre pathways "accuracy". However, an index such as the one introduced here allows to compare the both orientations and alignments of fibres in a pair-wise manner provides us with a measure that can locally quantify the difference between fibre fields, without any need of point to point correspondence.

***Ex-vivo* Experiments**: The maps of distances between reference fibre field $D_{high}$ and respectively $D_{low}$ and $D'_{low}$ are presented in Fig. 5.3. A higher level of

discrepancies is observed in the right ventricle area than in the left ventricle. This might be explained by the lower thickness of the wall in the RV. Their histograms are reported in Fig. 5.4. They show modes at 0.32 and $0.37.10^{-3}$. These distributions demonstrate little difference between cases. This result suggests that rotating the plane of acquisition does not significantly compromise the fibre tracts in a global manner. However, the maps indicate local differences that would suggest that, when choosing highly anisotropic voxel sizes, then the orientation of this anisotropy matters.

## 5.6 Conclusions

This chapter presented a new approach for the comparison of curves as resulted from fibre tractography process. Using the concepts of *currents*, a local measure of discrepancy between fibre tracts was introduced. This method was tested on synthetic fibre fields in order to measure the influence of noise introduce in tensor measurements onto the resulting fibre tractography. This approach was applied to *ex-vivo* explanted hearts. This method gave an insight into errors on the fibre orientation estimation due to an increase of the through-plane voxel size. Results tend to indicate that using fibre tractography outputs as object of comparison allows for a robust and smooth evaluation of the local differences between fibre fields. Globally, it was found that the fibre tractography results were relatively robust to the change of acquisition plane orientation. Additionally, it was found that, when increasing the through-plane voxel size, the fibre field misevaluation appears greater in the right ventricle area, which can be explained by the smaller thickness of the myocardial wall. Finally, an alternative application of this distance metric is presented in Appendix E, where the variability of the human cerebral anterior commissure is derived.

Chapter 6

# Cardiac In-Vivo DTI Group-wise Analysis using Prolate Spheroidal Coordinates

## Contents



## 6.1 Motivations

In Chapters 3 and 4, a data representation approach allowing a powerful and convenient analysis of DTI information in the left ventricle using PS coordinates was introduced. We embedded this representation in a dense approximation workflow. In this chapter we are interested in the application of these methods in a human *in-vivo* setting. As mentioned in Sec. 2.5, there are two major types of sequences that have proved successful in acquiring diffusion images in the beating heart. The first one is a Stimulated Echo technique (STEAM) derived from [Tseng 2003, Dou 2003]. The second is a Spin Echo based sequence from [Gamper 2007]. Here, two distinct acquisition experiments respectively based on these sequences are presented.

In the first experiment (using the STEAM sequence), both systolic and diastolic DTI data were acquired on 5 healthy volunteers. In the second (using the SE sequence), systolic DTI images were acquired on 5 healthy volunteers. From both these sets of data, the techniques presented in Chapters 3 and 4 are applied. Fibre architecture statistics and dense reconstructions are then reported. The results correlate well with previously reported *ex-vivo* studies, and confirm the feasibility and reproducibility of human beating heart DTI.

## 6.2 Acquisition Protocols

### 6.2.1 Local-look STEAM Sequence

For this protocol, imaging was performed on a 1.5T Philips clinical MRI system equipped with a 32 channel cardiac receiver array and a gradient system allowing a maximal gradient strength of 40mT/m at a slew rate of 200 mT/m/ms per channel. Cardiac DTI data was acquired using a diffusion weighted STEAM sequence [Tseng 2003]. The in-plane resolution was $2 \times 2mm^2$. The Field Of View (FOV) was $230 \times 105\text{mm}^2$ and the slice thickness was 8 mm. The Echo Time was 20 ms. A 60% partial Fourier sampling is used to reduce the acquisition time. Diffusion encoding was performed along 15 different directions uniformly sampled on the sphere, reaching a b-value of 500 $\text{s/mm}^2$. A number of 9 averages per direction are used. The duration of the diffusion encoding gradients was 3ms. Each direction was acquired in a separate breath-hold with a duration of 18 R-R (R-wave to R-wave) intervals each. To guarantee identical breath hold levels, a respiratory navigator with a gating window of 5 mm was placed on the right hemidiaphragm. The regular FID crushers were removed from the sequence and replaced by the diffusion encoding gradients. Field-of-view reduction (local-look) was implemented by applying the first slice-selective excitation pulse in phase encoding direction, while the refocusing pulses remained in slice direction. The sequence diagram is shown in Fig. 6.1. Systolic and diastolic rest periods were used as imaging window. The exact timing was determined based on high temporal resolution cine images in short axis and long axis views. Slices of the diffusion weighted acquisitions were manually placed in short axis view and their positions were adjusted for the difference in ventricular length in systole and diastole. Four to six slices along the LV were acquired for both cardiac phases. A B0 map was acquired covering the LV in order to perform image based shimming. Additionally, two 3D whole-heart acquisitions were performed covering the entire LV during the systolic and diastolic rest periods. This protocol was repeated on 5 healthy volunteers (2 males / 3 females), of age $23.5 \pm 4$.

Diffusion tensors were then directly reconstructed from the DWIs, solving the least square problem of Stejskal-Tanner equation 2.8. Examples of acquired datasets are shown in Fig. 6.2. For both volunteers, a DTI slice acquired in diastole (left) and systole (right) is presented. The first visual inspection confirms the circumferential pattern and the angle variation from epicardium to endocardium, in both phases. For the second volunteer, we intentionally show the RV diffusion tensors, in order to illustrate the potential of acquiring DTI targeted to the RV wall. Tensors seem to indicate circumferential directions, but do not present a significant angle variation within the wall depth.

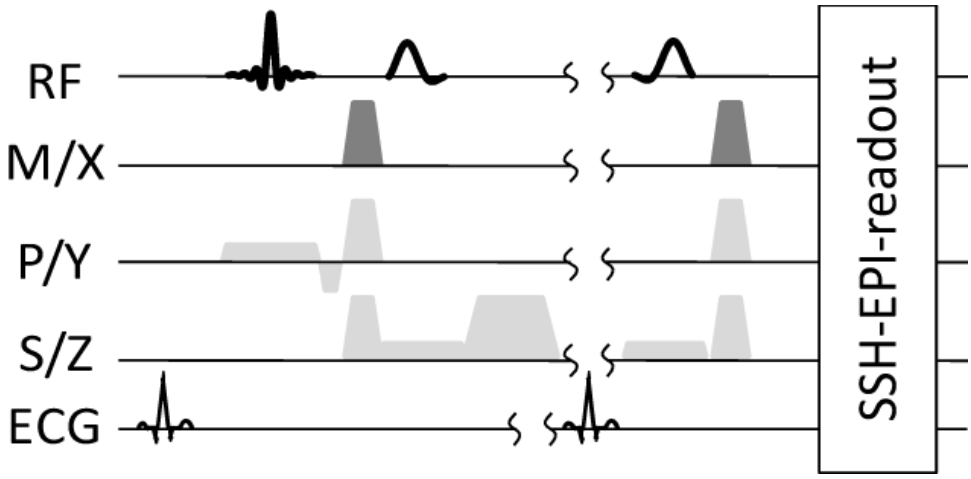


**Figure 6.1:** *Schematic of the local-look STEAM sequence with diffusion encoding gradients and a single-shot EPI readout*

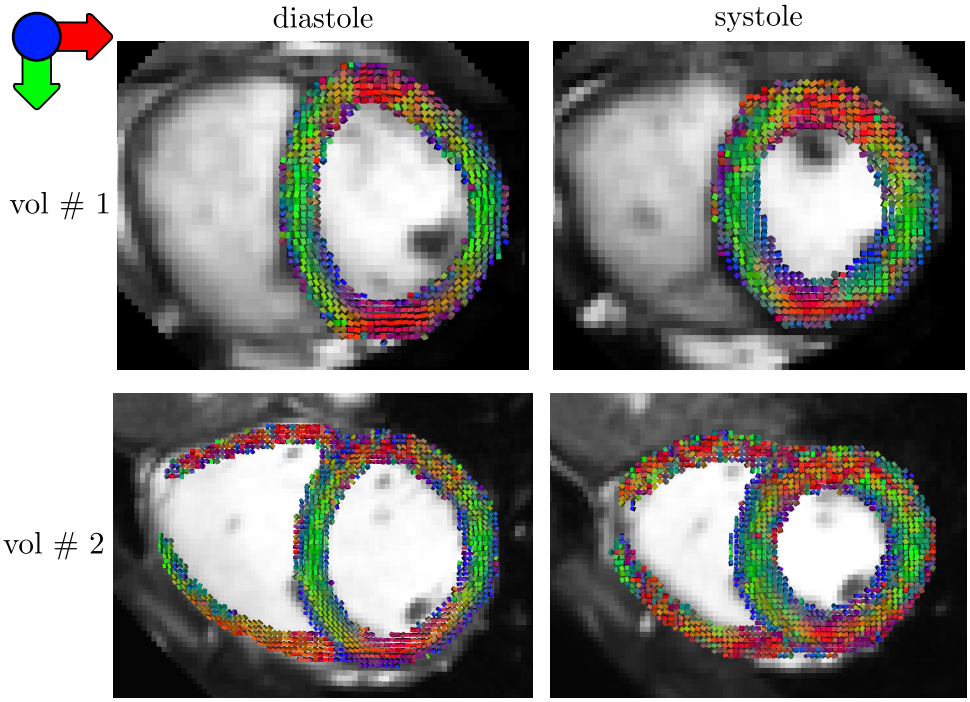


**Figure 6.2:** *Example of 2 volunteers' acquired DTI slices (without any processing), in systole and diastole. The circumferential patterns is clearly visible. Data in the right ventricle has been included for volunteer # 2 to demonstrate the potential of acquiring DTI targeted to the RV wall.*

### 6.2.2 Spin Echo Sequence

For this protocol, cardiac DTI was performed in 5 health subjects (2 males, 3 females) on a 1.5T clinical MR scanner (Philips, The Netherlands) equipped with a gradient system with maximal strength of 80 mT/m and a slew of 100 mT/m/ms per channel. A 32 channel cardiac coil array was used. The imaging protocol consisted of a B0 map for image based shimming, a trigger delay scout sequence for estimation of optimal trigger during systolic contraction [Stoeck 2011], the actual DTI acquisition, and a single breath hold 3D $T_2$ contrast enhanced whole heart acquisition (resolution $2 \times 2 \times 4$ mm$^3$). All sequences were ECG-triggered, and DWIs

were acquired during free breathing using a respiratory navigator, with a gating window of 5 mm, placed on the right hemidiaphragm. DTI acquisition was planned in short axis view of the heart and four to six slices were placed manually along the long axis of the LV. Imaging was performed using a diffusion weighted spin echo sequence with single shot echo planar imaging readout. Imaging parameters were as follows: TE/TR 59 ms/2R-R intervals, FOV: $230 \times 102$ mm$^2$, in-plane resolution: $2 \times 2$ mm$^2$, slice thickness: 8 mm. The echo time was shortened by the use of a rectangular FOV (local-look), applying the excitation pulse in phase encoding direction and the refocusing pulse in slice encoding direction [Gamper 2007]. Furthermore a partial Fourier coefficient of 0.63 was used and the echo pulse duration was further shortened applying the variable rate selective excitation (VERSE) technique [Hargreaves 2004]. Diffusion encoding was achieved by two bipolar gradients [Dou 2003] applied in 18 directions distributed on the unit sphere, creating a b-value of 500s/mm$^2$. A diagram of the sequence is presented in Fig. 6.3. Ten averages were acquired for each diffusion encoding direction and residual breathing offsets were corrected for by in-plane image registration during post processing. The total scan time was 10 to 15 minutes per DTI slice, depending on navigator efficiency. The trigger delay of the whole heart acquisition was set identical to the trigger delay of the diffusion weighted imaging.

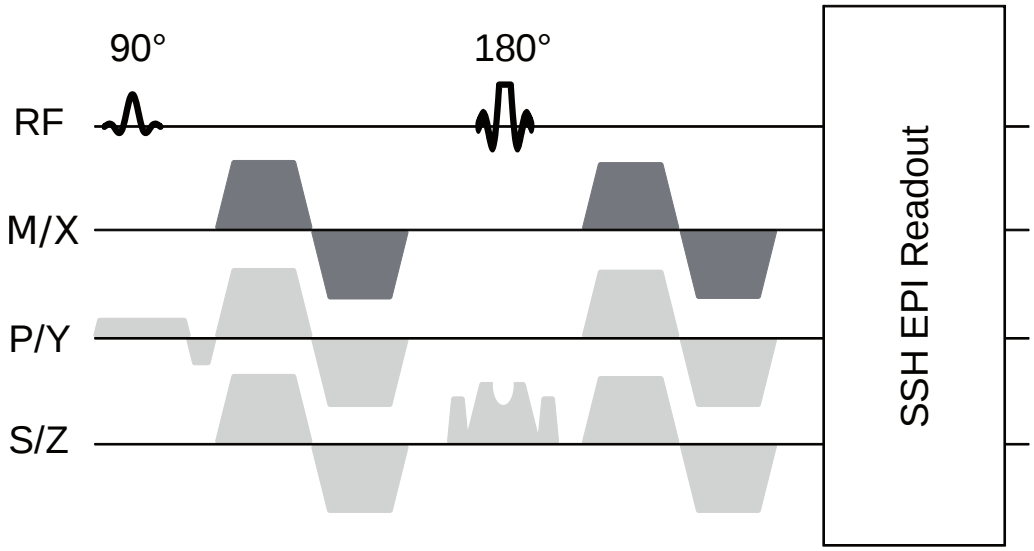


**Figure 6.3:** *Diffusion weighted spin echo pulse sequence with single shot EPI readout. Diffusion encoding is established with a pair of velocity compensating bipolar gradient. For local look imaging, the excitation pulse is applied in phase encoding direction, while the echo pulse remains in slice encoding direction. The echo pulse duration is shortened using VERSE*

Acquired datasets are shown in Fig. 6.4. Similarly to the previous acquisition, it is clear from Fig. 6.4(a) that the 5 volunteers share a very significant circumferential pattern of fibre orientations. The blue patches observed in the epicardial and endocardial boundaries (at the limit with the papillary muscles) present an early indicator of helix angle variation in agreement with the expected structure reported in the literature for *ex-vivo* hearts [Streeter 1973b, Scollan 2000, Lombaert 2011].

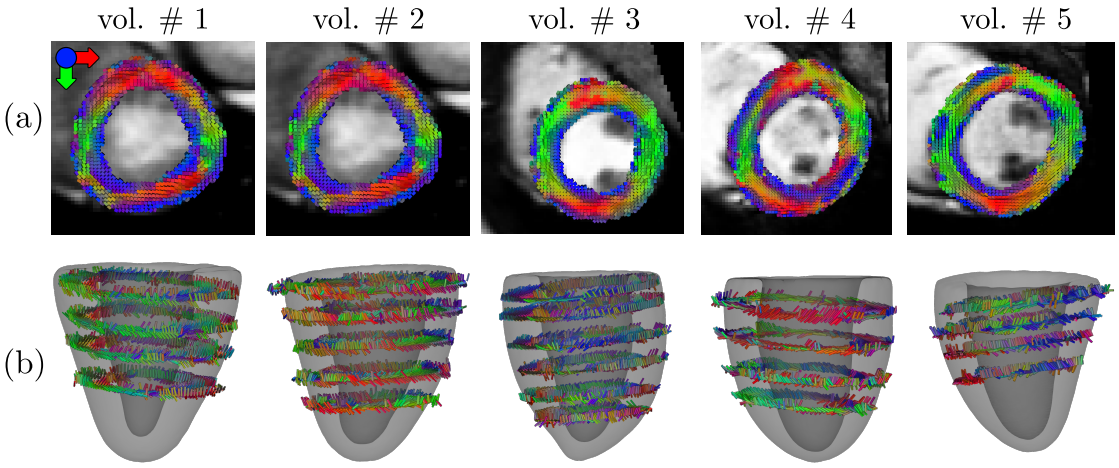


**Figure 6.4:** *Description of the population of N=5 volunteers. (a) One acquired DTI slice. Tensors are color-coded with the direction of their main eigenvector. (b) Distribution of the acquired slices for each volunteers, superimposed with the segmentation of the Left Ventricle (LV).*

## 6.3 Preliminary Processing

### 6.3.1 Misalignment Correction

The acquisition protocol described in 6.2.2 gives a series of 180 DWIs per slice, divided into 18 different gradient encoding directions. The residual misalignment between DWIs was found significant enough to alter the tensor reconstruction, making it necessary to correct for residual displacement. Correcting for DWI misalignment has been studied in the literature. [Andersson 2002] and later [Rohde 2004] address the problem of eddy-current distortion correction, jointly with the problem of (patient) motion correction in diffusion weighted MR, in the tensor reconstruction. Both eddy-currents and respiratory motion provoke potential distortions in our DWIs. In this experiment, the distortions **between** DWIs are assumed to be modeled by an in-plane rigid translation. In this section, the problem of realigning the DWIs under this hypothesis is addressed. The realignment is performed prior to averaging per direction using an approach very similar to the one detailed in [Oubel 2012]: in a first iteration $k = 0$, all DWIs $S_i$ are used to compute the mean diffusion image $S_r^0$. Each DWI is then rigidly registered to $S_r^0$, using the Mutual Information similarity metric, and a regular gradient descent optimization scheme, resulting in a rigid transformation $A_i^0$. In the following iteration $(k+1)$, the transformations $A_i^k$ are used as initialization for the registration algorithm, therefore avoiding successive resampling of the initial DWIs $S_i$. The operation is repeated until the mean square error (MSE) between two consecutive iterations is lower than a small threshold $\varepsilon$: $MSE(S_r^{k+1}, S_r^k) \leq \varepsilon$. In practice five iterations are sufficient for convergence.

To illustrate the result of this registration, the standard deviation image is computed: $\Sigma_S = \text{std}\{S_i\}_{i=1:N}$, before $(\Sigma_S)$ and after $(\Sigma_{S'})$ the registration process. This image characterizes the amount of signal change between diffusion direction at each position. It is therefore **not** expected to be null, as the signal intensity changes naturally with the diffusion encoding direction. However, if the $S_i$ are misaligned, it will induce some blurring of $\Sigma_S$. Two resulting images, for one acquisition, are shown in Fig. 6.5. This figure shows that the standard deviation image derived from

**Algorithm 3:** Register DWIs $(S_i)_{i=1:N}$

**Data**: The set of initial DWIs $(S_i)_{i=1:N}$, and a threshold $\varepsilon$
**Result**: The set of registered DWIs $S'_i$
**foreach** $i \in [1:N]$ **do** $A_i^0 \leftarrow \mathrm{Id}$;
$k \leftarrow 1$;
$S_r^0 \leftarrow E[S_i]$;
$e \leftarrow 1.0$;
**while** $e \geq \varepsilon$ **do**
  **for** $i = 1 \rightarrow N$ **do**
    $A_i^k \leftarrow$ inplaneregistration$(S_r^k, S_i)$ with $A_i^{k-1}$ as initialization;
  **end**
  $k \leftarrow k + 1$;
  $S_r^k \leftarrow E[A_i^k \circ S_i]$;
  $e \leftarrow MSE(S_r^k, S_r^{k-1})$;
**end**
**foreach** $i \in [1:N]$ **do** $S'_i \leftarrow A_i^{k-1} \circ S_i$)

registered DWIs (b) appears sharper than the one derived from original DWIs (a).

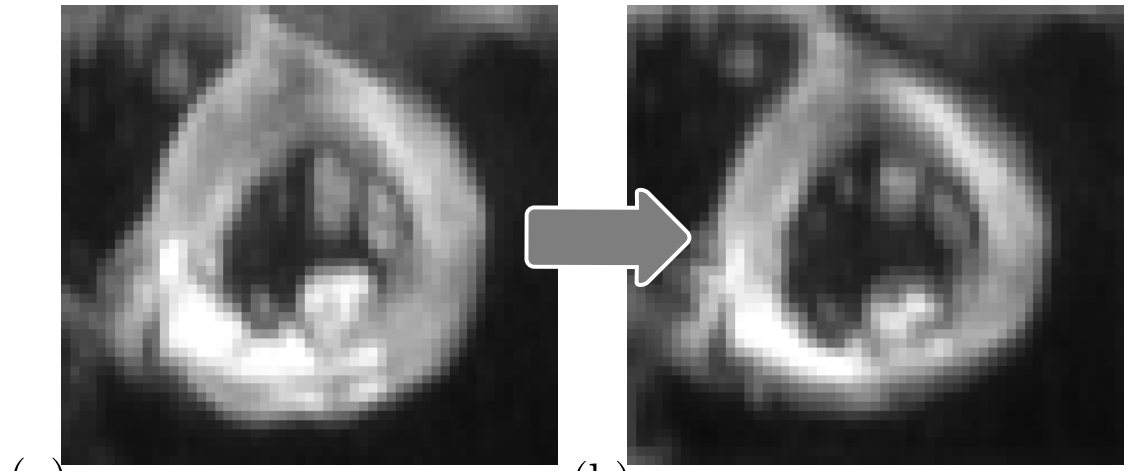


**Figure 6.5:** *Example of standard deviation maps from DWIs pre- (a) and post- (b) registration used for the SE data. The slight blurring due to residual small misalignments between DWIs is reduced in (b).*

When the STEAM protocol is used, the breath-hold acquisition produces very small misalignments compared to those observed in free-breathing. No significant improvement in the data was found by applying this registration algorithm on the STEAM data. Thus, this pre-processing step is discarded in this case.

### 6.3.2 Tensor Restoration and Normalization

In a healthy left ventricle, there is no reason to believe the diffusion properties of the tissue undergo major change throughout the ventricle wall. For instance, *ex-vivo* studies show little variation of the Fractional Anisotropy or the Mean Diffusivity (MD) through out the ventricle. Therefore the mean Apparent Diffusion Coefficient

($ADC_i$, or MD) should theoretically be close to homogeneous in this region. In an *in-vivo* setting, noise and movement artifacts often lead to diffusion signal attenuations (see Eq. 2.7) greater than 1. These observations are not physically relevant and prevent us from reconstructing the tensor at these locations. This is illustrated in Fig. 6.6(a) where, in this slice, the ventricle has 20% of its data centres where the tensor reconstruction is ill-posed (Eq. 2.8), and where the anisotropy is very heterogeneous. Whilst the tensor anisotropy is a quantity of interest, one can argue that the observed heterogeneity is genuine or caused by noise and motion in the DWIs and in the B0 signal. A classical solution to this ill-posedness of noisy diffusion MR system consists of replacing the non-positive tensors by the average of their neighbourhood. This approach assumes local smoothness of the tensor field, discarding all the information given by the DWI at the problematic location. In this work, on the other hand, smoothness of the mean diffusivity is assumed. Let us express the hypothesis that the diffusion properties of the tissue is smooth in the ventricular wall. The expression of the sum of the log-attenuations is written as follows:

$$\sum_N \log \frac{S_i}{S_0} = -3NADC_i \tag{6.1}$$

With N the number of gradient directions. The B0 signal from this equation can be extracted using classical logarithm rules:

$$S_0 = \sqrt[N]{\prod_N (S_i)}\ \exp(3ADC_i)$$

It is hypothesised that, with N sufficiently large (a good sampling of the sphere), the assumption of diffusion property homogeneity implies a positive constant $ADC = \bar{Y}$ throughout the ventricle wall. For instance, one can compute the expectation value of $ADC_i$ through the ventricle wall and choose it as the constant value: $\bar{Y} = E[ADC_i]$. Then an altered "*normalized*" B0 signal is derived:

$$\bar{S_0} = \sqrt[N]{\prod_N (S_i)}\ \exp(3E[ADC_i])$$

The *normalized* signal $\bar{S_0}$ is the product of the geometric mean of the diffusion signals with a geometric parameter $e^{3\bar{Y}}$ (greater than 1). Therefore the initial assumption of a constant diffusion property is obtained by using this normalized signal instead of the initial $S_0$ in the tensor reconstruction process. However, it is important to notice that using that normalized signal will bias the anisotropy property of the tensor (in both directions), towards the mean tensor of the ventricle. Additionally, it could potentially invalidate voxels that were previously well-posed (when ADC is underestimated). On the other hand, choosing a $\tilde{Y}$ greater than the local mean diffusivity is equivalent to a systematic overestimation of the observed mean diffusivity. This overestimation will relax the least square problem in Eq. 2.8:

$$\tilde{S_0} = \sqrt[N]{\prod_N (S_i)}\ \exp\big(3(ADC_i + f.E[ADC_i])\big) \tag{6.2}$$

For instance, the DTI slice shown in Fig. 6.6(b) corresponds to the normalization with an overestimation as in Eq. 6.2, with a factor of $f = 0.2$. Figure 6.6 demonstrate

the capacity of this restoration process to reconstruct tensors in previously ill-posed voxels. These new reconstructed tensors look coherent with their neighbours, suggesting that there was indeed valuable information in the initial DWIs, hidden by the ill-posedness of the system. A second observation is that the size of the tensors is smoother after normalization. This is due to the fact that the ADC relative overestimation is greater when ADC is lower. Thirdly, in areas where the system was well-posed initially, a slight alteration of the eigenvalues relative magnitude can be noticed, i.e. the tensor shape is altered. Indeed, using $\tilde{Y} = ADC_i + f.E[ADC_i]$ tends to push the tensors towards identity when $f > 0$. The shape bias provoked by this process was quantified by measuring the tensor FA with or without normalization. The FA is decreased by $0.063 \pm 0.049$ after normalization, which corresponds to 15% decrease. This property is very undesirable if statistics on tensor shape are needed. In consequence, the original un-normalized tensors are used for tensor shape analysis ($FA$, $c_p$, etc). However, since this process does not alter the tensor directions, and that it gives additional information about the fibre orientation arrangement, we performed the normalization on original DTI slices for the fibre orientation analysis (angles), using $f = 0.2$.

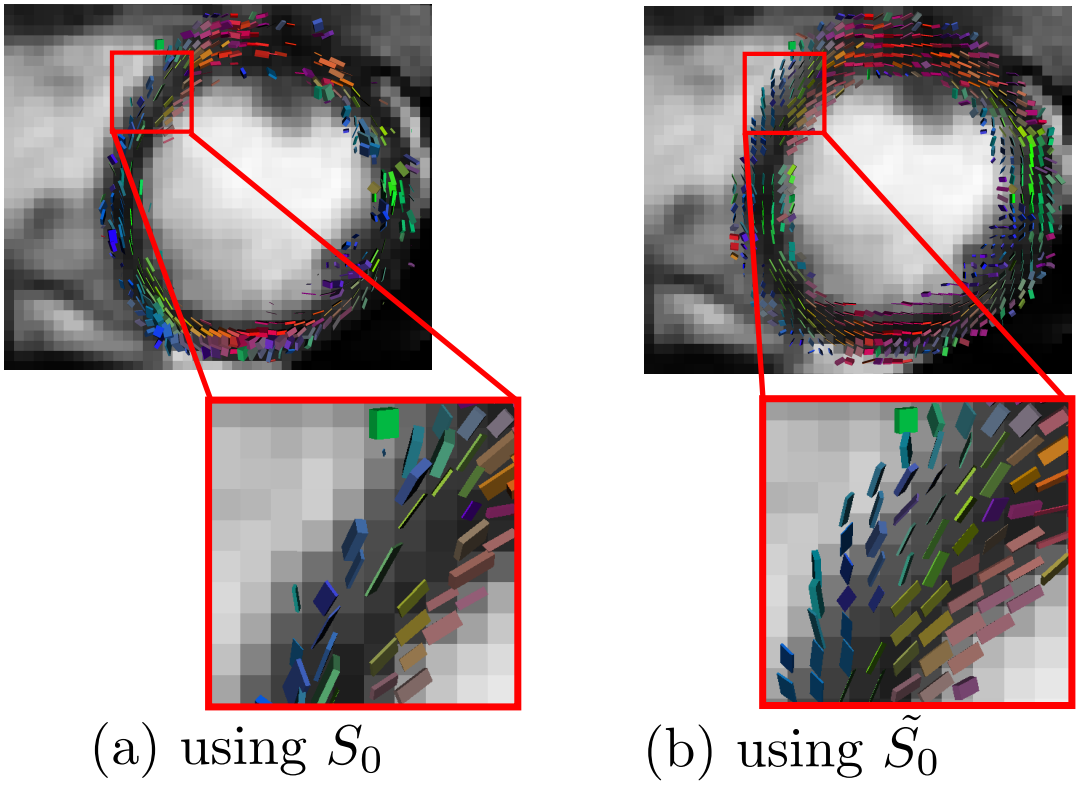


**Figure 6.6:** *Tensor Restoration/Normalization: Noise and motion artifact lead to wrong observations of the diffusion attenuations, and ultimately to ill-posed tensor reconstruction (a). Using a controlled normalization in Eq. 6.2 allows to recover the fibre orientation, at the price of a bias in the tensor shape recovery (b).*

## 6.4 Dual Phase Comparison of Fibre Architecture

By analysing strain and diffusion tensors, [Dou 2003] showed that fibre shortening and fibre shear contribute only little to myocardial thickening, while sheet

shear, sheet extension and shear normal thickening play a major role. In contrast, in [Chen 2005], excised rat hearts were fixated both in systole or diastole. Using DTI, a transmural change of helix angle by 10 deg. to 30 deg. between diastole and peak systole was found. Furthermore a significant reduction in magnitude of the sheet angle from diastole to peak systole was concluded in this study. In the present study, the STEAM acquisition allowed us to depict *in-vivo* fibre architecture of the human beating heart, in diastole and systole.

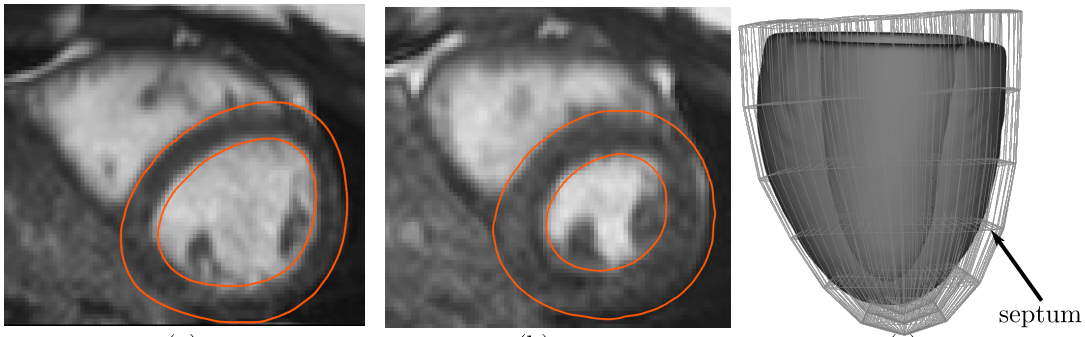


**Figure 6.7:** *(a,b) Segmentation contours (orange lines) with the anatomical image of one volunteer in the diastolic (a) and systolic (b) phase. (c) The segmentations of the left ventricle in diastolic phase (grid mesh) and systolic phase (plain mesh) are super-imposed.*

### 6.4.1 Data Cumulation and Distribution

A segmentation of the left ventricular wall as detailed in 3.4.1 was performed for each phase. The ventricular segmentation was stopped at the base prior to the valves. Care was taken to avoid including papillary muscles at the endocardial boundaries. Fig. 6.7 shows the segmentation contours in both phases. In Fig. 6.7(c), the change of shape between cardiac phases is illustrated by super-imposing the two segmentation volumes at scale.

As mentioned in Sec. 3.3.1, the PS coordinate system can potentially be used as a naturally normalized setup that facilitates group-wise statistics within a set of data. In this section, these concepts are applied on the two *in-vivo* databases. Transformations of Eq. 3.5 are applied to each of the $N^{STE}_{dias} = 5$, $N^{STE}_{sys} = 5$ and $N^{SE} = 5$ datasets. A normalization of the first component $\xi_1$ is then applied, with a target range corresponding to the mean of the measured lower and upper limits: $[0.39 \sim 0.65]$ in diastole and $[0.32 \sim 0.55]$ in systole.

The resulting transformed DTI information constitutes a homogeneous and naturally normalized set of data:

$$\begin{cases} \text{for each volunteer } v,\ P_v = \{x_i, D_{x_i}\}_v \\ \mathcal{A} \overset{def}{=} \{\Psi_v \circ \Phi_v(P_v)\}_{v=1:5} \end{cases} \tag{6.3}$$

Let us denote $\mathcal{A}^{STE}_{dias}$, $\mathcal{A}^{STE}_{sys}$ and $\mathcal{A}^{SE}$, the cumulated dataset respectively corresponding to the STEAM datasets in diastolic phase, the STEAM datasets in the systolic phase, and the SE datasets in systolic phase respectively.

These quantities are not straightforward to visualise, as they are expressed in the PS frame. Therefore, the inverse transformations of one volunteer $\Phi^{-1}_{v^*} \circ \Psi^{-1}_{v^*}$ is

applied to $\mathcal{A}$ to allow its visualisation in the template truncated ellipsoid volume (the choice of the volunteer here does not matter, we chose $v^* = v_1$ in each case). The resulting transformed tensor fields are shown in Fig. 6.8. Tensors are shown as segments pointing to their first eigenvectors. In the SE case, the total amount of slices is 23, resulting in 18350 measurement points(data centres) throughout the ventricle wall. In the STEAM cases, the total amount of slices are 16 and 15 respectively in diastolic and systolic phases, with 13189 and 13212 data centres. The cumulation of the volunteers datasets $\mathcal{A}$ illustrated in Fig. 6.8 shows an overall good coverage of data centres among the ventricle. As predicted, the area close to the apex is poorly populated. This is due to the challenge of acquiring this part of the LV, as the non-linear motion involved makes the acquisitions not representative of the actual anatomical fibre structure. However it has been possible to acquire data close to the apex using the STEAM sequence. The numerical boundaries in each direction are gathered in Table 6.1. Several interpretations can be drawn from this table. Firstly, the $\xi_1$ lower and upper limits are very stable amongst the datasets (and have very low standard deviations). This property partly justifies the hypothesis that the $\xi_1$ normalization performed between volunteers is not affecting the statistical significance of our findings. Second, a larger lower boundary in the $\xi_2$ coordinate is observed for the $\mathcal{A}^{SE}$ dataset. This is confirmed visually in Fig. 6.8(c) where the apex region is poorly populated in comparison to the first two datasets. Third, the $\xi_2$ upper boundary is relatively stable amongst datasets and close to $\pi/2$.

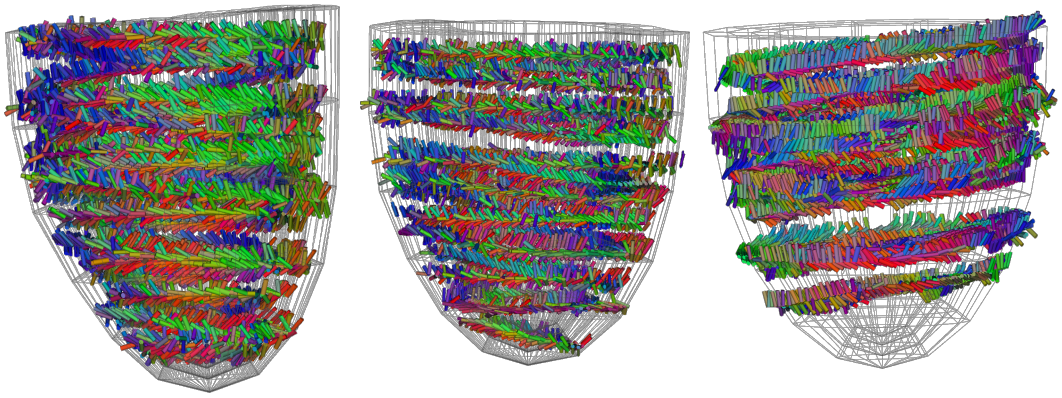

(a) (b) (c)

**Figure 6.8:** *The cumulations of the volunteers data $\mathcal{A}$ in each of the three acquisition scenarios. (a,b) using STEAM sequence respectively in diastole and systole ($\mathcal{A}^{STE}_{dia}$ and $\mathcal{A}^{STE}_{sys}$). They respectively contain 13189 and 13212 data centres. (c) using SE in systole ($\mathcal{A}^{SE}$), containing 18350 data centres.*

$\mathcal{A}$ can be used for comprehensive statistical analysis. For instance, one can calculate the main eigenvector directions of tensors $D_\xi$. As explained in Sec. 3.3.1, since these vectors are expressed against the PS contravariant basis $\mathcal{G}$, the extraction of meaningful information is straightforward. In this experiment, three different projections of interest from the acquired *in-vivo* tensors were extracted. That is, the helix, transverse and sheet angles, as described in Fig. 3.1, and defined in Eq. 3.3. Joint histograms of the three angles with respect to the normalized transmural depth $\xi_1$ are presented in Fig. 6.9. For the STEAM experiment, the same linear variation was found, with boundary values of $+48$ to $-41$ in diastole, with a correlation factor of 0.68, and $+59$ to $-41$ in systole (correlation factor of 0.72). For the SE experiment, the helix angle $\alpha$ was found to vary between $+55$ deg at the endocardium to $-30$ deg

| $\mathcal{A}$ | # sl. | # pts. | $\xi_1$ min | $\xi_1$ max | $\xi_2$ min | $\xi_2$ max |
|---|---|---|---|---|---|---|
| $\mathcal{A}^{STE}_{dias}$ | 25 | 13189 | $0.30 \pm 0.02$ | $0.60 \pm 0.04$ | $0.38 \pm 0.19$ | $1.57 \pm 0.05$ |
| $\mathcal{A}^{STE}_{sys}$ | 26 | 13212 | $0.24 \pm 0.04$ | $0.59 \pm 0.04$ | $0.35 \pm 0.21$ | $1.48 \pm 0.09$ |
| $\mathcal{A}^{SE}$ | 23 | 18350 | $0.31 \pm 0.02$ | $0.63 \pm 0.06$ | $0.49 \pm 0.28$ | $1.62 \pm 0.12$ |

**Table 6.1:** *PS description of the data repartition in the three cases. The mean boundary values amongst the set of respectively $N^{STE}_{dia}$, $N^{STE}_{sys}$ and $N^{SE}$ volunteer is shown, $\pm$ the 1 $\sigma$ deviation. The number of acquired slices is indicated (sl.), as well as the total number of data centres (pts).*

| $\mathcal{A}$ | endocardium ($\alpha_1$) | epicardium ($\alpha_2$) | corr. |
|---|---|---|---|
| $\mathcal{A}^{STE}_{dias}$ | $+51.6 \pm 28$ | $-45.3 \pm 29$ | 0.74 |
| $\mathcal{A}^{STE}_{sys}$ | $+53.2 \pm 24$ | $-46.4 \pm 28$ | 0.72 |
| $\mathcal{A}^{SE}$ | $+55.2 \pm 32$ | $-32.1 \pm 35$ | 0.58 |

**Table 6.2:** *Helix angle boundary values at endocardium and epicardium for $\mathcal{A}^{STE}_{dia}$, $\mathcal{A}^{STE}_{sys}$, and $\mathcal{A}^{SE}$, and the corresponding correlation coefficient.*

at the epicardium, with a correlation coefficient of 0.58. In all experiments, the transverse angle $\beta$ was found stable along the transmural depth with a mean equal to 0, and has consequently low correlation coefficients. This suggests that myocardial fibres show a very low deviation from circumferential direction. On the other hand, the distribution of the sheet angle $\gamma$ is changing significantly from diastole to systole, but does not seem to have a linear correlation with the transmural depth. This property is further studied in Sec. 6.5. Numerical results of the helical variation are reported in Table 6.2. A large correlation coefficient of the helix angle $\alpha$ with the $\xi_1$ coordinate is observed.

Using the cumulated datasets $\mathcal{A}^{STE}_{dia}$, $\mathcal{A}^{STE}_{sys}$, the joint histograms of the helix, transverse and sheet angles with respect to the transmural depth in both phases are reported in Fig. 6.9. The linear variation of $\alpha$ is clearly detectable in both phases. As reported in Table 6.2, the epicardial boundary value (denoted $\alpha_2$) shows no significant difference between phases. The transverse angle $\beta$ is very close to the zero-line, in both phases, suggesting that myocardial fibres keep their orientation parallel to the wall surface during the entire cardiac cycle.

### 6.4.2 Regional Analysis

The AHA division detailed in Sec. 3.3.1 was applied to the two datasets $\mathcal{A}^{STE}_{dia}$, $\mathcal{A}^{STE}_{sys}$, in order to evaluate the fibre orientation patterns specifically in each AHA regions. The helix angle $\alpha$ joint histogram against the transmural depth for each AHA zone for both phases is reported in Fig. 6.11. An erratic pattern at the apex is observed in both phases, due to a fewer number of data centres, and a lower SNR. The basal regions seem to share a higher linearity of the helix angle variation, compared to the apical regions (AHA regions 13-16). From these results, no significant differences between phases can be denoted.

A step further in the comparison between cardiac phases, bullseye plots of the Fractional Anisotropy (FA) and the Planar Coefficient ($c_p$) of the two datasets $\mathcal{A}^{STE}_{dia}$

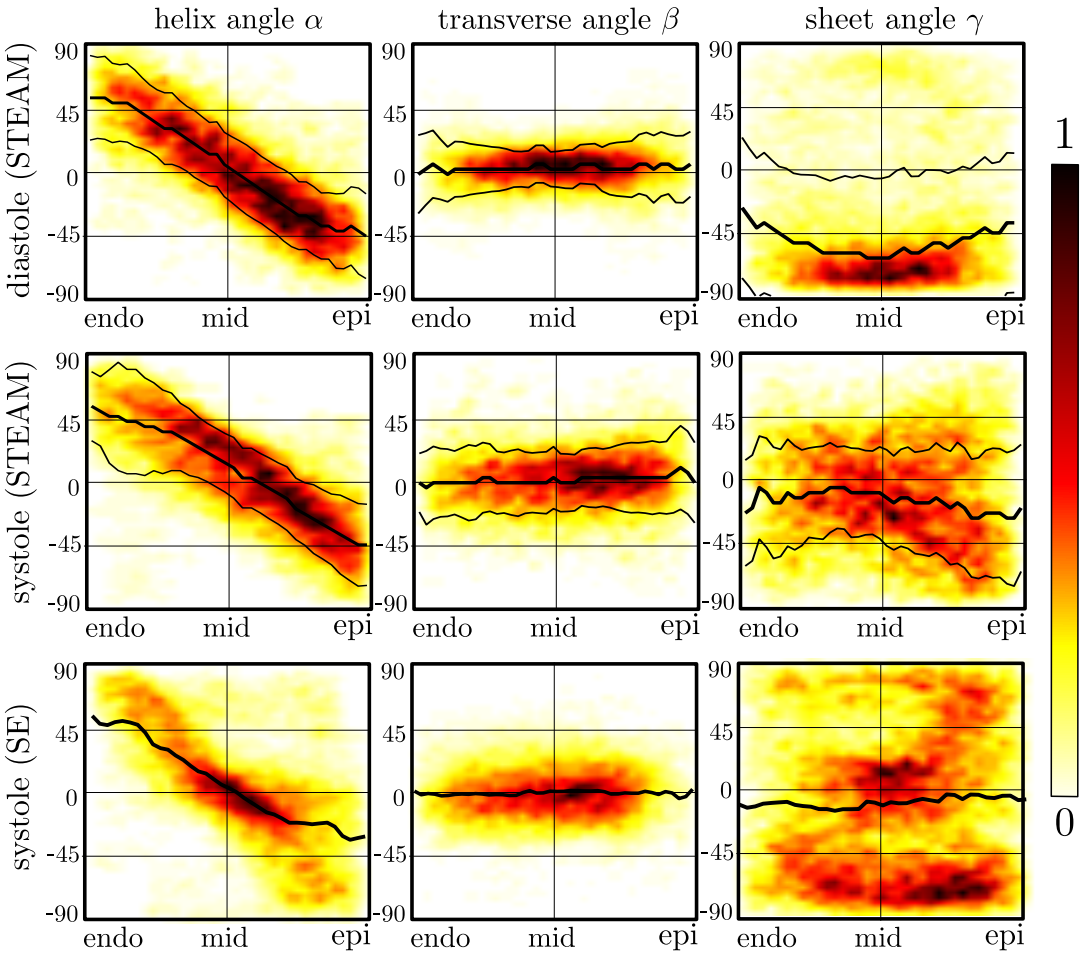


**Figure 6.9:** *Joint histograms of the three comprehensive angles $\alpha$, $\beta$, $\gamma$, derived from the projections of the tensors onto the PS contravariant basis $\mathcal{G}$, as defined in Eq. 3.3, against the first PS coordinate $\xi_1$, using STEAM in diastolic cardiac phase (top), STEAM in systolic cardiac phase (middle) and SE in systolic phase (bottom). The plain lines show the median value per column and their window at $1\sigma$.*

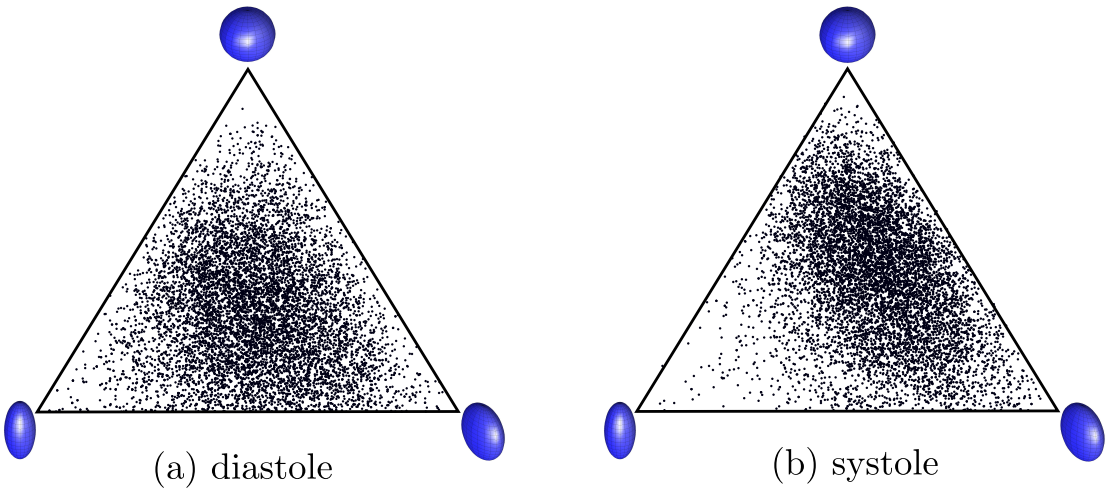


**Figure 6.10:** *Barycentric plots (extracted from coefficients $c_l$, $c_p$ and $c_s$, of the cumulated datasets $\mathcal{A}^{STE}_{dia}$ (left) and $\mathcal{A}^{STE}_{sys}$ (right), showing a more orthotropic distribution in diastole.*

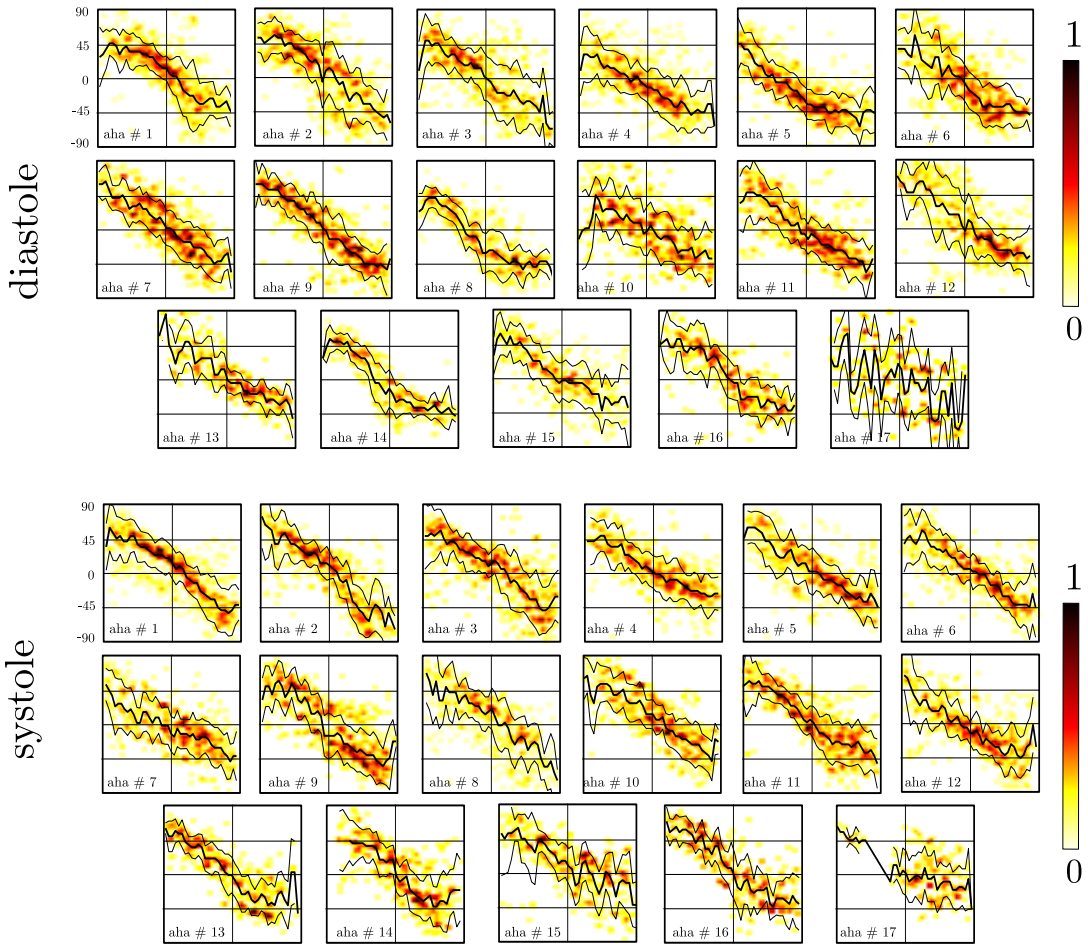


**Figure 6.11:** *Joint histogram of the helix angle against the transmural coordinate in each of the 17 AHA zones, for both the diastolic phase (using $\mathcal{A}^{STE}_{dia}$) and the systolic phase (using $\mathcal{A}^{STE}_{sys}$).*

and $\mathcal{A}^{STE}_{sys}$ are shown in Fig. 6.12. The FA shows a mode at 0.69 in diastole and 0.56 in systole. The planar coefficient $c_p$ shows a mode at 0.37 in diastole against 0.36 in systole, with similar distribution (Fig. 6.12(right)). The bullseye maps allow to denote a set of antero-septal regions where the FA is slightly greater than the rest of the myocardium in diastole. The FA values are significantly greater than the values found in *ex-vivo* studies [Lombaert 2012]. This high discrepancy may be due to fast tissue anisotropy decay after necrosis, as reported in [Eggen 2012]. FA values found in the current study are also greater than those reported in pathological rat hearts *ex-vivo* [Chen 2003]. Additionally, the FA difference between phases reported in the present study is found to be significant with a p-value of 0.09. This FA decrease during contraction was also reported *ex-vivo* in rats in [Chen 2005].

### 6.4.3 Cross-Correlation Comparison

Finally, the structure cross-correlation computation as detailed in Sec. 3.6.3 was applied to the two datasets $\mathcal{A}^{STE}_{dia}$ and $\mathcal{A}^{STE}_{sys}$. Resulting tensors $R_s(z)$ for $z = 1 \sim 17$ in both phases are reported in Fig. 6.13(a). It appears from these illustrations that there is a slight but noticeable discrepancy in the variability of the tensor field between diastole and systole. These cross-correlations are measuring the variability of the structure tensor of the sparse tensor field. The more anisotropic the cross-

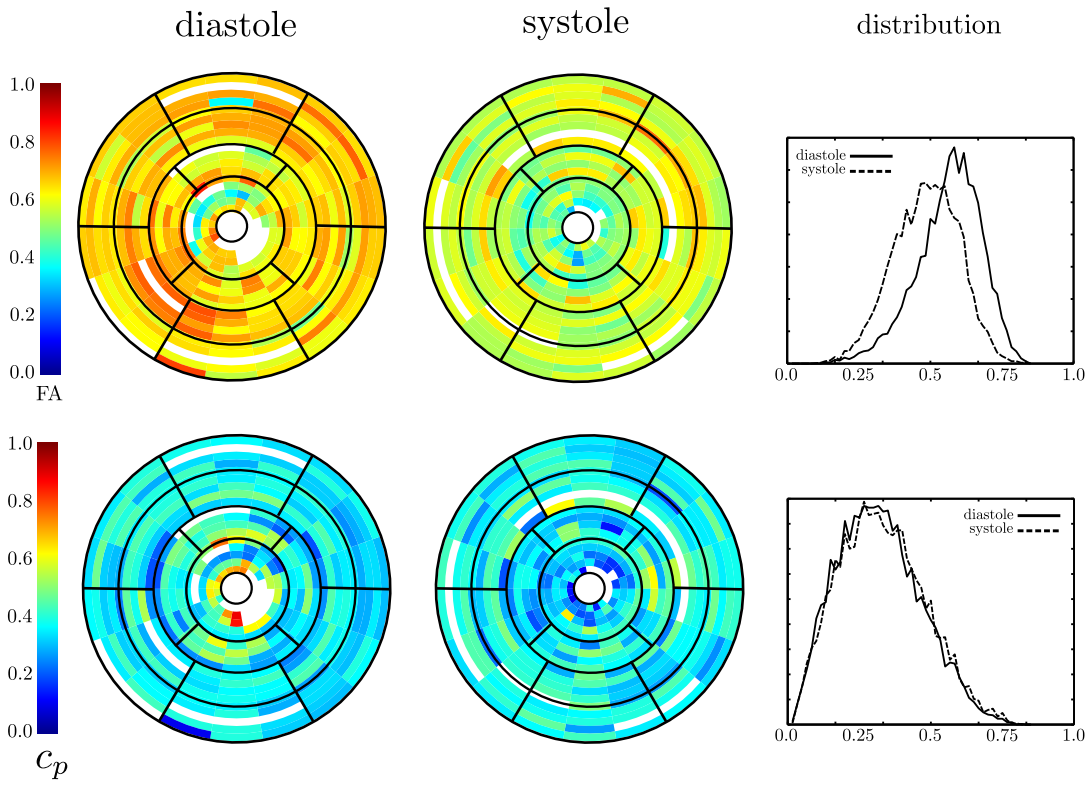


**Figure 6.12:** *Bullseye maps of the Fractional Anisotropy FA (top) and the Planar coefficient $c_p$ (bottom) in diastole (left) and systole (centre). The white regions denote area where there is no information. Their normalized distributions are reported on the right.*

correlation is, the more stable is the structure tensor within a region. To quantify the shape of these cross-correlation tensors, the Fractional Anisotropy and the planar coefficient of $R_z$ were computed. Scatter plots of these two quantities between phases are shown in Fig. 6.13(b). These plots indicate that, while there is no significant change in FA, $c_p$ is significantly greater in systole in all zones (apart from the apex).

### 6.4.4 Dense Approximation *In Vivo*

The dense approximation scheme detailed in Chap. 4 was first applied independently on each of the subjects' datasets (in both phases for the STEAM data), in the PS frame. The chart in Fig. 6.14 summarizes the workflow. A subsample of the resulting tensor fields for each case is presented in Fig. 6.15 as a mid-ventricular short axis section. The kernel bandwidth $H$ was chosen from the optimal bandwidth $H_{opt}^{SE}$ obtained in the case (N=7, SNR=10) for the SE experiment (see Sec. 4.3.1), as it corresponded to the mean measured *in vivo* slice distribution and noise levels. An increase of SNR and ventricular coverage in the STEAM data was observed. A different set of parameters was therefore used for the kernel sizes of the approximation operator. The optimal bandwidth obtained for the case-scenario (N=15,SNR=14) was chosen. The kernels were therefore $H_{opt}^{STE} = \mathrm{diag}(0.0129, 0.1293, 0.2731)$ and $H_{opt}^{SE} = \mathrm{diag}(0.0189, 0.1793, 0.3131)$. Fibre tractography was performed for each subject and a selection of fibres is shown in Appendix. D. All datasets show a characteristic double helical pattern, as found in histology studies [Streeter 1973b] and in ex-vivo DTI studies [Peyrat 2006, Lombaert 2011]. The transmural variation of fibre orientation is clearly visible from the short axis slices in Fig. 6.15.

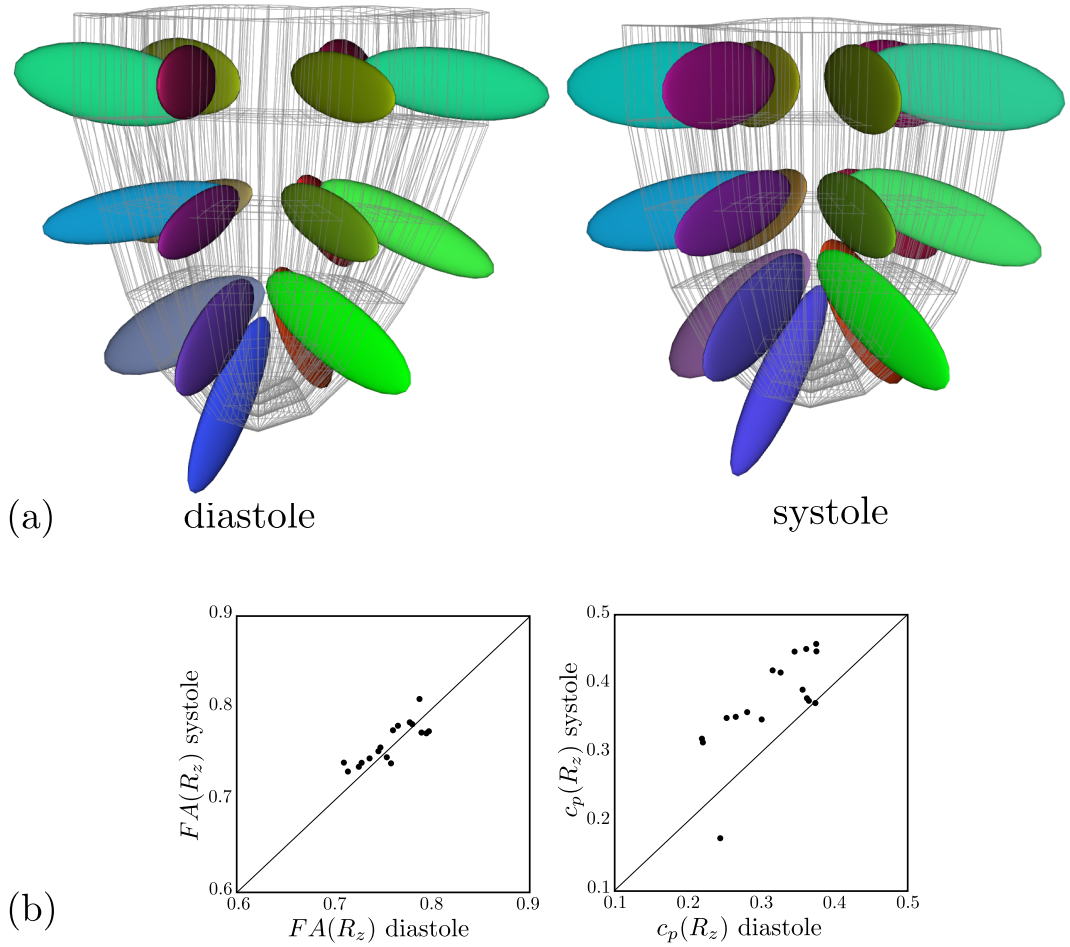


**Figure 6.13:** *(a) The ellipsoids represent the cross-correlations $R_z$ of the first eigenvectors of the tensor field Structure tensors within each AHA region $z$, in diastole (left) and systole (right). (b) Scatter plots of the FA (left) and the Planar coefficient $c_p$ of cross-correlation $R_z$ between phases.*

The dense approximation was then applied to the cumulated datasets $\mathcal{A}*$ illustrated in Fig. 6.8. The resulting dense tensor field was warped back to one of the volunteer's anatomical LV, and fibre tractography was performed (see Sec. 4.2.4). In Fig. 6.16, the resulting approximated tensor fields and fibre fields from $\mathcal{A}_{dia}^{STE}$ (left column) and $\mathcal{A}_{sys}^{STE}$ (right column) are shown. Fibres are color-coded with the local helix angle $\alpha$. The helical structure of the myocardial fibres is revealed by the fibre tractography maps in both phases.

## 6.5 *In-Vivo* Insight into the Laminae Structure

The laminar sheet organization of the heart has been observed in many *ex-vivo* studies [Spotnitz 1974, Costa 1999]. These studies have shown that cardiac myocytes are grouped in layers of approximately 4 cells thickness [LeGrice 1995] separated by cleavage (sheet) planes, that can be observed using high resolution imaging [Kohler 2003, Gilbert 2012]. The laminae arrangement is believed to strongly determine tissue shearing during contraction [Costa 1999]. Based on this hypothesis, [Arts 2001] were able to discriminate two distinct populations of laminae, and

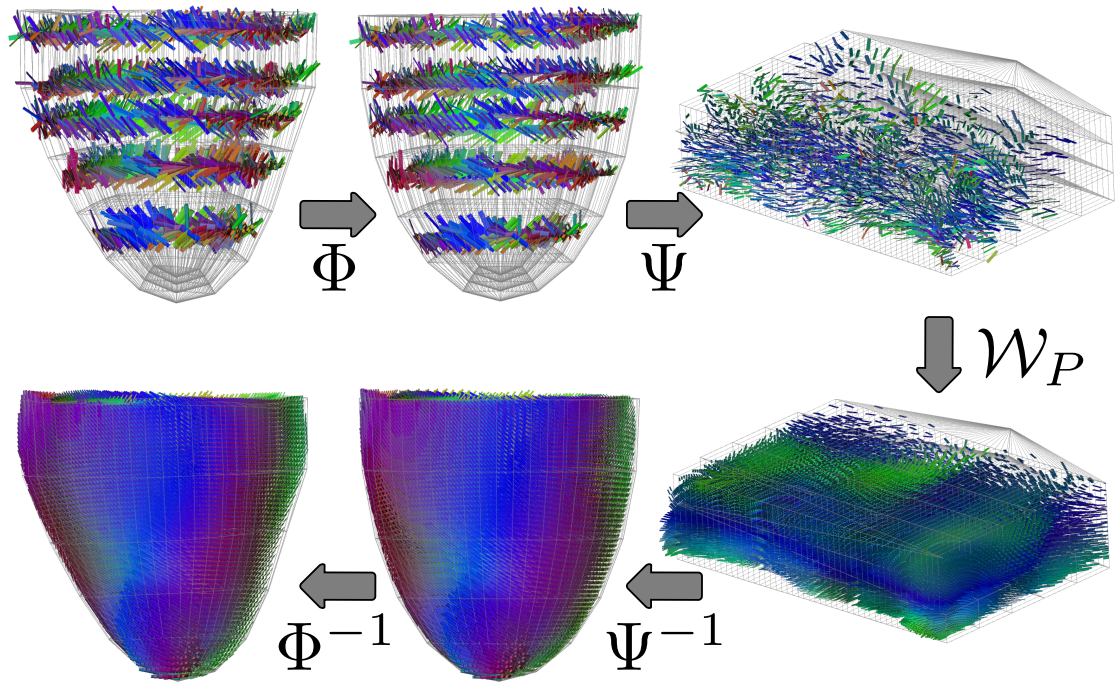


**Figure 6.14:** ***Workflow****: This chart illustrates the global workflow, for one dataset, from a set of DTI slices towards the full ventricular approximated tensor field. All operators are fully invertible and diffeomorphic, except $\mathcal{W}_P$. All illustrations are respectively at scale, apart from the PS frames (right), which have been expanded with an homothetic transformation to ease visualisation.*

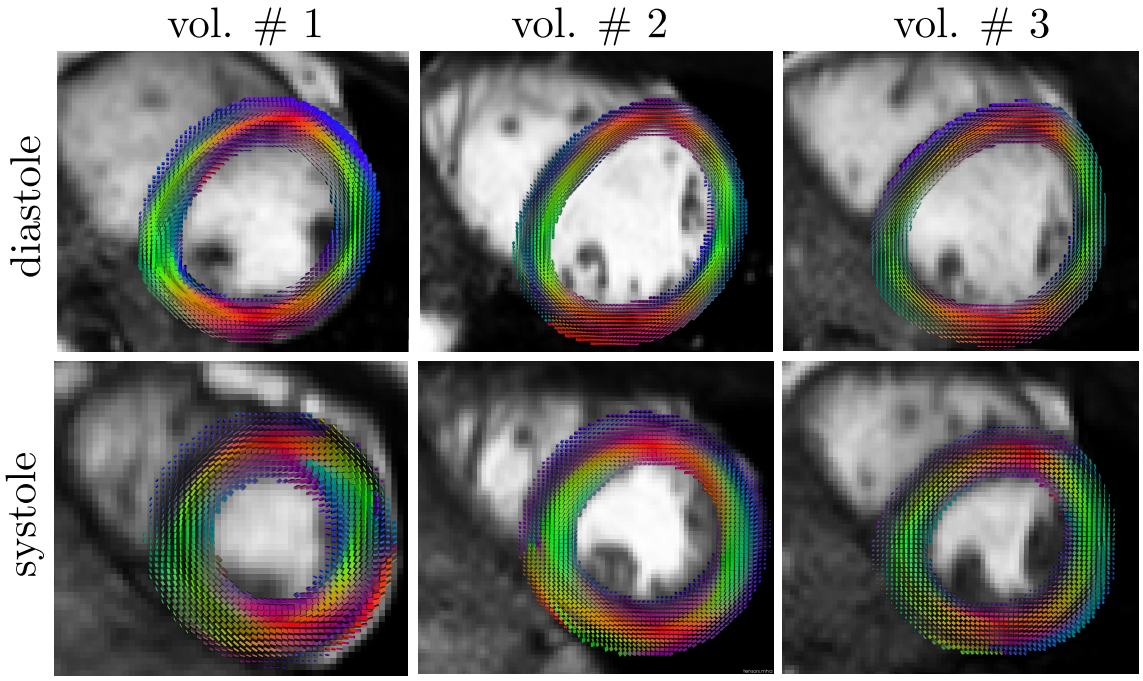


**Figure 6.15:** *Examples of approximated dense tensor fields. in diastole (top) and systole (bottom) for three different volunteers, using PS approximation operator described in Sec. 4.2.1.*

observed this dual-population pattern in excised canine hearts. This study reports measured sheet angle $\gamma$ scatter plots with respect to the transmural depth where

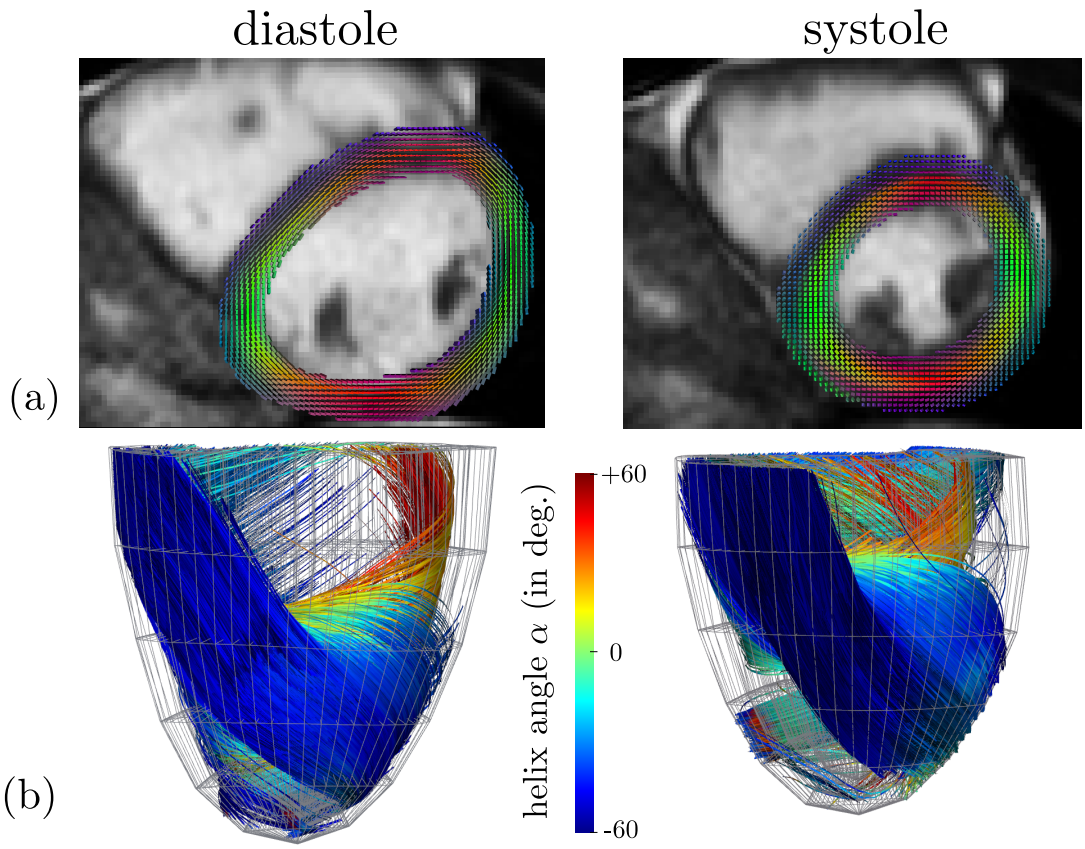


**Figure 6.16:** *(a) Approximated tensor fields from the cumulated datasets $\mathcal{A}_{dia}$ (left) and $\mathcal{A}_{sys}$ (right), and their respective fibre tractography reconstructions (b). Fibres are color-coded with the local helix angle $\alpha$.*

the two populations are clearly visible. In [Hooks 2007], the authors report a very strong correlation between the laminae structure and the local tissue electrical conductivity. In their experiment, they found a sheet angle predominantly negative, with no visible evidence of the dual-population. In this section we demonstrate that in-vivo DTI is capable of detecting discrepancies between diastolic and systolic laminae organization that agrees with previously reported histological studies.

Details of the acquisition can be found in Sec. 6.2.1. The third eigenvector $v_3$ of tensors was extracted at each voxel. The orientation of this vector is believed to be perpendicular to the underlying laminae plane [Kung 2011], as described in Fig. 6.17(a). Maps of $v_3$ orientations in systole and diastole are shown in Fig. 6.17(b). The discrepancy between phases is visible. In particular, the cleavage planes seem to be oriented parallel to the myocardial wall in diastole and arrange in a more complex structure where the planes are parallel to the short axis in the mid-wall region. The orientation of the sheet planes can be measured by the sheet angle as described in Sec. 3.3.2. The distribution of this angle in both phases is shown in Fig. 6.18(c). In this plot the mirroring of the distribution between phase is visible.

**Significance of the third eigenvector:** To test the hypothesis that v3 contains information, one can measure the relative magnitude of the second and third eigenvalues. The transverse anisotropy TA of a tensor can be defined as the ratio between the two last eigenvalues $TA = e_3/e_2$. If the mode of this ratio is close to unity, it would suggest that there is no information given by the third eigenvector direction. TA was extracted at each voxel of the datasets described in 6.4.1.

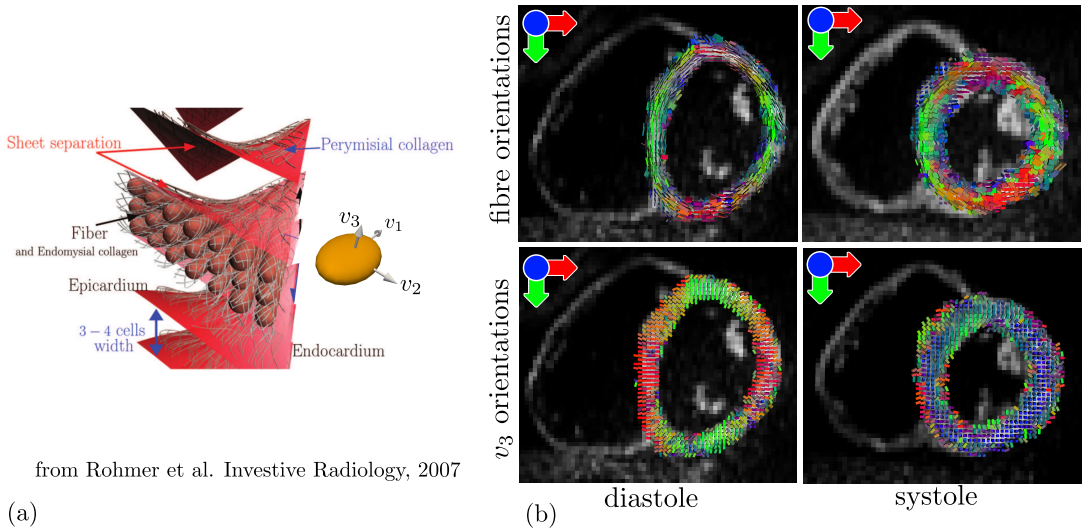


**Figure 6.17:** *(a) Schematics of the cardiac fibre architecture organized in laminae surfaces (b) Example of maps of the observed third eigenvector $v_3$ in diastole and systole.*

Its distribution in each phase was compared against the one computed from randomly distributed second and third eigenvalues. Let us first assume the hypothesis that there is no information contained by this direction. To materialize that hypothesis, two random variables $x_1$ and $x_2$ having similar Gaussian distributions are considered, and the random variable of the ratio $r = min(x_1, x_2)/max(x_1, x_2)$ is constructed. Under the "no information" hypothesis, TA would therefore have a distribution close to the one of $r$. Figure 6.18(d) presents the distribution of such random variable $r$ for normal distributions of mean $\mu = 0.7$ and standard deviation $\sigma = 0.2$ (thin line). The distribution of real transverse anisotropies TA for both phases are shown respectively in plain bold and dotted bold lines. Both distribution are significantly away from random ((p⟨0.0001)), therefore rejecting the "no information" hypothesis, and confirming the assumption that the information given by the third eigenvector direction is significant. The distributions show a noticeable difference between phases, suggesting, similarly to Fig. 6.12, that the tensors are more planar in diastole than in systole.

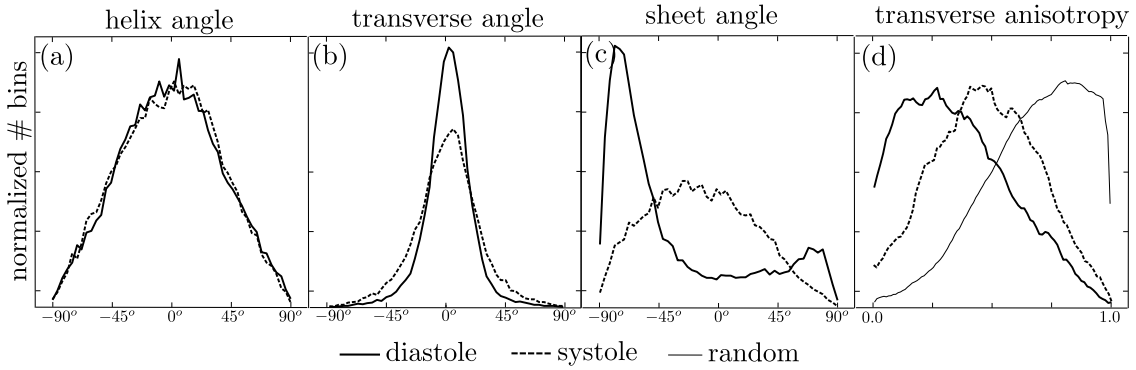


**Figure 6.18:** *(a,b,c) Distribution of the helix, transverse and sheet angle in diastole and systole from gathered in-vivo data. (d) Histogram of transverse anisotropy TA in both phases compared with the one of randomly distributed eigenvalues (thin line).*

**Plane tracking for laminae visualisation**: The $v_3$ maps shown in Fig. 6.17 (bottom) suggest a non-random arrangement of cleavage planes. In diastole, the

laminae are predominantly organized parallel to the wall surface, a visual confirmation of the histogram in Fig. 6.9 (top right). On the other hand, the organization seems more complex in systole.

To depict the 3D arrangement of these cleavage planes observed in systole, we propose to examine the corresponding dense approximated tensor field. Similarly to the concept of fibre tracking, it is hypothesised that one can spatially track, or span the laminae plane surface. From a starting position, it is assumed that the local laminae surface corresponds to the plane $(e_1, e_2)$ of the two first eigenvectors. To span the surface, one can track the laminar sheet from both $e_1$ and $e_2$ directions with a certain propagation rule. As described in 4.2.4, the fibre tractography algorithm used here has an advection-diffusion combined propagation (Eq. 4.9). We propose the following propagation for the sheet surface tracking:

$$v_{out} = c_p e_3 \times [e_3 \times v_{in}] + (1 - c_p)\big((1 - g)v_{in} + gD \cdot v_{in}\big) \tag{6.4}$$

where $e_3$ and $c_p$ are respectively the third eigenvector and the planar coefficient of $D$. The operator $\times$ is the cross product between vectors. One can notice that the linear coefficient $c_l$ of Eq. 4.9 was replaced by the planar coefficient $c_p$. Thereby confidence in the local third eigenvector is correlated to the planarity of the local tensor. The local direction $e_3 \times [e_3 \times v_{in}]$ can be seen as the normalized projection of $v_{in}$ onto the local tensor plane $(e_1, e_2)$.

To demonstrate the capabilities our plane tracking algorithm, it was applied to the *in-vivo* dense approximated tensor field in systole. Resulting tractograms are presented Fig. 6.19.

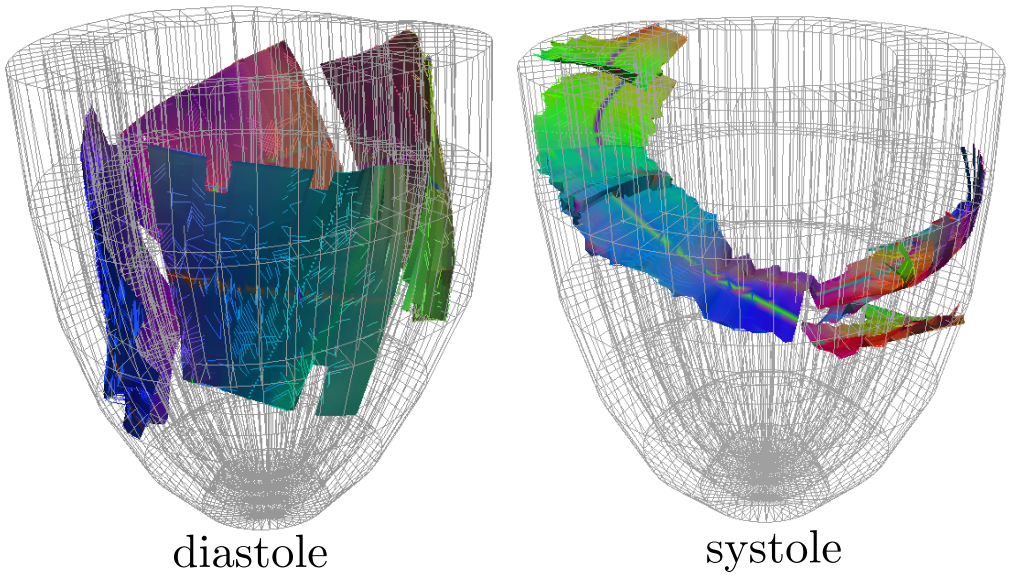


**Figure 6.19:** *Application of the surface tracking algorithm using propagation in Eq. 6.4 on the in-vivo approximated dense tensor field from $\mathcal{A}^{dia}_{STE}$ (left) and $\mathcal{A}^{sys}_{STE}$ (right).*

Previous histological studies [Spotnitz 1974, Costa 1999, LeGrice 1995] on the laminae organization and dynamics suggest that the sheet planes are changing orientation during the cardiac cycle. Specifically, [Spotnitz 1974] reports sheets parallel to the wall when the wall is the thinnest and going toward parallel to the short axis when the wall thickens (Fig. 2 in [Spotnitz 1974]). As illustrated in Fig. 6.17, our findings confirm this histological report by suggesting that laminae are organized

parallel to the myocardial wall in diastole and that, during contraction and wall thickening, the laminae spread to a more complex organization ("chevron pattern", as observed in [Costa 1999]) where the sheet planes tend to become parallel to the short axis plane in the mid-wall area (Figures 6.18 and 6.19). Furthermore, TA distributions in Figure 6.18(d) confirm the assumption that the information given by the third eigenvector is significant (p-value $<$ 0.001). The graphs also indicate a change of distribution between phases, suggesting that the tensors are more planar in diastole than in systole. This characteristic may be explained by fibre cell shortening and diameter increase during contraction, thereby allowing more diffusion perpendicular to the fibre direction. Additionally, Fig. 6.18(a,b,c) suggest that, as opposed to the sheet orientation, the fibre orientation does not change significantly between phase. In conclusion, this work represents to our knowledge the first report on laminae structure dynamics from in-vivo DT-MRI.

## 6.6 Discussions

### 6.6.1 Acquisition Limitations

Assessing *in-vivo* 3D DTI information on a beating heart is still a challenging task. The acquisition techniques used in our experiments remain difficult to reproduce and demand relatively long scanning time in a clinical setting. Breathing motion and position mismatch induce misalignments between DWIs. In this experiment, only the in-plane translation is corrected, and higher order distortions have not been addressed.

It is still unclear what is the optimal amount of directions to used. In [Frindel 2007], the authors benchmarked a number of combinations between number of directions and number of repetition against the quality of DTI images in *ex-vivo* hearts, and found that 12 directions with 4 repetitions would give optimal results, while other more general studies such as [Hasan 2001] suggest 6 directions. In a beating heart situation, the signal to noise ratio of DWI acquisitions is significantly lower than in the brain or in explanted organs, require higher number of both directions and repetitions. It became clear from these experiments that the Stimulated Echo (STEAM) acquisition protocol is giving more reproducible results than the Spin Echo (SE) one. However, the latter is easier to transfer to clinical practice as it does not require a large number of breath holds. Very recently, an *in-vivo* study reports a free-breathing version of the STEAM protocol [Nielles-Vallespin 2012], opening the gates of clinical translation of this protocol.

### 6.6.2 Dual-Phase Fibre Organization

The findings reported in this chapter reveal an *in-vivo* helix angle of $\Delta\alpha$ 97 and 99 deg. respectively in diastole and systole. These results, as well as their correlation with the transmural depth, concur significantly with previous *ex-vivo* studies [Greenbaum 1981, Peyrat 2006, Lombaert 2012]. The change of orientation between phases remain controversial. In [Chen 2005] they report ranges $\Delta\alpha$ of 96 deg. in diastole and 108 deg. in systole, but both with standard deviations of $\pm$10 deg. The range reported here therefore agrees with [Chen 2005]. However, we did not find significantly different $\Delta\alpha$ between phases. The local AHA segment analysis reveal similar patterns of helix angles in all 17 regions (with a more erratic behaviour

at the apex) in both phases. Based on these results, one can argue that there is no significant discrepancy of the helical fibre orientation throughout the ventricle and throughout the cardiac cycle, or none that could be detected with the current state of beating heart DTI acquisition. The *in-vivo* fibre tractography results reported here are in good correlation with *ex-vivo* studies, especially in [Peyrat 2009] and [Lombaert 2012].

A significant change of the Fractional Anisotropy of the tissue was found between phases. A mode of the FA at 0.69 was observed in diastole against 0.56 in systole, however with a relatively high p-value of 0.09. This difference can be physiologically explained by the tissue density being greater in diastole than systole, therefore decreasing the inter-cellular medium volume. In both phases the planar coefficient shows a relatively high mode at 0.36. In this chapter it was demonstrated that the ordering of the last two eigenvalues show significant difference with random behaviour, demonstrating that the third eigenvector direction contains meaningful information. A drastic difference was found in the organization patterns of the sheet angle $\gamma$ between diastole and systole, which is confirmed visually with third eigenvector maps. However it is our belief that there is no strong physiological justification of a strong structural change of the laminae organization during the cardiac cycle. Nevertheless, this chapter has shown laminae surface tracking results observed in systole, using a new propagation rule. These laminae planes have a similar appearance with the *ex-vivo* ones reported in [Rohmer 2007].

However, it is important to put these discrepancies in perspective with the limits of the acquisition. Especially, the motion involved during the systolic acquisition window can potentially influence the observed tensor shape, and might also explain the difference in sheet organization and structure variability reported in this chapter.

## 6.7 Conclusions

In this chapter the theoretical contributions of this thesis were put in practice with *in-vivo* experimental study. DTI data in both diastolic and systolic phases was acquired in a set of 5 healthy volunteers, and used the curvilinear analysis approach introduced in Chap. 3 to conduct a group-wise analysis of the fibre structure of the healthy left ventricular myocardium. These findings reveal little change of the helix and transverse angles during the cardiac cycle, with boundary values concurring with previously reported studies on *ex-vivo* hearts. The dense approximation scheme detailed in Chap. 4 was then applied. The resulting fibre tracts demonstrate a clear double helical fibre structure. Additionally, arguable differences were observed in the sheet organization and in the variability of the tensor shape between phases.

In conclusion, these results, together with some other recent *in-vivo* studies, bring the field of beating heart DTI acquisition to the rank of a feasible application, and can lead to a better understanding of the underlying structure of the heart - i.e. the arrangement of myocardial fibres - and its relationship with the cardiac function.

# Chapter 7
# Conclusions

## Contents



This thesis has shown that DTI provides the ability to image myocardial tissue in a non-invasive manner. In particular, the orientation of myofibres within the ventricle wall can be depicted *in-vivo* during the cardiac cycle. Coupled with advanced image processing and analysis techniques, this provides a tool to help apprehending the global fibre structure of the myocardium, and by extension understanding cardiac function. Additionally, it could help surgery planning and cardiac modelling of pathological situations.

Our goal throughout this thesis has been to show how advanced tensor/image processing, tensor field approximation, and data analysis, could overcome some limitations of *in-vivo* cardiac DTI acquisition. In the next section, the main contributions of this PhD thesis will be reviewed and perspectives for further research directions extending this work will be presented.

## 7.1 Contributions

### Methodological Contributions

One of the main contribution of this PhD is the integration of the curvilinearity of the object of interest in the statistical study and in the approximation process. Chapter 3 has shown that using an elastic and non-rigid registration algorithm, and changing coordinates towards a normalized prolate spheroidal frame, allows the description of left ventricular information in a physiologically relevant manner, and provides a continuous and adapted scheme for data analysis and processing. Additionally, a description of the variability of a set of tensors on arbitrarily distributed grid has been provided, with the computation of the structure matrix of such a set in PS coordinates. The advantages of these approaches have been demonstrated by applying them to *ex-vivo* canine hearts. The proposed method was evaluated with regard to its sensitivity to parameters. In particular, it was found to be robust to error accumulation, both position and directional error accumulation are found not significant.

Chapter 4 pushes the use of this curvilinear approach one step further by introducing a dense tensor field approximation scheme in PS coordinates. It was shown that approximation from sparsely distributed data centres is more optimally performed when it is applied in the PS frame rather than on a regular Cartesian frame. The fidelity of the introduced approach was demonstrated with the help of a

high-resolution *ex-vivo* human heart DTI dataset. This technique was shown to be particularly helpful when the data is very sparsely distributed across the ventricle. In this situation, it was illustrated that using the approximation operator in the PS frame helps recovering the full ventricular fibre architecture with low error on the local fibre orientations.

It is important to notice that the space occupied by the ventricular wall is highly non convex when viewed in a Cartesian frame. However, in the PS frame, the same volume becomes contained in a convex rectangular box. The Riemannian metric induced by redefining the approximation problem in PS coordinates becomes *geodesically convex* which is a very desirable property in such interpolation process.

Additionally, the influence of acquisition parameters on the final fibre tractography results has been investigated in Chapter 5. A method allowing the comparison of fibre fields without point correspondence was proposed. It was applied to an *ex-vivo* heart DTI acquisition and robustness to through-plane resolution and acquisition plane orientation was quantified.

## Contributions in Terms of Applications

The manuscript concludes with Chapter 6, where the methodologies introduced in this thesis were applied to *in-vivo* situations. In this chapter, it has been shown that human *in-vivo* cardiac DTI is possible in a reasonable acquisition time. Each short axis slice is acquired in 10 minutes, either using a modified version of the velocity compensated sequence introduced [Gamper 2007], or using an extension of the STEAM sequence as presented in [Dou 2002]. These sequences have been successfully applied to two small groups of 5 healthy volunteers each. Using the curvilinear data analysis approach, it was shown that the fibre orientations depicted by such techniques correlate with similar studies on *ex-vivo* hearts [Greenbaum 1981, Peyrat 2006, Lombaert 2012]. The findings reported here suggest that there is a significant change of Fractional Anisotropy and planar coefficient between diastole and systole. However, results reported in this thesis suggest no significant discrepancies in terms of fibre orientations between phases in a healthy situation.

By using the proposed curvilinear approximation scheme, the global fibre architecture of the healthy left ventricle *in-vivo* was reconstructed at end systole and end diastole. The resulting global arrangement of fibres is in good agreement with patterns found in *ex-vivo* specimen. To our knowledge it is the first reconstruction of the global fibre structure in healthy human left ventricle in different phases of the cardiac cycle.

## Software Contributions

In biomedical imaging in general, it is important that the methodological contributions are ensured to be re-usable in a sustainable manner. It has been an important aspect of this PhD to implement all the processing steps into a compact c++ set of commands. As detailed in App. D, they are gathered in a cross-platform c++ toolkit, from which the algorithms described in this thesis are available for further use. Additionally, a publicly available git repository [1] was released. This toolkit

[1] https://github.com/ntoussaint/Cardiac-Prolate-Spheroidal-ToolKit

is intended to be integrated in a innovative medical imaging platform called med-Inria 2.x (http://med.inria.fr), and is already used in external projects within the Asclepios research team at Inria Sophia Antipolis.

## 7.2 Perspectives

### Theoretical Perspectives

Adapting the coordinate system to the shape of the studied object, as presented in Chapter 3, can potentially be much more generalized. The PS coordinates are part of the set of 11 coordinate systems that are well-defined in the sense that the Laplace equation can be solved with separating variables. A generalization of the concepts described in Chapter 3 would consist of finding, out of these 11 coordinate systems, the most suitable one to describe an object of interest in a compact manner. Another approach that could be interesting to investigate would be to become independent from any coordinate system by only considering topological information, where only the curvature of the object will dictate the local metric tensor to use. This type of curvature-based approach is sometimes used in computer vision, such as in-painting [Chan 2001], although in our case we refer to topological curvature rather than scalar curvature within an image.

As mentioned in Chapter 3, an interesting development would be to extend the tensor variability in the spatial domain introduced here, to the variability in the tensor domain by computing the quantity tensor domain structure matrix. This measure could provide information on the mode of variations of a local set of tensors, such as within an AHA zone for instance, and be a adapted candidate for prior knowledge to incorporate into the localised approximation scheme described in 4.5.

Concerning the dense approximation scheme described in Chapter 4, it is clear that the (non-)control over the smoothing effect can be overcome by some further development of the technique. For instance, as mentioned in the conclusion of this Chapter, one might benefit from using the local variability of the tensor field as a prior for the kernel's bandwidth in the approximation scheme. Alternatively, [Pajevic 2002] suggests a multi-channel approximation scheme based on B-spline approach in each of the 6 independent components of the tensor. It may be possible to extend their concepts to our particular problem that is an arbitrarily distributed measure centres.

### Impact on Cardiac Modelling

As mentioned throughout the thesis, one of the potential application of *in-vivo* cardiac DTI is its use in patient specific electromechanical modelling of the cardiac function. It is still unclear how much the fibre orientations infer the model behaviour. For instance, it has been suggested that the fibre orientations can be taken from a synthetic model without biasing the mechanical or electrophysiological outcome of the model [Bovendeerd 1992, Niederer 2009]. However, in other studies the opposite conclusion has also been found [Wong 2010], where the authors suggest that a cardiac mechanical model is significantly sensitive to fibre orientations.

The answer to this difficult question might be found when, additionally to the cardiac mechanics and electrical activity, fibre orientations are imaged *in-vivo* using the work presented in this thesis. It would then be possible to perform simulations

using different sets of model parameters and compare to ground truth motion and conductivity patterns in order to quantify the impact of the fibre orientations on the accuracy of the modelling.

## DTI Information in Scar Area

Finally, an important development of this work is the translation to the understanding of the cardiac function dynamics after myocardial infarction. It has been shown *in-vivo* that the fibre structural arrangement is changing drastically in and around the infarct zone [Wu 2009]. These studies suggest that myocardial infarction is followed by an increase in ADC and a decrease in FA in the scar zone. They have been limited to a single short axis DTI slice. It could be of interest to extend the acquisition to a larger portion of the ventricle and, using the approaches described in this thesis, quantify the global remodelling [Chen 2003] of the myocytes within the left ventricle.

From the work and results presented in this PhD thesis, it is clear that *in-vivo* cardiac DTI, combined with adapted image processing and analysis methods such as those introduced here, will open the door for improved diagnosis and understanding of cardiac pathologies. It will allow personalised patient cardiac electromechanical modelling, could improve the prediction of patient response to certain treatment such as cardiac resynchronisation therapy and participate to the improvement of the understanding of the left ventricular structure and function.

Appendix A

# Inversion of the Prolate Spheroidal Transformation

We use the trigonometric and hyperbolic identities:

$$\cos^2 + \sin^2 = 1 \text{ and } \cosh^2 - \sinh^2 = 1$$

If we take the following notations from Eq. 3.1:

$$A = f^2 \qquad B = {x_1}^2 + {x_2}^2$$
$$C = {x_3}^2 \qquad \alpha = \sin^2(\xi_2)$$

then, using first and second definitions from Eq. 3.1, and the trigonometric identity, we obtain:

$$B = A \sinh^2(\xi_1)\alpha \tag{A.1}$$

$\sinh^2(\xi_1)$ is a function of $\alpha$, $A$, and $C$ using the third definition from Eq. 3.1 and the hyperbolic identity, which finally gives us a polynomial in $\alpha$:

$$A\alpha^2 + (-A + B + C)\alpha - B = 0$$

Of the two roots of this polynomial, one is positive and one is negative. Since $\alpha$ is a positive number by definition, only one root needs consideration:

$$\sin^2(\xi_2) = \frac{(A - B - C) + \sqrt{(A - B - C)^2 + 4AB}}{2A}$$

Since $\xi_2$ is an angle from 0 to $\pi$, $\sin(\xi_2)$ is always positive, therefore we can extract $\xi_2$. $\xi_1$ is also a positive number, thus we can extract it from Eq. A.1 when $\sin^2(\xi_2) \neq 0$ (everywhere but on the axis of revolution). When $\sin^2(\xi_2) = 0$, we can use $\sinh^2(\xi_1) = C/A - 1$, which holds true everywhere on the axis apart between foci, where Prolate Spheroidal coordinates are undefined. Note that this singularity can be noticed directly from the third line of Eq. 3.1 and by remembering that $\cosh(*) \geq 1$. In practice this singularity is never reached as it is always outside the ventricle wall. We can nevertheless extend the definition domain by its limit close to the axis of revolution, i.e. imposing $\xi_1 = 0$ in the segment between foci.

Finally, $\xi_3$ is simply obtained by dividing the second with the first line of Eq. 3.1: $\xi_3 = \arctan(x_2/x_1)$. If the point is on the axis of revolution, $\xi_3$ can take all allowed values. We use $\xi_3 = 0$ by convention.

Appendix B

# Contravariant Basis Vectors

The prolate spheroidal contravariant basis $\mathcal{G} = (g_1, g_2, g_3)$, defines the differential vectors for each of the coordinates: $g_i = \partial x / \partial \xi_i$.

$$
\begin{aligned}
g_1 &= f \begin{pmatrix} \cosh(\xi_1)\sin(\xi_2)\cos(\xi_3) \\ \cosh(\xi_1)\sin(\xi_2)\sin(\xi_3) \\ \sinh(\xi_1)\cos(\xi_2) \end{pmatrix} \\
g_2 &= f \begin{pmatrix} \sinh(\xi_1)\cos(\xi_2)\cos(\xi_3) \\ \sinh(\xi_1)\cos(\xi_2)\sin(\xi_3) \\ -\cosh(\xi_1)\sin(\xi_2) \end{pmatrix} \\
g_3 &= f \begin{pmatrix} -\sinh(\xi_1)\sin(\xi_2)\sin(\xi_3) \\ \sinh(\xi_1)\sin(\xi_2)\cos(\xi_3) \\ 0 \end{pmatrix}
\end{aligned} \tag{B.1}
$$

The basis $\mathcal{G}$ is direct and orthogonal, but not orthonormal. The norm of each column vector is also known as the local scale factor: $\|g_i\| = h_i$.

The calculation of the scale factors and the contravariant basis is involved in the "Finite Strain" reorientation for the induced transformation $\tilde{\Psi}$.

Appendix C

# The Cardiac Prolate Spheroidal ToolKit

Early in this project, it became necessary to build a sustainable implementation of the workflow, especially of the steps detailed in Chap. 3. The Insight ToolKit [Ibanez 2005] appeared to be a good choice of a c++ library to start with for such an implementation, for its parallelization capabilities and the features it offers. Therefore, throughout the PhD project, each data processing step of the workflow has been implemented on top of this library. We gathered all implemented features in a stand-alone toolkit, named the Cardiac Prolate Spheroidal ToolKit (CPSTK), and released the plain c++ code in a git repository [1].

The first and principal component of this toolkit is the `itk::ProlateSpheroidalTransform` class. It derives from an `itk::Transform` and is templated over the pixel precision. It corresponds exactly to the implementation of the $\Psi$ operator, as defined in Sec. 3.2. The transformation is defined with the 3D position Cartesian coordinates of three landmarks. That is, first the centre of basal section O (i.e. the origin of the coordinate system), second the apex A (OA is therefore the ellipsoid main axis length) and the mid-wall basal point B taken at the intersection between the LV and the RV, at the anterior wall region. (O,A,B) entirely define the coordinate system change. Especially, the eccentricity $\varepsilon$ and the semi foci distance $f$ are evaluated from those coordinates. The coordinate change can be "Forward" - from Cartesian towards prolate spheroidal coordinates $\Psi$ - or "Backward" - from prolate spheroidal towards Cartesian coordinates $\Psi^{-1}$. The user is invited to control the direction of the operator with `SetForward()` method. By definition, the inverse of the Forward transformation is the related Backward transformation. Therefore, accessing `GetInverse()` has the same effect as using the same transform but changing direction to "Backward". In the class member `ParametersType m_Parameters`, we naturally store the coordinates of O,A, and B. The method `GetJacobian()` is not implemented as it expects the Jacobian with respect to each of the transform's parameters, which is not defined. However, we provide the local Jacobian matrix with respect *to the coordinates* with the method `GetJacobianWithRespectToCoordinates()`, which, in this case, corresponds to the contravariant basis matrix $\mathcal{G}$, as well as access methods to the scale local factors $h_i$ and the Jacobian determinant $\Pi h_i$. The class therefore allows the user to switch back and forth between Cartesian and prolate spheroidal coordinates using the classical methods `TransformPoint()` and `TransformVector()`.

The entire toolkit is built around this class. We provide a certain number of `itk` filters that achieve specific tasks, such as the intersection of a data structure with a specific AHA zone, a.k.a. `itk::LimitToAHAZoneImageFilter`, which uses a `itk::ProlateSpheroidalTransform` as parameter in order to perform the intersection. Another important key filter of the toolkit is the

[1] http://github.com/ntoussaint/Cardiac-Prolate-Spheroidal-ToolKit/

`itk::GaussianInterpolationTensorMeshFilter(2)`. These classes are a concrete implementation of the approximation and local approximation operators $\mathcal{W}_P$ and $\mathcal{W}'_P$ as defined in Chap. 4. The input of this filter is an *unstructured* mesh with tensor information at each node, that is, our raw data $P = (x_i, D_{x_i})_{i=1:M}$. One of the most high level filter is the class `itk::ExtrapolateTensorField`, that concatenates other filters to provide an implementation of the global dense approximation of a tensor field in the prolate spheroidal frame. It expects the set of data centres $P$ for input, as well as the domain of definition $\Omega$ (in the form of a binary image), the non-linear displacement fields $\Phi$ and $\Phi^{-1}$, the prolate spheroidal transform that corresponds to the operator $\Psi$, and the kernel sizes $K_H^z$. We gather in Table C.1 a non exhaustive list of classes contained in the toolkit.

| Class Name | Description |
|---|---|
| `itk::ProlateSpheroidalTransform` | Transformation class from Cartesian coordinates to PS Coordinates |
| `itk::KaiserBesselKernelFunction` | Kaiser Bessel kernel used for density estimation and non-parametric regression |
| `itk::LimitToAHAZoneImageFilter` | Crop a (tensor)image with an AHA zone |
| `itk::ExtrapolateTensorField` | Dense Approximation filter |
| `itk::TensorMeshStatistics` | Compute tensor statistics in the PS frame |
| `itk::GaussianInterpolationTensor...` | Implements the approximation operator $\mathcal{W}_P$ |
| `itk::WarpTensorMeshFilter` | Warp a tensor mesh with a displacement field (FS strategy) |
| `itk::TensorMeshIO` | Read/Write tensors embedded in a (unstructured) mesh |
| `itk::TensorMeshToImageFilter` | switch between unstructured mesh and regular grid representation of tensors |

**Table C.1:** *Main classes of the* **CPSTK** *toolkit and their description.*

For an easy access to the user, we embed the main features into a single binary, named `cpstk`, utilizing a system of `Command`/`Factory` combination. Through command-line, the user can therefore easily process each step of the work-flow detailed in this thesis. In Fig C.1 we show the output of the help message of the `cpstk` binary. It details all features and provides a short description of them. Each line represents a call to the corresponding `Command` that implements the actual feature.

All filters derived from `itk::ImageToImageFilter` and therefore take advantage of their *multi-thread* implementation. Additionally, we extended the *multi-threading* concepts to `itk::MeshToMeshFilter` filters. Indeed, if an operation has to be computed on each node of the mesh, and does not depend on the result of this operation on other nodes, then one could consider using parallel computing to perform the task separately in each node. In our work-flow, one of the most computationally expensive task is the dense approximation, as it is an $N \times M$ operation, where $N$ is the number cardinality of our measures $P$, and $M$ the cardinality of the domain $\Omega$. The parallel implementation of `itk::GaussianInterpolationTensorMeshFilter`

```
johndoe@localadmin-laptop> ptk --help
Software Prolate Spheroidal ToolKit (c)KCL 2012, version 1.1.0

Author: Nicolas Toussaint (nicolas.toussaint@kcl.ac.uk)

King's College London freely grants the non-exclusive right to use the Software for RESEARCH
PURPOSES ONLY. Every user of the Software will communicate to the author
(nicolas.toussaint@kcl.ac.uk) their remarks as to the use of the Software.

Available commands:
        aha-image       ::      Crop an image to an AHA zone in the Prolate Spheroidal sense
        aha-tensors     ::      Crop a a tensor image/mesh to an AHA zone in the Prolate Spheroidal sense
        apply-image     ::      Apply a rigid transformation to an image without resampling
        apply-mesh      ::      Apply an affine transformation to a vtk mesh
        apply-tensors   ::      Apply a rigid transformation to a tensor image without resampling
        atlas           ::      Create an tensor atlas from a set of tensors in prolate coordinates
        domain          ::      Create an ellipsoidal domain image out of a prolate sph. transform
        extract         ::      Extract meaningful information in prolate spheroidal coordinates
        extrapolate     ::      Tensor Field Dense Approximation from Sparse Data
        find            ::      Find a prolate spheroid approximating an LV segmentation mesh
        image2mesh      ::      Converts a tensor image into a tensor mesh structure
        itk2vtk         ::      Convert a tensor image (or a list of tensor images) into a vtkUnstructuredGrid structure
        mesh2image      ::      Converts a tensor mesh structure into a tensor image
        res-image       ::      Resample a 3D image to a reference field-of-view
        res-tensors     ::      Resample a 3D tensor image to a reference field-of-view
        rotate          ::      Rotate a Prolate Spheroid according to a vtk file describing the antero-posterior line
        stats           ::      Compute statistics in prolate sph. coordinates over a set of tensors
        synthesize      ::      Create a synthetic tensor map out of some cardiac LV fibre structure information


johndoe@localadmin-laptop> ptk extract

Extract meaningful information in prolate spheroidal coordinates

Usage:
-i    [input tensor image (default : input.vtk)]
-pr   [prolate transform used]
-f1   [forward displacement field (default : forward.mha)]
-f2   [backward displacement field (default : backward.mha)]
-o    [output csv file where cost function values are stored (default: output.csv)]
-s    [sheet-angle distribution instead of elevation (default 0)]
```

**Figure C.1:** *Screen shot of the* CPSTK *command-line tool. The help message lists the available* Commands. *The commands are stand-alone and handled through a system of factory registration. Each command comes with a usage message.*

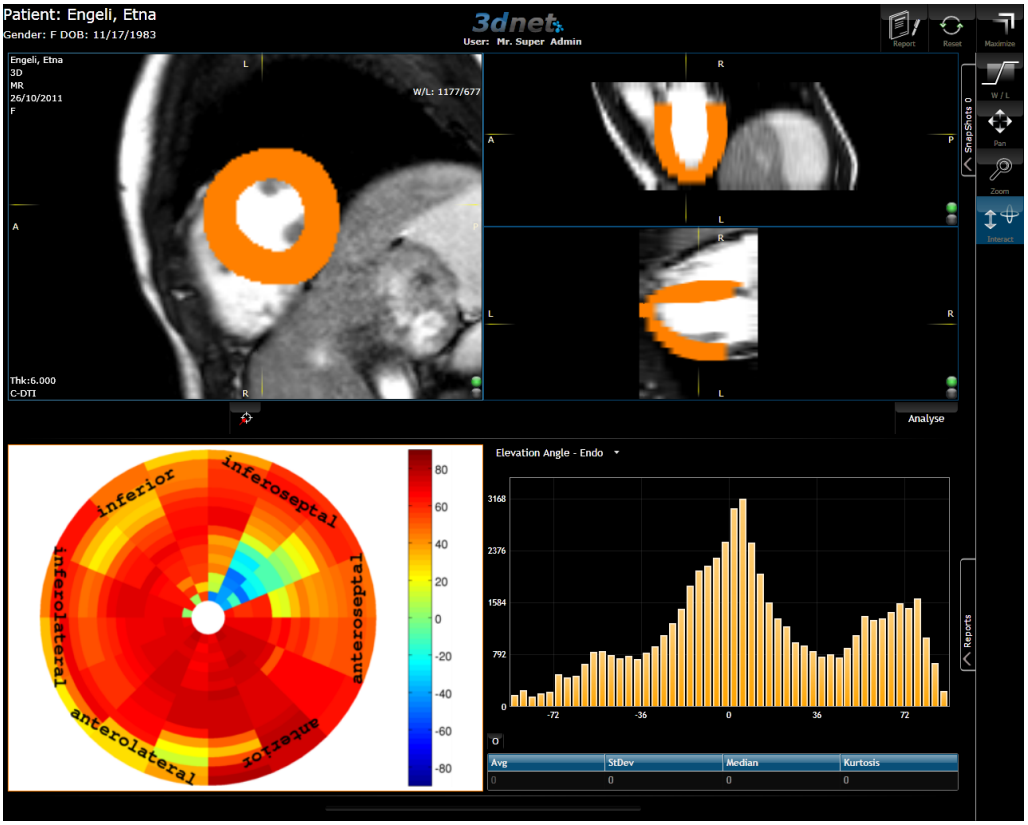


**Figure C.2:** *Screen shot of the prototype built for the 3D-Net platform, showing the volunteer's anatomy image, the left ventricle segmentation, a bull's eye graph of the $\beta$ angle distribution, and its corresponding histogram.*

and `itk::GaussianInterpolationTensorMeshFilter2` allows an acceleration factor equal to the number of threads of the computer. For example, the dense approx-

imation of a dataset with $N = 19000$ measure centre, and $M = 64000$ for $\Omega$, takes 49.5 seconds on a dual core computer. Another computationally expensive task is the evaluation of the structure tensors, as detailed in Sec. 3.6.3. The results shown in this section concern a DTI tensor unstructured field of N=35000 nodes, and the structure tensors are evaluated on the same grid (i.e. $M = N$). The computational cost of the gradient operator is $N^2$, but there is a linear regression of size $N \times 6$ to solve at each node. The total computational time is for instance 1 minute 3 seconds on a 12 core computer, for the dataset described above.

CPSTK is open-source, and only depends on ITK, VTK and the Tensor Toolkit [2], and is therefore straightforward to set up. It compiles under any platform, especially Windows, MacOSX, Ubuntu and other unix systems. There is a Doxygen documentation available [3]. It is planned to be used in the MedINRIA platform [4] for cardiac analysis purposes. We also embedded part of the analysis features provided by the toolkit in a prototype for the 3D-Net platform [5]. It aims at deploying the capabilities of the toolkit to a wild range of clinical and researcher users. We show in Fig. C.2 an early version of this prototype.

[2] www.gforge.inria.fr/projects/ttk

[3] http://ntoussaint.github.com/Cardiac-Prolate-Spheroidal-ToolKit/Doxygen

[4] www.med.inria.fr

[5] http://www.3dnetmedical.com

Appendix D

# *In-Vivo* Tractography Results

In Chapter 6, *in-vivo* measurements of DTI data on 5 healthy volunteers using the STEAM sequence were presented. DTI was performed at end systole and end diastole phases. The dense approximation scheme (see Chap. 4) was used to reconstruct the 3D dense tensor field for each volunteer (and in both phases). Fibre tractography was then performed on these approximated tensor fields. The results are presented in the following figure. Fibres are color coded with the local helix angle.

The variation of helix angle between epicardial and endocardial regions is clear in all datasets for both phases. We notice a net increase of the angle around the septum (left on the images). Although in some cases angle differences are visible between phases, it is not clear whether or not those discrepancies are genuine or due to different noise patterns, or bias in the acquisition or even the image processing analysis.

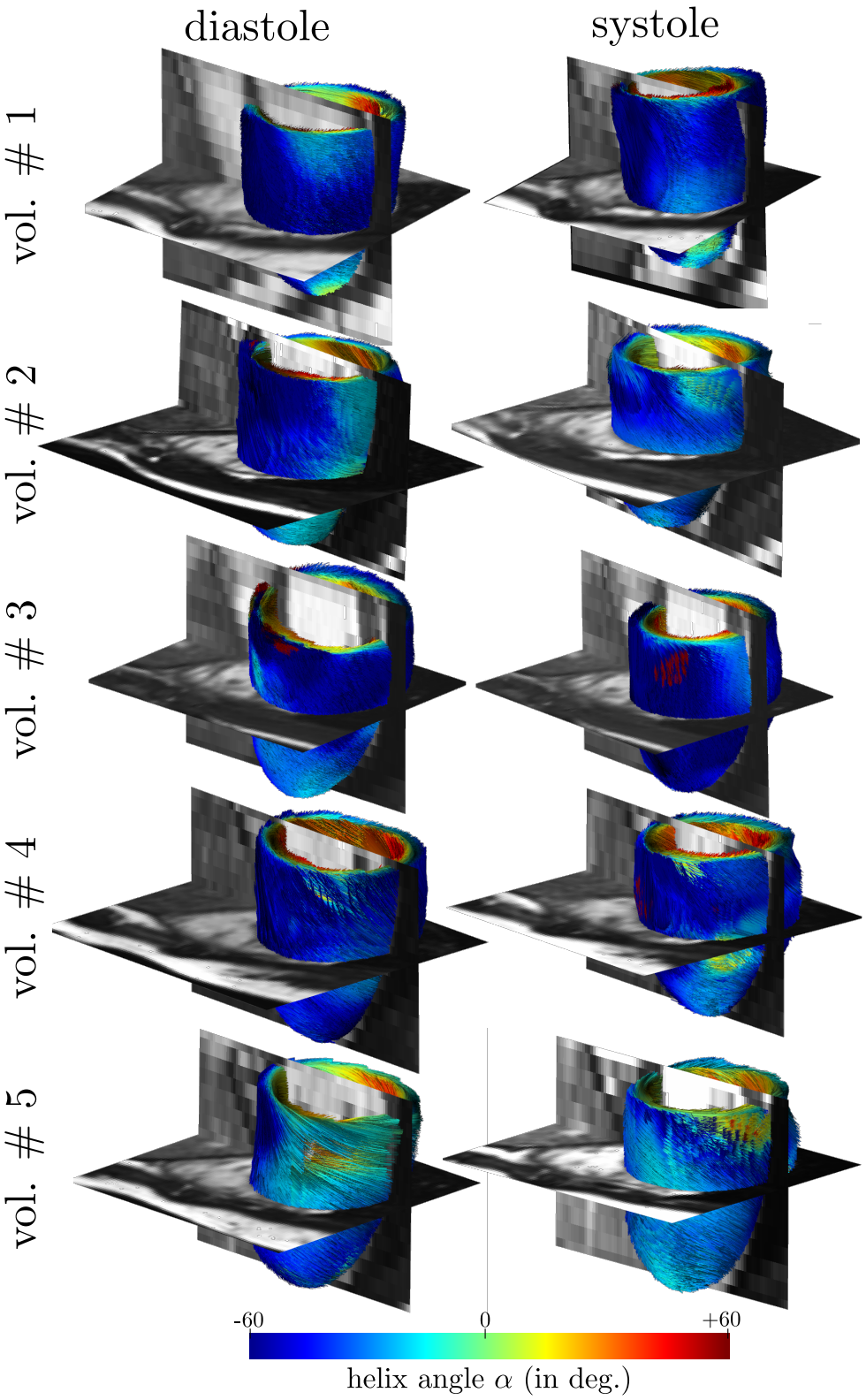


**Figure D.1:** *In-vivo fibre tractography of the left ventricle for 5 healthy volunteers (line-wise), at end diastole (left) and end systole (right). The fibres are color-coded with the local tensor's helix angle.*

Appendix E

# Dissimilarities of the Anterior Commissure using DTI

## Contents



An extensive use of the distance index introduced in Chapter 5 has been done in a collaborative work with P.G Batchelor, J.P. Linn, G.C. Edwards and M. Patel and was published in [Patel 2010]. The present chapter presents the main results found in this study.

## E.1 Introduction

The anterior commissure is a critical interhemispheric pathway in animals, yet its connections in humans are not clearly understood. Its distribution has shown to vary greatly between species, and it is thought that in humans it may convey axons from a larger territory than previously thought. The aim of this study was to use anatomical mapping methods to observe the anterior commissure fibre tracts and compare their distribution, against previously reported anatomical understanding.

The cerebral hemispheres are interconnected by the corpus callosum (CC) and the anterior, posterior and hippocampal commissures. The largest of these connections is the CC spanning across the length of the cerebral hemispheres, providing the majority of interhemispheric information transfer. In those who have complete sections of the CC, it has been shown that motor, language, cognitive and behavioural functions can remain unaffected [Spencer 1988, Berlucchi 1995]. This suggests alter native routes play a part, and in particular the anterior commissure (AC), as seen in Fig. E.1, has been shown to provide many interhemispheric routes for information [Risse 1978]. Investigating these connections of the AC may be important in the understanding of epileptic spread between the hemispheres, since both the CC and the hippocampal commissure have been shown to be critical in the contralateral spread of electrical potentials [Spencer 1988]. Limiting seizure spread in those with uncontrolled epilepsy is possible by sectioning the commissural fibres and has shown to prevent an unconscious state during seizures [Spencer 1988, Amacher 1976]. It is common to leave the AC intact during surgical procedures for epilepsy, and it may

be possible for epileptic potentials to travel through this pathway, inducing bilateral spread [Spencer 1988]. The mid-sagittal cross-sectional area of the AC has been shown to be 1% of the CC area, and variations in the area are thought to represent the distribution of interhemispheric communication [Foxman 1986]. Hypertrophy of the AC especially in congenital agenesis of the CC may be due to re-routing of some neuronal axons for better functional compensation [Fischer 1992, Bamiou 2007]. An increase in the total number of axons passing through the AC without hypertrophy has also been observed in acallosal mice, suggesting it can be used as an alternative pathway for information transfer [Livy 1997]. Distribution of the AC to various parts of the brain in animals has been shown to vary greatly between species [Horel 1981, Pandya 1973].

For species that do not possess a CC, the AC is the largest and most critical interhemispheric pathway, carrying the CC-related functions [Bamiou 2007, Pandya 1973]. Relatively less work has looked at the human AC, and until recently it was presumed that the commissure has connections similar to non-human primates, but is now thought to convey axons from a much larger territory [Di Virgilio 1999]. The AC in humans is classically divided into two distinct tracts, the anterior and posterior limbs. The anterior limb connects to the olfactory bulbs, their nuclei and the inferior-posterior orbital gyri and is thought to be a minor component of the AC fibre tracts [Di Virgilio 1999, Barr 1974]. It is thought that phylogenetically as the functions of the olfactory complex regress, connections of the AC appear to shift to neocortical regions in the temporal lobes, to which the corpus callosum does not project [Pandya 1973, Fox 1948, KAROL 1971]. The posterior limb travels within the basal part of the striatum and into the temporal cortex towards the amygdala [Turner 1979], temporal pole [Demeter 1990], parahippocampal, inferior temporal and fusiform gyri [Di Virgilio 1999, Jacobson 2008, Demeter 1990]. Additional afferent from the occipital cortex, precentral gyrus and central fissure have been described through the posterior limb [Di Virgilio 1999]. Studies in humans looking at the fibres passing through the AC have mostly involved dissections of the brain, followed by staining and tracing. However, with recent advances in MRI neuroimaging techniques tractography from DTI data enables the construction of pathways of high water diffusion that are associated with white matter fibre tracts in the brain, thereby allowing visualisation and investigation of connections between different brain regions, in vivo and noninvasively. This can be used to better comprehend the fibre connections through the AC. DTI uses a set of diffusion-weighted MR images acquired in at least six directions to enable estimation of the diffusion tensor in each voxel. Tractography algorithms, such as streamlines, can then display the path of the principle direction of diffusion in anisotropic tissue until termination in areas of low anisotropy. Large anisotropic diffusion is observed in white matter, where molecular motion is greater parallel to the myelinated axonal fibres rather than perpendicular to them [Bihan 2001]. Fibres reconstructed, therefore, represent paths of the most probable direction of molecular diffusion, hence along the axonal fibres. DTI has shown distribution of the AC fibres to the amygdala and temporal pole as well as the ventrolateral temporo-occipital cortex [Jellison 2004, Catani 2002, Catani 2005], supporting Di Virgilio et al. [Di Virgilio 1999] who illustrated through dissection that the AC receives axons from the inferior occipital cortex in man and that these connections are not present in macaque [Rockland 1986]. This study aims to use DTI-based tractography with an anatomical mapping tool to look at the AC fibres and to compare the distribution

findings with published anatomical understanding.

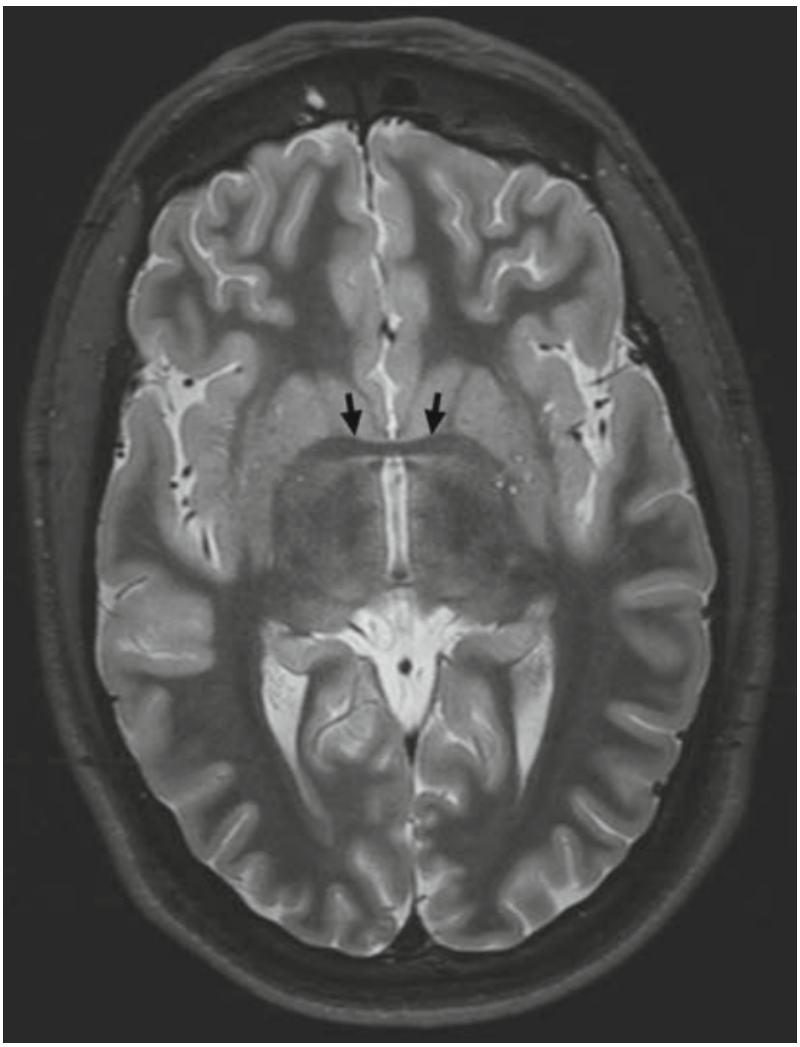

**Figure E.1: Anterior commissure:** *Inversion recovery sequence image of an axial slice at the level of the anterior commissure, highlighting its connection between both hemispheres*

## E.2 Subjects and image acquisition

Data were acquired from eight healthy subjects using a Philips Achieva 3T MRI system with an eight-channel head coil. Two DTI data sets were acquired from each subject with b-values of 0, $1000 s/mm^2$ and 0, $1500 s/mm^2$ , respectively. Echoplanar imaging with a simple Stejskal-Tanner sequence was used with a TR/TE of 10, 313/55 and 18750/50.5 ms, respectively, with acquisition times of 7 min 38 s and 12 min 58 s. A lower TE was used with a b-value of $1500 s/mm^2$ to compensate for the reduced signal-to-noise ratio at this higher diffusion weighting. Other acquisition parameters were $2 \times 2 \times 2$ mm voxels, 60 slices, FOV = 224 mm, matrix size = $112 \times 112$, partial Fourier = 0.678, SENSE factor = 2 and 32 diffusion-encoding directions. This was repeated on a separate occasion with three of the subjects using identical acquisition parameters in order to assess reproducibility.

Conventional T2-weighted volumes were acquired for anatomical localisation of the fibre tracts in each subject with a TR/TE of 3,000/80 ms and voxel size of $0.449 \times 0.449 \times 4$ mm. STIR (short TI inversion recovery) images with a TR/TE/TI of 4,811/9.1/200 ms, voxel size of $0.449 \times 0.449 \times 2$ mm and slice spacing of 2 mm were also acquired in the sagittal plane from each subject to produce images for optimum visualisation of the AC for size measurements and region of interest selection.

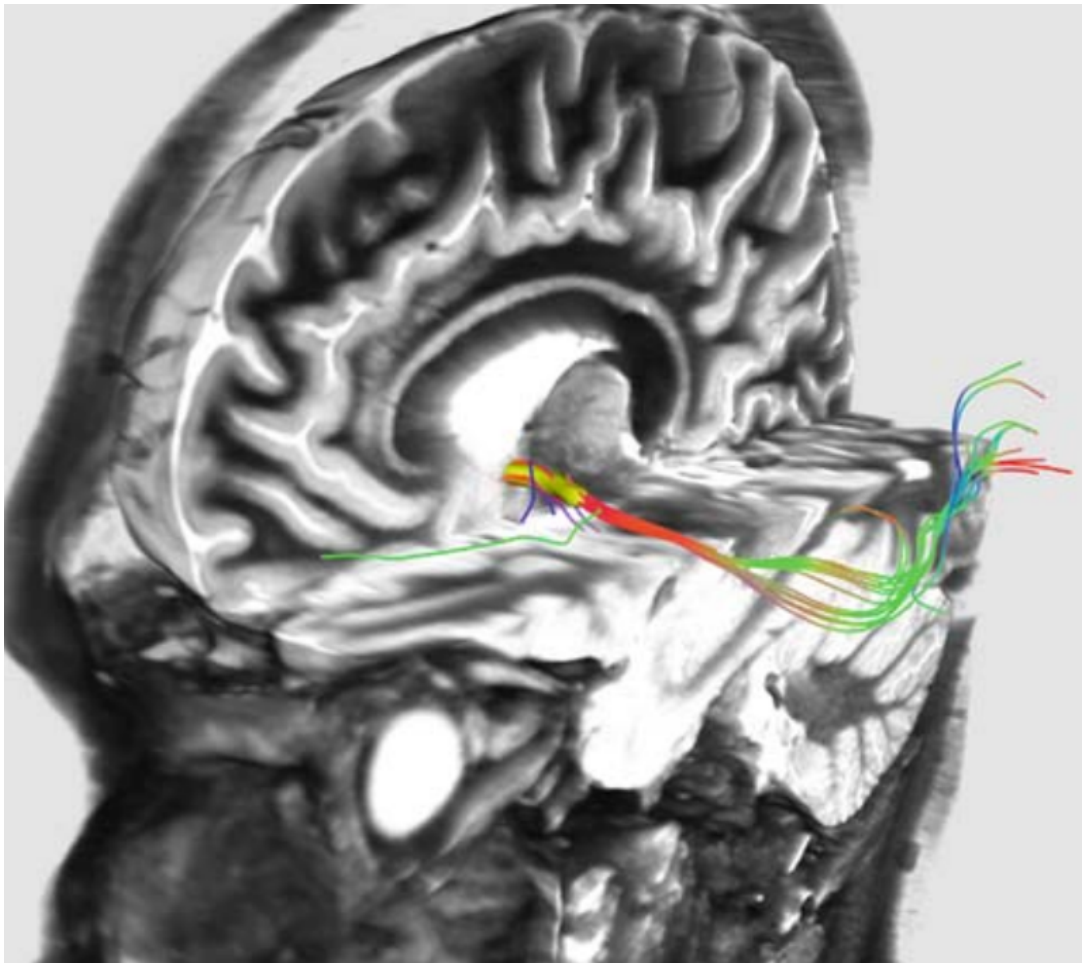

**Figure E.2:** *Image showing the anterior commissure fibres from a single subject projected onto the three-dimensional T2-weighted volume, for assessing distribution of the tracts*

## E.3 Data processing

The STIR data sets were registered with the b=0 volume from the DTI data using rigid manual landmark-based methods in MedINRIA ImageFusion [Toussaint 2007] to produce transformation matrices. Points that were clearly visible on both images were selected, including along the border of the AC and edges of the globus pallidus and lateral ventricles. Tensor estimation and fibre tracking was performed for each of the data sets in MedINRIA DTI Track [Toussaint 2007] using the standard streamline approach for tractography [Fillard 2003, Xu 2002], in which every

voxel of the data set was used as a seed point. The algorithm introduced a stabilisation "advection" vector to minimise fluctuations introduced by low anisotropy regions (especially planar tensors) [Weinstein 1999]. The parameter controlling the smoothness of the tracking process is a factor between 0 and 1. A weighting factor of 0.20 was chosen as advised by [Weinstein 1999] which affects "how much the propagation should be encouraged to puncture through planar tensor areas". In this framework, this parameter replaces an angle threshold used in the basic streamline approach. The anisotropy threshold was set to 0.3. All fibres were generated prior to the region of interest selection, using every valid voxel of the data set, where every voxel containing a positive tensor with a fractional anisotropy greater than or equal to 0.3 as seed point.

These fibre fields were then transformed using the previously acquired matrices, and the STIR images were used to pro- duce two three-dimensional regions of interest either side of the AC, by manually drawing around the AC on up to three sagittal slices either side of the midline. After this, only fibres passing through both AC regions of interest from one hemisphere to the other were retained. In total, there were AC fibre tracts from 22 unique data sets. Six of these data sets from three subjects were unus- able as no interhemispheric fibre connections through the AC were produced on tractography. The AC fibre data for each of the remaining five subjects were then manually registered with each other using rigid landmark-based registration to ensure the AC was not translated across subjects. A Procrustes algorithm is used by MedINRIA ImageFusion to perform this registration [Fitzpatrick 2001]. Initially, several landmarks distant from the AC were used, such as the tips of the lateral ventricles, edges of the globus pallidus and vertex of the brain for correcting obvious misorientation. Landmarks were then focussed around the AC for more subtle alignments, including the most inferior-posterior point in the AC as well as recognisable neuroanatomical features such as the inferior border of septum pellucidum, the anterior border of the fornix and the inferior portion of the corpus callosum. It was then possible to produce a combined map of the total AC fibres across the five subjects. The T2-weighted volumes were also registered with the b=0 volume using rigid manual landmark-based methods. The AC fibre bundles were visualised on the T2-weighted volumes, as seen in Fig. 2, along with the STIR volumes to assess distribution of the fibres.

## E.4 Reproducibility of tractography

The fibres tracked through the AC from the different diffusion-weighted and repeat acquisitions are shown in Fig. E.3 for the five subjects. Although the distribution of the major fibre bundles appear similar when scans are repeated, the number of fibres does vary, especially when the diffusion weighting is increased. The number of fibres passing through the AC, its crosssectional area in the midline and its relation to the CC size are shown in Fig E.4, omitting the subjects in whom tractography was unsuccessful. Using linear regression, a good correlation was found between the AC mid-sagittal cross-sectional area and the number of fibres passing through it at a b-value of 1,000 $s/mm^2$ , although there was greater variation of fibre numbers at a b-value of 1,500 $s/mm^2$ .

Fibre tracking revealed large differences in the distribution of AC fibres across subjects. Tractography from subject 1, as seen in Fig. E.3, showed a large proportion

of fibres in the posterior limb of the AC travelling bilaterally above the hippocampus into the parietal lobe, especially into the inferior parietal lobule where the majority terminated. Another bundle carried on further to the superior parietal lobule and postcentral gyrus, with a smaller bundle to the precentral gyrus. The other portion of the posterior limb entered the temporal lobe towards the amygdala, but much more so on the right than left side. There was no anterior limb of the AC visible. Although there was a wide distribution of fibres from the AC through the posterior limb, the fibre field similarity maps showed a large Hilbert distance projected onto the parietal lobe fibres and fibres crossing the corpus callosum and a small Hilbert distance in the main trunk of the posterior limbs, as shown in Fig. E.5.

Tractography from subject 2 showed posterior limb fibres travelling into the occipital lobe bilaterally, with a larger number on the left. There were also temporal lobe fibres through this limb, with a large number on the right. The anterior limb contained fibres towards the orbitofrontal cortex bilaterally. Fibre field similarity maps showed a large Hilbert distance in the left temporal lobe, where there were fewer fibres than on the right and a relatively small Hilbert distance in the anterior limbs. Tractography from subject 3 showed a very small number of fibres compared to the other subjects, although the majority of these made up the anterior limb bilaterally towards the orbitofrontal cortex. The posterior limb showed small numbers of fibres into the occipital lobe and the temporal lobe bilaterally. Fibre field similarity maps showed a large Hilbert distance in the occipital lobes and a relatively small Hilbert distance in the body of the AC. Tractography from subject 4 showed bundles travelling into the parietal and temporal lobes bilaterally. The anterior limb fibres towards the orbitofrontal cortex were also present on the right. Fibre field similarity maps showed a large Hilbert distance in the anterior limb and body of the AC. Tractography from subject 5 showed the posterior limb fibres to the occipital lobe and temporal lobe mostly on the right, as well as the anterior limb fibres for a short distance bilaterally towards the orbitofrontal cortex. Fibre field similarity maps showed a large Hilbert distance in the right posterior limb and relatively low Hilbert distance in the body of the AC.

## E.5 Discussion

Using tractography the fibres passing through the AC for five of the subjects were isolated, fibre distributions were determined, and the fibre field similarity for each subject was calculated. The distribution of fibres through the AC was shown in all subjects to pass via the posterior limb to the temporal lobe and either the occipital or parietal lobes. The temporal lobe connections of the AC fibres to the amygdala and temporal pole were seen in the majority of subjects, as described in the literature [Turner 1979, Demeter 1990, Jacobson 2008, Johnston 2008]. The parietal lobe fibres were seen in two of the five subjects, and occipital lobe fibres in the remaining three subjects. This is in line with results from the dissection study by Di Virgilio et al. [Di Virgilio 1999], which showed connections to the occipital cortex, central fissure and precentral gyrus, as well as DTI studies showing fibres from the AC extending to the ventrolateral occipital cortex [Jellison 2004]. The anterior limb which extends towards the orbitofrontal cortex after passing through the AC was visible to some extent bilaterally in four of the five volunteers and has been described in the literature [Barr 1974]. This data is consistent with observations

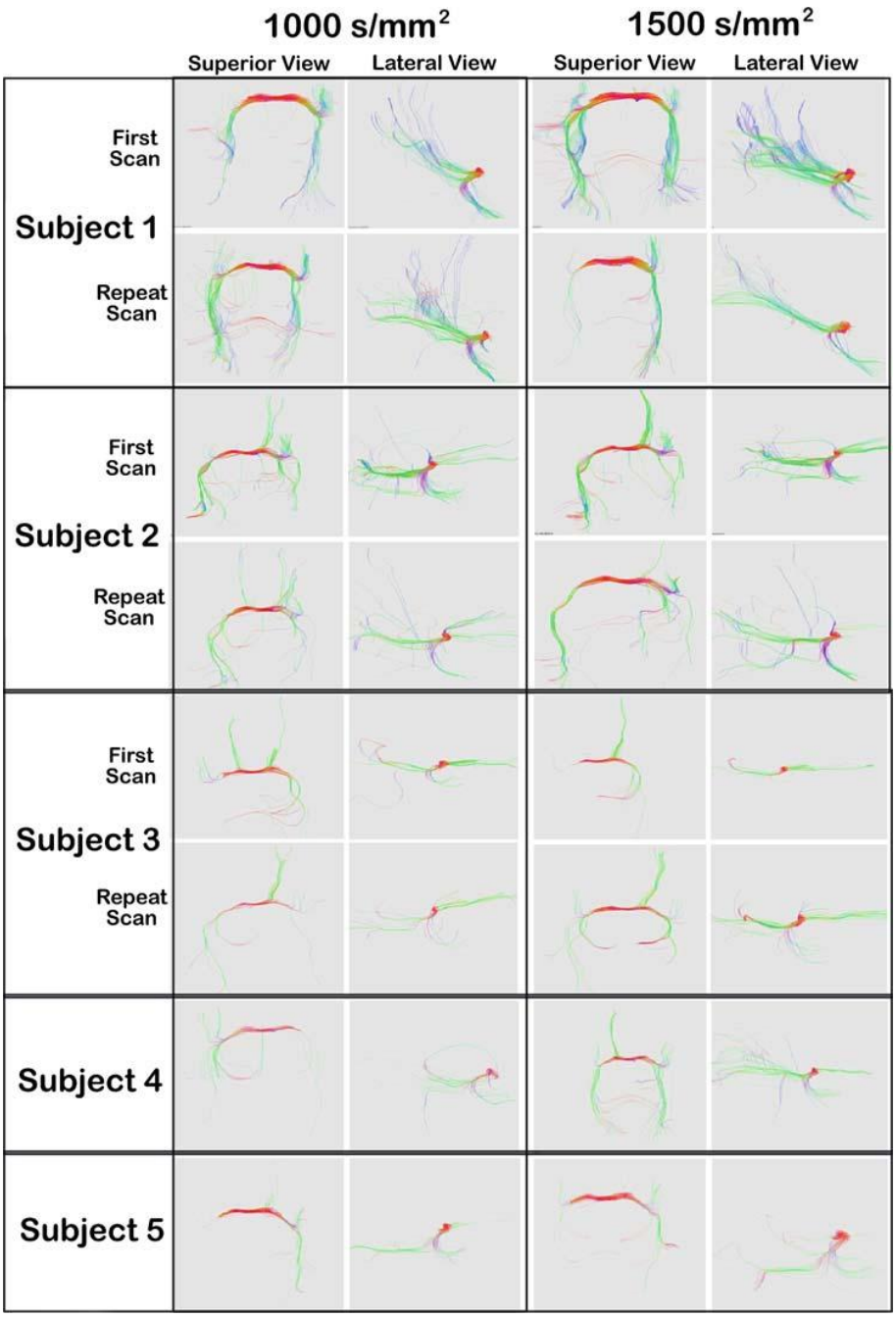


**Figure E.3:** *Fibres tracked through the AC in the five subjects, with differences between diffusion weightings and the first and repeat scans. The two views shown are the superior and right lateral views of the fibres.*

from Di Virgilio et al. [Di Virgilio 1999], suggesting that axons to the AC may be conveyed from a larger territory than previously proposed, specifically from parts of the occipital cortex and various parts of the parietal lobe. This may be due to connections of the AC shifting phylogenetically to neocortical areas where the corpus callosum does not project [Pandya 1973, Fox 1948, KAROL 1971].

As shown in E.4, the CC area varied between 54 and 299 times the AC cross-sectional area; hence, the AC being 0.3-1.8% of the CC area. This supports the

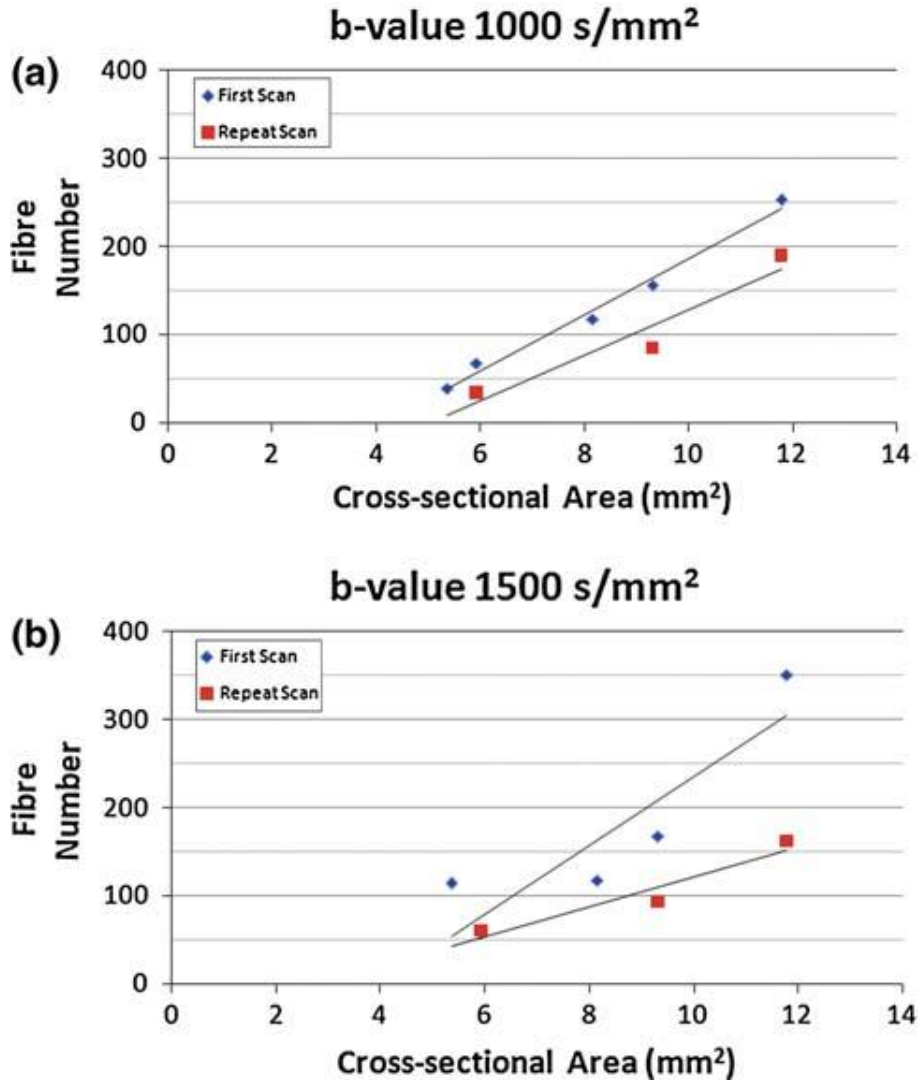


**Figure E.4:** *Graphs showing the relationship between the anterior commissure mid-sagittal cross-sectional area and the number of fibres tracked through it for a the acquisitions at* $1000s/mm^2$ *and b acquisitions at* $1500s/mm^2$.

study by Foxman et al. [Foxman 1986] that the AC area is about 1% of the CC cross-sectional area. It has been suggested that a larger commissural area would have more nerve fibres crossing between the hemispheres, and consequently those cognitive functions that rely on only one hemisphere are more likely to be shared, and therefore less dependent on that one hemisphere [Kimura 1999]. The correlation between AC fibre number and cross-sectional area was as expected and shown not be a result of postprocessing techniques. A b-value of 0, 1,000 $s/mm^2$ is typically the standard value used for clinical DWI [Mukherjee 2008]. As the b-value increases, the signal intensity decreases as the contributions of T1 and T2 weighting decrease, leading to a reduced signal-to-noise ratio as DWI signals are closer to the background noise level [Jones 2004a], but having an increased diffusion sensitivity [Mori 2006, Meyer 2000]. This may explain why the repeat scans with a b-value of 1,000 $s/mm^2$ were more consistent than at 1,500 $s/mm^2$ . Due to the higher level of background

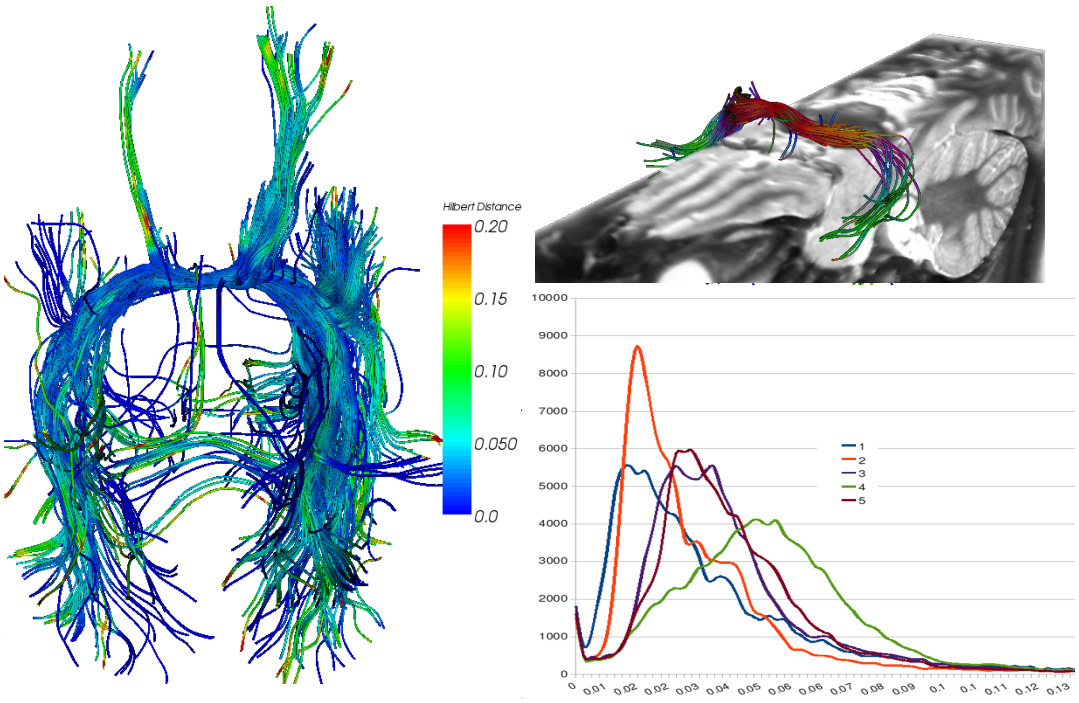


**Figure E.5:** *Image showing the fibre field similarity map produced for subject 1 from a superior view of the brain. The fibres are colour labelled with the Hilbert distance, a measure of the local distance between each subjects' fibre tracts and the combined map. The histogram represents the Hilbert norms for each of the subjects 1-5.*

noise, there was much greater variation when scans were repeated, and consequently the number of fibres passing through the AC also varied considerably. At a b-value of 1,500 $s/mm^2$ , there will have been greater diffusion sensitivity and consequently better estimation of fibre direction where nerve fibres cross, and so it may suggest the general increase in fibre numbers when compared with a b-value of 1,000 $s/mm^2$ . One observation noted was that out of the eight subjects, there were five in which results were obtained, and the remaining three subjects' data sets could not be used due to a lack of AC fibres passing from one hemisphere to the other. As seen in Fig. E.4, two of those subjects had AC cross-sectional areas of below 2 $mm^2$ , which were consider- ably smaller than the subjects in which tractography through the AC was successful. The last subject had an AC cross-sectional area of 7.04 $mm^2$ which is in the middle of the successful range of areas, yet there were still no fibres produced on tractography. Fibres were produced in the structures surrounding the AC, such as the fornix, yet none passed through the AC itself.

The fibre field similarity measure provided a novel approach to calculation and visualisation of the distance between bundles for a particular region of interest, using fibre data between subjects. This technique can aid in the segmentation of white matter bundles within the brain, by identifying the extent to which fibres are anatomically distant from the population map. Fibres that appear to have a large Hilbert distance may be classed as outlying fibres which do not lie close to the overall population fibre bundles. This along with other fibre characteristics such as curvature and torsion appears to have applications for looking at normal versus abnormal

fibre tracts for example in the presence of a tumour [Batchelor 2006]. Although the fibre field similarity measures and maps are very useful, there were limitations in this study as comparing across subjects meant that any large anatomical differences between the subjects would affect the fibre field similarity calculations, causing a larger Hilbert distance to be displayed if for example the brain size was significantly different to the population.

There are also several limitations when using DTI to look specifically at fibres through the AC. Since microscopic information is averaged over the volume of the voxel, in areas where anatomically large fibre tracts come close to smaller fibre bundles, a proportion of fibres closest to the larger tracts appear to follow incongruent paths indicative of falsely reconstructed fibre paths. This could be the case with the posterior limb of the AC, as anatomically the axons pass posteriorly before turning anteriorly into the temporal lobe. Lying close to this bundle is the inferior longitudinal fasciculus and fronto-occipital fasciculus, which transverse the entire length of the brain and enter the temporal and occipital lobes, respectively [Catani 2008]. Since these pass fairly close to the AC axons, it may be possible that with DTI several fasciculi fibres are picked up erroneously as AC fibres to the occipital lobe. Anatomical differences of crossing white matter tracts between subjects may explain the inter-subject variation of AC distribution as seen in Fig. E.3, as it causes premature termination of the streamlines at various points along the AC fibres. Intra-subject comparisons of the AC fibres shows fairly similar tracts, although these differences may be explained by changes in the magnetic field inhomogeneities due to the time difference between the first and repeat scans. Ways to overcome the effects due to crossing fibres would be to first improve the imaging resolution, for example by using fast spin-echo DTI which allows sub-millimetre voxel sizes, and also means that multiple voxels can characterise the smaller anterior commissures in subjects [Gui 2008]. Secondly, other methods apart from conventional streamline tractography can be used, such as high angular resolution diffusion imaging (HARDI) and Q-ball imaging (QBI), which allow better reconstruction in areas with crossing fibres [Dong 2004, Alexander 2007]. It is at present difficult to trust the connectivity maps of the AC, but these methods may help define the normal anatomy of the AC which is still under question from past dissection studies and recent DTI work. They may also help overcome the unsuccessful AC tractography in the last subject from Fig E.4, where the problem may be related to the angle at which the AC and the fornix are related. The fornix branches off the AC just prior to the AC crossing from one hemisphere to the other. If the angle of the white matter tract is steeper within the AC than the fornix, it may be possible that the fibres reconstructed represent those of only the fornix. Therefore, HARDI and QBI would be more appropriate and allow a more reliable reconstruction of the AC fibre tracts, hence giving a better understanding of the posterior limb connections of the AC, and how the AC cross-sectional area relates to distribution.

## E.6 Conclusion

This DTI study has shown that the AC may play a more important role in inter-hemispheric communication than currently presumed by conveying axons from a wider territory, specifically from the occipital cortex and parietal lobes. This may be clinically relevant in the spread of electrical potentials from one hemisphere to

the other in patients with epilepsy. The study has also looked at the reproducibility of the AC fibre tracts using DTI, confirming the previously recognised temporal and orbitofrontal projections, and given a novel approach to quantifying and visualising characteristics of these fibre tracts through fibre field similarity measures and maps. However, further work with improved technical and processing methods is required to more accurately characterise these AC fibres and its normal anatomy.

# Bibliography


[Alexander 2000] Andrew L. Alexander, Khader Hasan, Gordon Kindlmann, Dennis L. Parker and Jay S. Tsuruda. *A geometric analysis of diffusion tensor measurements of the human brain.* Magnetic Resonance in Medicine, vol. 44, no. 2, pages 283–291, 2000. (Cited on page 15.)

[Alexander 2001] D.C. Alexander, C. Pierpaoli, P.J. Basser and J.C. Gee. *Spatial transformations of diffusion tensor magnetic resonance images.* Medical Imaging, IEEE Transactions on, vol. 20, no. 11, pages 1131 –1139, nov. 2001. (Cited on page 29.)

[Alexander 2002] D.C. Alexander, G.J. Barker and S.R. Arridge. *Detection and modeling of non-Gaussian apparent diffusion coefficient profiles in human brain data.* Magnetic Resonance in Medicine, vol. 48, no. 2, pages 331–340, 2002. (Cited on pages 10, 12 and 15.)

[Alexander 2007] Andrew L. Alexander, Jee Eun Lee, Mariana Lazar and Aaron S. Field. *Diffusion Tensor Imaging of the Brain.* Neurotherapeutics, vol. 4, no. 3, pages 316 – 329, 2007. (Cited on page 110.)

[Amacher 1976] A. L. Amacher. *Midline commissurotomy for the treatment of some cases of intractable epilepsy. Preliminary report.* Child's Brain, vol. 2, no. 1, pages 54 – 58, 1976. (Cited on page 101.)

[Andersson 2002] Jesper L.R. Andersson and Stefan Skare. *A Model-Based Method for Retrospective Correction of Geometric Distortions in Diffusion-Weighted EPI.* NeuroImage, vol. 16, no. 1, pages 177 – 199, 2002. (Cited on page 72.)

[Arsigny 2006] Vincent Arsigny, Pierre Fillard, Xavier Pennec and Nicholas Ayache. *Log-Euclidean metrics for fast and simple calculus on diffusion tensors.* Magn Reson Med, vol. 56, no. 2, pages 411–421, Aug 2006. (Cited on pages 14, 46 and 49.)

[Arts 2001] T. Arts, K. D. Costa, J. W. Covell and A. D. McCulloch. *Relating myocardial laminar architecture to shear strain and muscle fiber orientation.* American Journal of Physiology - Heart and Circulatory Physiology, vol. 280, no. 5, pages H2222–H2229, 2001. (Cited on page 82.)

[Bamiou 2007] Doris-Eva Bamiou, Sanjay Sisodiya, Frank E. Musiek and Linda M. Luxon. *The role of the interhemispheric pathway in hearing.* Brain Research Reviews, vol. 56, no. 1, pages 170 – 182, 2007. (Cited on page 102.)

[Barr 1974] Murray L. Barr. The human nervous system: An anatomical viewpoint. (2nd ed). Harper and Row, 1974. (Cited on pages 102 and 106.)

[Basser 1994] P. Basser, J. Mattiello and D. Le Bihan. *MR diffusion tensor spectroscopy and imaging.* Biophysical Journal, vol. 66, pages 259–267, 1994. (Cited on page 12.)

[Basser 1996] P.J. Basser and C. Pierpaoli. *Microstructural and Physiological Features of Tissues Elucidated by Quantitative-Diffusion-Tensor MRI.* Journal of Magnetic Resonance in Medicine, vol. 111, pages 209–219, 1996. (Cited on pages 3, 12 and 15.)

[Basser 2000] P.J. Basser, S. Pajevic, C. Pierpaoli, J. Duda and A. Aldroubi. *In vivo fiber tractography using DT-MRI data.* Magnetic Resonance in Medicine, vol. 44, pages 625–632, 2000. (Cited on pages 50 and 61.)

[Basser 2007] Peter J. Basser and Sinisa Pajevic. *Spectral decomposition of a 4th-order covariance tensor: Applications to diffusion tensor MRI.* Signal Processing, vol. 87, no. 2, pages 220 – 236, 2007. (Cited on page 36.)

[Batchelor 2005] P. G. Batchelor, M. Moakher, D. Atkinson, F. Calamante and A. Connelly. *A rigorous framework for diffusion tensor calculus.* Magnetic Resonance in Medicine, vol. 53, no. 1, pages 221–255, 2005. (Cited on pages 13 and 14.)

[Batchelor 2006] P. G. Batchelor, F. Calamante, J.-D. Tournier, D. Atkinson, D. L. G. Hill and A. Connelly. *Quantification of the shape of fiber tracts.* Magnetic Resonance in Medicine, vol. 55, no. 4, pages 894–903, 2006. (Cited on page 110.)

[Berlucchi 1995] G. Berlucchi, S. Aglioti, C.A. Marzi and G. Tassinari. *Corpus callosum and simple visuomotor integration.* Neuropsychologia, vol. 33, no. 8, pages 923 – 936, 1995. (Cited on page 101.)

[Bigun 1987] J. Bigun and G.H. Granlund. *Optimal orientation detection of linear symmetry.* In First International Conference on Computer Vision, ICCV (London), pages 433–438, 1987. (Cited on page 32.)

[Bihan 2001] D. Le Bihan, J.F. Mangin, C. Poupon, C. Clark, S. Pappata, N. Molko and H. Chabriat. *Diffusion Tensor Imaging : CConcepts and Applications.* Journal Of Magnetic Resonance Imaging, vol. 13, no. 4, pages 534–546, 2001. (Cited on page 102.)

[Bovendeerd 1992] P.H.M. Bovendeerd, T. Arts, J.M. Huyghe, D.H. van Campen and R.S. Reneman. *Dependence of local left ventricular wall mechanics on myocardial fiber orientation: A model study.* Journal of Biomechanics, vol. 25, no. 10, pages 1129 – 1140, 1992. (Cited on pages 2 and 91.)

[Bovendeerd 1994] P.H.M. Bovendeerd, J.M. Huyghe, T. Arts, D.H. van Campen and R.S. Reneman. *Influence of endocardial-epicardial crossover of muscle fibers on left ventricular wall mechanics.* Journal of Biomechanics, vol. 27, no. 7, pages 941 – 951, 1994. (Cited on page 2.)

[Brox 2003] Thomas Brox, Mikael Rousson, Rachid Deriche and Joachim Weickert. *Unsupervised Segmentation Incorporating Colour, Texture, and Motion.* Computer Analysis of Images and Patterns, pages 353–360, 2003. (Cited on page 13.)

[Catani 2002] Marco Catani, Robert J. Howard, Sinisa Pajevic and Derek K. Jones. *Virtual in Vivo Interactive Dissection of White Matter Fasciculi in the Human Brain.* NeuroImage, vol. 17, no. 1, pages 77 – 94, 2002. (Cited on page 102.)

[Catani 2005] Marco Catani and Dominic H. ffytche. *The rises and falls of disconnection syndromes.* Brain, vol. 128, no. 10, pages 2224–2239, October 2005. (Cited on page 102.)

[Catani 2008] Marco Catani and Michel Thiebaut de Schotten. *A diffusion tensor imaging tractography atlas for virtual in vivo dissections.* Cortex, vol. 44, no. 8, pages 1105 – 1132, 2008. (Cited on page 110.)

[Cerqueira 2002] Manuel D. Cerqueira, Neil J. Weissman, Vasken Dilsizian, Alice K. Jacobs, Sanjiv Kaul, Warren K. Laskey, Dudley J. Pennell, John A. Rumberger, Thomas Ryan and Mario S. Verani. *Standardized Myocardial Segmentation and Nomenclature for Tomographic Imaging of the Heart.* Circulation, vol. 105, no. 4, pages 539–542, 2002. (Cited on pages 24 and 56.)

[Chan 2001] Tony F. Chan and Jianhong Shen. *Nontexture Inpainting by Curvature-Driven Diffusions.* Journal of Visual Communication and Image Representation, vol. 12, no. 4, pages 436 – 449, 2001. (Cited on page 91.)

[Chen 2003] Junjie Chen, Sheng-Kwei Song, Wei Liu, Mark McLean, J. Stacy Allen, Jie Tan, Samuel A. Wickline and Xin Yu. *Remodeling of cardiac fiber structure after infarction in rats quantified with diffusion tensor MRI.* Journal of Heart Circulation and Physiology, vol. 285, pages 946–954, 2003. (Cited on pages 3, 80 and 92.)

[Chen 2005] Junjie Chen, Wei Liu, Huiying Zhang, Liz Lacy, Xiaoxia Yang, Sheng-Kwei Song, Samuel A. Wickline and Xin Yu. *Regional ventricular wall thickening reflects changes in cardiac fiber and sheet structure during contraction: quantification with diffusion tensor MRI.* American Journal of Physiology - Heart, vol. 289, no. 5, pages 1898–1907, 2005. (Cited on pages 76, 80 and 87.)

[Costa 1996] K D Costa, P J Hunter, J S Wayne, L K Waldman, J M Guccione and A D McCulloch. *A Three-Dimensional Finite Element Method for Large Elastic Deformations of Ventricular Myocardium: II - Prolate Spheroidal Coordinates.* J Biomech Eng, vol. 118, no. 4, pages 464–472, Nov 1996. (Cited on pages 23 and 24.)

[Costa 1999] K.D. Costa, Y. Takayama, A.D. McCulloch and J.W. Covell. *Laminar fiber architecture and three-dimensional systolic mechanics in canine ventricular myocardium.* American Journal of Physiology-Heart and Circulatory Physiology, vol. 276, no. 2, pages H595–H607, 1999. (Cited on pages 82, 86 and 87.)

[Demeter 1990] Steven Demeter, Douglas L. Rosene and Gary W. Van Hoesen. *Fields of origin and pathways of the interhemispheric commissures in the temporal lobe of macaques.* The Journal of Comparative Neurology, vol. 302, no. 1, pages 29–53, 1990. (Cited on pages 102 and 106.)

[Descoteaux 2007] Maxime Descoteaux, Elaine Angelino, Shaun Fitzgibbons and Rachid Deriche. *Regularized, fast, and robust analytical Q-ball imaging.* Magnetic Resonance in Medicine, vol. 58, no. 3, pages 497–510, 2007. (Cited on page 16.)

[Di Virgilio 1999] Gabrielle Di Virgilio, S. Clarke, Gianpaolo Pizzolato and Thomas Schaffner. *Cortical regions contributing to the anterior commissure in man.* Experimental Brain Research, vol. 124, pages 1–7, 1999. (Cited on pages 102, 106 and 107.)

[Dice 1945] Lee R. Dice. *Measures of the Amount of Ecologic Association Between Species.* Ecology, vol. 26, no. 3, pages pp. 297–302, 1945. (Cited on page 40.)

[Dierckx 2009] Hans Dierckx, Alan Benson, Stephen Gilbert, Michael Ries, Arun Holden, Henri Verschelde and Olivier Bernus. *Intravoxel Fibre Structure of the Left Ventricular Free Wall and Posterior Left-Right Ventricular Insertion Site in Canine Myocardium Using Q-Ball Imaging.* In Functional Imaging and Modeling of the Heart, volume 5528 of *Lecture Notes in Computer Science*, pages 495–504. Springer Berlin (Heidelberg), 2009. (Cited on page 21.)

[Dong 2004] Qian Dong, Robert C. Welsh, Thomas L. Chenevert, Ruth C. Carlos, Pia Maly-Sundgren, Diana M. Gomez-Hassan and Suresh K. Mukherji. *Clinical applications of diffusion tensor imaging.* Journal of Magnetic Resonance Imaging, vol. 19, no. 1, pages 6–18, 2004. (Cited on page 110.)

[Dou 2002] Jiangang Dou, Timothy G. Reese, Wen-Yih I. Tseng, and Van J. Wedeen. *Cardiac Diffusion MRI Without Motion Effects.* Magnetic Resonance in Medicine, vol. 48, pages 105–114, 2002. (Cited on pages 20 and 90.)

[Dou 2003] Jiangang Dou, Wen-Yih I. Tseng, Timothy G. Reese and Van J. Wedeen. *Combined Diffusion and Strain MRI Reveals Structure and Function of Human Myocardial Laminar Sheets In-Vivo.* Magnetic Resonance in Medicine, vol. 50, pages 107–113, 2003. (Cited on pages 19, 68, 71 and 75.)

[Dru 2009] Florence Dru and Tom Vercauteren. *An ITK Implementation of the Symmetric Log-Domain Diffeomorphic Demons Algorithm.* Insight Journal – 2009 January - June, May 2009. (Cited on page 27.)

[Durrleman 2008] Stanley Durrleman, Xavier Pennec, Alain Trouvé, Paul Thompson and Nicholas Ayache. *Inferring brain variability from diffeomorphic deformations of currents: an integrative approach.* Medical Image Analysis, vol. 12, no. 5, pages 626–637, 2008. PMID: 18658005. (Cited on page 62.)

[Edelman 1994] Rolbert R. Edelman, Jochen Gaa, Evan Loh Van J. Wedeen, Joshua M. Hare and Wei Li Pottumarthi Prasad. *In Vivo Measurement of Water Diffusion in the Human Heart.* Magnetic Resonance in Medicine, vol. 32, no. 3, pages 423 – 428, 1994. (Cited on pages 3 and 18.)

[Eggen 2012] Michael D. Eggen, Cory M. Swingen and Paul A. Iaizzo. *Ex vivo diffusion tensor MRI of human hearts: Relative effects of specimen decomposition.* Magnetic Resonance in Medicine, vol. 67, no. 6, pages 1703–1709, 2012. (Cited on pages 36 and 80.)

[Einstein 1905] Albert Einstein. *Über die von der molekularkinetischen Theorie der Wärme geforderte Bewegung von in ruhenden Flüsigkeiten suspendierten Teilchen.* Annalen der Physik, vol. 322, no. 8, pages 549 – 560, 1905. (Cited on page 9.)

[Fernandez-Teran 1982] M. A. Fernandez-Teran and J. M. Hurle. *Myocardial fiber architecture of the human heart ventricles.* The Anatomical Record, vol. 204, no. 2, pages 137–147, 1982. (Cited on pages 1, 2 and 38.)

[Fieno 2004] David S. Fieno, Hanns B. Hillenbrand, Wolfgang G. Rehwald, Kathleen R. Harris, Robert S. Decker, Michele A. Parker, Francis J. Klocke, Raymond J. Kim and Robert M. Judd. *Infarct Resorption, Compensatory Hypertrophy and Differing Patterns of Ventricular Remodeling Following Myocardial Infarctions of Varying Size.* Journal of American College of Cardiology, vol. 43, pages 2124–2131, 2004. (Cited on pages 2 and 3.)

[Fillard 2003] P. Fillard and G. Gerig. *Analysis Tool For Diffusion Tensor MR.* In MICCAI'03, volume 2 of *LNCS*, pages 979–980. Springer, November 2003. (Cited on pages 50 and 104.)

[Fillard 2005] Pierre Fillard, Vincent Arsigny, Xavier Pennec, Paul Thompson and Nicholas Ayache. *Extrapolation of Sparse Tensor Fields: Application to the Modeling of Brain Variability.* In Gary Christensen and Milan Sonka, editeurs, Information Processing in Medical Imaging, volume 3565 of *Lecture Notes in Computer Science*, pages 357–376. Springer Berlin / Heidelberg, 2005. (Cited on page 45.)

[Fillard 2007] Pierre Fillard, Vincent Arsigny, Xavier Pennec and Nicholas Ayache. *Clinical DT-MRI Estimation, Smoothing and Fiber Tracking with Log-Euclidean Metrics.* IEEE Transactions on Medical Imaging, vol. 26, no. 11, pages 1472–1482, 2007. (Cited on page 45.)

[Fillard 2011] Pierre Fillard, Maxime Descoteaux, Alvina Goh, Sylvain Gouttard, Ben Jeurissen, James Malcolm, Alonso Ramirez-Manzanares, Marco Reisert, Ken Sakaie, Fatima Tensaouti, Ting Yo, Jean-FranÃ§ois Mangin and Cyril Poupon. *Quantitative evaluation of 10 tractography algorithms on a realistic diffusion MR phantom.* NeuroImage, vol. 56, no. 1, pages 220 – 234, 2011. (Cited on pages 16, 61 and 62.)

[Fischer 1992] M. Fischer, S. B. Ryan and W.B. Dobyns. *Mechanisms of interhemispheric transfer and patterns of cognitive function in acallosal patients of normal intelligence.* Arch. Neruol., vol. 49, no. 3, pages 271–277, 1992. (Cited on page 102.)

[Fitzpatrick 2001] J.M. Fitzpatrick and J.B. West. *The distribution of target registration error in rigid-body point-based registration.* Medical Imaging, IEEE Transactions on, vol. 20, no. 9, pages 917 –927, sept. 2001. (Cited on page 105.)

[Fox 1948] Clement A. Fox, Robert R. Fisher and Salvatore J. Desalva. *The distribution of the anterior commissure in the monkey (Macaca Mulatta). Experimental studies.* The Journal of Comparative Neurology, vol. 89, no. 3, pages 245–277, 1948. (Cited on pages 102 and 107.)

[Foxman 1986] Brett T. Foxman, Jeffrey Oppenheim, Carol K. Petito and Michael S. Gazzaniga. *Proportional anterior commissure area in humans and monkeys.* Neurology, vol. 36, no. 11, page 1513, 1986. (Cited on pages 102 and 108.)

[Frindel 2007] C. Frindel, M. Robini, S. Rapacchi, E. Stephant, Yue-Min Zhu and P. Croisille. *Towards In Vivo Diffusion Tensor MRI on Human Heart using Edge-Preserving Regularization.* In IEEE Engineering in Medicine and Biology Society, pages 6007 –6010, aug. 2007. (Cited on page 87.)

[Frindel 2009] Carole Frindel, Marc Robini, Pierre Croisille and Yue-Min Zhu. *Comparison of Regularization Methods for Human Cardiac Diffusion Tensor MRI.* Medical Image Analysis, vol. 13, no. 3, pages 405 – 418, 2009. (Cited on pages 45 and 66.)

[Gamper 2007] Urs Gamper, Peter Boesiger and Sebastian Kozerke. *Diffusion Imaging of The In Vivo Heart Using Spin Echoes - Considerations on Bulk Motion Sensitivity.* Magnetic Resonance in Medicine, vol. 57, pages 331–337, 2007. (Cited on pages 20, 21, 68, 71 and 90.)

[Garrido 1994] Leoncio Garrido, Van J. Wedeen, Kenneth K. Kwong, Upshur M. Spencer and Howard L. Kantor. *Anisotropy of Water Diffusion in the Myocardium of the Rat.* Circulation Research, vol. 74, pages 789–793, 1994. (Cited on page 3.)

[Gates 2004] W. Lawrence Gates. *Derivation of the Equations of Atmospheric Motion in Oblate Spheroidal Coordinates.* Journal of the Atmospheric Sciences, vol. 61, pages 2478–2487, 2004. (Cited on page 23.)

[Gilbert 2012] Stephen H. Gilbert, David Benoist, Alan P. Benson, Ed White, Steven F. Tanner, Arun V. Holden, Halina Dobrzynski, Olivier Bernus and Aleksandra Radjenovic. *Visualization and quantification of whole rat heart laminar structure using high-spatial resolution contrast-enhanced MRI.* American Journal of Physiology - Heart and Circulatory Physiology, vol. 302, no. 1, pages H287–H298, 2012. (Cited on page 82.)

[Glaunès 2008] J. Glaunès, A. Qiu, I. Michael, Miller and L. Younes. *Large Deformation Diffeomorphic Metric Curve Mapping.* International Journal of Computer Vision, vol. 80, no. 3, pages 317–336, may 2008. (Cited on page 62.)

[Goergen 2011] Craig Goergen and David Sosnovik. *From Molecules to Myofibers: Multiscale Imaging of the Myocardium.* Journal of Cardiovascular Translational Research, vol. 4, pages 493–503, 2011. (Cited on pages 2 and 3.)

[Greenbaum 1981] R A Greenbaum, S Y Ho amd D G Gibson, A E Becker and R H Anderson. *Left ventricular fibre architecture in man.* British Heart Journal, vol. 45, pages 248–263, 1981. (Cited on pages 24, 87 and 90.)

[Grimm 1976] A. F. Grimm, K. V. Katele, Hun-Lin Lin and J. Fletcher. *Fiber bundle direction in the mammalian heart.* Basic Research in Cardiology, vol. 71, pages 381–388, 1976. (Cited on page 2.)

[Gui 2008] Minzhi Gui, Huiling Peng, John D. Carew, Maciej S. Lesniak and Konstantinos Arfanakis. *A tractography comparison between turboprop and spin-echo echo-planar diffusion tensor imaging.* NeuroImage, vol. 42, no. 4, pages 1451 – 1462, 2008. (Cited on page 110.)

[Hansen 1992] P. C Hansen. *Analysis of Discrete Ill-Posed Problems by Means of the L-Curve.* SIAM Review, vol. 34, no. 4, page 561, 1992. (Cited on page 56.)

[Härdle 1985] Wolfgang Karl Härdle and James Stephen Marron. *Optimal Bandwidth Selection in Nonparametric Regression Function Estimation.* Annals of Statistics, vol. 13, no. 4, pages 1465–1481, 1985. (Cited on page 46.)

[Hargreaves 2004] Brian A. Hargreaves, Charles H. Cunningham, Dwight G. Nishimura and Steven M. Conolly. *Variable-Rate Selective Excitation for Rapid MRI Sequences.* Magnetic Resonance in Medicine, vol. 52, pages 590–597, 2004. (Cited on page 71.)

[Hasan 2001] Khader M. Hasan, Dennis L. Parker and Andrew L. Alexander. *Comparison of gradient encoding schemes for diffusion-tensor MRI.* Journal of Magnetic Resonance Imaging, vol. 13, no. 5, pages 769–780, 2001. (Cited on page 87.)

[Helm 2005] Patrick Helm, Mirza F. Beg, Michael I. Miller and Raimond L. Winslow. *Measuring and Mapping Cardiac Fiber and Laminar Architecture Using Diffusion Tensor MR Imaging.* Annals of the New York Academy of Sciences, vol. 1047, no. 1, pages 296–307, 2005. (Cited on page 3.)

[Helm 2006] Patrick A. Helm, Laurent Younes, Mirza F. Beg, Daniel B. Ennis, Christophe Leclercq, Owen P. Faris, Elliot McVeigh, David Kass, Michael I. Miller and Raimond L. Winslow. *Evidence of Structural Remodeling in the Dyssynchronous Failing Heart.* Circulation Research, vol. 98, no. 1, pages 125–132, January 6/20, 2006. (Cited on page 3.)

[Hooks 2007] Darren A. Hooks, Mark L. Trew, Bryan J. Caldwell, Gregory B. Sands, Ian J. LeGrice and Bruce H. Smaill. *Laminar Arrangement of Ventricular Myocytes Influences Electrical Behavior of the Heart.* Circulation Research, vol. 101, no. 10, pages e103–e112, 2007. (Cited on page 84.)

[Horel 1981] James A. Horel and Dennis J. Stelzner. *Neocortical projections of the rat anterior commissure.* Brain Research, vol. 220, no. 1, pages 1 – 12, 1981. (Cited on page 102.)

[Hsu 1998] E. W. Hsu, A. L. Muzikant, S. A. Matulevicius, R. C. Penland and C. S. Henriquez. *Magnetic Resonance Myocardial Fiber-Orientation Mapping With Direct Histological Correlation.* Am J Physiol Heart Circ Physiol, vol. 274, pages 1627–1634, 1998. (Cited on page 3.)

[Hsu 2001] Edward W. Hsu, David L. Buckley, Jonathan D. Bui, Stephen J. Blackband and John R. Forder. *Two-component diffusion tensor MRI of isolated perfused hearts.* Magnetic Resonance in Medicine, vol. 45, no. 6, pages 1039–1045, 2001. (Cited on page 16.)

[Ibanez 2005] L. Ibanez, W. Schroeder, L. Ng, J. Cates*et al. The ITK software guide*. Kitware Inc, 2005. (Cited on page 95.)

[Jackson 1991] John I. Jackson, Craig H. Meyer and Dwight G. Nishimura. *Selection of a Convolution Function for Fourier Inversion Using Gridding*. IEEE Transactions on Medical Imaging, vol. 10, no. 3, pages 473–478, September 1991. (Cited on page 46.)

[Jacobson 2008] Stanley Jacobson and Elliott M. Marcus. Neuroanatomy for the neuroscientist. Springer, July 2008. (Cited on pages 102 and 106.)

[Jansons 2003] Kalvis M Jansons and Daniel C Alexander. *Persistent angular structure: new insights from diffusion magnetic resonance imaging data*. Inverse Problems, vol. 19, no. 5, page 1031, 2003. (Cited on page 16.)

[Jellison 2004] Brian J. Jellison, Aaron S. Field, Joshua Medow, Mariana Lazar, M. Shariar Salamat and Andrew L. Alexander. *Diffusion Tensor Imaging of Cerebral White Matter: A Pictorial Review of Physics, Fiber Tract Anatomy, and Tumor Imaging Patterns*. American Journal Of Neuroradiology, vol. 25, pages 356–369, 2004. (Cited on pages 102 and 106.)

[Johnston 2008] James M. Johnston, Neil Vaishnavi, Matthew D. Smyth, Dongyang Zhang, Biyu J. He, John M. Zempel, Joshua S. Shimony, Abraham Z. Snyder, and Marcus E. Raichle. *Loss of Resting Interhemispheric Functional Connectivity after Complete Section of the Corpus Callosum*. Journal of NeuroScience, vol. 28, no. 25, pages 6453–6458, 2008. (Cited on page 106.)

[Jones 1999] DK Jones, MA Horsfield and A. Simmons. *Optimal strategies for measuring diffusion in anisotropic systems by magnetic resonance imaging*. Magnetic Resonance in Medicine, vol. 42, no. 3, pages 515–525, 1999. (Cited on page 13.)

[Jones 2002] Derek K. Jones, Lewis D. Griffin, Daniel C. Alexander, Marco Catani, Mark A. Horsfield, Robert Howard and Steve C.R. Williams. *Spatial Normalization and Averaging of Diffusion Tensor MRI Data Sets*. NeuroImage, vol. 17, no. 2, pages 592 – 617, 2002. (Cited on page 45.)

[Jones 2004a] Derek K. Jones and Peter J. Basser. *"Squashing peanuts and smashing pumpkins": How noise distorts diffusion-weighted MR data*. Magnetic Resonance in Medicine, vol. 52, no. 5, pages 979–993, 2004. (Cited on page 108.)

[Jones 2004b] D.K. Jones. *The effect of gradient sampling schemes on measures derived from diffusion tensor MRI: A Monte Carlo study*. Magnetic Resonance in Medicine, vol. 51, no. 4, pages 807–815, 2004. (Cited on page 13.)

[Kanai 1995] Anthony Kanai and Guy Salama. *Optical Mapping Reveals That Repolarization Spreads Anisotropically and Is Guided by Fiber Orientation in Guinea Pig Hearts*. Circulation Research, vol. 77, pages 784–802, 1995. (Cited on page 2.)

[KAROL 1971] E. A. KAROL and D. N. PANDYA. *The distribution of the corpus callosum in the Rhesus monkey*. Brain, vol. 94, no. 3, pages 471–486, 1971. (Cited on pages 102 and 107.)

[Kimura 1999] Doreen Kimura. Sex and cognition. MIT Press, Cambridge, 1999. (Cited on page 108.)

[Kindlmann 2007a] G. Kindlmann, D.B. Ennis, R.T. Whitaker and C.-F. Westin. *Diffusion Tensor Analysis With Invariant Gradients and Rotation Tangents.* Medical Imaging, IEEE Transactions on, vol. 26, no. 11, pages 1483 –1499, nov. 2007. (Cited on pages 14 and 15.)

[Kindlmann 2007b] Gordon Kindlmann, Raúl San José Estépar, Marc Niethammer, Steven Haker and Carl-Fredrik Westin. *Geodesic-loxodromes for diffusion tensor interpolation and difference measurement.* In Proceedings of the 10th international conference on Medical image computing and computer-assisted intervention - Volume Part I, MICCAI'07, pages 1–9, Berlin, Heidelberg, 2007. Springer-Verlag. (Cited on page 14.)

[Knutsson 2011] Hans Knutsson, Carl-Fredrik Westin and Mats Andersson. *Representing Local Structure Using Tensors II.* In Anders Heyden and Fredrik Kahl, editeurs, Image Analysis, volume 6688 of *Lecture Notes in Computer Science*, pages 545–556. Springer Berlin / Heidelberg, 2011. 10.1007/978-3-642-21227-7-51. (Cited on page 32.)

[Kohler 2003] Sascha Kohler, Karl-Heinz Hiller, Christiane Waller, Peter M. Jakob, Wolfgang R. Bauer and Axel Haase. *Visualization of myocardial microstructure using high-resolution $T_2^*$ imaging at high magnetic field.* Magnetic Resonance in Medicine, vol. 49, no. 2, pages 371–375, 2003. (Cited on page 82.)

[Kung 2011] Geoffrey L. Kung, Tom C. Nguyen, Aki Itoh, Stefan Skare, Neil B. Ingels, D. Craig Miller and Daniel B. Ennis. *The presence of two local myocardial sheet populations confirmed by diffusion tensor MRI and histological validation.* Journal of Magnetic Resonance Imaging, vol. 34, no. 5, pages 1080–1091, 2011. (Cited on page 84.)

[Lamata 2011] Pablo Lamata, Steven Niederer, David Nordsletten, David C. Barber, Ishani Roy, D. Rod Hose and Nic Smith. *An accurate, fast and robust method to generate patient-specific cubic Hermite meshes.* Medical Image Analysis, vol. 15, no. 6, pages 801 – 813, 2011. (Cited on page 43.)

[Lazar 2003] Mariana Lazar, David M. Weinstein, Jay S. Tsuruda, Khader M. Hasan, Konstantinos Arfanakis, M. Elizabeth Meyerand, Benham Badie, Howard A. Rowley, Victor Haughton, Aaron Field and Andrew L. Alexander. *White matter tractography using diffusion tensor deflection.* Human Brain Mapping, vol. 18, no. 4, pages 306–321, 2003. (Cited on page 50.)

[LeGrice 1995] I. J. LeGrice, B. H. Smaill, L. Z. Chai, S. G. Edgar, J. B. Gavin and P. J. Hunter. *Laminar structure of the heart: ventricular myocyte arrangement and connective tissue architecture in the dog.* American Journal of Physiology - Heart and Circulatory Physiology, vol. 269, no. 2, pages H571–H582, 1995. (Cited on pages 2, 82 and 86.)

[LeGrice 2001] I. J. LeGrice, Y. Takayama and J. W. Covell. *The Architecture of the Heart: a Data-based Model.* Philosophical Transactions: Mathematical, Physical and Engineering Sciences, vol. 359, pages 1217–1232, 2001. (Cited on pages 23 and 24.)

[Livy 1997] D.J. Livy, P.M. Schalomon, M. Roy, M.C. Zacharias, J. Pimenta, R. Lent and D. Wahlsten. *Increased Axon Number in the Anterior Commissure of Mice Lacking a Corpus Callosum.* Experimental Neurology, vol. 146, no. 2, pages 491 – 501, 1997. (Cited on page 102.)

[Lombaert 2011] Hervé Lombaert, Jean-Marc Peyrat, Pierre Croisille, Stanislas Rapacchi, Laurent Fanton, Patrick Clarysse, Hervé Delingette and Nicholas Ayache. *Statistical Analysis of the Human Cardiac Fiber Architecture from DT-MRI.* In Leon Axel and Dimitris Metaxas, editeurs, Proceedings of FIMH Conference 2011, volume 6666 of *LNCS*, pages 171–179. Springer, May 2011. Best Paper Award. (Cited on pages 34, 71 and 81.)

[Lombaert 2012] H. Lombaert, J. Peyrat, P. Croisille, S. Rapacchi, L. Fanton, F. Cheriet, P. Clarysse, I. Magnin, H. Delingette and N. Ayache. *Human Atlas of the Cardiac Fiber Architecture: Study on a Healthy Population.* IEEE transactions on medical imaging, 2012. (Cited on pages 3, 80, 87, 88 and 90.)

[Mall 1911] Franklin P. Mall. *On the muscular architecture of the ventricles of the human heart.* American Journal of Anatomy, vol. 11, no. 3, pages 211–266, 1911. (Cited on page 1.)

[Mansi 2011] T. Mansi, X. Pennec, M. Sermesant, H. Delingette and N. Ayache. *iLogDemons: A Demons-Based Registration Algorithm for Tracking Incompressible Elastic Biological Tissues.* Int. J. of Computer Vision, vol. 92, no. 1, pages 92 – 111, 2011. (Cited on page 27.)

[Meyer 2000] Joel R. Meyer, Arturo Gutierrez, Bryan Mock, Delon Hebron, Jordan M. Prager, Michael T. Gorey and Daniel Homer. *High-b-value Diffusion-weighted MR Imaging of Suspected Brain Infarction.* Magnetic Resonance in Medicine, vol. 21, pages 1821–1829, 2000. (Cited on page 108.)

[Mori 2006] Susumu Mori and Jiangyang Zhang. *Principles of Diffusion Tensor Imaging and Its Applications to Basic Neuroscience Research.* Neuron, vol. 51, no. 5, pages 527 – 539, 2006. (Cited on page 108.)

[Mukherjee 2008] P. Mukherjee, S.W. Chung, J.I. Berman, C.P. Hess and R.G. Henry. *Diffusion Tensor MR Imaging and Fiber Tractography: Technical Considerations.* Journal of Neuroradiology, vol. 29, no. 5, pages 843–852, 2008. (Cited on page 108.)

[Niederer 2009] Steven Niederer, Kawal Rhode, Reza Razavi and Nick Smith. *The Importance of Model Parameters and Boundary Conditions in Whole Organ Models of Cardiac Contraction.* In Nicholas Ayache, Hervé Delingette and Maxime Sermesant, editeurs, Functional Imaging and Modeling of the Heart, volume 5528 of *Lecture Notes in Computer Science*, pages 348–356. Springer Berlin / Heidelberg, 2009. (Cited on page 91.)

[Niederer 2011] S.A. Niederer, G. Plank, P. Chinchapatnam, M. Ginks, P. Lamata, K.S. Rhode, C.A. Rinaldi, R. Razavi and N.P. Smith. *Length-dependent tension in the failing heart and the efficacy of cardiac resynchronization therapy.* Cardiovascular research, vol. 89, no. 2, pages 336–343, 2011. (Cited on page 4.)

[Nielles-Vallespin 2012] Sonia Nielles-Vallespin, Choukri Mekkaoui, Peter Gatehouse, Timothy Reese, Jennifer Keegan, Steven Collins, Peter Speier, Thorsten Feiweier, Marcel Jackowski, David Sosnovik and David Firmin. *Diffusion tensor MRI of the human heart In Vivo with a navigator based free breathing approach.* In Society of Cardiac Magnetic Resonance in Medicine (SCMR), volume 14, pages 1–2. BioMed Central, 2012. (Cited on page 87.)

[Nielsen 1991] P. M. Nielsen, I. J. Le Grice, B. H. Smaill and P. J. Hunter. *Mathematical Model of Geometry and Fibrous Structure of the Heart.* Am J Physiol Heart Circ Physiol, vol. 260, pages 1365–1378, 1991. (Cited on page 23.)

[Oubel 2012] Estanislao Oubel, Mériam Koob, Colin Studholme, Jean-Louis Dietemann and François Rousseau. *Reconstruction of scattered data in fetal diffusion MRI.* Medical Image Analysis, vol. 16, no. 1, pages 28 – 37, 2012. (Cited on page 72.)

[Pajevic 2002] Sinisa Pajevic, Akram Aldroubi and Peter J. Basser. *A Continuous Tensor Field Approximation of Discrete DT-MRI Data for Extracting Microstructural and Architectural Features of Tissue.* Journal of Magnetic Resonance, vol. 154, no. 1, pages 85 – 100, 2002. (Cited on pages 45, 59, 60 and 91.)

[Pandya 1973] Deepak N. Pandya, Eduardo A. Karol and Padmakar P. Lele. *The distribution of the anterior commissure in the squirrel monkey.* Brain Research, vol. 49, no. 1, pages 177 – 180, 1973. (Cited on pages 102 and 107.)

[Parker 2000] Geoffrey J.M. Parker, Julia A. Schnabel, Mark R. Symms, David J. Werring and Gareth J. Barker. *Nonlinear smoothing for reduction of systematic and random errors in diffusion tensor imaging.* Journal of Magnetic Resonance Imaging, vol. 11, no. 6, pages 702–710, 2000. (Cited on page 59.)

[Patel 2010] Markand Patel, Nicolas Toussaint, Geoffrey Charles-Edwards, Jean-Pierre Lin and Philip Batchelor. *Distribution and fibre field similarity mapping of the human anterior commissure fibres by diffusion tensor imaging.* Magnetic Resonance Materials in Physics, Biology and Medicine, vol. 23, pages 399–408, 2010. 10.1007/s10334-010-0201-3. (Cited on page 101.)

[Pennec 2005a] X. Pennec, P. Fillard and N. Ayache. *A Riemannian Framework for Tensor Computing.* International Journal of Computer Vision, vol. 66, no. 1, pages 41–66, 2005. (Cited on page 14.)

[Pennec 2005b] X. Pennec, R. Stefanescu, V. Arsigny, P. Fillard and N. Ayache. *Riemannian elasticity: a statistical regularization framework for non-linear registration.* Med Image Comput Comput Assist Interv Int Conf Med Image Comput Comput Assist Interv, vol. 8, no. Pt 2, pages 943–950, 2005. (Cited on page 31.)

[Perrin 2005] M. Perrin, C. Poupon, Y. Cointepas, B. Rieul, N. Golestani, C. Pallier, D. RiviÃ¨re, A. Constantinesco, D. Le Bihan and J. Mangin. *Fiber Tracking in q-Ball Fields Using Regularized Particle Trajectories.* In Gary Christensen and Milan Sonka, editeurs, Information Processing in Medical Imaging, volume 3565 of *Lecture Notes in Computer Science*, pages 595–634. Springer Berlin (Heidelberg), 2005. (Cited on page 16.)

[Peyrat 2006] Jean-Marc Peyrat, Maxime Sermesant, Xavier Pennec, Chenyang Xu Hervé Delingette, Elliot R. McVeigh and Nicholas Ayache. *A Computational Framework for the Statistical Analysis of Cardiac Diffusion Tensors: Application to a Small Database of Canine Hearts.* IEEE Transactions in Medical Imaging, vol. 25, no. 5, pages 612–625, 2006. (Cited on pages 3, 29, 34, 81, 87 and 90.)

[Peyrat 2009] Jean-Marc Peyrat. *Comparison of Cardiac Anatomy and Function: Statistics on Fibre Architecture from DT-MRI and Registration of 4D CT Images.* Phd thesis, Nice Sophia Antipolis University, November 2009. (Cited on pages 35 and 88.)

[Phillips 1979] SJ Phillips, A. Rosenberg, D. Meir-Levi and E. Pappas. *Visualization of the coronary microvascular bed by light and scanning electron microscopy and x-ray in the mammalian heart.* Scanning Electron Microscopy, no. 3, page 735, 1979. (Cited on page 16.)

[Powell 2008] M. J. D. Powell. *Developments of NEWUOA for Minimization Without Derivatives.* Journal of Numerical Analysis, pages 1–16, February 2008. (Cited on page 49.)

[Reese 1995] Timothy G. Reese, Robert M. Weisskoff, R. Neil Smith, Bruce R. Rosen, Robert E. Dinsmore and Van J. Wedeen. *Imaging Myocardial Fiber Architecture In-Vivo With Magnetic Resonance.* Magnetic Resonance in Medicine, vol. 34, pages 786–791, 1995. (Cited on pages 3 and 19.)

[Risse 1978] G.L. Risse, J. LeDoux, S.P. Springer, D.H. Wilson and M.S. Gazzaniga. *The anterior commissure in man: Functional variation in a multisensory system.* Neuropsychologia, vol. 16, no. 1, pages 23 – 31, 1978. (Cited on page 101.)

[Rockland 1986] K.S. Rockland and D.N. Pandya. *Topography of occipital lobe commissural connections in the rhesus monkey.* Brain Research, vol. 365, no. 1, pages 174 – 178, 1986. (Cited on page 102.)

[Rohde 2004] GK Rohde, AS Barnett, PJ Basser, S. Marenco and C. Pierpaoli. *Comprehensive approach for correction of motion and distortion in diffusion-weighted MRI.* Magnetic Resonance in Medicine, vol. 51, no. 1, pages 103–114, 2004. (Cited on page 72.)

[Rohmer 2006] D. Rohmer and G. T. Gullberg. *A Bloch-Torrey Equation for Diffusion in a Deforming Media.* Rapport technique, University of California, 2006. Technical report Paper LBNL-61295. (Cited on pages 12, 23 and 24.)

[Rohmer 2007] Damien Rohmer, Arkadiusz Sitek and Grant T Gullberg. *Reconstruction and visualization of fiber and laminar structure in the normal human heart from ex vivo diffusion tensor magnetic resonance imaging (DTMRI) data.* Investigative Radiology, vol. 42, no. 11, pages 777–789, Nov 2007. (Cited on page 88.)

[Scollan 1998] D. F. Scollan, Alex Holmes, Raimond Winslow and John Forder. *Histological validation of myocardial microstructure obtained from diffusion*

*tensor magnetic resonance imaging.* American Journal of Physiology - Heart and Circulatory Physiology, vol. 275, no. 6, pages H2308–H2318, 1998. (Cited on pages 3 and 24.)

[Scollan 2000] D. F. Scollan, A. Holmes, J. Zhang and R. L. Winslow. *Reconstruction of Cardiac Ventricular Geometry and Fiber Orientation Using Magnetic Resonance Imaging.* Annals of Biomedical Engineering, vol. 28, pages 934–944, 2000. (Cited on page 71.)

[Seemann 2006] G. Seemann, D.U.J. Keller, D.L. Weiss and O. Dössel. *Modeling human ventricular geometry and fiber orientation based on diffusion tensor MRI.* In Computers in Cardiology, 2006, pages 801 –804, sept. 2006. (Cited on pages 2 and 44.)

[Sermesant 2008] M. Sermesant, J.M. Peyrat, P. Chinchapatnam, F. Billet, T. Mansi, K. Rhode, H. Delingette, R. Razavi and N. Ayache. *Toward patient-specific myocardial models of the heart.* Heart Failure Clinics, vol. 4, no. 3, pages 289–301, 2008. (Cited on pages 2 and 44.)

[Sosnovik 2009] David Sosnovik, Ruopeng Wang, Guangping Dai, Timothy Reese and Van Wedeen. *Diffusion MR tractography of the heart.* Journal of Cardiovascular Magnetic Resonance, vol. 11, pages 1–15, 2009. (Cited on page 3.)

[Spencer 1988] Susan S. Spencer. *Corpus Callosum Section and Other Disconnection Procedures for Medically Intractable Epilepsy.* Epilepsia, vol. 29, pages S85–S99, 1988. (Cited on pages 101 and 102.)

[Spotnitz 1974] Henry M. Spotnitz, William D. Spotnitz, Thomas S. Cottrell, David Spiro and Edmund H. Sonnenblick. *Cellular basis for volume related wall thickness changes in the rat left ventricle.* Journal of Molecular and Cellular Cardiology, vol. 6, no. 4, pages 317 – 331, 1974. (Cited on pages 82 and 86.)

[Stejskal 1965] E.O. Stejskal and J.E. Tanner. *Spin Diffusion Measurements: Spin Echoes in the Presence of a Time-Dependant Field Gradient.* Journal Of Chemical Physics, vol. 42, pages 288–292, 1965. (Cited on pages 10, 12 and 18.)

[Stoeck 2011] Christian T. Stoeck, Nicolas Toussaint and Sebastian Kozerke. *Adaptative Trigger delay for Cardiac Diffusion Weighted MR.* In Book of Abstracts, International Society in Magnetic Resonance in Medicine, Sockholm, June 2010 (ISMRM'10), 2011. (Cited on page 70.)

[Streeter 1969] Daniel D. Streeter, Henry M. Spotnitz, Dali P. Patel, John Ross and Edmund H. Sonnenblick. *Fiber Orientation in the Canine Left Ventricle during Diastole and Systole.* Circulation Research, vol. 24, no. 3, pages 339–347, 1969. (Cited on page 2.)

[Streeter 1973a] Daniel D. Streeter and William T. Hanna. *Engineering Mechanics for Successive States in Canine Left Ventricular Myocardium.* Circulation Research, vol. 33, pages 656–664, 1973. (Cited on page 24.)

[Streeter 1973b] Daniel D. Streeter and William T. Hanna. *Engineering Mechanics for Successive States in Canine Left Ventricular Myocardium (II. Fiber Angle and Sarcomere Length).* Circulation Research, vol. 33, pages 656–664, 1973. (Cited on pages 71 and 81.)

[Streeter 1979] Daniel Streeter. Gross Morphology and Fiber Geometry of the Heart, volume 1, pages 61–112. American Physiology Society, 1979. (Cited on page 2.)

[Tournier 2004] J.-Donald Tournier, Fernando Calamante, David G. Gadian and Alan Connelly. *Direct estimation of the fiber orientation density function from diffusion-weighted MRI data using spherical deconvolution.* NeuroImage, vol. 23, no. 3, pages 1176 – 1185, 2004. (Cited on page 16.)

[Toussaint 2007] N. Toussaint, J.C. Souplet and P. Fillard. *MedINRIA: Medical Image Navigation and Research Tool by INRIA.* In Proc. of MICCAI'07 Workshop on Interaction in medical image analysis and visualization, Brisbane, Australia, 2007. (Cited on page 104.)

[Toussaint 2008] N. Toussaint, T. Mansi, H. Delingette, Nicholas Ayache and M. Sermesant. *An Integrated Platform for Dynamic Cardiac Simulation and Image Processing: Application to Personalised Tetralogy of Fallot Simulation.* In Proc. Eurographics Workshop on Visual Computing for Biomedicine (VCBM), Delft, The Netherlands, 2008. (Cited on page 27.)

[Tseng 1999] Wen-Yih I. Tseng, Timothy G. Reese, Robert M.Weisskoff and Van J. Wedeen. *Cardiac Diffusion Tensor MRI In Vivo Without Strain Correction.* Magnetic Resonance in Medicine, vol. 42, pages 393–403, 1999. (Cited on pages 3, 19 and 21.)

[Tseng 2003] Wen-Yih I. Tseng, Van J. Wedeen, Timothy G. Reese, R. Neal Smith and Elkan F. Halpern. *Diffusion Tensor MRI of Myocardial Fibers and Sheets: Correspondence With Visible Cut-Face Texture.* Magnetic Resonance in Medicine, vol. 42, pages 17–31, 2003. (Cited on pages 68 and 69.)

[Tuch 2002] David S. Tuch, Timothy G. Reese, Mette R. Wiegell, Nikos Makris, John W. Belliveau and Van J. Wedeen. *High angular resolution diffusion imaging reveals intravoxel white matter fiber heterogeneity.* Magnetic Resonance in Medicine, vol. 48, no. 4, pages 577–582, 2002. (Cited on page 15.)

[Tuch 2004] David S. Tuch. *Q-ball imaging.* Magnetic Resonance in Medicine, vol. 52, no. 6, pages 1358–1372, 2004. (Cited on page 16.)

[Turk 1999] G. Turk and J.F. O'brien. *Variational implicit surfaces.* Technical Report, Georgia Institute of Technology, 1999. (Cited on page 27.)

[Turner 1979] Blair H. Turner, Mortimer Mishkin and Margaret E. Knapp. *Distribution of the anterior commissure to the amygdaloid complex in the monkey.* Brain Research, vol. 162, no. 2, pages 331 – 337, 1979. (Cited on pages 102 and 106.)

[Ursell 1985] PC Ursell, PI Gardner, A Albala, JJ Fenoglio and AL Wit. *Structural and electrophysiological changes in the epicardial border zone of canine myocardial infarcts during infarct healing.* Circulation Research, vol. 56, no. 3, pages 436–451, 1985. (Cited on page 2.)

[Usyk 2000] T.P. Usyk, R. Mazhari and A.D. McCulloch. *Effect of Laminar Orthotropic Myofiber Architecture on Regional Stress and Strain in the Canine Left Ventricle.* Journal of Elasticity, vol. 1, pages 143–164, 2000. (Cited on page 13.)

[Vadakkumpadan 2012] F. Vadakkumpadan, H. Arevalo, C. Ceritoglu, M. Miller and N. Trayanova. *Image-Based Estimation of Ventricular Fiber Orientations for Personalized Modeling of Cardiac Electrophysiology.* Medical Imaging, IEEE Transactions on, vol. PP, no. 99, page 1, 2012. (Cited on pages 44 and 61.)

[Vendelin 2002] Marko Vendelin, Peter H. M. Bovendeerd, Jüri Engelbrecht and Theo Arts. *Optimizing ventricular fibers: uniform strain or stress, but not ATP consumption, leads to high efficiency.* American Journal of Physiology - Heart and Circulatory Physiology, vol. 283, no. 3, pages H1072–H1081, 2002. (Cited on page 2.)

[Weinstein 1999] David Weinstein, Gordon Kindlmann and Eric Lundberg. *Tensorlines: advection-diffusion based propagation through diffusion tensor fields.* In Proceedings of the conference on Visualization '99: celebrating ten years, VIS '99, pages 249–253, Los Alamitos, CA, USA, 1999. IEEE Computer Society Press. (Cited on pages 50 and 105.)

[Westin 2002] C.-F. Westin, S. Maier, H. Mamata, A. Nabavi, F. Jolesz and R. Kikinis. *Processing and Visualization for Dffusion Tensor MRI.* Medical Image Analysis, vol. 6, no. 2, pages 93–108, 2002. (Cited on page 15.)

[Wong 2010] Ken Wong, Florence Billet, Tommaso Mansi, Radomir Chabiniok, Maxime Sermesant, Hervé Delingette and Nicholas Ayache. *Cardiac Motion Estimation Using a ProActive Deformable Model: Evaluation and Sensitivity Analysis.* In Oscar Camara, Mihaela Pop, Kawal Rhode, Maxime Sermesant, Nic Smith and Alistair Young, editeurs, Statistical Atlases and Computational Models of the Heart, volume 6364 of *Lecture Notes in Computer Science*, pages 154–163. Springer Berlin / Heidelberg, 2010. (Cited on page 91.)

[Wu 2006] Ming-Ting Wu, Wen-Yih I. Tseng, Mao-Yuan M. Su, Chun-Peng Liu, Kuan-Rau Chiou, Van J. Wedeen, Timothy G. Reese and Chien-Fang Yang. *Diffusion Tensor Magnetic Resonance Imaging Mapping the Fiber Architecture Remodeling in Human Myocardium After Infarction.* Circulation, vol. 114, no. 10, pages 1036–1045, 2006. (Cited on pages 2 and 3.)

[Wu 2007] Ed X. Wu, Yin Wu, John M. Nicholls, Jie Wang, Songyan Liao, Shuguang Zhu, Chu-Pak Lau and Hung-Fat Tse. *MR Diffusion Tensor Imaging Study of Postinfarct Myocardium Structural Remodeling in a Porcine Model.* Magnetic Resonance in Medicine, vol. 58, pages 687–695, 2007. (Cited on page 3.)

[Wu 2009] Ming-Ting Wu, Mao-Yuan M. Su, Yi-Luan Huang, Kuan-Rau Chiou, Pinchen Yang, Huay-Ben Pan, Timothy G. Reese, Van J. Wedeen and Wen-Yih I. Tseng. *Sequential Changes of Myocardial Microstructure in Patients Postmyocardial Infarction by Diffusion-Tensor Cardiac MR.* Circulation: Cardiovascular Imaging, vol. 2, pages 32–40, 2009. (Cited on page 92.)

[Xu 2002] D. Xu, S. Mori, M. Solaiyappan, P.C.M. van Zijl. and C. Davatzikos. *A framework for callosal fiber distribution analysis.* NeuroImage, vol. 17, pages 1131–1143, 2002. (Cited on page 104.)

[Yang 2012] Feng Yang, Yue-Min Zhu, Isabelle E. Magnin, Jian-Hua Luo, Pierre Croisille and Peter B. Kingsley. *Feature-based interpolation of diffusion tensor fields and application to human cardiac DT-MRI.* Medical Image Analysis, vol. 16, no. 2, pages 459 – 481, 2012. (Cited on page 55.)

[Zipoy 1966] David M Zipoy. *Topology of Some Spheroidal Metrics.* Journal of Mathematical Physics, vol. 6, page 1137, 1966. (Cited on page 23.)